Alma Mater Studiorum – Università di Bologna

DOTTORATO DI RICERCA IN ASTRONOMIA

Ciclo XXIII
Settore Scientifico Disciplinare: FIS/05

Background minimization issues for next generation hard X-ray focusing telescopes

PhD Thesis of:
Valentina Fioretti

Supervisor:
Prof. Giorgio G. C. Palumbo

PhD Coordinator:
Prof. Lauro Moscardini

Co–Supervisor:
Dott. Giuseppe Malaguti

Esame finale 2011

Scuola di Dottorato in Science Matematiche, Fisiche e Astronomiche
PhD Thesis in Astronomy

This PhD Thesis has been carried out
at the INAF/IASF Bologna as part
of the institute's research activities

Two statisticians are out hunting when one of them sees a duck. The first takes aim and shoots, but the bullet goes sailing past six inches too high. The second statistician also takes aim and shoots, but this time the bullet goes sailing past six inches too low. The two statisticians then give one another high fives and exclaim, "Got him!".

Anonymous, from Wolfram MathWorld

Contents

Abstract **xix**

1 The hard X-rays in focus **1**
1.1 Introduction . . . 1
1.2 The technological concept . . . 2
1.3 The background minimization as key requirement . . . 4
1.4 Simbol-X and NHXM as case studies . . . 5
1.5 A cook book for background evaluation . . . 8

2 Hard X-ray view of AGN: the state of the art **9**
2.1 The scientific case . . . 10
2.2 Observations and data analysis . . . 11
2.3 Spectral analysis . . . 13
2.3.1 Simple model . . . 14
2.3.2 Partial covering model . . . 14
2.3.3 Double power law model . . . 15
2.3.4 Compton reflection . . . 15
2.4 3C 452 . . . 15
2.4.1 Extraction of the AGN emission . . . 16
2.4.2 Spectral fitting . . . 17
2.5 3C 105 . . . 19
2.5.1 Spectral fitting . . . 19
2.6 Swift J0318.7+6828 . . . 21
2.6.1 Spectral fitting . . . 23
2.7 Swift J0918.5+0425 . . . 24
2.7.1 Spectral results . . . 24
2.8 Long term variability . . . 25
2.8.1 3C 452 . . . 26
2.8.2 3C 105 . . . 28
2.8.3 Swift J0318.7+6828 . . . 28
2.8.4 Swift J0918.5+0425 . . . 29

2.9 Summary and discussion . . . 29
2.10 The NHXM view . . . 31

3 The space radiation environment 35
3.1 The diffuse photonic background . . . 37
3.2 Cosmic rays . . . 38
3.2.1 Solar modulation . . . 40
3.2.2 The geomagnetic cut-off . . . 41
3.2.3 GCR model . . . 44
3.3 Trapped particles . . . 46
3.4 Albedo particles . . . 49
3.4.1 Albedo charged particles . . . 50
3.4.2 Albedo photons . . . 51
3.4.3 Albedo neutrons . . . 56
3.5 Soft protons . . . 57
3.6 Earth's shielding . . . 60
3.7 The modelled space radiation environment . . . 61

4 Shielding design 65
4.1 Interaction with matter . . . 66
4.1.1 The photonic component . . . 66
4.1.2 Charged particles . . . 68
4.1.3 Neutrons induced background . . . 70
4.2 Active and passive shielding . . . 71
4.3 The perfect shielding . . . 72
4.3.1 No alignment tolerance case (T = 0) . . . 72
4.3.2 Alignment tolerance (T≠ 0) case . . . 73
4.4 Simbol-X passive shielding design . . . 74
4.4.1 DSC passive shielding . . . 74
4.4.2 MSC passive shielding . . . 74
4.4.3 MSC passive shielding mass . . . 79
4.5 NHXM passive shielding . . . 80
4.6 Shielding analytical optimization: the IXO case . . . 81
4.6.1 IXO X-ray attenuation requirements . . . 82
4.6.2 Single layer configuration results . . . 83
4.6.3 Graded shielding configuration . . . 87
4.6.4 General results and missing ingredients . . . 90

5 BoGEMMS: the Bologna Geant4 Multi-Mission Simulator 93
5.1 The algorithm in three steps . . . 94
5.1.1 Physics processes . . . 95

5.1.2 Geant4 output . . . 96
5.2 Analysis . . . 97
5.2.1 Normalization of an isotropic flux in space . . . 97
5.3 Preliminary tests . . . 99
5.3.1 Interaction with a slab . . . 99
5.3.2 Interaction with a box . . . 100

6 Background evaluation 103
6.1 Simbol-X background . . . 103
6.1.1 MSC passive shielding optimization . . . 104
6.1.2 Detection efficiency . . . 107
6.1.3 DSC background results . . . 112
6.2 NHXM background . . . 116
6.2.1 Background results . . . 117
6.2.2 Characterization of the shielding efficiency . . . 119
6.3 Soft protons induced background . . . 119
6.3.1 Soft protons funnelling . . . 121
6.3.2 Interaction with the XMM-Newton optics . . . 123
6.3.3 Interaction with the Simbol-X optics . . . 126

7 The background in LEO: general results 127
7.0.4 The simulation set–up . . . 128
7.1 Case A background evaluation . . . 129
7.1.1 Background sources . . . 132
7.1.2 CXB component . . . 135
7.1.3 Proton component . . . 136
7.1.4 Electron and positron component . . . 138
7.1.5 Albedo photons component . . . 138
7.1.6 Albedo neutrons component . . . 139
7.2 Case B background evaluation . . . 140
7.3 Case C background evaluation . . . 142
7.4 AC threshold analysis . . . 144
7.5 Summary of the results . . . 145

8 Summary and future remarks 149

A Derivation of a perfect shielding geometry parameters 153

B The BoGEMMS physics list 155
B.1 Particles . . . 155
B.2 Electromagnetic processes . . . 155
B.3 Hadronic processes . . . 157

List of Figures

1.1 A schematic view of the operating mode of an indirect imaging system, at left, respect to a focusing telescope, at right. For the same effective area A_{Eff}, the X-ray grazing angle reflection allows to collect the X-ray photons in a much smaller detection area. 3

1.2 Artist view of the NHXM satellite in space, from Tagliaferri et al. (2010). The four mirror modules are hosted by the platform at top-right, while the four cameras are on the opposite platform (the four collimators are visible), connected by an extendable bench. 6

1.3 The New Hard X-ray Mission sensitivity, in red, and, as comparison, the sensitivity reached by INTEGRAL/ISGRI and BeppoSAX/PDS, indirect imaging and collimated instruments respectively. At low energies the two lines refer to two different operating modes of the low energy detector. Picture from the INAF/OAB NHXM webpage. 7

2.1 Chandra/ACIS (left panel) and Suzaku/XIS1 (right panel) 0.5 - 2 keV images of 3C 452, with the 1.4 GHz VLA radio map superimposed with green contours. The white circle indicated the Suzaku 2.2' radius extracting region. 16

2.2 *Left panel*: Chandra/ACIS spectrum of the 2.2' radius region centred on the AGN (black), the AGN alone (red) and the extended region with the AGN region subtracted (green). *Right panel*: Suzaku/XIS1 observed spectrum (black) and simulated spectra of the AGN emission alone (red) and the extended emission (green). 17

2.3 Folded (left panel) and unfolded (right panel) spectra and best fit models of 3C 452: Black = XIS-FI, Red = XIS-BI, Green = HXD/PIN, Blue = Swift/BAT. 18

2.4 Folded (left panel) and unfolded (right panel) spectra and best fit models of 3C 105: Black = XIS-FI, Red = XIS-BI, Green = HXD/PIN, Blue = Swift/BAT. 19

2.5 Folded (left panel) and unfolded (right panel) spectra and best fit models of Swift J0318.7+6828: Black = XIS-FI, Red = XIS-BI, Green = HXD/PIN, Blue = Swift/BAT. 23

2.6 Folded (left panel) and unfolded (right panel) spectra and best fit models of Swift J0918.5+0425: Black = XIS-FI, Red = XIS-BI, Green = HXD/PIN, Blue = Swift/BAT. 24

2.7 The background unsubtracted PIN (at the top), background (in the middle) light curves and their ratio (at the bottom) of J0918.5+0425 are plotted before (left panel) and after (right panel) the removal of the background corrupted time interval. The goodness of the ratio fit by a constant function is also reported for the two cases. . 25

2.8 Unfolded spectrum of 3C 105 as observed by Swift/XRT (2006-07-11/16, black line), Chandra/ACIS (2007-12-17, red line), Suzaku/XIS (2008-02-05, green line) and XMM-Newton (2008-02-25, blue line). 28

2.9 Folded (left panel) and unfolded (right panel) simulated spectra of 3C 105 as seen by NHXM, for the same ~ 40 ks exposure. The black and red lines refer to the LED and HED respectively. 31

2.10 The expected NHXM background used as input for the 3C 105 simulation. The horizontal lines refer to a Non X-ray Background level of $1 \times 10^{-3}$and 2×10^{-4} cts cm^{-2} s^{-1} keV^{-1} for the LED and HED respectively. 32

3.1 Compilation of observations of the extragalactic high energy background from Oberlack (2010). 37

3.2 Daily averaged intensity of the ACE Electron, Proton, and Alpha Monitor (EPAM) P3 channel, centered on about 0.14 MeV. 39

3.3 The differential spectra of cosmic rays for Hydrogen, Helium, Carbon, and Iron given by Simpson (1983). The solid line shows the Hydrogen spectrum corrected for the solar modulation. 40

3.4 *Left panel*: Effect of the solar activity (top) on the flux of secondary neutrons (bottom), generated by cosmic rays interactions with the atmosphere, detected by the Neutron Monitor of Thule, Greenland (courtesy of the Bartol Research Institute, University of Delaware). *Right panel*: Number of sunspots prediction of the solar cycle 24 according to the NASA NOAA (National Oceanic and Atmospheric Administration) Space Weather Prediction Center of Boulder, Colorado. 41

3.5 Level of solar modulation as a function of time, from late 1997 through August 2008, using the ACE CRIS C, O, Mg, Si and Fe data (courtesy of the ACE team). 42

3.6 Contours map of the cut-off rigidity for a 450-km orbiting spacecraft as given by Smart & Shea (2005). 43

3.7 *Left panel*: The distribution of the low energy cut-off as a function of the dipole shell parameter L along the magnetic equator. *Right Panel*: The low energy cut-off of GCR protons as given by the magnetic latitude for a LEO (altitude = 550 km, red line) and HEO (altitude = 70000 km, blue line) orbit. The orizontal dashed line refers to a rigidity cut-off of 1 MeV. 44

3.8 *Left panel*: Primary proton spectrum, as modelled by Mizuno et al. (2004), expected in LEO for a magnetic latitude of 80° (red line) and 20° (blue line), with a solar modulation $\Phi = 650$ MV (thick line), 800 MV (medium line) and 1100 MV (thic line). *Right panel*: GCR proton flux integrated from 10 MeV to 100 GeV as a function of the solar modulation parameter Φ (MV) for a HEO (red line) and LEO orbit (blue line), computed for a magnetic latitude of 20°. 45

3.9 The total differential proton flux modelled for the HEO Simbol-X (red line) and LEO NHXM (blue line) missions. The low energy protons arising below the geomagnetic cut-off in the NHXM case are due to the CR interaction with the Earth's atmosphere (albedo protons, see Sec. 3.4) 46

3.10 The count rate (left panel) and corrispondent spacecraft altitude (right panel) of the protons and electrons impinging on the XMM-Newton spececraft as detected by the Low Energy (LE) radiation monitor along a 48 hr exposure. Both plots are taken from the XMM live radiation monitor feed. 47

3.11 *Top panel*: Radiationm belts leaking in LEO detected by the Rosat (altitude = 575 km, $\lambda_{\rm m} = 53°$) South Atlantic Anomaly Detector (SAAD, Snowden et al. (1992)); the SAA is the central peak, while the polar regions are reached by the outer belt electrons. *Bottom panel*: Omnidirectional SAA electrons and protons flux (left) detected by the Compton Gamma Ray Observatory (CGRO) mission (altitude = 500 km, Dean et al. (2003) and references therein) and SAA induced temporal variation of the background count rate (right) of the Suzaku/HXD detectors (Kokubun et al. 2007). 48

3.12 The air shower produced by the CR interaction with the Earth's atmosphere as reported in Dean et al. (2003). 49

3.13 Albedo electrons and positrons spectra as expected for the NHXM orbit, based on observations of the AMS and MARYA-2 experiments and provided by the AGILE team. 50

3.14 *Left panel*: The Earth X-ray albedo as observed by INTEGRAL/SPI (Churazov et al. 2007), INTEGRAL/IBIS (Türler et al. 2010) and Swift/BAT (Ajello et al. 2008). The thin dotted lines show the decomposition of the Churazov et al. (2007) observation in CXB reflection (< 50 keV) and the CR induced emission at higher energies, while the black line refers to the CXB flux for comparison. *Right panel*: The total X-ray albedo modelled for the NHXM (red line) and the Swift/BAT (blue line) orbit. The latter is shown in comparison with the real Swift/BAT observation (continuous black line), while the dotted black line is the modelled CXB induced component, which, in units of solid angle, does not depend on the orbit inclination and it results to be the same fot both orbits. 53

3.15 The maximum latitude region intercepted by a LEO spacecraft orbiting at a magnetic inclination $\lambda_{\rm m}$. 54

3.16 The Earth's atmosphere γray albedo as expected along the NHXM orbit (red line, Mizuno et al. (2004)) and as a comparison, the computed spectrum of Dean et al. (1989) at the geomagnetic equator (green line) and the albedo observed by the Agathe experiment (Lavigne et al. 1982) at $\lambda_{\rm m} = -23.5°$. The black line is the modelled X-ray albedo which connects to the γ-ray emission at 1 MeV. 55

3.17 The omnidirectional albedo neutron flux, at solar monimum, as modelled by Armstrong & Colborn (1992), continuous line , and Morris et al. (1995), dashed line, for two orbital positions: altitude of 450 km at $\lambda_{\rm m} = 42°$ (blue lines) and altitude of 550 km at the geomagnetic equator (red line). 57

3.18 Folded light curve of soft proton flares detected by XMM-Newton EPIC/pn along 10 orbits, selecting the events with E> 10 keV, FLAG = 0 and PATTERN = 0 (Fioretti et al. 2006). 58

3.19 Differential flux, in prot. $\rm cm^{-2}\ s^{-1}\ keV^{-1}\ sr^{-1}$, of the low energy protons as detected by the Equator-S (red line, from Nartallo (2002)) at $\sim$ 70000 km altitude, and by the ACE mission (blue line, from Spiga et al. (2008)) in L1. 59

3.20 The modelled space radiation environment in HEO (top panel) and LEO (bottom panel). The latter refers to the NHXM orbit. 62

4.1 The dependence of the dominant process, among the photoelectric effect, Compton scattering and pair production, on the material atomic number and incident photon energy. 67

4.2 Stopping power in Lead (Pb) for protons (left panel) and electrons (right panel), as given by the PSTAR and ESTAR NIST databases respectively. 69

4.3 The basic simplified geometry of the passive shielding assembly with no misalignment effects (left panel) and with the addition of a lateral tolerance $\pm$T (right panel). The blue horizontal line on the top indicates the external optics diameter, $\mathbf{D_{opt}}$. The green lines represent the sky screen (on the top, with total diameter $\mathbf{D_{Screen}}$) and collimator walls (on the bottom, with height **H**). The purple line on the bottom is the detection plane which has a dimension of $\mathbf{D_{det}}$ and is separated by **s** from the collimator walls. **FL** is the telescope focal length. The horizontal red lines in the right panel account for the spacecrafts alignment tolerance. 73

4.4 a): Face-on MSC geometry and main dimensions (misures in mm). b): 3D view of the spacraft with height dimension (misures in mm). The arrow shows the DSC direction on flight. 75

4.5 3D view of the mirror module (left) and zoom (right) on the MSC adapter (misures in mm). The arrow shows the DSC direction in flight. 75

4.6 *Left panel*: The CXB flux, in photons cm^{-2} s^{-1} keV^{-1}, calculated at three different energies as a function of the emission solid angle (in sr). *Blue line*: the CXB flux at 5 keV; *red line*: the CXB flux at 30 keV; green line: the CXB flux at 80 keV. The continuous horizontal black line refers to the total maximum background level. The dotted and dashed vetical lines are respectively the solid angle covered by the adapter holes and by the MSC passive shielding on the focal plane. *Right panel*: The sky screen diameter as a function of the collimator height with (blue line) and without (red line) the lateral dithering. 78

4.7 The sky screen diameter as a function of the collimator height with (blue line) and without (red line) the lateral dithering 81

4.8 Schematic view of the passive shielding system optimization process. 82

4.9 Au (left panel) and Ta (right panel) X-ray transparency (%) as a function of the incident photon energy for a thickness of 259 μm (red line), 200 μm (green line) and 150 μm (blue line). The black horizontal and dashed lines show the instruments maximum allowed transparency and the energy for which is required respectively. . 84

4.10 X-ray transparency (%) for a 150 μm thich Au (red line) and a 200 μm thick (blue line) Ta layer. 84

4.11 Simplified not-in-scale design of the passive shielding system (in purple) on the IXO focal plane assembly. 85

4.12 CXB induced residual X-ray background on the IXO focal plane for a Au (left panel) and Ta (right panel) composition. *Blue line*: incident CXB flux; *red continuous line*: residual background flux; *red dashed line*: fluorescence lines; *yellow boxes*: maximum allowed background level required by each instrument. 86

4.13 CXB induced residual X-ray background for an Au thickness of 800 μm (left panel) and a Ta thickness of 900 μm (right panel). 87

4.14 Residual background for a main absorber of Au (150 μm LoS) and a grading of Sn + Cu + Al + C in order to shield the CXB up to 40 keV (Case A, left panel) and 80 keV (Case B, right panel). 89

4.15 Residual background for a main absorber of Au (150 μm LoS) and a grading of Al + C in order to shield the CXB up to 40 keV (Case A). 89

4.16 Residual background for a main absorber of Au and the grading Set 1 (Case A) using a C thickness of 0.5 mm. 90

4.17 Residual background for a main absorber of Ta (200 μm LoS) and a grading of Sn + Cu + Al + C in order to shield the CXB up to 40 keV (Case A, left panel) and 80 keV (Case B, right panel). 90

4.18 Residual background for a main absorber of Ta (200 μm LoS) and a grading of Al + C in order to shield the CXB up to 40 keV (Case A). 91

5.1 The BoGEMMS architecture: the simulator, composed by the physics and geometry libraries, receives in input the particle flux and the configuration file setting the geometry, the physics processes and the output file, that is finally produced in FITS format and read by the IDL based analysis software, which returns in the end the background and AC spectral files. 95
5.2 The energy distribution of X-ray photons exiting a slab of 1.5 mm thick Ta after the CXB interaction, for the activation of the low energy (red line) and standard (green line) electromagnetic processes. The dashed lines refer to the Ta fluorescence emission. 96
5.3 Angular and spatial distribution of the simulated particles. 98
5.4 The Geant4 3D model of a slab of Tantalum (at right) placed in front of the simplified NHXM hybrid focal plane, composed by the LED (in yellow) and the HED (in red). The green lines show the trajectory of the CXB photons emitted by a parallel beam from the right. 99
5.5 Photons exiting from the 1.5 mm thick Ta slab after the CXB interaction and directed to the focal plane (left panel) and to the sky (right panel). 100
5.6 *Left panel*: CXB induced residual background (red line) reaching the focal plane for a 1.5 mm thick Ta shielding. The dashed lines refer to the Ta K fluorescence lines. *Right panel*: CXB induced background on LED (blue line) and HED (red line) for a 1.5 mm thick Ta layer completely surrounding the focal plane. 101

6.1 The Simbol-X Geant4 mass model on which is based the background simulation. The DSC is shown in grey at the left, while the MSC passive shielding is shown in red. The green line is the telescope axis, passing through the collimator aperture (in purple). 104
6.2 Face-on (a), lateral (b) and backside (c) visualization of the MSC passive shielding mass model: the hexagonal sky screen and adapter cover are shown in red while the blue cylinder approximates the mirror module. In (b) and (c) panels the DSC direction is on the left. 105
6.3 MSC passive shielding residual backgrund induced by the CXB interaction for a total mass budget of 15 kg. The simulation is performed for a main absorber of Pb (top panels) and Ta (bottom panels), with (right panels) and without (left panels) the addition of the graded layers. 106
6.4 The Simbol-X DSC Geant4 mass model wired view. Part of the collimator is visible at the top, the rectangular shape is the external Al box, while the two detectors are placed in the center. The green line is the trajectory followed by 1 MeV photon beam, crossing the focal plane without interacting and then partially reflected by bottom surface. 107
6.5 Schematized configuration of the Simbol-X focal plane as given by Dirks et al. (2006). The Mirror Spacecraft (MSC) is at the top. The LED is represented in red while the HED is shown in light blue. 108

6.6 Interaction of a monochromatic planar beam of 100 keV photons (green lines) with LED (in grey). The source surface is a square (8 cm side) placed above the focal plane (on the right). The base ring of annular shape shadows the LED and the detection active area is reduced to a circle. The red lines are electrons. 109
6.7 Simbol-X total detection efficiency (continuous line) resulting from the Geant4 simulation of the pixellated configuration compared to the analytical absorption efficiency (dotted line) calculated with the NIST attenuation coefficients. 111
6.8 Schematized view of the active and passive shielding on board the Simbol-X DSC. Figure from Chipaux et al. (2008). 112
6.9 LED, blue line, and HED, red line, CXB induced background spectra in the 0.5 - 20 keV and 5 - 100 keV energy ranges respectively. The AC is switched on, i.e. the coincidence events with the active shield are removed, and the plotted counts refer to a maximum pattern of 4. The vertical dashed lines show the K fluorescence of the passive layers. 113
6.10 LED, blue line, and HED, red line, GCR induced background spectra in the 0.5 - 20 keV and 5 - 100 keV energy ranges respectively, in "AC off" (left panel) and "AC on" (right panel) for a pattern $\leq$ 4. The vertical dashed lines show the K fluorescence of the passive layers and of the HED Cd and Te materials. 114
6.11 Percentage of dead time affecting the LED for a read-out time of 256 μs as a function on the AC count rate. The dead time is calculated following a simple, nonparalyzable (continuous line) and a paralyzable response model (continuous–dotted line). . . . 115
6.12 *Left panel*: The Geant4 mass model of the camera hosting the X-ray detectors. The red box surrounds the LED and HED and it is contituted by the plastic AC, placed externally, and the passive graded layers. The green structure is the passive collimator, and the whole camera is less than 1.5 m long. *Right panel*: A zoom to the LED (in yellow) and HED (in red) detectors hosted within the camera. The collimator aperture is visible in the right part of the image. 116
6.13 Attenuation efficiency of a Tantalum main absorber, based on the X-ray attenuation coefficients provided by the NIST database, for a Line of Sight (LoS) thickness of 1.5 mm (continuous line), 1 mm (dotted line) and 0.5 mm (dashed line). 117
6.14 The NHXM LED (blue line) and HED (red line) simulated background spectra induced by the CXB flux, in "AC off" (left panel) and "AC on" (right panel) mode. 118
6.15 The NHXM LED (blue line) and HED (red line) simulated background spectra induced by the proton flux, in "AC off" (left panel) and "AC on" (right panel) mode.119
6.16 Probability distribution of the energy loss (top panel) and angular distribution (bottom panel), as respects the telescope axis, of 500 keV protons after the interaction with an XMM mirror shell. The red and light blue lines refer to the activation of the multiple and Firsov scattering for an incident angle, as respects the telescope axis, of 0.2° and 3°, while the green and blue lines refer to the only multiple scattering, for the same incident angles as the Firsov case. 122

6.17 The XMM-Newton simplified Geant4 model: the mirror module is at right, the EPIC/pn is visualized in yellow and the circular blue structure in front of the detector is the thick filter. 123
6.18 The radial distribution of the detected protons, in prot. mm^{-2}, for radial bins of 5 mm. The left panel refers to total proton flux, while the right panels shows the protons generating a count below 10 keV. 124
6.19 The image of the simulated soft proton flare. The counts rate is plotted in unit of cts s^{-1} per pixel. 124
6.20 The simulated proton induced background spectrum (in red) compared to the observation (in blue) of the EPIC/pn (left panel) and EPIC/MOS (right panel). The intial energy distribution of the protons generating the counts is shown in black. 125
6.21 The simulated proton induced background spectrum below 10 keV, and the related energy distribution 125
6.22 The energy (left panel) and angular (right panel) distribution of the protons exiting the Simbol-X optics. Only the multiple scattering is applied. 126

7.1 The modelled space radiation environment in LEO for the NHXM orbit. 128
7.2 The box Geant4 mass model as seef from the side (the mirror module is at the top). The left and right figures refer to an external and internal AC configuration respectively. 128
7.3 LED (top panel) and HED (bottom panel) background spectra for the Case A configuration in "AC off" mode for each class of emitted particles. The black line refers to the total background flux. The AC threshold is 200 keV. 130
7.4 LED (top panel) and HED (bottom panel) background spectra in "AC on" mode for each class of emitted particles. The black line refers to the total background flux. The AC threshold is 200 keV. 131
7.5 LED (left panel) and HED (right panel) energy distribution of the photons that finally interact with the detection plane, for the Case A configuration in "AC off" mode. 134
7.6 LED (left panel) and HED (right panel) energy distribution of the electrons that finally interact with the detection plane, for the Case A configuration in "AC off" mode. 134
7.7 CXB induced photons generating the counts on the LED (left panel) and HED (right panel). *black line*: Photons energy distribution; *red line*: photons induced energy deposits on the focal plane. 135
7.8 Proton induced photons generating the counts on the LED (left panel) and HED (right panel). *black line*: Photons energy distribution; *red line*: Photons induced energy deposits on the focal plane. 137
7.9 Proton induced electrons generating the counts on the LED (left panel) and HED (right panel). *black line*: Electrons energy distribution; *red line*: Electrons induced energy deposits on the focal plane. 137

7.10 Electron induced photons (left panel) and electrons (right panel) generating the counts on the HED. *black line*: Energy distribution; *red line*: Energy deposits on the focal plane. 138
7.11 The X-ray albedo induced photons generating the counts on the LED (left panel) and HED (right panel). *black line*: Energy distribution; *red line*: Energy deposits on the focal plane. 139
7.12 The γ-ray albedo induced photons generating the counts on the LED (left panel) and HED (right panel). *black line*: Energy distribution; *red line*: Energy deposits on the focal plane. 139
7.13 The albedo leaking neutrons generating the counts on the LED (left panel) and HED (right panel). *black line*: Energy distribution; *red line*: Energy deposits on the focal plane. 140
7.14 LED (left panel) and HED (right panel) background spectra for the CaseB configuration in "AC off" mode for each class of emitted particles. The black line refers to the total background flux. The AC threshold is 200 keV. 140
7.15 LED (left panel) and HED (right panel) background spectra for the Case B configuration in "AC on" mode for each class of emitted particles. The black line refers to the total background flux. The AC threshold is 200 keV. 141
7.16 LED (top panel) and HED (bottom panel) background spectra for the Case C configuration in "AC off" mode for each class of emitted particles. The black line refers to the total background flux. The AC threshold is 200 keV. 142
7.17 LED (top panel) and HED (bottom panel) background spectra for the Case C configuration in "AC on" mode for each class of emitted particles. The black line refers to the total background flux. The AC threshold is 200 keV. 143
7.18 AC count rate (left panel) and a comparison (right panel) of the LED (blue line) and HED (red line) background levels as a function of the AC thresholds. 145
7.19 LED (left panel) and HED (right panel) energy averaged background levels, in "AC on" mode, for different AC thresholds. To be noted that the y-axis is plotted in a logarithmic scale. 145
7.20 The LED, left panel, and HED, right panel, energy averaged background levels, in "AC off" and "AC on" mode respectively, for the Case A (external plastic AC, red columns), Case B (internal plastic AC, green columns) and Case C (internal NaI AC, yellow columns). 146
7.21 The AC count rate for the Case A (external plastic AC, red columns), Case B (internal plastic AC, green columns) and Case C (internal NaI AC, yellow columns). 147

List of Tables

1.1 Main NHXM top level scientific requirements. 6

2.1 Description of the sources main properties and radio, optical, host galaxy classification from literature. 12
2.2 Suzaku XIS and HXD/PIN observations log. 13
2.3 The best fit parameters resulting from the analysis of the Suzaku XIS and HXD/PIN spectra with the addition of the 9-month averaged BAT spectrum. 20
2.4 Observed and absorption corrected flux and luminosity in the 0.5 - 2 keV, 2 - 10 keV, 10 - 40 keV and 14 - 195 keV energy ranges. 22
2.5 The spectral properties from the Chandra, XMM-Newton and Swift/XRT data as analyzed here or collected from literature. 27
2.6 Comparison of the best fit parameters of the 3C 105 spectral analysis as observed by Suzaku and expected for NHXM. 32

3.1 Orbital parameters of the major high energy mission currently operative as a comparison with the planned orbit of the Simbol-X and NHXM missions. 36
3.2 Solid angle, in sr, covered by each class of background source for a HEO and LEO orbit. 60
3.3 Energy range and integrated flux of the modelled background sources in HEO and LEO. 61

4.1 Atomic number, density and Kα fluorescence energy of the main absorber materials under study. 71
4.2 Atomic number, density and Kα fluorescence energy of grading materials under study. 71
4.3 Basic trade–off analysis definitions. 74
4.4 DSC collimator baseline configuration. 74
4.5 DSC collimator segments size. 74
4.6 MSC sky screen dimensions. 76
4.7 MSC adapter dimensions. 77
4.8 Thickness and mass of MSC passive shielding required to absorb the 99% of photons at 40 keV (main absorber) and the 99% of fluorescence photons for the graded layers. 79
4.9 NHXM baseline dimensions for the passive shielding trade-off analysis. 80

4.10 NHXM sky screen diameter for a perfect shielding. 80
4.11 IXO instruments X-ray background and attenuation requirements. 82
4.12 Single layer materials under study and their main properties. 83
4.13 Grading thickness and surface density for a main absorber of Au 88
4.14 Grading thickness and surface density for a main absorber of Ta 88

6.1 LED and HED Geant4 configuration. 108
6.2 Analytical evaluation of LED and HED absorption efficiency. 111
6.3 The Simbol-X LED and HED energy averaged background level in cts cm^{-2} s^{-1} keV^{-1}. 114
6.4 The proton induced background counts pattern distribution for LED and HED. . . 115
6.5 Composition and mass budget of the NHXM preliminary shielding design. 117
6.6 The NHXM LED and HED energy averaged background level in cts cm^{-2} s^{-1} keV^{-1}.119
6.7 The fraction of proton induced background counts generated by a first interaction with the listed external volumes. 120
6.8 The composition and thickness of the thick optical blocking filter. The layer number starts from the closest position to the detector. 123

7.1 Background count rate, in cts cm^{-2} s^{-1} keV^{-1}, for the Case A configuration. The last two columns show the fraction of LED and HED counts triggered by the AC and the total AC count rate (in cts s^{-1}). The AC threshold is 200 keV. 129
7.2 Percentage of detected counts generated by photons, electrons, positrons and neutrons in "AC off" mode ("others" collects the sum of counts induced by others particles). The total values are normalized for the number of detected counts induced by each class of particles and the simulated exposure time. 133
7.3 Percentage of detected counts generated by photons, electrons, positrons and neutrons in "AC on" mode ("others" collects the sum of counts induced by others particles). The total values are normalized for the number of detected counts induced by each class of particles and the simulated exposure time. 133
7.4 Background count rate, in cts cm^{-2} s^{-1} keV^{-1}, for the Case B configuration, resulting from an AC threshold of 200 keV. 141
7.5 Background count rate, in cts cm^{-2} s^{-1} keV^{-1}, for the Case C configuration, resulting from an AC threshold of 200 keV. 143

Acronyms

AC: Anticoincidence

ACIS: Advanced CCD Imaging Spectrometer

AGN: Active Galactic Nucleus

BGO: Bismuth Germanate, BiGdO

BI: Back-Illuminated

BAT: Burst Alert Telescope

BoGEMMS: Bologna Geant4 Multi-Mission Simulator

CCD: Charge-Coupled Device

CTE: Charge Transfer Efficiency

CZT: Cadmium Zinc Telluride, CdZnTe

CR: Cosmic Ray

CXB: Cosmic X-ray Background

DSC: Detector Spacecraft

EPIC: European Photon Imaging Camera

ES: Equator-S

FITS: Flexible Image Transport System

GCR: Galactic Cosmic Ray

GPS: General Particle Source

HEW: Half Energy Width

HED: High Energy Detector

HEO: High Elliptical Orbit

HXD: Hard X-ray Detector

FI: Front-Illuminated

FL: Focal Length

FOV: Field of View

FPA: Focal Plane Assembly

FWHM: Full Width Half Maximum

HPD: Half Power Diameter

HXD: Hard X-ray Detector

IC: Inverse Compton

LED: Low Energy Detector

LEO: Low Earth Orbit

MOS: Metal Oxide Semi-conductor

MSC: Mirror Spacecraft

NIEL: Non Ionizing Energy Loss

NIR: Near Infrared

NLR: Narrow Line Region

NXB: Non X-ray Background

PSF: Point Spread Function

RS: Raymond-Smith

SAA: South Atlantic Anomaly

SEE: Single Event Effect

SEP: Solar Energetic Particle

SEU: Single Event Upset

SMBH: Super Massive Black Hole

XIS: X-ray Imaging Spectrometer

Abstract

The hard X-ray band (10 - 100 keV) has been only observed so far by collimated and coded aperture mask instruments, with a sensitivity and an angular resolution lower than two orders of magnitude as respects the current X-ray focusing telescopes operating below 10 - 15 keV. The technological advance in X-ray mirrors and detection systems is now able to extend the X-ray focusing technique to the hard X-ray domain, filling the gap in terms of observational performances and providing a totally new deep view on some of the most energetic phenomena of the Universe. In order to reach a sensitivity of 1 μCrab in the 10 - 40 keV energy range, a great care in the background minimization is required, a common issue for all the hard X-ray focusing telescopes. In the present PhD thesis, a comprehensive analysis of the space radiation environment, the payload design and the resulting prompt X-ray background level is presented, with the aim of driving the feasibility study of the shielding system and assessing the scientific requirements of the future hard X-ray missions. A Geant4 based multi-mission background simulator, BoGEMMS, is developed to be applied to any high energy mission for which the shielding and instruments performances are required. It allows to interactively create a virtual model of the telescope and expose it to the space radiation environment, tracking the particles along their path and filtering the simulated background counts as a real observation in space. Its flexibility is exploited to evaluate the background spectra of the Simbol-X and NHXM mission, as well as the soft proton scattering by the X-ray optics and the selection of the best shielding configuration. Altough the Simbol-X and NHXM missions are the case studies of the background analysis, the obtained results can be generalized to any future hard X-ray telescope. For this reason, a simplified, ideal payload model is also used to select the major sources of background in LEO. All the results are original contributions to the assessment studies of the cited missions, as part of the background groups activities.

Chapter 1

The hard X-rays in focus

1.1 Introduction

X-rays are emitted from energetic phenomena throughout the Universe, powered by strong gravity (around compact stars and black holes) and magnetic fields (neutron stars), shocks (supernova remnants) and extended potential wells (clusters of galaxies). In order to overcome the opacity of the Earth's atmosphere, sensitive X-ray instruments must be taken to high altitude by balloons, rockets and satellites. For this reason, X-ray Astronomy has become only recently possible, with the first non-solar celestial X-ray source (Sco X–1) discovered in 1962 with Geiger counters on a sounding rocket flight (Giacconi et al. 1962).
The first imaging X–ray telescope, mounting Wolter–1 grazing angle optics, to orbit the Earth was launched in 1978 on board the HEAO–2 (Einstein) satellite. Operating in the 0.2 – 20 keV energy range, it recorded a tremendous improvement of signal-to-noise and angular resolution compared to collimated counter devices. The advance in X-ray mirror technology below 10 keV can be found, at present, in the unprecedented angular resolution (0.5") and collection area (4300 cm^2 at 1.5 keV) of respectively Chandra and XMM-Newton missions, reaching a sensitivity around 1 μCrab. On the other hand, the hard X–ray band (10 – 100 keV) has been observed up to now by collimated (e.g. SAS–3, BeppoSAX/PDS) and coded aperture masks (e.g. INTEGRAL/IBIS, Swift/BAT) instruments, with a gap of two orders of magnitude in terms of sensitivity and angular resolution. This unexplored observational window will be fullfilled by the future hard X–ray focusing telescopes, thanks to the advance in mirror technology (e.g. multilayers) and detection systems (e.g. CdTe based instruments), providing a breakthrough on a number of hot astrophysical issues including: a black holes census, the physics of accretion, particle acceleration mechanisms, the effects of radiative transfer in highly magnetized plasmas and strong gravitational fields. Several missions have been proposed, from the NASA Nustar, scheduled for launch in 2012, to the more recent New Hard X–ray Mission (NHXM, Tagliaferri et al. (2010)) proposed to the ESA call for medium missions by an european joint team. These missions, although with different scientific goals, will be equipped with broad band (up to 80 keV) high angular resolution ($<$ 20 arcsec HEW for NHXM) grazing incidence mirrors, with a 10 meter focal length, in order to achieve

an unprecedented sensitivity of 1 μCrab[1] in the 10–30 keV band. Given the direct dependance of the minimum detectable flux from the background radiation, great care in the background minimization is a common requirement for all future hard X-ray telescopes.

1.2 The technological concept

In a focusing X-ray telescope, the X-ray photons are funnelled to the focal plane by means of double grazing angle reflections by paraboloid hyperboloid (Wolter type I) optics (Giacconi et al. 1969). The total reflection of X-ray is only possible for incident angles lower than a critical angle α_c, which depends on the energy of the incident photons E and the density of the reflecting medium ρ as follows:

$$\alpha_c \propto \frac{\sqrt{\rho}}{E} . \tag{1.1}$$

High reflection efficiency is achieved for smooth surfaces (5 - 10 Å) and the deposition of heavy metal coatings (e.g. Au, Pt) on the X-ray optics shells. The previous formula also sets an upper limit to the energy distribution of the focused photons. For example, the critical reflecting angle for Platinum ($\rho = 21.4$ g cm^3) is 0.8° at 5 keV and $< 0.15°$ at 30 keV.
The total effective area, A_{Eff} of a grazing angle X-ray telescope is given by:

$$A_{Eff} \propto FL^2 \times \alpha_c^2 \times Refl^2 , \tag{1.2}$$

where FL is the focal length and Refl the X-ray optics reflectivity.
The limited reflectivity in the hard X-ray energy range of the flown X-ray optics, the energy dependance of the critical angle and a focal length lower than 8 m, limited by the available physical space in the launcher, cause the effective area to fall off for energies $> 10 - 15$ keV, limiting the operative energy range of the present X-ray telescopes (e.g. XMM-Newton, Chandra). For this reason, the hard X-ray domain has been observed at present by means of indirect imaging instruments (e.g. INTEGRAL/IBIS, Swift/BAT), based on the coded aperture technique (Renaud et al. 2006), or non imaging collimated detectors (e.g. BeppoSAX/PDS, Suzaku/HXD) where the X-ray photons are simply collected within the aperture defined by the collimator. The main consequences of the lack of focusing telescopes above 10 keV is the reduced angular resolution, from $< 1''$ for the Chandra/ACIS detector to $\sim 12'$ for INTEGRAL/IBIS, and, most of all, the loss of 2 - 3 order of magnitude in sensitivity, i.e. the minimum detectable flux, respect to the values achieved below 10 keV by Chandra and XMM-Newton.
The tremendous gap in the observing performance is due to the extended detection surface, of the same order of the area where the photons are collected, required by a non focusing intrument. This implies the development of detectors covering a surface of ~ 1 m^2, which in turn poses several problems on the feasibility of such systems in space and on the background level. A comparison of the different X-ray collecting modes of an indirect imaging system respect to a focusing telescope is shown in Figure 1.1. For the same effective area, an X-ray grazing angle focusing telescope allows to drastically reduce the detection system because the photons are funnelled to a significantly

[1] A flux of 1 μCrab in the 10 - 30 keV energy range is equivalent to 1.28×10^{-14} erg cm^{-2} s^{-1}.

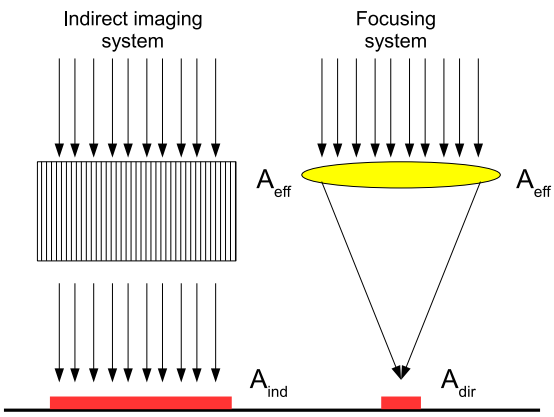

Figure 1.1: A schematic view of the operating mode of an indirect imaging system, at left, respect to a focusing telescope, at right. For the same effective area A_{Eff}, the X-ray grazing angle reflection allows to collect the X-ray photons in a much smaller detection area.

smaller area.

If we define B the background level, T the exposure time, ΔE the energy range and A_d the detection area, and assume the latter being approximately equal to the effective area A_{Eff}, the minimum detectable flux of a non focusing system is described by:

$$F_{min} \propto \frac{1}{A_{Eff}} \sqrt{\frac{B\, A_d}{T\, \Delta E}} \approx \sqrt{\frac{B}{A_d\, T\, \Delta E}}\,, \tag{1.3}$$

i.e. the sensitivity depends on $A_d^{-1/2}$, and in order to increase it by 10, the detection surface must be 100 times higher.

As example, the coded aperture CdTe instrument IBIS/ISGRI on board INTEGRAL operates between 15 keV and 1 MeV, with an effective area of 2600 cm^2 and a sensitivity of ~ 200 μCrab in the 20 - 40 keV band. If we want te achieve the Chandra sensitivity, ~ 0.5 μCrab, in the hard X-ray domain, a detection area $> 10^5$ cm^2 would be needed, which is totally unfeasible.

The extension of the X-ray grazing angle focusing technique above 10 - 15 keV is the only way to achieve a real breakthrough in the observation of the hard X-ray Universe. The development of a hard X-ray focusing telescope is today possible thanks to many technological advances in the field:

- Multilayers based X-ray optics (Pareschi et al. 2005) allowing a good reflectivity, and consequently a sufficient effective area, in the tens of keV but still ensuring a wide field of view.

- A hybrid focal plane, composed by two overlapped detection planes, sharing the same axis. A Silicon based detectors operates in the low energy range (as, for example, the XMM-Newton EPIC/pn), while high resolution up to 80 - 100 keV is achieved thanks to the development of CZT semiconductors as hard X-ray detectors, with a larger band-gap respect to Si, no need for significant cooling and high photoelectric cross section at tens of keV (Tumer et al. 2004).

- A longer focal length (> 10 m), in order to increase the effective area above 10 keV, can

be achieved by means of deployable structure that extends the distance between the mirror module and the focal plane when the spacecraft is in space or by means of the formation flight technique, where the optics and the detectors are placed on two different spacecraft and then connected by a laser pointing. In the latter solution, the focal length must be longer than 20 m to avoid a collision between the two modules.

1.3 The background minimization as key requirement

The sensitivity of a focusing X-ray telescope is given by:

$$F_{min} = n_{\sigma} \frac{\sqrt{B \cdot A_d}}{\varepsilon \cdot \eta \cdot (1-\beta) \cdot A_{eff}^{i} \cdot \sqrt{N \cdot T \cdot \Delta E}} \qquad \text{phot. cm}^{-2}\text{s}^{-1}\text{keV}^{-1} . \tag{1.4}$$

The parameter of Equation 1.4 are described as follows:

Parameter	Description	unit
B	Background flux	cts cm $^{-2}$s^{-1}keV^{-1}
A_d	Spot area of each of each X-ray shell	cm^2
A^i_{eff}	Effective area of the i-shell	cm^2
N	Total number of X-ray optics shells	/
η	Fraction of X-ray photons reflected to A_d	/
ε	Quantum efficiency	/
β	Dead area fraction	/
n_σ	Detection statistics significancy	/
T	Exposure time	s
Δ E	Energy bandwidth	keV

The effective area A_{eff} is much larger than the spot area A_d, allowing to increase sensitivity. However, ensuring a large effective area above 10 keV is not enough to reach a sensitivity of 1 μCrab if the background level is too high. The minimum detectable flux is in fact strictly connected to the total background level, defined in this context as the sum of all the events not generated by the observed astrophysical source. As a result, the ability of revealing the nature of the X-ray sources, from the physics processes generating the X-ray photons to the geometry and composition of the emitters, is strictly connected to the knowledge of the background noise environment. The essential problem is that the observation of the X-ray Universe must be performed beyond the Earth's atmosphere. In such intense radiation fields, high energy particles interact with the spacecraft and instruments material, generating cascades of secondaries into the focal plane, so that it is difficult to disentangle the few counts produced by the celestial source from the complex X-ray background noise arising from all directions.
The minimization of the background flux must face several problems, enhanced by the development of new technological solution:

- The hard X-ray domain is strongly affected by the charged particles induced background. As a result, the passive high absorbing material surrounding the focal plane of the current

soft X-ray telescope must be coupled to an active shields that triggers if a particles deposits a certain amount of energy, allowing the removal of the related background count. The anticoincidence system, however, can increase the observation dead time, and a dedicated feasibility study is required.

- The long focal length avoids the use of a optical bench connecting the focal plane to the mirror module, implying the search for alternative shielding geometries that must be feasible to space applications.

- The longer focal length also increases the plate scale, i.e. the region of the detector subtended by a certain angle at the focal length distance, so that the surface brightness of the target covers a greater detector surface and the background contribution is higher.

1.4 Simbol-X and NHXM as case studies

The Simbol-X observatory (Ferrando et al. 2004) was a CNES–ASI innovative mission aimed to focus the entire X-ray energy range, from 0.5 to 80 keV, by means of Ni–electroforming multilayers X-ray optics placed at a focal length of 20 m from the detection plane. Such a long focal length is achieved thanks to the formation flight technology, placing the mirror module and the focal plane on two distinct spacecrafts. A high quantum efficiency along the entire energy range is guaranteed by the combination of two detectors, a Low Energy Detector (LED) covering the 0.5 - 20 keV, and a High Energy Detector (HED) sensitive from 5 to 80 keV. The LED and HED shared the same axis, so that the X-ray photons had to cross the LED and, if above the LED operative range, the HED plane. The Simbol-X mission was ready to start the Phase B study in early 2009, when the CNES budget issues declared the mission aborted.
As an evolution of the HEXIT–SAT project (Fiore et al. 2004; Pareschi & the HEXIT-SAT and SIMBOL-X collaborations 2004) and after the cancellation of the Simbol–X mission, the New Hard X-ray Mission (NHXM) is a hard X-ray mission (Tagliaferri et al. 2010) proposed by a joint european team to the ESA medium mission call in 2010.
NHXM has been designed to provide a real breakthrough on a number of hot astrophysical issues including, confirming the outstanding scientific throughput of the Simbol-X mission (Fiore et al. 2008): a black holes census, the physics of accretion, particle acceleration mechanisms, the effects of radiative transfer in highly magnetized plasmas and strong gravitational fields. It will be equipped with four broad band (0.5 – 80 keV) high angular resolution (< 20 arcsec HEW) grazing incidence mirrors (Pareschi et al. 2009), with a 10 meter focal length, achieved after launch by means of a deployable structure. Three of the four telescopes will have at their focus identical spectral-imaging cameras, based on the Simbol-X focal plane design, while X-ray imaging polarimetric cameras, covering the 2 – 35 keV band with unprecedented sensitivity, will be placed at the focus of the fourth. The use of a polarimeter on board an X-ray telescope will allow for the first time to study in detail at the same time the polarization and spectroscopic properties of the Universe.
The top scientific requirements of the NHXM X-ray imaging spectrometers, as defined by the core scientific objectives, are summarized in Table 1.1, and in agreement with the values required by

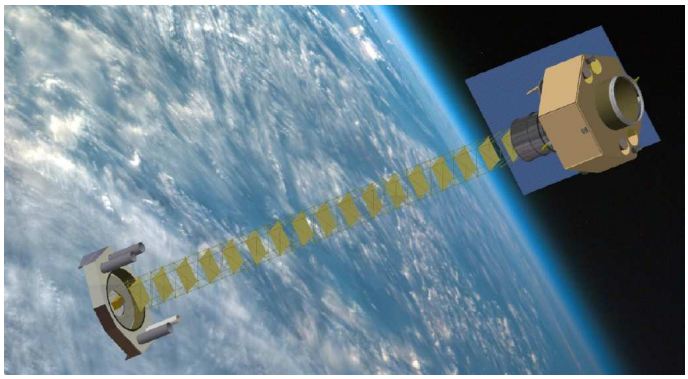

Figure 1.2: Artist view of the NHXM satellite in space, from Tagliaferri et al. (2010). The four mirror modules are hosted by the platform at top-right, while the four cameras are on the opposite platform (the four collimators are visible), connected by an extendable bench.

the Simbol-X mission, due to the similarity in the focal plane design and scientific goals.

Parameter	Requirement
Energy band	0.2 - 80 keV
Field of view (at 30 keV)	$\geq 12'$ (diameter)
On-axis effective area	≥ 100 cm^2 at 0.5 keV ≥ 1000 cm^2 at 2 - 5 keV ≥ 600 cm^2 at 8 keV ≥ 350 cm^2 at 30 keV ≥ 100 cm^2 at 70 keV
On-axis sensitivity	< 1 μCrab (3σ, T = 1 Ms) at 10–40 keV
Angular resolution (HPD)	$\leq 20''$ for E$<$ 30 keV $\leq 40''$ at 60 keV
Background level	$\leq 1 \times 10^{-3}$ cts cm^{-2} s^{-1} keV^{-1} for LED (AC off) $\leq 2 \times 10^{-4}$ cts cm^{-2} s^{-1} keV^{-1} for HED (AC on)

Table 1.1: Main NHXM top level scientific requirements.

The maximum allowed background level for the LED does not require the removal of the coincidence counts with the active shield (AC off), on the contrary the HED background takes into account only the ancticoincidence events (AC on). If the background requirement is satisfied, the NHXM

sensitivity would be below μCrab in the 10 - 40 keV band (for deep, 1 Ms long survey observations), 2 - 3 orders of magnitude lower respect to the INTEGRAL/ISGRI and BeppoSAX/PDS instrument (Figure 1.3).

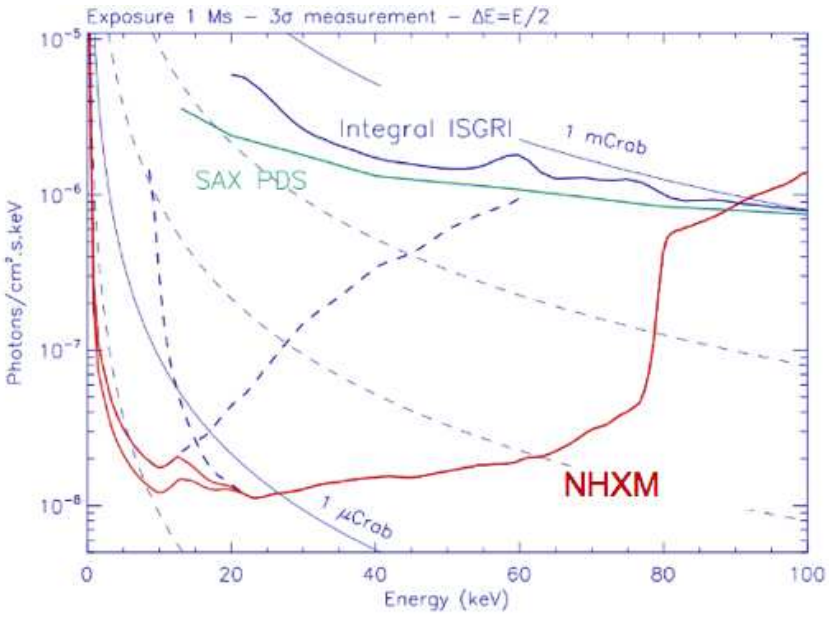

Figure 1.3: The New Hard X-ray Mission sensitivity, in red, and, as comparison, the sensitivity reached by INTEGRAL/ISGRI and BeppoSAX/PDS, indirect imaging and collimated instruments respectively. At low energies the two lines refer to two different operating modes of the low energy detector. Picture from the INAF/OAB NHXM webpage.

The improvements in the X-ray Astronomy fields given by such deep and high resolution observations are so many that an entire PhD thesis would be needed. For this reason, we selected one of the major scientific topics, the search of Compton thick AGN and the study of the accretion-reflection processes (Chapter 2), to show a comparison between the actual status of the X-ray observations and the future NHXM view of the hard X-ray domain.
In the present thesis, the Simbol-X and NHXM missions are used as case studies for the background minimization of a hard X-ray focusing telescope. However, the same technological concept is shared by many of the proposed future hard X-ray missions: the NASA Nustar (Harrison et al. 2011), the NASA/JAXA ASTRO–H (Takahashi et al. 2010) or the ESA–NASA International X-ray Observatory (IXO, Barcons et al. (2011)). In other words, these missions have to deal with the same background minimization issues of Simbol-X and NHXM, so that all the results presented here can be generalized to any future X-ray telescope. In fact, part of the shielding optimization is dedicated to the IXO mission assessment study.
This is especially true because the Simbol-X satellite was planned to fly on a high elliptical orbit, while for NHXM a low Earth orbit has beed chosen. These two orbits, as explained in detail in Chapter 3, common for the past and most of the future missions, imply a different space radiation environment and, as a consequence, different background sources. As a result, we can affirm that

a comprehensive study of the background minimization issues for a general hard X-ray focusing telescope is presented.

1.5 A cook book for background evaluation

The aim of the background group of a space mission is twofold: it must drive the design of the shielding system, to be used as input for the engineering feasibility study, and evaluate the total background level, to be used as input in the calibration phase and in the development of the ground-based data filtering.
The working process that leads from the knowledge of the particle environment to the characterization of the background flux and energy distribution can be summarized in the following steps, reflecting the structure of the present thesis:

1. Modelling of the space radiation environment expected for the planned orbit (Chapter 3).
2. Definition of the shielding design required for the selected background sources, given by the analysis of the space particles interaction with matter (Chapter 4).
3. Preliminary shielding design optimization achieved by means of analytical computations of the shielding absorption efficiency and induced residual background (Chapter 4).
4. Development of Monte Carlo simulations of the whole telescope, allowing the tracking and characterization of the particles interaction (both primaries and secondaries) with the spacecraft and detectors materials, and the consequent analysis algorithms for both the on board and ground based data treatment (Chapter 5).
5. The background spectra and count rate production, the characterization of the spacecrafts components and particles generating the background counts and final definition of the shielding design (Chapters 6 and 7).

All the results presented here have been included in the assessment studies of the Simbol-X and NHXM missions, as part of the respective background group activities.
At the end of the thesis, the reader won't find any "magic" background value to be associated to the cited missions. The reason is that the background evaluation is a growing process strictly connected to the evolving status of the mission, so that it can not be definitive until the mission is assembled. On the contrary, the general results achieved in the background analysis (see Chapter 8) represent an important tool for the development of any next generation hard X-ray telescope.

Chapter 2

Hard X-ray view of AGN: the state of the art

Absorption by circumnuclear gas and dust surrounding the accreting supermassive black hole (SMBH) is a common feature of Active Galactice Nuclei (AGN). According to the unified model (Antonucci 1993), different observational features can be explained on the basis of the AGN orientation with respect to the observer, such that an object is classified as unobscured Type 1 AGN if the central broad line region appears in the optical spectrum, while the lack of these features occurs if the nuclear regions are seen at larger inclination angles and the line if sight intercept optically thick cold matter distributed in a toroidal geometry covering $\sim 80\%$ of the solid angle. This model is supported by both X-ray (Bassani et al. (1999), Tozzi et al. (2006), Cappi et al. (2006)) and IR observations (Alonso-Herrero et al. (2006), Fiore et al. (2008)), where a large fraction of AGN presents column densities greater than 3×10^{22} cm^{-2}.

If the bulk of the SMBH growth is expected during an obscured phase of the AGN evolution (Hopkins et al. 2006), and its accretion is tightly connected to the galaxy bulge evolution and starburst activity in a feedback process (Ferrarese & Merritt (2000), Brandt & Hasinger (2005)), the complete census of the obscured AGN is a fundamental issue to unlock the growth history of the Universe. In the local universe, about 50% of optically selected Seyfert 2 (Risaliti et al. (1999), Guainazzi et al. (2005)) is Compton thick ($N_H > 1.5 \times 10^{24}$ cm^{-2}). Current synthesis models of the Cosmic X-ray Background (CXB), given by the contribution of unobscured and obscured AGN integrated over the cosmic time (Setti & Woltjer (1989), Comastri et al. (1995)), predict that a high percentage of Compton thick AGN contribute to the energy density peak at 30 keV (Gilli et al. 2001).

Despite the high penetrating power of X-ray photons, the nature of this population is still elusive due to strong biases against their detection, because the nucleus is almost blocked by the thick absorber below 10 keV. In this context, hard X-ray surveys above 10-15 keV performed in the recent years by the coded aperture Swift/BAT (14 - 195 keV, Tueller et al. (2010)) and INTEGRAL/IBIS (10 - 100 keV, Beckmann et al. (2009)), so far represent an unique tool to obtain a complete, unbiased sample of AGN for column densities $< 3 \times 10^{25}$ cm^{-2}.

Such a detailed analysis requires more than the N_H evaluation. Other important observational clues are found along the entire X-ray spectrum: from the large equivalent widths of the Fe K line to the flattened slope and the broad bump peaking around 20 - 30 keV due to Compton down-scattering of high energy photons.
The development of wide band X-ray focusing telescopes, covering the full X-ray energy range, represents a fundamental breakthrough in the search for highly absorbed AGN and the study of the composition and geometry of the surronding matter. Waiting for that moment, the actual state of the art of AGN hard X-ray spectral analysis can be achieved by combining the power of the soft X-ray observations, the NASA/JAXA Suzaku X-ray Imaging Spectrometers (XIS) in this case, to the detection performed by hard X-ray collimated or indirect imaging instruments.
The Suzaku collimated Hard X-ray Detector (HXD) extends the bandpass of the XIS up to 600 keV with an unprecedented sensitivity in the 10 - 100 keV energy range (Takahashi et al. 2007). Its energy range is exploited to study within the same Suzaku observation the soft/hard X-ray emission of four AGN from the 9-month Swift/BAT survey (Tueller et al. 2008). Hydrogen column density, scattered/reflected emission, properties of the Fe K line are fully analyzed along with their variability, while the 9-month averaged Swift/BAT spectrum helps to better constrain the spectral shape in the hard X-ray domain.
Some important results are obtained from the present analysis. Other features, left unresolved due to the spectral quality of the data, could be fullfilled by the next generation hard X-ray missions: in Section 2.10 the comparison between the Suzaku observation and the NHXM simulated view of one of our targets is shown as an example of the potential improvement in the spectral analysis, if the background requirement, which defines the top level scientific goals of the mission, is satisfied.
The spectral analysis results presented here will be fully reported in Fioretti et al. in prep.

2.1 The scientific case

The Swift/BAT 9-month catalog collects 153 AGN, all with BAT fluxes (14-195 keV) in excess of 10^{-11} erg cm^{-2} s^{-1} and an average redshift of 0.03. Among them, four of the most luminous BAT AGN ($44.73 < \mathrm{LogL_{BAT}} < 45.31$) have been selected as targets of follow-up Suzaku observation.
The reason behind the choice to focus on absorption and reflection of high X-ray luminosity AGN is the dependency of the obscured fraction of AGN on the luminosity function. The difficulty in mapping the space density of highly obscured AGN in the local Universe is overcome by the big uncertainties in the determination of the column density distribution as a function of luminosity and cosmic time, which is strictly correlated to the accretion history and evolution of AGN. While there is still a big debate on the redshift distribution of obscured AGN (La Franca et al. (2005), Ballantyne et al. (2006), Treister et al. (2010)), in the last decade both X-ray (Ueda et al. (2003), La Franca et al. (2005)), optical (Simpson 2005) and infrared (Fiore et al. 2009) seem to confirm the inverse proportionality of the obscured population as a function of the luminosity, with a moderately obscured to unobscured sources ratio decreasing from 4 to 1 for $L_X \leq 10^{42}$ and $L_X \geq 10^{45}$ respectively (Gilli et al. 2007). In this context, the full characterization of the obscuring matter surrounding high luminosity AGN helps to disentangle the various interpretations (Hasinger

(2008), Diamond-Stanic et al. (2009)) and to better constrain the N_H-L_X correlation.

2.2 Observations and data analysis

The targets of our analysis are Swift J2246.0+3941 (3C 452), J0407.4+0339 (3C 105), J0318.7+6828 and J0918.5+0425. Their basic information is summarized in Table 2.1, listing also the host galaxy, AGN radio and optical classification collected from literature. The first two targets, J2246.0+3941 and J0407.4+0339, are well-known 3C catalog FRII Radio Galaxies, and we will refer to them as 3C 452 and 3C 105, while J0318.7+6828 is an FRII Giant Radio Galaxy (GRG) with a linear size of 2 Mpc. Optical spectra, available for all the sources, identify our targets as Type II AGN. The latter, and farthest, J0918.5+0425 has been identified as AGN for the first time by the 9-month Swift/BAT survey, but then removed from the 22-month survey because of variability (Tueller et al. 2010).

The Japanese Suzaku (ASTRO-E2) X-ray mission, launched in 2005, achieves its wide (0.2–600 keV) X-ray range through the combination of four imaging CCD cameras, the X-ray Imaging Spectrometers, with a non-imaging, collimated Hard X-ray Detector (HXD). Each XIS detector, three front (XIS-0,2,3) and one back illuminated (XIS-1), is located in the focal plane of a dedicated X-ray telescope with a bandpass in the range 0.2 keV – 12 keV, while the HXD consists of Si PIN photo-diodes and GSO scintillation counters, covering respectively the 10 keV – 70 keV and 40 keV – 600 keV energy range (Mitsuda et al. (2007)).

Suzaku observed our sources (in HXD nominal pointing) between 2007 June and 2008 February (see observations details in Table 2.2). Since the FI (front illuminated) XIS-2 detector became inoperable on 2006 November, no XIS-2 data are available for our sources. We present the analysis of XISs and HXD/PIN data, since the flux of our targets was too faint to be detected by HXD/GSO. In addition to the Suzaku data, in the spectral analysis we also integrate the BAT spectra in the 14 keV – 195 keV band, time averaged over the 9-month survey, to better constrain the fit.

Except for 3C 105, characterized by shorter detections, the net (dead time corrected) exposure spans from about 60 to 80 ks for the XIS-BI, and from about 50 to 65 ks for the high energy detector.

Observation products (spectra, images, light curves) are extracted from the cleaned version 2.3.12.25 processed events files distributed by the Suzaku team, using the most recent `HEAsoft` package. The XIS source spectra and light curves, generated combining together the 3×3 and 5×5 edit modes in `xselect`, are extracted from circular regions, with a radius ranging from 2.2' to 4.2'. The minimum 2.2' radius region is used for 3C 452, allowing to take more than 80% of the point source photons (see Suzaku technical description) while avoiding contamination from external sources in the field, while a 4.2' radius region collects the 99% of the point source flux. Background spectra are extracted from nearby free emission regions of about 2.2–5 arcmin radius. After producing the rmf and arf response matrices with the `xisrmfgen` and `xissimarfgen` tools provided by the Suzaku team, we combine the two XIS-FI spectra and responses with `addascaspec` for faster spectral fits, grouping (with `grppha`) both XIS-FI and XIS-BI source spectra using a factor greater than 25 cts/bin.

List of Targets[a]

Source	R.A.	Dec.	Redshift	Log L_{BAT}[b]	Optical type[c]	Radio type[d]	Host Galaxy[e]	Ref.[f]
3C 452	341.4532	39.6877	0.0811	44.73	Sy 2	FRII RG	E	1, 2, 3
3C 105	61.8186	3.7071	0.089	44.83	Sy 2	FRII RG	?	1, 2, 3
J0318.7+6828	49.5791	68.4921	0.0901	44.85	Sy1.9	FRII GRG	?	4, 5
J0918.5+0425	139.5011	4.4184	0.1564	45.31	QSO 2	/	Merg?	4

[a]The position and redshift (J2000 coordinates) are taken from the NASA/IPAC Extragalactic Database.
[b]Logarithm of the luminosity in the 14–195 keV band in erg s^{-1} from the BAT 9-month AGN survey.
[c]FRII RG = Fanaroff-Riley Class II Radio Galaxy; GRG = Giant Radio Galaxy.
[d]GRG = Giant Radio Galaxy; Sy = Seyfert; QSO = Quasar; / = No radio counterpart is associated to the source.
[e]AGN host galaxy is indicated as E (elliptical), ? (optical image too faint to be classified), Merg? (possible galaxy merging).
[f]1 = Laing et al. (1994), 2 = Jackson & Rawlings (1997), 3 = Black et al. (1992), 4 = Tueller et al. (2008), 5 = Schoenmakers et al. (1998)

Table 2.1: Description of the sources main properties and radio, optical, host galaxy classification from literature.

Suzaku Observation Log

Source	Obs ID	Date	Exposure[a]	Ct. Rate[a]
3C 452	702073010	2007-06-16	66696, 57383	0.037, 0.039
3C 105	702074010	2008-02-05	38319, 45518	0.031, 0.024
J0318.7+6828	702075010	2007-09-22	77140, 65631	0.091, 0.027
J0918.5+0425	702076010	2007-11-04	61019, 51899	0.024, 0.006

[a]Exposure time (s) and background subtracted count rate (cts s^{-1}) for XIS-BI (back-illuminated) and HXD/PIN, respectively in the 0.5–10 keV and 10–30 keV band

Table 2.2: Suzaku XIS and HXD/PIN observations log.

Being the HXD/PIN a non-imaging detector, a model of the time-variable Non X-ray Background (NXB) is provided by the HXD team (dead time corrected) with a systematic uncertainty of about 1.3% at 1σ confidence level in the 15 - 40 keV band for a 10 ks exposure (Mizuno et al. (2008)). Since the NXB event rate is 10 times higher than the real background to suppress the Poisson error, the particle background spectra and light curves are increased by a factor of 10 using respectively the `fparkey` and `fcalc` tools. A common Good Time Interval (GTI) between the PIN cleaned event file and the NXB is created to obtain source dead time corrected spectra and light curves. In addition to the NXB, the PIN still suffers from Cosmic X-ray Background (CXB) contamination (about 5%). It is estimated by using the PIN response file for the flat emission distribution (provided by the HXD team) and then simulated with `xspec` using the HEAO-1 CXB spectrum (Boldt (1987)). The particle background and CXB spectra are combined using `mathpha`. The PIN response files type, available from the Suzaku CALDB as generated in June 2009, are chosen according to the HXD nominal pointing and the observation epoch.

2.3 Spectral analysis

Using the X-ray spectral fitting package `Xspec v12` (Arnaud (1996)), three main models are tested to describe the primary emission from the AGN. Each target is initially fitted with the simplest case; if the model is not able to describe the spectrum or the fit is significantly improved by introducing additional components, then we adopt more complex models. In addition to the continuum emission, a gaussian profile is added to characterize the Fe Kα fluorescence line at 6.4 keV (`zgauss`) as result of reprocessing in the sorrounding material (e.g. accretion disk, torus). If the spectrum does not show a significant fluorescence line, we derive un upper limit of the equivalent width, fixing the line centroid (at the source rest frame) at 6.4 keV.
We use the `zphabs` code to model the photoelectric absorption by cold matter across the line of sight using cross sections from Balucinska-Church & McCammon (1992). The neutral absorption taking place in our galaxy is accounted for (even when not explicitly mentioned) with the `tbabs`

model (Wilms et al. (2000)). The galactic column density, from the HI map of Dickey & Lockman (1990), is provided by the `nh` program of the `HEAsoft` package and listed in Table 2.3. Solar abundances as given by Anders & Grevesse (1989) are assumed throughout the analysis, while cosmological parameters of $H_0 = 70$ km s^{-1} Mpc^{-1}, $\Omega_M = 0.27$ and $\Omega_{vac} = 0.73$ are used as given by the default `Xspec v12` settings.

2.3.1 Simple model

The X-ray continuum emission from a type II AGN is characterized, as a first-order approximation, by an absorbed power law (Mushotzky et al. (1993)), resulting from thermal Comptonization of soft seed accretion disk photons by a hot diffuse corona (Haardt & Maraschi (1991)). Defining as N_H and $\sigma(E)$ the column density and photoelectric cross section of the cold matter sorrounding the black hole, this simple model takes the form $F(E) = \exp\{-N_H\sigma(E)\}\ E^{-\Gamma}$ (Γ represents the photon index), translated as `zphabs*zpowerlaw` in Xspec terminology.
We assume the absorber to be neutral, altough the presence of ionized absorbers in Radio Loud AGN has been recently found (e.g in the BLRG 3C 445, Braito et al. (2011)), because the data quality does not allow such a detailed analysis.

2.3.2 Partial covering model

Several type II AGN spectra show, in addition to the absorbed primary emission, a secondary less absorbed, or not absorbed at all, emission at lower energies (Turner et al. (1997)). Many interpretations could be applied to this observational feature: 1) the result of contamination by other sources (e.g. X-ray binaries/starburst emission, Maiolino et al. (1998)); 2) a clumpy, dusty absorber that partially covers the nucleus (Malaguti et al. (1999)); 3) AGN light scattered back into our line of sight by hot gas (Matt et al. (1996)); 4) the sum of unresolved emission lines from photoionized gas (Bianchi et al. (2006)).
Given the point spread function (PSF) of the XIS instruments, with the Suzaku imaging capabilities alone we can't rule out the presence of other sources. For this reason, both the Swift/XRT and, when available, the XMM-Newton and Chandra images of our targets are analyzed to check the presence of contamination by point sources or the lobes of the associated radio galaxy.
If we interpret the secondary component as intrinsic emission from the AGN, this complex spectrum can be described by the partial covering model (see Holt et al. (1980)), where a fraction of the primary emission escapes without being absorbed. It requires the hydrogen column density and the covering fraction of the partial absorber (f_c), and can be written as $F(E) = \{f_c \exp\{-N_H\sigma(E)\} + (1 - f_c)\}\ E^{-\Gamma} = M(E)\ E^{-\Gamma}$ where $M(E)$ represents the partial covering fraction absorption, or `zpcfabs` in Xspec. This model is useful to describe not only a clumpy absorber but also scattered nuclear emission escaping from different regions and redirected to our line of sight, assuming the same slope for the scattered power law. In this paper we will refer to the value $1 - f_c$ as the scattering fraction f_{scatt} of the absorbed power law. The partial covering code takes the form `zpcfabs*zpowerlaw`. If $f_c < 1$, a fraction $(1 - f_c)$ of the primary emission escapes without being absorbed, while a $f_c = 1$ returns the simple absorbed model.

The soft X-ray emission could also be thermal, due to collisionally ionized diffuse gas that could be present in the host galaxy or nearby the AGN itself (Isobe et al. 2002), or the sum of unresolved lines by photoionized gas (Reeves et al. 2010). The XIS spectral resolution does not allow to disentangle the two sources, and we only search for the additional presence of thermal gas with the `apec` component to better constrain the scattered/partially covered power law.

2.3.3 Double power law model

In general, the second, scattered power law could be absorbed by less dense clouds and characterized by a different slope than the direct emission. The third model increases the complexity of the fit by adopting two different absorbed power laws, in the form $F(E) = \exp\{-N_H^a \sigma(E)\}\ E^{-\Gamma^a} + \exp\{-N_H^b \sigma(E)\}\ E^{-\Gamma^b}$, where a and b mark distinct values, or `zphabs*zpowerlaw + zphabs*zpowerlaw` in Xspec.

2.3.4 Compton reflection

Given the extended energy range of the PIN, the additional contribution of Compton reflection by optically thick matter could arise in the hard part of the spectrum. The Xspec `pexrav` code models the angle-dependent Compton reflection of an incident exponentially cut-off power law by a plane-parallel, semi-infinite medium of cold electrons approximating an accretion disk (Magdziarz & Zdziarski (1995)). In the present work, we apply this code to a more general case where the AGN primary radiation could be reflected by optically thick matter present in the accretion disk or in the sorrounding torus/absorber (see the caveats in Murphy & Yaqoob (2009)), resulting as sum of the incident cut-off power law and the reflection component. The amount of reflection depends on both geometry and composition of the reflector, parametrized in the model by the inclination of the reflecting material and the gas abundance, with the possibility of varying the Fe abundance alone. The model also returns the relative strength R (rel_{refl} in the code) of the reflection component to that of the incident cut-off power law component, defined as $R \equiv \Omega/2\pi$, where Ω is the solid angle covered by the reflector. If $R = 0$, then the pexrav model translates into a simple exponentially cut-off power law. Each model (simple model, partial covering model, double power law model) is tested with and without the addition of the `zphabs*pexrav` code for all the sources. When a significant reflection component is not found from the spectral fitting, we evaluate an upper limit to the relative reflection by fitting the spectra with a partially covered pexrav model, in the form `zpcfabs*pexrav`. As previously noted, for $R = 0$ this model turns into a partial covering model.

2.4 3C 452

The source 3C 452 is a FRII radio galaxy with a symmetrical double-lobe morphology and a total angular extent of about $1' \times 4'$ (Black et al. (1992)). It does not lie in a rich cluster and it is free from thermal X-ray emission related to the intracluster medium (Isobe et al. (2002), hereafter I02). From the Hubble observation, no UV excess (Wills et al. (2002)) and optical central compact core is detected (Chiaberge et al. (2002)), while the NICMOS near-IR instrument reveals a faint

compact source 1" southwest of the nucleus (Madrid et al. (2006)), confirmed by the weak mid-IR core detected by Spitzer (Ogle et al. (2006)).
The Chandra/ACIS instrument observed the source on the August of 2001: a detailed spectral analysis of both lobes and central AGN emission is reported by I02, with results regarding the AGN properties confirmed by the work of Evans et al. (2006). From the I02 paper, the soft X-ray emission from the extended radio structure is fitted by a power law, interpreted as Inverse Compton (IC) and significant in the $2-5$ keV band, with the addition of the Raymond-Smith (RS) thermal emission in the $0.5-2$ keV band from hot, diffuse gas associated to the host galaxy. The sum of these two models describes, more generally, the extended X-ray emission of 3C 452, while the X-ray spectrum of the nucleus is accumulated within a circular region of 5" radius. Hodges-Kluck et al. (2010) confirms the thermal and power law emission mix throughout the region covered by the radio lobes, altough with the nonthermal emission dominant near the hot spots, but they associate the thermal emission to the radio galaxy cocoon or a bounding shock and not to the actual IGM.

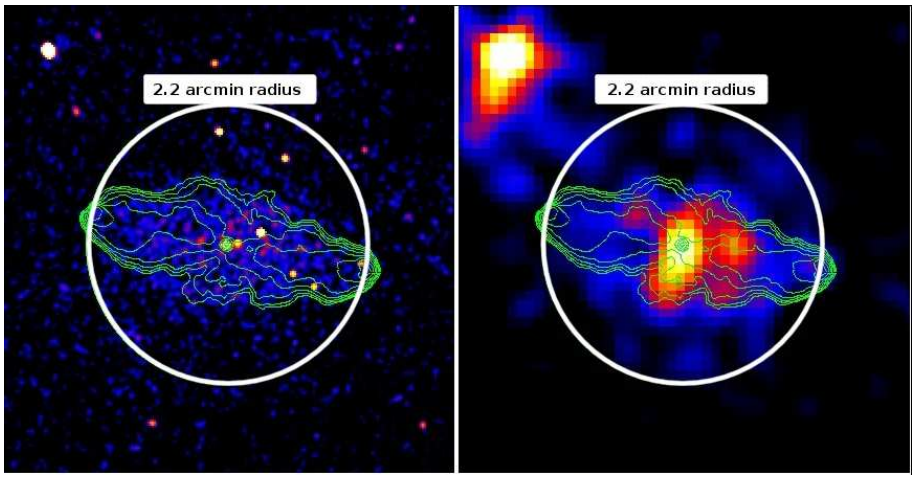

Figure 2.1: Chandra/ACIS (left panel) and Suzaku/XIS1 (right panel) 0.5 - 2 keV images of 3C 452, with the 1.4 GHz VLA radio map superimposed with green contours. The white circle indicated the Suzaku 2.2' radius extracting region.

2.4.1 Extraction of the AGN emission

In the analysis of the Suzaku/XIS image, the required extracting region of the central point source covers part of the extended radio galaxy because of the wider PSF respect to Chandra/ACIS: the AGN emission is contaminated by the diffuse one at energies lower than 3 keV. This can be clearly seen in Figure 2.1, showing the Chandra/ACIS and XIS1 smoothed image of 3C 452, in the 0.5 - 2 keV energy range, respectively in the left and right panel, while the white circle refers to the 2.2' radius extracting region. The 1.4 GHz Very Large Array (VLA) radio map (Laing R.A. unpublished) is superimposed with green contours: the soft, cocoon shaped, X-ray emission traces the radio contours in the ACIS image.
Since we want to analyze the spectrum of the AGN, it is necessary to discriminate the X-ray

photons of the central core from the extended emission. The lobes emission contamination in the XIS spectrum is checked by simulating the diffuse and core detection of the XIS1 on the basis of the ACIS observation, using the `xissim` tool. We extract the ACIS total spectrum from the same region on which the Suzaku 3C 452 analysis is based: the central core counts are taken from a 6" circular region, while the extended emission results from subtracting the core region from the total one (Figure 2.2, top panel). We would like to note that in the latter external sources in the field are also taken into account. Applying the XIS1 response matrix, we then obtain the count rate of

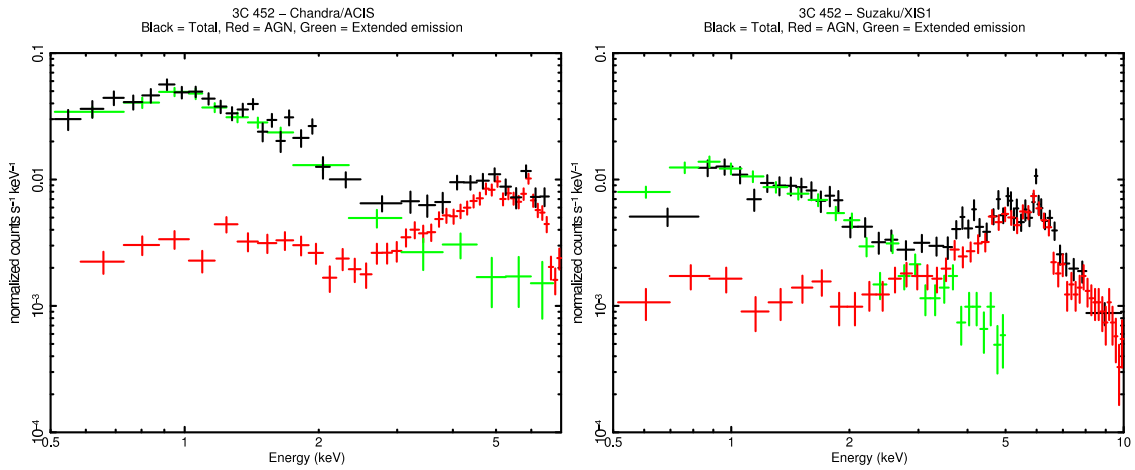

Figure 2.2: *Left panel*: Chandra/ACIS spectrum of the 2.2' radius region centred on the AGN (black), the AGN alone (red) and the extended region with the AGN region subtracted (green). *Right panel*: Suzaku/XIS1 observed spectrum (black) and simulated spectra of the AGN emission alone (red) and the extended emission (green).

a fake XIS1 detection of the two components.

The bottom panel of Figure 2.2 shows the simulated XIS1 detection (the AGN emission in red and the extended emission in green) and, as a comparison, the real observation (in black), which turns to be the sum of the diffuse and central core emission. Since the simulation well reproduces the real detection, the Suzaku/XIS spectra are contaminated by the diffuse emission below 3 keV. In order to model the AGN emission, two ways are possible: 1) the XIS spectrum is analyzed only above 3 keV, losing all the information regarding the possible presence of a scattered/partially covered component; 2) The model of the soft X-ray emission, based on the I02 results, is added to the AGN model, and the full energy band XIS spectrum (0.5 - 10 keV) is analyzed. The latter option is chosen, exploring in this way the presence of a partially covered emission.

2.4.2 Spectral fitting

We analyze the spectrum in the full energy band, form soft to hard, adding together the XIS (FI and BI in the 0.5 - 10 keV energy range), the PIN (10 - 30 keV) and the 9 months averaged BAT (14 - 195 keV) data. The normalization between XIS and PIN flux is accounted for using a 1.18 factor in the PIN model, given by the cross-correlation of the Crab observation in HXD

nominal pointing, while the BAT normalization is kept free. The extended emission is modelled with `zpowerlaw + raymond` (the thermal emission fitting is based on the calculations of Raymond & Smith (1977)), with a power law photon index of 1.68 and a gas temperature of 1.36 keV. Given the extended structure of the diffuse emission, we do not expect a significant variability along the 6 years time interval of the two observations. However, a possible change in flux of 20% due to the different instrumental response is taken into account, finding a cross correlation factor of 0.8 in the Suzaku spectrum. The simple absorbed power law leaves an excess in the PIN spectrum, and the reflection component is needed. In the `pexrav` model we can't confine the high energy cut off, which is fixed at 200 keV, nor the inclination and chemical composition of the reflector, which are fixed at 63°. (the default value) and solar abundance respectively. The partial covering model does not improve the fit, given the model-crowded soft band, but it allows to fix an upper limit to the scattering fraction, which turns to be below 0.5%. The residual power law absorption results not well constrained and it is removed from the model. The best fit model is `zpcfabs*zpowerlaw + zgauss + pexrav`, and the main parameters are reported in Table 2.3.

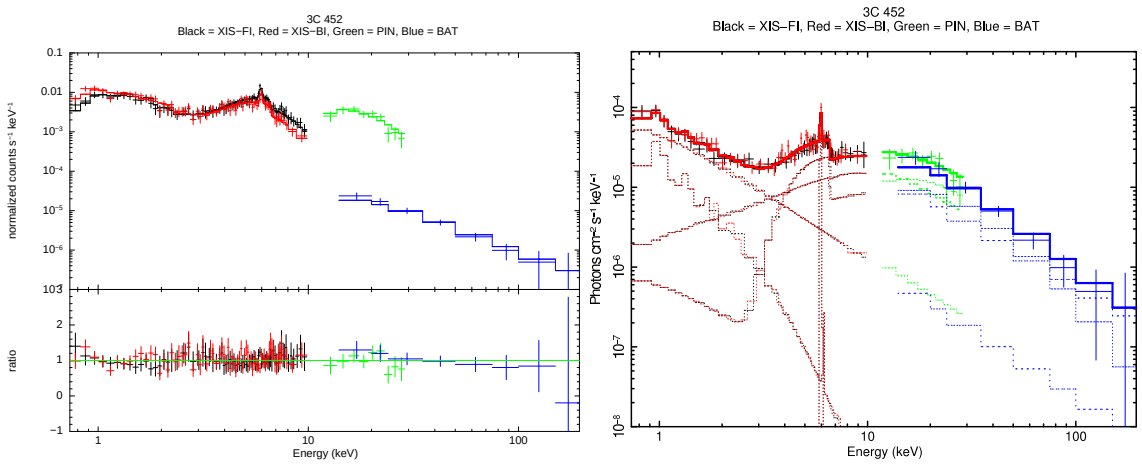

Figure 2.3: Folded (left panel) and unfolded (right panel) spectra and best fit models of 3C 452: Black = XIS-FI, Red = XIS-BI, Green = HXD/PIN, Blue = Swift/BAT.

The source 3C 452 is highly absorbed, with a local H equivalent column density of 4×10^{23} cm^{-2}. The hard energy band of the spectrum is dominated by Compton reflection of the intrinsic power law photons onto a cold, thick matter, and the source seems to see the absorber covering a solid angle greater than 4π: the relative strength of the reflection component to the transmitted one, R, results higher than 400. This value is unphysical, but it can be mathematically explained as the result of a not homogeneous absorber, with a significant fraction of the solid angle covered by a gas thicker than that along the line of sight (Risaliti (2002)). The nuclear emission is flattened, with a power law photon index of 1.55, while the average Seyfert II slope ranges from 1.7 to 1.9 (Turner & Pounds (1989), Nandra & Pounds (1994)). The Fe Kα line is centered at 6.43 keV (in

the source rest frame) and narrow, with an EW of 164 eV.

2.5 3C 105

The source 3C 105 is a FRII narrow line radio galaxy, with a spatial size of 764 kpc (Baum et al. (1988), Hardcastle et al. (1998)), associated to an elliptical host galaxy (Donzelli et al. (2007)). From the radio map of Leahy et al. (1997), both jets are detected but the radio emission is dominated by the southern hotspot complex and the wealth of other knots and structure in the complex is suggestive for the authors of a rapidly evolving, transient system. Chandra detected X-ray emission from the core and southern hot spot of 3C 105 on December 2007 (Massaro et al. (2010), hereafter M10), both from the region where the jet appears to enter the hot spot and at the terminal hotspot itself. No extended, thermal X-ray emission is detected. A faint, unresolved NIR source is visible 4" to the west-southwest off the nucleus (Madrid et al. (2006)), while we couldn't find any information on the UV emission from literature. Given the shorter exposure respect to the other sources, we extract the counts from a 4.2' radius region, that includes also the southern hotspot, to collect up to 99% source X-ray photons.

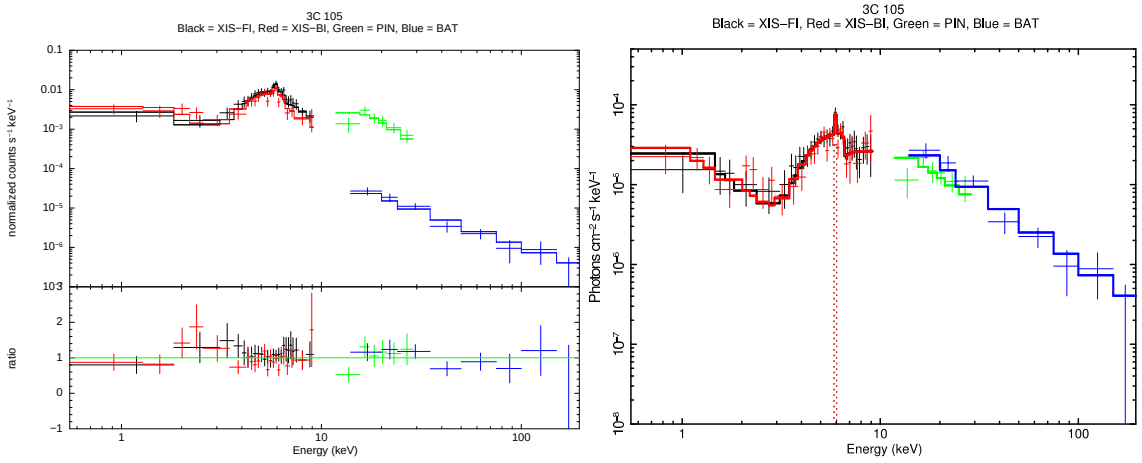

Figure 2.4: Folded (left panel) and unfolded (right panel) spectra and best fit models of 3C 105: Black = XIS-FI, Red = XIS-BI, Green = HXD/PIN, Blue = Swift/BAT.

2.5.1 Spectral fitting

Following the procedure reported in Sec. 2.3, the X-ray spectrum of 3C 105, given by the sum of the XIS, PIN and BAT data, is initially fitted by a simple, absorbed, power law model, which leaves a strong residual in the soft. The addition of thermal emission (with the `apec` model) requires a too high gas temperature (> 2 keV) to fit the data, while a typical value of 0.65 keV is observed in Seyfert 2 galaxies (Guainazzi et al. (2005)). The best fit is given by the partial covering model, with

Suzaku Spectral Fits Results

Source	n_H [a] [10^{22} cm^{-2}]	N_H [b] [10^{22} cm^{-2}]	Γ	f_{scatt} [c]	Fe K E [d] [keV]	Fe K EW [d] [eV]	R [e]	BAT Norm. [f]	χ^2/d.o.f
3C 452	0.12	$43.52^{+10.85}_{-6.92}$	$1.55^{+0.14}_{-0.11}$	$< 0.5\%$	$6.43^{+0.03}_{-0.03}$	164^{+44}_{-45}	> 400	$0.90^{+0.25}_{-0.15}$	116.76/175
3C 105	0.12	$45.96^{+6.24}_{-6.56}$	$1.78^{+0.20}_{-0.19}$	$1.4^{+0.9}_{-0.5}\%$	$6.40^{+0.07}_{-0.05}$	136^{+75}_{-62}	< 1.8	$1.68^{+0.61}_{-0.45}$	68.18/97
J0318.7+6828	0.35	$5.26^{+0.42}_{-0.41}$	$1.55^{+0.08}_{-0.08}$	$1.2^{+0.7}_{-0.8}\%$	6.4(f)	63^{+32}_{-27}	< 1.4	$1.08^{+0.27}_{-0.23}$	167.68/172
J0918.5+0425	0.035	$16.33^{2.27}_{-2.13}$	$1.72^{+0.20}_{-0.19}$	$0.9^{+0.6}_{-0.4}\%$	6.4(f)	< 98	< 2.6	$1.74^{+1.16}_{-0.87}$	79.21/132

[a] Galactic column density provided by the `nh` tool, using the HI map by Dickey & Lockman (1990).
[b] Source intrinsic column density.
[c] Fraction of the scattered component relative to the intrinsic power law.
[d] Centroid energy and equivalent width respect to the whole continuum of the Fe fluorescence Kα line at the rest frame of the source redshift.
[e] The relative strength of the reflection component to the transmitted one, defined as R= $\Omega/2\pi$, where Ω is the solid angle of the reflector viewed from the nucleus.
[f] Normalization factor of the BAT flux respect to the XIS detection.

Table 2.3: The best fit parameters resulting from the analysis of the Suzaku XIS and HXD/PIN spectra with the addition of the 9-month averaged BAT spectrum.

the scattered power law modelling the excess at softer energies. Using a double power law, with different column density and photon index, the same set of spectral parameters is found. The best fit model is `zpcfabs*zpowerlaw + zgauss` (Fig. 2.4). While the addition of Compton reflection does not improve the fit, we can evaluate an upper limit to the relative reflection, allowing to effectively rule out the presence of Compton reflection. In order to do so, we fit the spectrum with a partially covered `pexrav` model, in the form `zpcfabs*pexrav + zgauss`. The composition and line of sight angle are settled following the model default values (solar abundance composition and 63° inclination angle). If R is equal to 0, the `pexrav` model translates into a partially covered power law, which is our best fit model. Fixing the column density, scattering fraction and normalization to the best fit values (see Table 2.3), we calculate the relative reflection confidence range as a function of the power law slope.

Adding together the 9-month averaged BAT spectrum to the Suzaku observation, a normalization factor of 1.7 for the BAT spectrum is needed, i.e. the BAT flux is about 60% higher than the Suzaku detection, in the same band, which implies a possible long term variability (see Sec. 2.8). The source 3C 105 intrinsic power law emission is highly absorbed by a $N_H \sim 5 \times 10^{23}$ cm^{-2}, while the 1.4% of the nuclear X-ray photons are scattered at lower energies and reach the observer unabsorbed.

As previously noted, the XIS extracted region cover also the radio galaxy southern hotspot. From the work of M10, its X-ray emission is much more fainter respect to the core: its flux results to be about 30% in the 1 - 2 keV energy range and less than 2% in the 2 - 7 keV band. However, since we interpret the soft X-ray excess as scattered nuclear emission, we check for a possible external contamination by comparing their fluxes. Table 2.4 reports a summary, for all the sources, of the flux and luminosity emitted in the main bands with (left value) and without (right value) absorption (galactic and local). In the 0.5 - 2 keV energy range we obtain an absorbed flux of 50×10^{-15} erg cm^{-2} s^{-1}. From M10, the total flux of the southern hotspot region, in the 0.5 - 2 keV energy range, is 5×10^{-15} erg cm^{-2} s^{-1}, 10 times lower than the Suzaku/XIS observation. If a contamination is present, it falls within the uncertainty of the scattering factor.

The spectral shape of 3C 105 differs from the XIS analysis of Winter et al. (2009a) (W09a hereafter), especially in the power law slope and scattering fraction. This is due to the addition of the PIN data that allow to constrain the photon index to a steeper value. The source is not dominated by Compton reflection in the hard band, and the reflection relative strength upper limit is 1.8, translating into a covering solid angle less than 3.6π. A narrow, 136 eV EW, Fe Kα line, centered at 6.4 keV is found.

2.6 Swift J0318.7+6828

The source J0318.7+6828 is identified as a FRII GRG. The optical spectrum (INT telescope in La Palma) is typical of a narrow line AGN, while the optical image shows a faint galaxy-like object (Schoenmakers et al. (1998)) associated to the radio core but the resolution is not enough to clarify the host morphology. We couldn't find any information on the IR or UV maps from literature, even if IR emission, mostly in the K_s band, is found within 30" from the source position in the Two

FLUX AND LUMINOSITY[a]

	Flux in 10^{-12} erg cm^{-2} s^{-1}				Log Luminosity in erg s^{-1}			
Source	0.5 - 2 keV	2 - 10 keV	10 - 40 keV	14 - 195 keV	0.5 - 2 keV	2 - 10 keV	10 - 40 keV	14 - 195 keV
3C 452	0.01, 1.79	1.85, 6.59	14.46, 14.97	37.78, 38.01	41.20, 43.45	43.47, 43.88	44.36, 44.38	44.78, 44.78
3C 105	0.05, 5.11	2.11, 8.28	9.00, 9.82	22.92, 23.26	41.99, 44.00	43.62, 44.21	44.25, 44.29	44.66, 44.66
J0318.7+6828	0.06, 2.55	4.47, 6.03	10.23, 10.34	32.19, 32.24	42.08, 43.71	43.96, 44.09	44.32, 44.32	44.81, 44.81
J0918.5+0425	0.01, 1.45	1.55, 2.87	4.05, 4.15	11.33, 11.37	41.84, 44.00	44.03, 44.29	44.44, 44.45	44.89, 44.89

[a]Fluxes and luminosity are reported with both the galactic and local absorption (left value of each column) and as intrinsic, not absorbed, emission (right value of each column) for the following main energy bands: 0.5 - 2 keV, 2 - 10 keV, 10 - 40 keV and 14 - 195 keV.

Table 2.4: Observed and absorption corrected flux and luminosity in the 0.5 - 2 keV, 2 - 10 keV, 10 - 40 keV and 14 - 195 keV energy ranges.

Micron All Sky Survey (2MASS) at IPAC. XMM–Newton observed J0318.7+6828 on February 2007 (a detailed analysis can be found in Winter et al. (2008), hereafter W08): the source image, from the XMM/pn event file, in the 0.5 - 2 keV energy range does not show the presence of external sources and/or contamination by extended emission. With a radio galaxy angular size of 15' (2 Mpc at z = 0.09), the giant radio lobes are well outside the Suzaku/XIS extracting region.

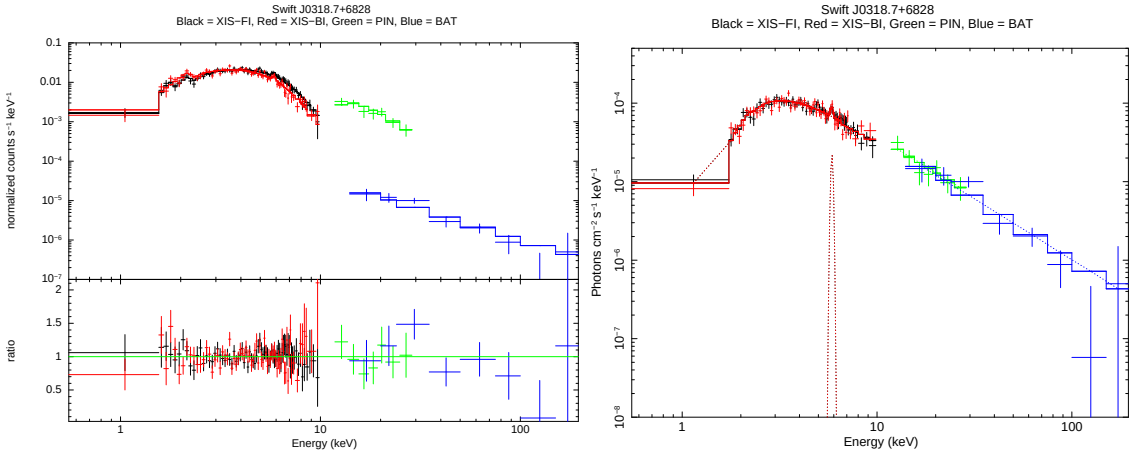

Figure 2.5: Folded (left panel) and unfolded (right panel) spectra and best fit models of Swift J0318.7+6828: Black = XIS-FI, Red = XIS-BI, Green = HXD/PIN, Blue = Swift/BAT.

2.6.1 Spectral fitting

A simple, absorbed power law can fit with sufficient accuracy the source J0318.7+6828, even in the soft 0.5 - 2 keV energy band, but the best fit is gained by modelling its emission with a partially covered power law. A gaussian is then added to model the faint Fe fluorescence line, fixing its rest energy at 6.4 keV, and the best fit model takes the form `zpcfabs*zpowerlaw + zgauss` (Fig. 2.5). No significant reflection is found in the hard part of the spectrum: we evaluate the upper limit to a possible Compton hump following the same procedure applied to 3C 105 (see Sec. 2.5.1). The double power law parameters can not be well constrained because of the data quality, so this model is rejected. A gaussian is then added to model the faint Fe fluorescence line, fixing its rest energy at 6.4 keV.

The nuclear emission is absorbed by a column density of $N_H \sim 5 \times 10^{22}$ cm^{-2}, about an order of magnitude lower than the previous 3C sources, and the partial covering model returns a scattering factor of 1.2%. The power law photon index appears, as in the case of 3C 452, flatter than the mean value associated to Seyfert galaxies. If reflection is present, the spectral fitting reports an upper value of 1.4 to its relative strength, i.e. the absorbing matter subtends a solid angle lower than 2.8π.

2.7 Swift J0918.5+0425

The source Swift J0918.5+0425, the farthest among our sample (z = 0.15644) and the only radio quiet AGN, can be defined peculiar for many reasons. Detected by Rosat/PSPC on March 2000, the source has been identified as AGN only after the 9-month Swift/BAT survey. After being classified as a QSO Type II (Tueller et al. (2008)) AGN, J0918.5+0425 has been removed from the second BAT survey release because of variability. The Suzaku and Swift X-ray spectra are the only X-ray data available, at present, while no additional studies in the other bands, except for the catalogue of Swift/BAT AGN optical spectra (Winter et al. 2010), are published. Its optical counterpart from the SDSS[1] shows a peculiar double lobed galaxy-like object, maybe the site of a galaxy merging, but the resolution is not enough to disentangle its components.

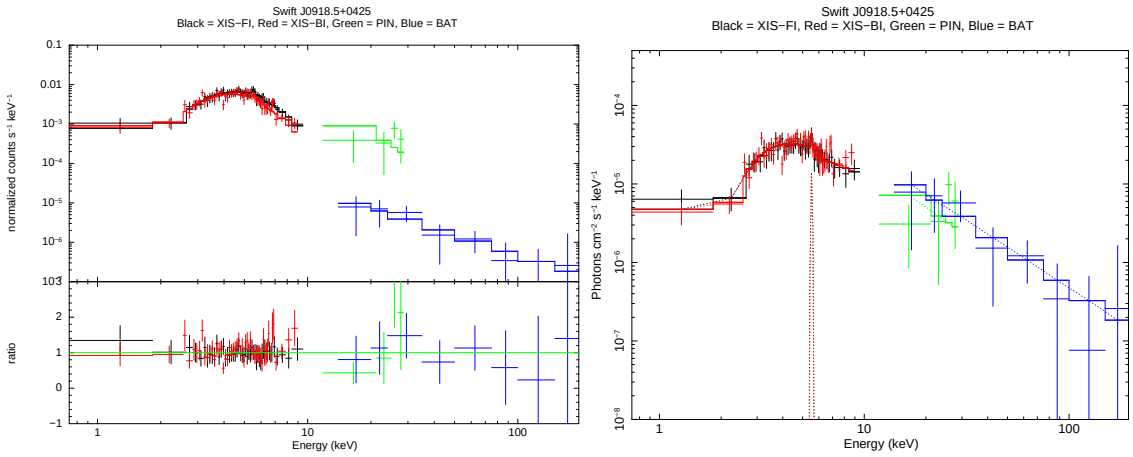

Figure 2.6: Folded (left panel) and unfolded (right panel) spectra and best fit models of Swift J0918.5+0425: Black = XIS-FI, Red = XIS-BI, Green = HXD/PIN, Blue = Swift/BAT.

2.7.1 Spectral results

The PIN extracted spectrum results to be not consistent to both the XIS and BAT spectra. This could be related to a low statistics significancy due to the low count rate or to an uncorrect particle background model, which contributes about 95% of the total count rate. In order to check the latter hypothesis, we compute the ratio between the total detected count rate and the NXB: being the source emission strongly affected by the particle background, we should obtain a constant value.

As shown in Figure 2.7 (top panel), after 9×10^4 s (spacecraft time), the ratio deviates from the constant behaviour. We remove the corrupted time interval: the PIN exposure time decreases from 52 to 43 ks, with an average count rate of 0.01 cts s^{-1}. The ratio resulting from the cleaned PIN light curve (Figure 2.7, bottom panel) can now be well fitted (χ^2/dof = 18.10/18) by a constant

[1]Sloan Digital Sky Surver (SDSS), www.sdss.org

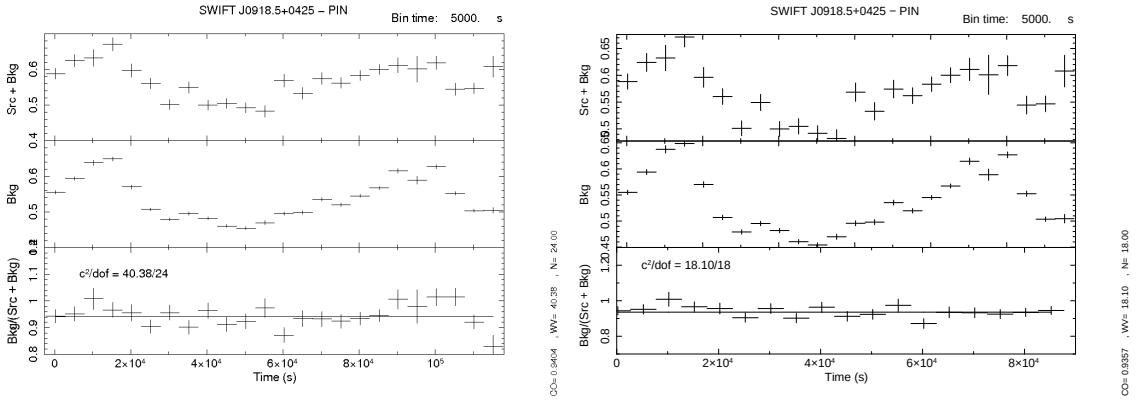

Figure 2.7: The background unsubtracted PIN (at the top), background (in the middle) light curves and their ratio (at the bottom) of J0918.5+0425 are plotted before (left panel) and after (right panel) the removal of the background corrupted time interval. The goodness of the ratio fit by a constant function is also reported for the two cases.

function, and the PIN spectrum is consistent with the XIS and BAT data (Figure 2.6). Following the same procedure described for the other sources, the best fit model is given by a partially covered power law, in the form `zpcfabs*zpowerlaw`. Adding a gaussian profile to model the Fe Kα emission, we can evaluate an upper limit to the line intensity, fixing the centroid rest frame energy at 6.4 keV.

The X-ray spectrum of J0918.5+0425 is modelled by a partially covered power law, resulting in a 0.9% scattered factor. The source is moderately absorbed ($N_H \sim 2 \times 10^{23}$ cm^{-2} local column density) and shows a weak Fe fluorescence line (EW < 90 eV). It must be underlined the powerful luminosity in the 2 - 10 keV, the highest among our sample: the intrinsic, unabsorbed value is 2×10^{44} erg s^{-1}, which confirms the QSO nature of the source as reported by the Swift/BAT AGN catalogue.

2.8 Long term variability

Strong variability is found in the X-ray emission of AGN, from intrinsic changes in the source flux to variability in the spectral properties (column density, photon index) and absorbed/emitted features (Mushotzky et al. (1993)). The study of these variances and their time scales can provide information on the size and geometry of the emitting X-ray region (McHardy et al. (2006)), the physical conditions of the X-ray reprocessing media (Miniutti et al. (2007)) and/or the physical properties of the absorbing material close to the black hole (Miller et al. (2008)).

On the contrary, if the line of sight to the source is blocked by obscuring matter, the direct emission is absorbed and only the scattered photons by distant, cold matter can reach the observer, losing any trace of variability. A Compton thick AGN, where little to no high direct emission escapes

below 10 keV while the hard energy part of the spectrum is dominated by reflection, can be traced by the lack of variability, both in flux and spectral shape. It is the case of Circinus, with no significant change along 9 years of observations (Winter et al. (2009b) and references therein), and the mildly Compton thick source NGC 4945 (Itoh et al. (2008)).
Here we report a comparison of the Suzaku spectral analysis results with other observations, to look for long term (time scales of months/years) variability (see Sobolewska & Papadakis (2009) for a review).
The spectral properties obtained from the analysis of Chandra, XMM-Newton and Swift/XRT data are collected from literature (see Table 2.5). In the case of 3C 105, where a simple model is applied, differences in terms of photon index or column density could fall within the uncertainty of our best fit model. For other sources, the X-ray spectral analysis has not been published yet (e.g. the XMM-Newton observation of 3C 452). While a detailed analysis of these observations is not the aim of this work, we perform a comparison with the Suzaku results by fitting these spectra with our best fit model, letting the normalization free to vary for changes in luminosity and adding the 9-month averaged BAT data to constrain the photon index. If the source can not be described by our best fit parameters, then we look for intrinsic variations in the spectral parameters, with the assumption that our best fit model reflects the physical properties of the AGN. In the case of the XRT data analysis the Fe K line is not modelled because of the low energy resolution of the instrument. The Swift/XRT data filtering is performed by means of the HEASARC `xrtpipeline` following the standard event screening criteria using the CALDB release of the observatin epoch. The Chandra/ACIS analysis is based on the cleaned event files of the Chandra archive third reprocessing (ASCDSVER = 7.6.11.3, CALDB = 3.4.2). For the XMM-Newton/pn data, we reduce the data following the standard procedures as adviced by the XMM-Newton SOC using `SAS v.10.0.0`. The extracting regions range from 50“ - 60“ for the XRT images to 30” and 7“ for XMM-Newton and Chandra images respectively.

2.8.1 3C 452

The spectral parameters of 3C 452 are in good agreement with the detailed analysis of the Chandra observation performed by I02 and Evans et al. (2006). They also confirm the presence of the reflection component and the narrow Fe K feature. In the analysis of the XMM-Newton observation (the Swift/XRT detection is not available) we include the thermal emission as modelled by I02 (accounted for by the normalization of the extended emission in the Suzaku analysis) and the scattering component. As for the XIS analysis, a partially covered power law coupled with strong reflection gives a good fit (χ^2/d.o.f = 296/291) to the data. We find a low fraction of scattered emission ($< 0.9\%$) with an uncertainty due to the presence of thermal photons. The spectral properties of 3C 452, i.e. high column density, flattened photon index, narrow Fe K line and strong reflection, do not show variability among a time lapse of 6 years. This results, coupled with an unchanged absorption corrected 2 - 10 keV luminosity, confirm 3C 452 as a highly absorbed, reflection dominated source.

Spectral Fits Results from Chandra/XMM-Newton/Swift XRT

Source	Instr.[a]	Obs. Date	Model[b]	N_H[c] $[10^{22}$ cm$^{-2}]$	Γ[c]	f_{scatt}[d]	Fe K E, EW[e] [keV]	Refl.[f]	Log $L_{[2-10keV]}$[g] $[10^{44}$ erg s$^{-1}]$	Ref.[h]
3C 452	C	2002-08-27	E	59^{+9}_{-9}	$1.66^{+0.28}_{-0.21}$	/	$6.40^{+1.0}_{-0.7}$, < 0.22	Y	0.7(unabs)	1
	C	2002-08-27	E	57^{+9}_{-8}	1.7(f)	/	6.4(f), 0.1(f)	Y	1.(pow)	2
	S+B	2007-06-16	D	$43.5^{+10.9}_{-6.9}$	$1.55^{+0.14}_{-0.11}$	$< 0.5\%$	$6.43^{+0.03}_{-0.03}$, 0.164	Y	0.8(unabs)	4
	X+B	2008-11-30	F	$63.9^{+8.5}_{-7.2}$	1.5(p)	$< 0.9\%$	$6.44^{0.03}_{-0.03}$, 0.15	Y	1.1(unabs)	4
3C 105	SX+B	2006-07-11/16	C	$38.6^{+4.9}_{-4.0}$	1.9(p)	$< 0.2\%$	/	N	3.4(unabs)	4
	C+B	2007-12-17	C	$52.6^{+7.3}_{-5.9}$	1.9(p)	$< 0.2\%$	6.4(f), 0.09	N	2.7(unabs)	4
	S+B	2008-02-05	C	$45.9^{+6.2}_{-6.6}$	$1.78^{+0.20}_{-0.19}$	$1.4^{+0.9}_{-0.5}\%$	$6.40^{+0.07}_{-0.05}$, 0.136	N	1.6(unabs)	4
	X+B	2008-02-25	C	48.4^{+14}_{-10}	1.9(p)	$< 0.5\%$	6.4(f), 0.09	N	1.8(unabs)	4
J0318.7+6828	X	2006-01-29	C	$4.10^{+0.48}_{-0.41}$	$1.52^{+0.12}_{-0.11}$	$3.3^{+0.9}_{-0.9}\%$	6.4(f), $0.044^{+0.04}_{-0.04}$	N	1.5(obs)	3
	SX	2006-03-29	A	$3.70^{+1.74}_{-1.83}$	$1.73^{+0.48}_{-0.55}$	/	/	N	0.8(obs)	3
	SX	2006-04-05	A	$3.66^{+1.44}_{-1.41}$	$1.44^{+0.40}_{-0.46}$	/	/	N	1.0(obs)	3
	S+B	2007-09-22	C	$5.26^{+0.42}_{-0.41}$	$1.72^{+0.20}_{-0.19}$	$1.2^{+0.6}_{-0.4}\%$	6.4(f), 0.063	N	1.2(unabs)	4

[a]Observatory name: S = Suzaku/XIS, B = Swift/BAT, C = Chandra/ACIS, X = XMM-Newton/EPIC, SX = Swift/XRT.
[b]The best fit models: A = N_H*PL, B = N_H*PL + Gauss, C = Pcfabs*PL + Gauss, D = Pcfabs*PL + Gauss + Pexrav, E = N_H*PL + Gauss + Pexrav + Th, F = Pcfabs*PL + Gauss + Pexrav + Th. All the models include the presence of the galactic absorption, not shown here for simplicity.
[c]Source intrinsic column density and primary power law photon index (p indicates a value pegged at the upper - lower limit of 1.9 - 1.5).
[d]Where modelled, the fraction of the scattered component relative to the intrinsic power law.
[e]Centroid energy and equivalent width respect to the whole continuum of the Fe fluorescence Kα line at the rest frame of the source redshift.
[f]Y = present, N = not found, / = not modelled
[g](obs) = observed, (unabs) = absorption corrected, (pow) = power law.
[h]1 = Isobe et al. (2002), 2 = Evans et al. (2006), 3 = Winter et al. (2009a), 4 = here.

Table 2.5: The spectral properties from the Chandra, XMM-Newton and Swift/XRT data as analyzed here or collected from literature.

2.8.2 3C 105

The X-ray analysis of 3C 105 has been published by W09a (Swift/XRT), Ajello et al. (2008) (Swift/XRT + BAT) and Massaro et al. (2010) (Swift/XRT, Chandra/ACIS and XMM-Newton/pn). While they generally confirm the strong absorption ($> 3 \times 10^{22}$ cm^{-2}), differences in the photon index and column density values are found. The use of simple absorbed power laws to model the spectrum and the lack of information regarding the source luminosity do not allow to correctly interpret the changes as intrinsic variability. After summing the four available Swift/XRT observations, spanning a time interval of 5 days, we try to model the Swift/XRT, Chandra/ACIS and XMM-Newton spectra with our results but the source changes do not fall within the uncertainty of our best fit model. The spectral analysis results are listed in 2.5: the lack of reflection and the narrow Fe K line are confirmed but the scattering fraction falls below 0.2% for both Chandra and Swift observations, and below 0.5% for the XMM-Newton detection. These changes are coupled to an absorption corrected 2 - 10 keV luminosity decreasing more than 50% from the middle of 2006 to the first months of 2008. A slight variability ($\sim 10 - 20\%$) in the column density is also found. The intrinsic variable nature of 3C 105 is clearly visible in 2.8, where

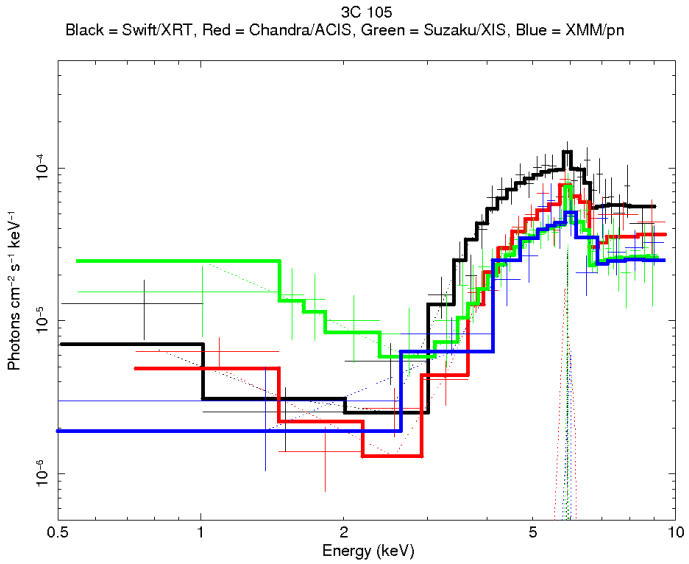

Figure 2.8: Unfolded spectrum of 3C 105 as observed by Swift/XRT (2006-07-11/16, black line), Chandra/ACIS (2007-12-17, red line), Suzaku/XIS (2008-02-05, green line) and XMM-Newton (2008-02-25, blue line).

the unfolded spectra of the four observations are plotted together: higher intrinsic luminosity is associated to lower values of the scattering fraction.

2.8.3 Swift J0318.7+6828

A detailed analysis and comparison of the Swift/XRT and XMM-Newton observations of J0318.7+6828 is reported in W08: flux variability is found with the XMM detection showing the

source to be brighter by $\sim 30\%$ two months before the two XRT observations. Suzaku detected the source more than 1 year and a half later: column density, power law slope and the Fe Kα feature are consistent with the previous results, but the scattered emission at lower energies is significantly lower than the XMM-Newton observation. The observed luminosity in the 2 - 10 keV resulting from our analysis is 0.9×10^{44} erg s^{-1}, consistent with the values given by the XRT observation. We confirm the long term variability reported by W08: the source is seen more luminous and more scattered in early 2006, then after two months the X-ray power decreases of about 30% (no information is available for the scattering component in the XRT data) and the same luminosity is found after more than 1 year. The scattering factor shows a strong decrease from the XMM to the Suzaku observation.

2.8.4 Swift J0918.5+0425

As already noted, the Suzaku observation of J0918.5+0425 represents the first attempt to study its extended X-ray emission after the extreme hard X-ray luminosity found by the BAT survey. Except for a detection in the soft band by Rosat, the Swift/XRT view J0918.5+0425 is the only available observation to look for variability. Unfortunately, the count level is low (46 counts in the whole band) and it is not statistically significant below 3 keV. We are able to fit the data with our best fit model, after removing the gaussian profile. However this is probably due to the uncertainty of the XRT detection and not to the lack of variability. In fact, the flux in the 2 - 10 keV band is about 50% lower than the XIS observation and almost four times lower than the 9-month averaged BAT flux extrapolated in the same energy range. We conclude that the source shows long term variability, but longer exposure are needed for a detailed analysis.

2.9 Summary and discussion

Among our sample, 3C 452 is certainly the only candidate as a Compton thick AGN:

1. The source spectrum shows both high absorption ($N_H \sim 4 \times 10^{23}$ cm^{-2}) and strong Compton reflection, which also affects the intrinsic power law photon index. The relative strength of the reflection is consistent with a not homogeneous absorber where a large fraction of the subtended solid angle is composed by gas optically thicker than the crossed amount along the line of sight;

2. The spectral parameters of the source keep coherent values in a time lapse of 6 years. The lack of variability is a trace of reflection dominated emission, because the nuclear intrinsic variability is diluted by radiation coming from the torus, covering a much larger region.

3. Altough the soft X-ray band is contaminated by the extended thermal gas and the lobes IC emission, a low scattering fraction ($< 0.5\%$) is found, confirmed by the XMM observation where the PSF allow to extract only the AGN region. This aspect is coupled with an extremely high ratio of the intrinsic 2 - 10 keV to the O[III] luminosity (see Winter et al. (2010) for the optical properties of the sample), classifies 3C 452 as "hidden" AGN, where,

according to Ueda et al. (2007) and Eguchi et al. (2009), the source is seen face-on and the equatorial region is covered by Compton thick matter. This scenario would be consistent with the hypothesis of a not homogeneous absorber.

4. The EW of the fluorescence iron line is lower than what expected from a Compton thick AGN and consistent with the evaluated column density, for an inclination angle $> 60°$ (Ghisellini et al. (1994),Ikeda et al. (2009)). However such a low EW could be justified by a Fe abundance lower than the solar value, in particular an EW = 164 eV is obtained for a Fe abundance in the range 0.2-0.3 (Ballantyne et al. (2002)). The quality data only allows to evaluate an upper limit to the Fe abundance of 0.7.

The cited properties assume more importance when comparing 3C 452 with 3C 105. Despite the comparable column density, as long as the redshift, X-ray luminosity and radio properties, 3C 105 seems to be not reflection-dominated and it is characterized by strong long term variability. These differences would be explained, for 3C 452, by a complex, clumpy absorber with extended regions of Compton thick matter, or by a highly photoionized absorber in 3C 105, suppressing the Compton reflection. It is clear that **high sensitivity, high spectral resolution hard X-ray observations are necessary to determine the presence of reflection in 3C 105 and fully understand the dichotomy between these two sources**.
The most prominent feature of 3C 105 is the strong variability in flux and scattering fraction found by comparing our results with the Chandra, XMM-Newton and XRT observations. The flux variability is also confirmed by the high normalization factor between the PIN and BAT data (~ 1.7). A luminosity variability, especially in time scales of months/years for Type 2 AGN, is not surprising, while a change in the scattered/partially covered emission is peculiar, and, coupled with the flux changes, it could reveal the distance and extension of the scattering region. Among the four observations, the highest scattering component ($\sim 1.4\%$) is found in the XIS detection. This could imply that we are including in the source model some external component. However, no external point sources or extended thermal emission are detected from the analysis of the high resolution Chandra/ACIS image, while a possible contamination of the southerm hotspot would be below the scattering factor value, considering also the statistical uncertainties (see Sec. 2.5.1). In addition, the analysis of the XIS spectrum of 3C 105 reported in W08 returns a higher scattering fraction ($\sim 2.7\%$). If the scattering component is intrinsically variable, then it can be differently interpreted according to the proposed models:

1. The arising power law in the soft band is nuclear emission escaping through a partially covered medium. A change in its intensity can be associated to the motion of the clouds along the line of sight, as Risaliti et al. (2002) models the variability in the absorbing column density. Extending their computation to this case and using the 3C 105 M_{BH} as given by Winter et al. (2010), a $\Delta N_H = 5 \times 10^{23}$ and a time delay of 50 days (Chandra/Suzaku observations time lapse) result to an absorber distance < 1 pc for a density $\rho < 10^9$ cm^{-3}.

2. The soft emission is scattering from a distant region (e.g. the NLR). A change in the nuclear flux results in a change of the scattered emission, with a time delay given by the distance

of the scattering region from the nucleus. An increase in luminosity can also increment the ionization of the surrounding medium, increasing the scattering efficiency.

Since we do not find absorption in the scattering component, it is unlikely that a fraction of the highly obscured intrinsic emission can arise from the most inner regions of the torus without absorption. On the contrary, the second hypothesis correlates well with the high variability of the absorption corrected X-ray luminosity and the low L2 − 10keV/OIII ratio. The same variability behaviour is found in J0318.7+6828, altough with less intensity. This AGN is the less absorbed of our sample ($N_H \sim 4 \times 10^{22}$ cm^{-2}). The scattering fraction from the XIS analysis is about half of the value from the XMM-Newton observation, altough the first requires a wider extracting region. We conclude that the variability of the soft scattered emission seems an ubiquitous property of these two sources, but a dedicated X-ray monitoring across time is needed to effectively relate these findings to the geometry and composition of the scattering/partially covering region.
Finally, the farthest source of our sample, J0918.5+0425, results to be a moderately absorbed Type 2 AGN. The strong variability that led this source to be removed from the 22-month BAT survey is confirmed by comparing the XRT, Suzaku and 9-month averaged BAT data. However, longer exposures and a finer spatial resolution are needed for a more detailed analysis.

2.10 The NHXM view

A simulation of the 0.5 - 80 keV X-ray view of 3C 105 as it would be observed by the NHXM LED and HED X-ray imaging spectrometers, at the focus of a hard X-ray focusing telescope, has been developed, on the basis of the response files and simulation script provided by the NHXM team. The extracting region is a 30“ radius circle, corresponding to a 4 times and 2 times HEW at E

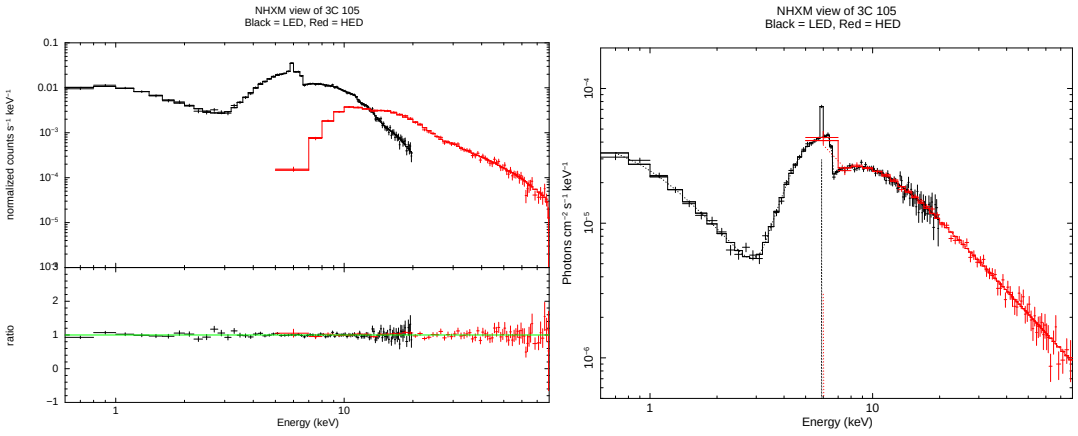

Figure 2.9: Folded (left panel) and unfolded (right panel) simulated spectra of 3C 105 as seen by NHXM, for the same ∼ 40 ks exposure. The black and red lines refer to the LED and HED respectively.

Simulation Best Fit Results of 3C 105

Mission	$N_H{}^a$ [10^{22} cm^{-2}]	Γ	$f_{scatt}{}^b$	Fe K E^c [keV]	Fe K EW^d [eV]	χ^2/d.o.f
Suzaku	$45.96^{+6.24}_{-6.56}$	$1.78^{+0.20}_{-0.19}$	$1.4^{+0.9}_{-0.5}$%	$6.40^{+0.07}_{-0.05}$	136^{+75}_{-62}	68.18/97
NHXM	$46.55^{+1.05}_{-0.85}$	$1.78^{+0.02}_{-0.02}$	$1.39^{+0.08}_{-0.07}$%	$6.40^{+0.03}_{-0.02}$	141^{+18}_{-14}	155.88/163

[a]Source intrinsic column density.
[b]Fraction of the scattered component relative to the intrinsic power law.
[c]Centroid energy and equivalent width respect to the whole continuum of the Fe fluorescence Kα line at the rest frame of the source redshift.

Table 2.6: Comparison of the best fit parameters of the 3C 105 spectral analysis as observed by Suzaku and expected for NHXM.

$<$ 10 keV and in the 20 - 60 keV energy range for LED and HED respectively. The resulting folded and unfolded spectra are shown in Figure 2.9.
The gain in sensitivity respect to the Suzaku/HXD and Swift/BAT instruments translates into a higher spectral significancy, clearly visible in the NHXM simulated spectra, allowing to better characterize the source. Also to be noted the full X-ray energy band coverage of the NHXM instruments. In Table 2.6 the best fit parameters from the Suzaku observation are compared to the present simulation, to underline the ability to constrain the column density, the slope, the scattering fraction and the Fe K properties.

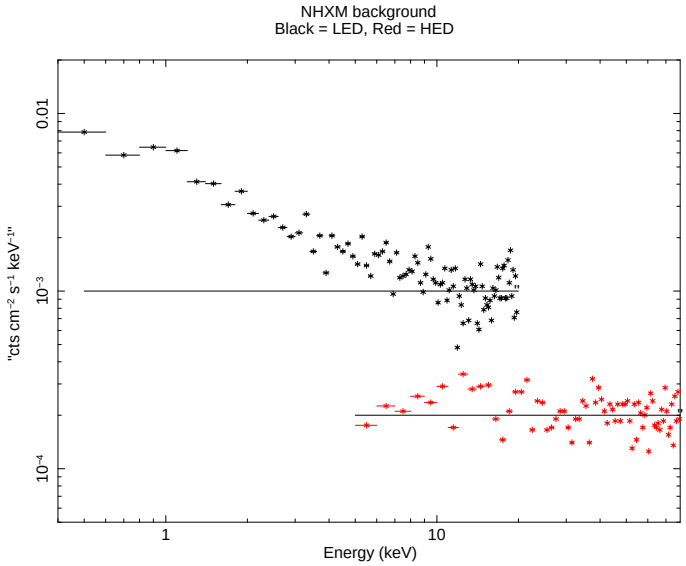

Figure 2.10: The expected NHXM background used as input for the 3C 105 simulation. The horizontal lines refer to a Non X-ray Background level of $1 \times 10^{-3}$and 2×10^{-4} cts cm^{-2} s^{-1} keV^{-1} for the LED and HED respectively.

The outstanding NHXM spectrum quality is however based on a fundamental assumption, defining the present scientific performance: the background level. In order to simulate the NHXM spectra, the total background level is setted as the sum of the unresolved CXB, entering the FOV, and a constant Non X-ray Background, due to the contribution of all the events not generated by the focused photons (e.g. particle background, decays, stray-light).
The background spectrum used as input for the present simulation is plotted in Figure 2.10. The unresolved CXB is assumed to be 50% (LED) and 90% (HED) for a 0.5 μCrab and 10 μCrab sensitivity below 10 keV and in the 20 - 60 keV energy range respectively. The power law shape of the CXB arises at lower energies and it is visible in the LED background spectrum. The requirement for the NXB is 1×10^{-3} (LED, AC off) and 2×10^{-4} (HED, AC on) cts cm^{-2} s^{-1} keV^{-1}.
The background minimization process that leads from the definition of the impinging space particle flux to the evaluation and characterization of the background count rate and spectral distribution is the aim of the present thesis.

Chapter 3

The space radiation environment

The first step in the background evaluation of a X-ray telescope is the detailed modelling of the radiation environment surrounding the spacecraft, which of course also depends on the mission orbit. The interaction of cosmic rays and solar wind particles with the Earth's magnetosphere gives rise to a region of trapped particles in the near-Earth environment. First discovered by Van Allen and his collaborators on Explorer I (Van Allen 1959), the so-called Van-Allen belts are principally composed by energetic protons and electrons contained by the Earth magnetic field in a toroidal region following the Earth dipole lines (see Sec. 3.3). These trapped particles, extending from a radius of $\sim$ 6400 km up to 10 Earth radii, pose a significant radiation threat to electronic systems: the detectors are switched off and protected by additional filters to avoid serious damages. The first requirement for every planned high energy space mission is the minimization of the time spent in the radiation belts. Three different orbits have been chosen/planned so far for the X-ray space missions:

- Low Earth Orbit (LEO): the spacecraft follows a nearly equatorial path below the radiation belts, with an altitude in the range 160 - 1000 km above the Earth's surface and an orbital period of about 90 minutes. The magnetosphere shields most of the cosmic rays, with an efficiency depending on the orbit inclination respect to the magnetic axis. At the same time the satellite is exposed to high fluxes of low energy secondaries produced by the interaction of charged particles with the Earth's atmosphere. Recently flown hard X-ray (e.g. Swift, Suzaku) and γ-ray (e.g. Agile, Fermi) missions are in LEO.

- High Elliptical Orbit (HEO): the high eccentricity of the elliptical orbit, reaching extreme apogees ($>$ 100000 km) allows to spend most of the operating time beyond the radiation belts and to be less interrupted by the frequent passages in the Earth's shadow, as it happens in LEO. The two major X-ray focusing telescopes, XMM-Newton and Chandra, follow this path. The orbit is less particle-crowded respect to the near-Earth environment, but it is exposed to high fluxes of energetic cosmic rays, while semi-trapped low energy protons can be funnelled by the X-ray optics and reach the focal plane.

- Second Lagrange Point (L2): the L2 point, located nearly 1.5 million km from the Earth, is

a gravitational saddle point, where spacecraft can remain well far from the belts at roughly constant distance from the Earth throughout the year by small station-keeping maneuvers. With the same side of the spacecraft always pointed to the Sun, calibration is simpler and the telescope achieves an uninterrupted view of the sky. On the other hand, at this distance the spacecraft is slight beyond the shadow of the Earth's umbra, and so exposed to the solar wind in addition to the unshielded galactic cosmic ray flux. The IXO mission is planned to orbit around the L2 point with a semi-major axis of 800000 km.

Each orbit defines a set of critical issues in the background minimization, so that the definition of the orbit follows the settlement of the scientific goals and the general design of the mission.
In this chapter a general overview of the space radiation environment as expected for the Simbol-X and NHXM mission, in HEO and LEO respectively, is given along with the detailed modelling of the major sources of background. These models will be used as input spectra in the background simulation. Among the orbit, other important parameters (e.g. solar modulation of the cosmic rays, mission duration) can influence the instrumental background. Where possible, the worst case is assumed to obtain a conservative evaluation of the background level. The orbital parameters of Simbol-X and NHXM, compared to a selection of operative high energy missions, are listed in the following Table:

Orbital parameters

Mission	Orbit	Altitude [km]	Perigee [km]	Apogee [km]	Inclination [deg.]
XMM-Newton	HEO	/	7000	114000	40
Chandra	HEO	/	5900	143000	68
INTEGRAL	HEO	/	9000	153000	52
Swift	LEO	~ 600	/	/	20.6
Suzaku	LEO	568	/	/	31.9
Agile	LEO	550	/	/	< 5
Fermi	LEO	550	/	/	28.5
Simbol-X	HEO	/	20000	180000	40
NHXM	LEO	550	/	/	< 5

Table 3.1: Orbital parameters of the major high energy mission currently operative as a comparison with the planned orbit of the Simbol-X and NHXM missions.

3.1 The diffuse photonic background

The high energy photonic background is a diffuse, nearly isotropic emission in the X-ray and γ-ray band, discovered as a serendipitous result in the well-known first detection of Sco-X1 (Giacconi et al. 1962) and then confirmed at higher energies by the Ranger lunar probe (Metzger et al. 1964). The Cosmic X-ray Background (CXB) extends up to hundreds of keV. Below 1 keV, the CXB is galactic, originating from the hot plasma in the Local Hot Bubble, the Galactic Disk and the Galactic Halo (Lumb et al. 2002). At higher energies the CXB radiation is accounted for by the integrated emission of unresolved AGN over the cosmic time, with a high fraction of highly absorbed AGN contributing to the hard part (20 - 40 keV) of the spectrum. As fully exploited in Chapter 2, the search for Compton thick AGN, totally absorbed below 10 keV, is one of the key scientific objectives of the future hard X-ray focusing telescopes, along with the characterization of the AGN obscuring matter. However, when dealing with background minimization issues, the same photons that can potentially reveal the AGN cosmic history become one of the major sources of the X-ray background by reaching the focal plane from directions outside the X-ray optics. Since the CXB is described by an inverse broken power law, the contribution to the background is higher in the soft energy range.

In the γ-ray regime, the diffuse emission has different origin. According to Abdo et al. (2010a), the γ-ray background is the sum of the galactic emission, produced by the cosmic rays interacting with the galactic interstellar gas, and an extragalactic component, still a matter of debate but probably due to unresolved blazar ($< 40\%$ from Abdo et al. (2010)), starburst galaxies and γ-ray bursts, plus true diffuse emission. Here we neglect the galactic component, despite intensities 10 times higher than the extragalactic emission (Strong et al. 2004), because it is highly anisotropic and restricted to a small solid angle ($\sim 0.7\pi$ sr for $|b| < 10°$).

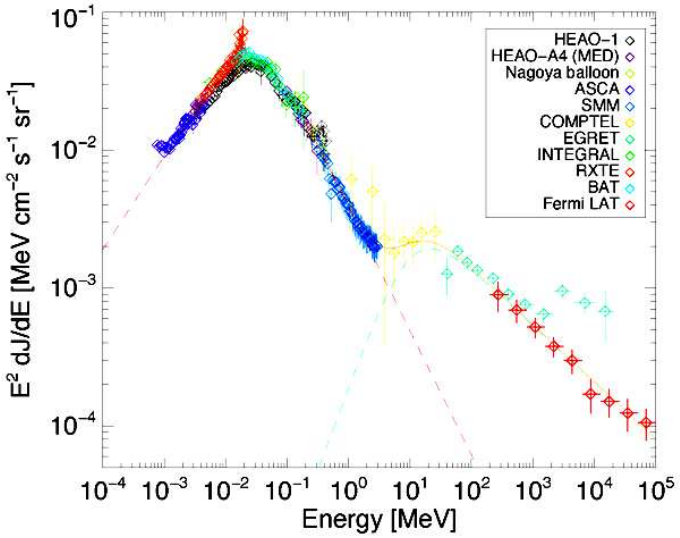

Figure 3.1: Compilation of observations of the extragalactic high energy background from Oberlack (2010).

In Figure 3.1 Oberlack (2010) updates the compilation of the extragalactic diffuse background detections of Ajello et al. (2008) with the addition of the first-year Fermi LAT observation. The dashed red line is a fit to the CXB spectrum, peaking in power at $\sim$ 25 keV, which is able to describe the diffuse emission up to few MeV. Since the AGN X-ray emission is believed to fall off at hundreds of keV because of the energy cut-off of the thermal electrons (Zdziarski et al. 2000), the smooth connection up to $\sim$ 4 MeV is theoretically interpreted by Inoue et al. (2008) as the contribution of additional nonthermal electrons with a soft spectrum. A second, flatter broken power law describes the high energy component (dashed blue line) extending up to 100 GeV.
Since we are not interested in the detailed fitting of each component contributing to the diffuse background, the Gruber et al. (1999) X-ray and γ-ray background spectrum in the 3 keV - 100 GeV range, where data from the HEAO-1 (Marshall et al. 1980), COMPTEL (Kappadath et al. 1996) and EGRET (Sreekumar et al. 1998) missions are fitted together, represents a simplified but efficient way to model the entire extragalactic photonic emission. The differential flux, in photons cm^{-2} s^{-1} keV^{-1} sr^{-1}, is composed by a simple exponential at lower energies and three summed power laws above 60 keV, in the form:

$$\mathrm{F}\,(3-60\,\mathrm{keV}) = 7.877\mathrm{E}^{-1.29}\mathrm{e}^{-\mathrm{E}/41.13} \tag{3.1}$$

$$\mathrm{F}\,(>60\,\mathrm{keV}) = 0.0259\left(\frac{\mathrm{E}^{-6.5}}{60^{-5.5}}\right) \tag{3.2}$$

$$+ \quad 0.504\left(\frac{\mathrm{E}^{-2.58}}{60^{-1.58}}\right) \tag{3.3}$$

$$+ \quad 0.0288\left(\frac{\mathrm{E}^{-2.05}}{60^{-1.05}}\right)\,. \tag{3.4}$$

The diffuse X-ray and γ-ray radiation is not affected by the solar activity and/or the Earth's magnetic field. The only difference between Simbol-X and NHXM orbits is the Earth's shielding that reduces the omnidirectionale flux in LEO (see Sec. 3.6). The Gruber's spectrum is extended here to lower energies (1 keV) and cut at 100 MeV because, because its contribution to the X-ray background is negligible for E> 100 MeV, and we will generally refer to this background source as CXB.

3.2 Cosmic rays

An important source of background in high energy instruments are Cosmic Rays, in large majority protons. The term "Cosmic Ray" (CR) usally defines any particle of extraterrestrial origin, from Galactic CR, probably originated from supernovae and other highly energetic events (Biermann et al. 1995), to particles of solar origin, like the Solar Energetic Particles (SEP), or produced by shocks in the outer eliosphere (Anomalous CR, Barth (1997)).
Below 100 MeV, the dominant population is given by the SEP, ejected from the Sun during flares or Coronal Mass Ejections and carried by the solar wind where they are fully ionized by shocks. These solar particle events, mainly occurring during solar maximum (see 3.2.1), last several days at a time and comprise both protons and heavier ions with variable compositions (see Ryan et al.

(2000) for a review). Given the highly variable and anisotropic nature of this events, for missions operating outside the radiation belts the observations are compromised for high levels of SEP and a continuous monitoring of the solar activity is required. The Chandra X-ray Observatory Center, for example, follows a near-real-time solar-proton alert system, using data from the ACE[1] Electron, Proton, and Alpha Monitor (EPAM, see Fig. 3.2) to hide the ACIS during extreme solar events.

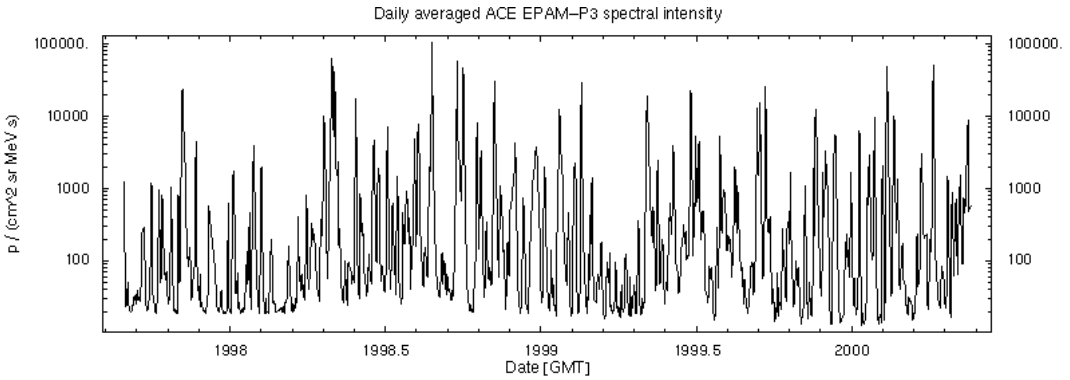

Figure 3.2: Daily averaged intensity of the ACE Electron, Proton, and Alpha Monitor (EPAM) P3 channel, centered on about 0.14 MeV.

The Anomalous CR, contributing to the fluxes in the range 10 - 50 MeV/nucleon, are single ionized nuclei reaching the top of the Earth's atmosphere and are believed to originate in the neutral interstellar gas that diffuses into the eliosphere and is then ionized by solar radiation. This component is seen only during solar minimum, and because of its low impact on the background level will be neglected.

First discovered in the early 900s by V. Hess with ionization chambers on balloon flights, the Galactic CR represent the dominant component of the CR flux in the Earth's vicinity, with energies ranging from $\sim$ 100 MeV up to 100 GeV (O'Dell et al. 2000). The GCR are composed of about 98% nuclei (87% Hydrogen, 12% Helium and 1% heavier nuclei, Simpson (1983)) and 2% leptons ($>$ 90% electrons, Adriani et al. (2009)). The differential flux for a given species i is well described by a power law of the form:

$$\mathrm{J_i(E_k)} \propto \mathrm{E_k^{-\gamma_i}} \tag{3.5}$$

where $\mathrm{E_k}$ is the kinetic energy per nucleon and γ_i is the spectral index, in the range 2.5 - 2.7 according to the different nuclear species. The deviation from a pure power law below 10 GeV in Figure 3.3 is a direct consequence of the modulation induced by the solar wind, while the low energy cut-off is produced by Earth's magnetic field shielding. Both these effects must be taken into account when modelling the GCR. Given the high percentage of protons, the contribution of electrons and positrons to the CR induced background is neglected, and the GCR flux will be treated as a proton flux.

[1]Advanced Composition Explorer, Gold et al. (1998)

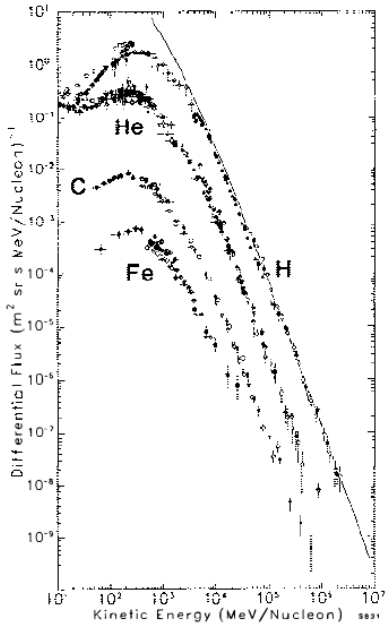

Figure 3.3: The differential spectra of cosmic rays for Hydrogen, Helium, Carbon, and Iron given by Simpson (1983). The solid line shows the Hydrogen spectrum corrected for the solar modulation.

3.2.1 Solar modulation

The solar magnetic activity varies with time, defining the so-called solar cycle which is directly dependent on the number of sunspots appearing on the Sun's surface. Studies of the solar activity from cycle 12 to 22 (from 50s to 90s) have determined that the length of the solar period ranged from 9 to 13 years, with 11.5 being the average (Stassinopoulos et al. 1996). According to Barth (1997), the solar cycle can be divided into a 7 year maximum phase and a relatively quiet 4 year minimum phase. This variability influences the intensity of the solar wind, which streams out from the Sun's corona at velocities as high as 120 km s^{-1} and creates the interplanetary magnetic field (IMF). GCR particles entering the heliosphere are scattered by IMF irregularities and undergo convection and adiabatic deceleration in the expanding solar wind (Heber et al. 2009). As a result, the GCR anti-correlates with solar activity (Fig. 3.4, left panel), following its cyclic pattern (Shikaze et al. (2003), Wiedenbeck et al. (2005)). The solar wind has also the effect of shaping the Earth's magnetic field: the result of the balance between the Earth and solar wind magnetic pressures is the magnetosphere, starting from $\sim$ 10 Earth radii at dayside (the "bow shock") and reaching tails up to $\sim$ 300 radii in the anti-solar directions. About 99% of the solar wind particles pass around the magnetosphere, so that spacecrafts in LEO can not be reached by the SEP.
The planning of a high energy space mission must take into account the solar phase: a period of solar maximum is preferable, since the GCR induced background level is lower, but always keeping in mind that the Sun also operates as source of high energy particles that depend on the Sun activity. We are currently two years into cycle 24. Following the predictions of Hathaway et al. (1993), the Sun activity will reach its maximum in 2013, but, on the basis of the expected low

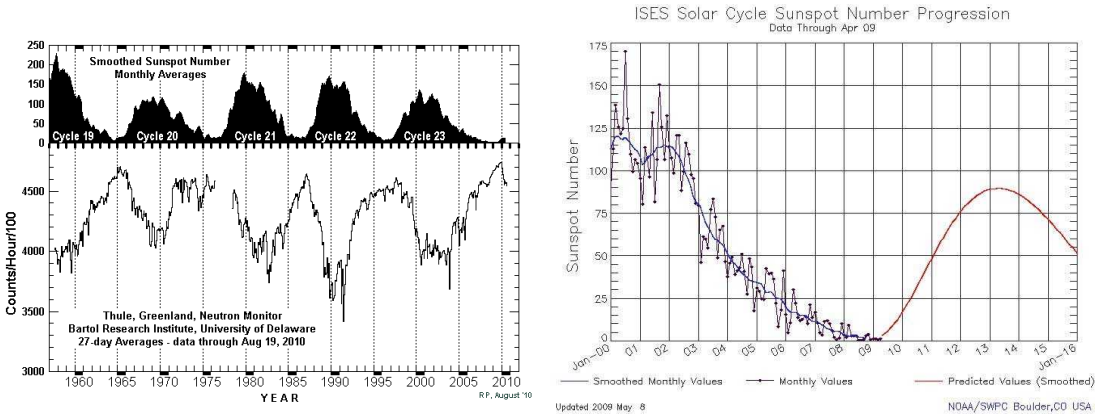

Figure 3.4: *Left panel*: Effect of the solar activity (top) on the flux of secondary neutrons (bottom), generated by cosmic rays interactions with the atmosphere, detected by the Neutron Monitor of Thule, Greenland (courtesy of the Bartol Research Institute, University of Delaware). *Right panel*: Number of sunspots prediction of the solar cycle 24 according to the NASA NOAA (National Oceanic and Atmospheric Administration) Space Weather Prediction Center of Boulder, Colorado.

number of sunspots, it will be a quiet activity phase (Figure 3.4, right panel).

The GCR modulation induced by the solar activity is commonly characterized by the solar modulation parameter Φ, in the force-field approximation proposed by Gleeson & Axford (1968). In practice, the energy loss of the cosmic rays due to diffusional, convectional and adiabatic interactions with the solar wind is integrated into a single modulation parameter Φ (in units of megavolts, MV). The quantity $Ze\Phi$, where e is the magnitude of the electron charge and Z is the atomic number of the particle, is the loss of the particle potential energy when moving from the solar wind boundary to the Earth (see Li et al. (2008) for a complete solution of the GCR transport equation). The GCR solar modulation as a function of time can be derived from the analysis of the GCR spectra detected by the ACE Cosmic Ray Isotope Spectrometer (CRIS[2]) (Wiedenbeck et al. 2005): the modulation parameter Φ can vary from by a factor of ~ 3 from ~ 300 MV at solar minimum to ~ 1200 MV at solar maximum (see Figure 3.5).

3.2.2 The geomagnetic cut-off

The flux and spectral distribution of the charged particles impinging onto the spacecraft is influenced by the Earth's magnetic field, which provides varying degrees of protections according to the spacecraft position along its orbit. Charged particles moving in a magnetic field undergo a vector force that results in a curved path. If we define the particle charge and momentum as Ze and p, the rigidity R is the momentum per unit charge:

$$\mathrm{R} = \frac{\mathrm{pc}}{\mathrm{Ze}} \tag{3.6}$$

$$= \frac{\mathrm{A}}{\mathrm{e}}\sqrt{\mathrm{E_k^2} + 2\mathrm{m_p c^2 E_k}} \tag{3.7}$$

[2]http://www.srl.caltech.edu/ACE/ASC/DATA/ftp/pub/ace/level3/index.html

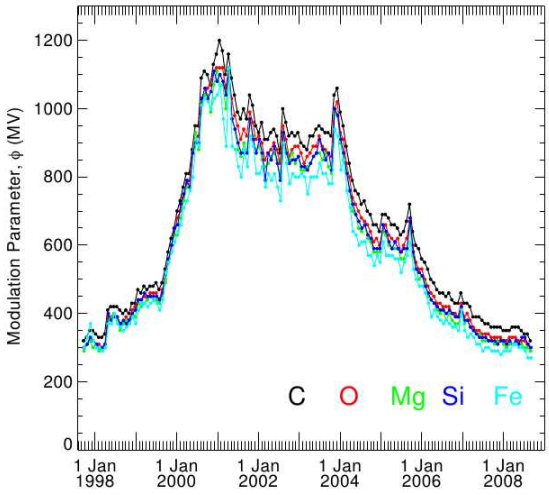

Figure 3.5: Level of solar modulation as a function of time, from late 1997 through August 2008, using the ACE CRIS C, O, Mg, Si and Fe data (courtesy of the ACE team).

where A is the particle's mass in amu, E_k is the kinetic energy and $m_p c^2$ is the proton rest mass. The rigidity is measured in units of electron volts/number of charge units, i.e. volts or ,more often, gigavolts (GV). For a proton of kinetic energy 1 GeV, the previous relation translates into:

$$R = \sqrt{E_k^2[\mathrm{GeV}] + 2 \cdot 0.938 \cdot E_k[\mathrm{GeV}]} \simeq 1.7\,\mathrm{GV} \tag{3.8}$$

When interacting with the Earth's magnetic field, the particle follows a trajectory of curvature radius ρ around the magnetic field component perpendicular to the momentum, $B_\perp$, given by:

$$\rho = \frac{R}{B_\perp} = \frac{pc}{B_\perp \cdot Ze}\,. \tag{3.9}$$

A higher momentum particle, i.e. a higher kinetic energy particle, will have a higher resistance to be deflected by the magnetic field. On the contrary, for a given particle rigidity, an higher magnetic strength will reflect the particle, as it happens in near Earth environment: charge particles that have a low rigidity are deflected at a certain depth in the magnetosphere and, given the R - E_k relation, the spectrum of cosmic rays is characterized by a low energy cut off. The equation of charged particle motion in a magnetic field does not have a closed form but numerical solutions can be calculated for any position of the Earth's magnetic field by combining the International Geomagnetic Reference Field (IGRF) models to massive computer simulations (Smart & Shea (2005) and references therein), as given by the rigidity world map isocontours for an altitude of 450 km of Fig. 3.6.

However, it is possible to study the effect of the orbital parameters on the geomagnetic cut-off by using the Störmer's equation in the approximation of a dipolar field geometry (Störmer 1930). Defined λ_m the magnetic latitude, ε and ϕ the zenith and azimuthal angles of the incoming particles (the latter measured from the north magnetic axis), $M_\oplus$ the Earth's dipole moment and

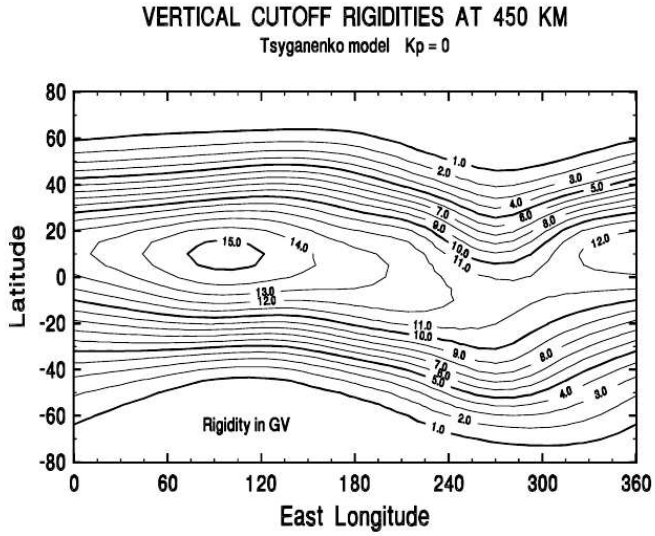

Figure 3.6: Contours map of the cut-off rigidity for a 450-km orbiting spacecraft as given by Smart & Shea (2005).

r the distance from the dipole center of the Earth, the cut-off rigidity R_c in a dipole field is:

$$R_c = \frac{M_\oplus}{r^2}\left[\frac{\cos^4\lambda_m}{\left(1+\sqrt{1\mp\sin\varepsilon\,\sin\phi\,\cos^3\lambda_m}\right)}\right]\ \text{GV}. \tag{3.10}$$

The $\mp$ refers to positively/negatively charged particles respectively. The combination of the zenith and azimuthal angles gives a higher cut-off for positively (negatively) charged particles arriving from eastern (western) direction. As a results, at lower energies the GCR flux is not isotropic but exhibits an East-West asymmetry. This effect is not taken into account here ($(\varepsilon,\,\phi) = (0,0)$) because we are interested in the omnidirectional flux. Since we are only considering the proton component of the GCR, we will use only the minus sign for the rigidity cut-off computation. The Earth dipole moment is obtained by multiplying the g_1^0 term (in units of G) of the IGRF most recent release by the cube of the average Earth radius (in cm). The IGRF-11 release reports a magnetic field of 2.95 μG for 2010, which translates into a dipole moment of 7.6×10^{25} G cm^3. However we will refer to a $M_\oplus = 8.1 \times 10^{25}$ G cm^3, the magnetic strength in the 50s, as used by most of the authors cited here, in order to compare our results. The differences in the computed rigidity cut-off fall anyway within the errors of the dipole field approximation. A magnetic field of 1 Gauss has the same energy density of 1 statvolt/cm, where the statvolt is a unit of electrical potential in the cgs system units ($\sim$ 300 volts in the S.I. system), so that the magnetic dipole moment $M_\oplus = 8.1 \times 10^{25}$ G cm^3 = $2.43{\times}10^{19}$ GV cm^2. The Equation 3.10 for protons can be rewritten as:

$$R_c = 14.9 \times \left(\frac{1+h}{R_\oplus}\right)^{-2} (\cos\lambda_m)^4\ \text{GV} \tag{3.11}$$

$$= \sqrt{E_c^2[\text{GeV}] + 2\cdot 0.938\cdot E_c[\text{GeV}]} \tag{3.12}$$

where h is the orbit altitude. The distribution of the energy cut-off in the dipole magnetic field is shown in Figure 3.7 (left panel). The number in the horizontal magnetic equator is the dipole shell parameter L (= $r/R_\oplus$ of the B-L McIlwain coordinate system: the magnetic strenght at 7 Earth radii, in the equatorial plane, is the same as in the polar near-Earth region, i.e. the two point share the same low energy cut-off. For the same altitude, the ridigity cut-off is lower for high magnetic latitudes. This is clear in right panel of Figure 3.7, where the low energy cut-off is plotted as a function of the inclination for an altitude of 550 km (LEO, red line) and of 70000 km (HEO, blue line). An energy cut-off < 10 MeV, which characterizes the HEO orbits, is obtained also for a high magnetic latitude ($> 70°$) LEO orbit. Low inclinations are required for LEO mission to exploit the Earth's magnetic shielding.

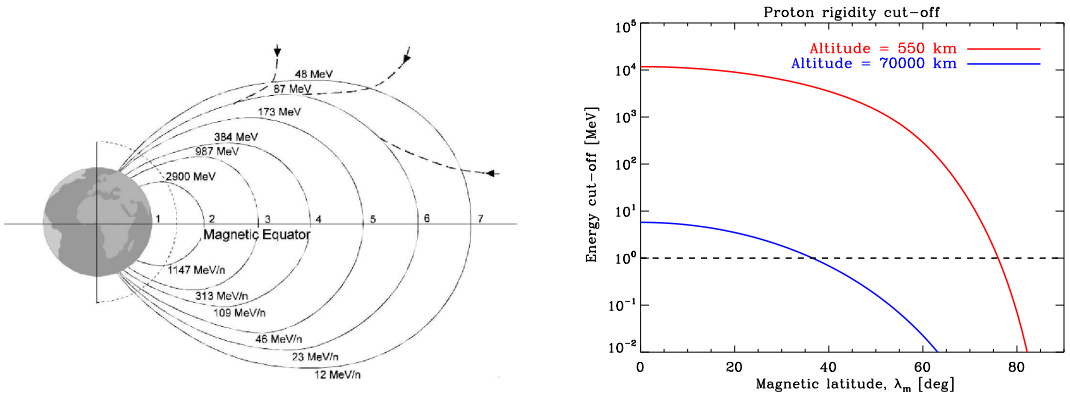

Figure 3.7: *Left panel*: The distribution of the low energy cut-off as a function of the dipole shell parameter L along the magnetic equator. *Right Panel*: The low energy cut-off of GCR protons as given by the magnetic latitude for a LEO (altitude = 550 km, red line) and HEO (altitude = 70000 km, blue line) orbit. The orizontal dashed line refers to a rigidity cut-off of 1 MeV.

3.2.3 GCR model

Mizuno et al. (2004) provides a nice GCR proton flux model as a function of the solar modulation and the geomagnetic cut-off, which is able to reproduce the primary proton spectrum in the high geomagnetic latitude region as detected by the AMS (Alcaraz et al. 2000b), BESS (Sanuki et al. 2000), LEAP (Seo et al. 1991), IMAX (Menn et al. 2000) and CAPRICE (Boezio et al. 1999) experiments. Here we use their model to explore the effect of the solar modulation and geomagnetic cut-off in LEO (altitude = 550 km) for two orbital inclinations, 20° and 80°. The latter case, as explained in Sec. 3.2.2, also reproduces the typical GCR spectrum in HEO.
The model modifies the ridigity dependence, in power law form, of Alcaraz et al. (2000b), by introducing a shift in energy due to the solar modulation, as defined by Gleeson & Axford (1968), and the low energy cut-off. The differential flux F_{p^+}, in prot. cm^{-2} s^{-1} MeV^{-1} sr^{-1}, takes the

form:

$$F_{p^+} = 2.39\,10^{-3} \times [R(E_k + \Phi)]^{-2.83} \quad (3.13)$$

$$\times \frac{(E_k + m_p)^2 - m_p^2}{(E_k + m_p + \Phi)^2 - m_p^2} \quad (3.14)$$

$$\times \frac{1}{1 + (R(E_k + \Phi)/R_c)^{-12}}\,, \quad (3.15)$$

with the particle energy and solar modulation expresses in GeV e GV respectively. The particle ridigity as a function of $(E_k + \Phi)$ is taken from Equation 3.8. The resulting proton spectrum, from 10 MeV to 100 GeV, is plotted in Figure 3.8 (left panel). The solar activity influences the

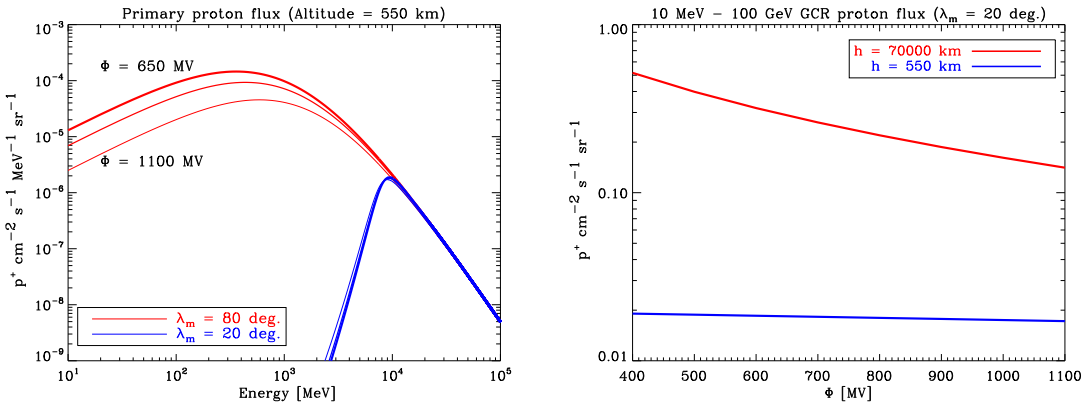

Figure 3.8: *Left panel*: Primary proton spectrum, as modelled by Mizuno et al. (2004), expected in LEO for a magnetic latitude of 80° (red line) and 20° (blue line), with a solar modulation Φ = 650 MV (thick line), 800 MV (medium line) and 1100 MV (thic line). *Right panel*: GCR proton flux integrated from 10 MeV to 100 GeV as a function of the solar modulation parameter Φ (MV) for a HEO (red line) and LEO orbit (blue line), computed for a magnetic latitude of 20°.

proton flux at the lower energies (< 1 GeV) and only for high latitude regions, while for equatorial orbits this effect is hided by the geomagnetic cut-off that shields the incoming protons up to 10 GeV. If we integrate the proton flux along its energy range, from 10 MeV to 100 GeV, the total rate of protons at solar minimum ($\Phi \sim 400$ MV) is about a factor 3 higher than at solar maximum ($\Phi \sim 1100$ MV) for a HEO orbit (or a high inclination LEO orbit), as shown in Figure 3.8 (right panel). In the evaluation of the GCR induced background level in HEO, the input proton flux is modelled for a phase of solar minimum following a conservative approach: all the results must be considered as an upper limit of this background component.

Figure 3.9 shows the differential total proton flux for the two case studies, Simbol-X (HEO, red line) and NHXM (LEO, blue line), used as input for the present background evaluation. The Simbol-X proton spectrum has been computed by Claret (2006) for a solar minimum, using the SPENVIS[3] tool, as part of the Simbol-X phase A study (red line). The blue line refers to the NHXM expected total proton flux[4]: the primary GCR component is based on the AMS data (Alcaraz et al. 2000b)

[3]Space Environment Information System, BIRA–IASB/ESA–ESTEC, http://www.spenvis.oma.be

[4]The NHXM proton flux is based on the analysis of the AGILE mission radiation environment and courtesy of the AGILE team (Tavani et al. 2009).

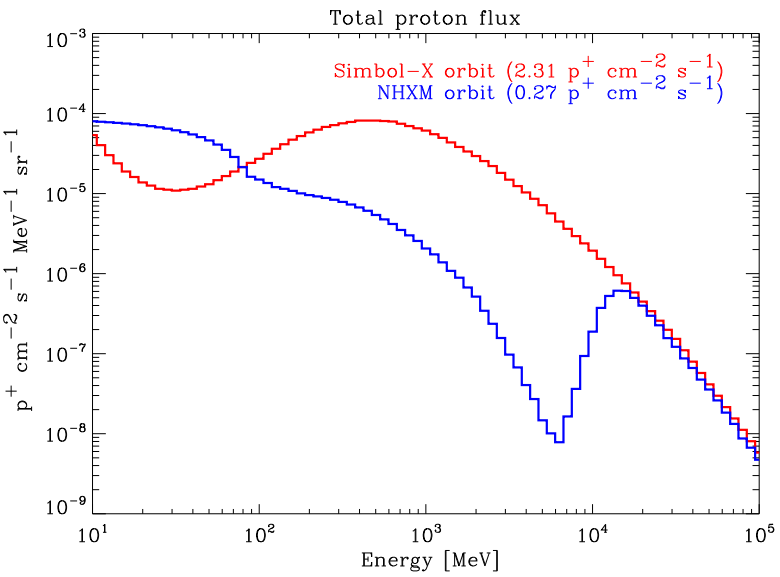

Figure 3.9: The total differential proton flux modelled for the HEO Simbol-X (red line) and LEO NHXM (blue line) missions. The low energy protons arising below the geomagnetic cut-off in the NHXM case are due to the CR interaction with the Earth's atmosphere (albedo protons, see Sec. 3.4)

and it is visible at higher energies with a rigidity cut-off at about 10 GeV. Below the geomagnetic shielding a secondary proton component arises due to the albedo protons trapped in the near-Earth environment. This particle population characterizes only the LEO missions, and it is described in Sec. 3.4.

3.3 Trapped particles

The Van Allen magnetospheric trapped particles, mainly protons and electrons, can be divided into two belts along the equatorial plane: an inner belt centered at about 1.5 Earth radii and an outer belt centered at about 5 Earth radii. Protons are the main contributors to the inner belt, with energies up to 600 MeV. The electrons distribution is separated into two zones, with higher energies electrons (several MeV) in the inner zone ($<$ 2 Earth radii) and lower energy electron ($<$ 1 MeV) in the outer region ($>$ 3 Earth radii). The intermediate region is called "slot" and it is characterized by less intense particles fluxes. Respect to protons, the outer belt electrons can reach low altitudes ($\sim$ 500 km) in the polar regions. While a complete understanding of the processes and sources originating the radiation belt is still missing, the two main contributors are the solar wind leaking into the magnetosphere for the outer belt and the cosmic rays interaction with the Earth's atmosphere for the inner protons (Selesnick et al. 2007). As a results, the solar cycle has opposite effects on electron and proton levels. The increase in the solar activity causes an expansion of the atmosphere which interacts with the low altitude edges of the radiation belt producing a subsequent decrease of the trapped proton population. At the same time, the higher

occurance of solar flares (100 times higher than in solar minimum according to Reames et al. (1994)) injects particles into the magnetosphere increasing the electrons level.
The trapped particles models commonly used are the NASA AP-8 and AE-8 (Vette 1991) for protons and electrons respectively ("A" is for Aerospace Corporation). Based on data from 43 satellites, they are the most complete models in terms of radiation belts regions coverage, altough with some extrapolations, and particle energy ranges, form 0.04 to 500 MeV for protons and from 0.04 to 7 MeV for electrons. However, they are static model, i.e. they do not take into account the time variation of the magnetic environment, as the secular change of the Earth's magnetic field or the influence of magnetic storms on the particles intensity (Daly et al. 1996). For some applications, the AP-8 and AE-8 models could underestimate the level of hazard due to the radiation environment. Dynamical models of the trapped particles are currently available for particular regions, as the CRRESPRO and CRRESELE models, for protons and electrons respectively, based on data from the CRRES satellite (Meffert & Gussenhoven (1994), Brautigam & Bell (1995)) or the SAMPEX/PET model for low altitude protons based on measurements made by the Proton/Electron Telescope onboard the SAMPEX satellite (Heynderickx et al. 1999). Waiting for a complete dynamical description of the trapped particles belt, both models, static and dynamic, should be used.
Missions operating in HEO switch off the instruments when passing through the radiation belts to avoid damages. Figure 3.10 (left panel) show the count rate of high energy protons and electrons (E> 50 keV) detected by the Low Energy Radiation Monitor on board the XMM-Newton telescope, while the right panel indicated the corrispondent spacecraft altitude. Below $\sim$ 60000 km, the rate of particles impinging onto the spacecraft suddenly increases as the telescope crosses the belts. The

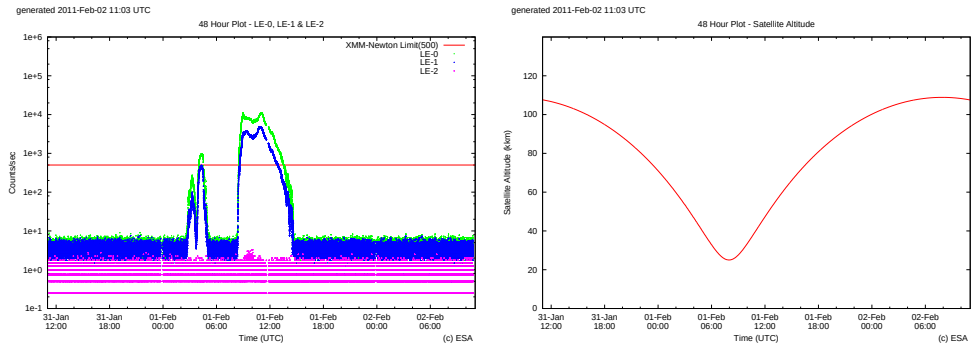

Figure 3.10: The count rate (left panel) and corrispondent spacecraft altitude (right panel) of the protons and electrons impinging on the XMM-Newton spececraft as detected by the Low Energy (LE) radiation monitor along a 48 hr exposure. Both plots are taken from the XMM live radiation monitor feed.

XMM instruments start to perform scientific observations above a satellite elevation of 46000 km, but only if the radiation background is low enough. The spacecraft spends 138 ks of the 48-hour orbital period above 46000 km, and because of the radiation background, on average about 132 ks can be used to perform scientific observations with the EPIC and RGS instruments.
In LEO, the spacecraft orbits below the damaging trapped populations, but the radiation belts

can still affect the background level due to the South Atlantic Anomaly (SAA). The SAA is a depression of the radiation belt due to an off-set of the dipole center respect to the Earth's center to the North. This shift, coupled with the inclination of the magnetic and rotation axis, causes the trapped particles to reach low altitudes regions ($\sim$ 500 km) in the South East of Brazil (Figure 3.11, top panel). The electron composition of the SAA is extremely high respect to protons (Figure 3.11,

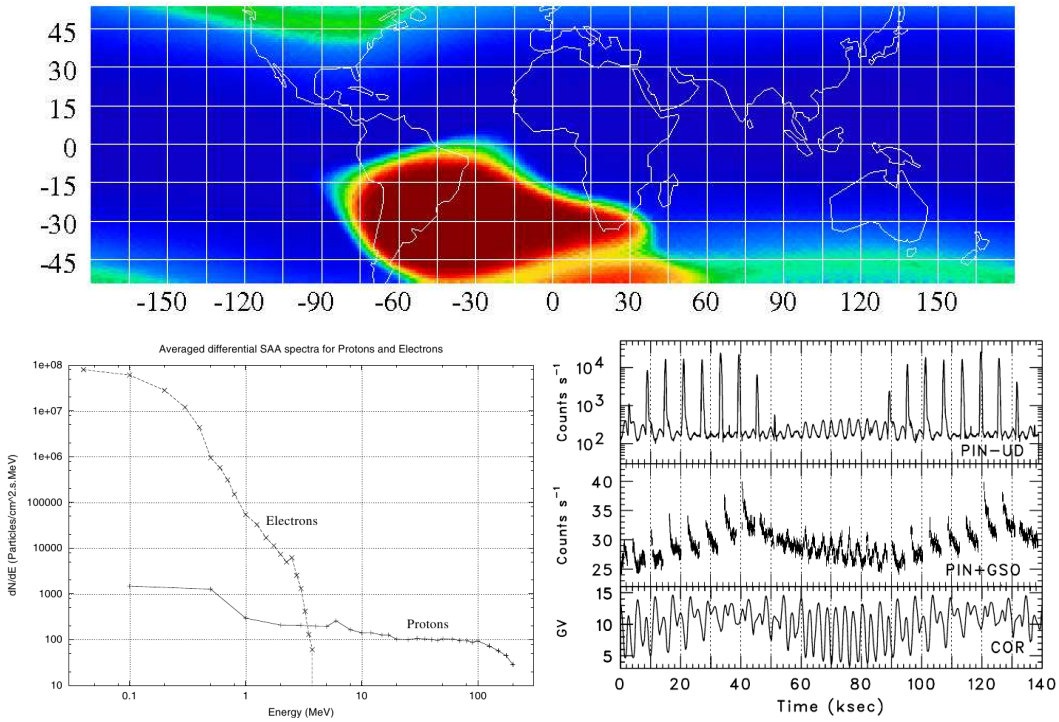

Figure 3.11: *Top panel*: Radiationm belts leaking in LEO detected by the Rosat (altitude = 575 km, $\lambda_m = 53°$) South Atlantic Anomaly Detector (SAAD, Snowden et al. (1992)); the SAA is the central peak, while the polar regions are reached by the outer belt electrons. *Bottom panel*: Omnidirectional SAA electrons and protons flux (left) detected by the Compton Gamma Ray Observatory (CGRO) mission (altitude = 500 km, Dean et al. (2003) and references therein) and SAA induced temporal variation of the background count rate (right) of the Suzaku/HXD detectors (Kokubun et al. 2007).

bottom-left panel), with a day-average flux at 40 keV of $\sim 5 \times 10^4$ cm^{-2} s^{-1} MeV^{-1} for electrons and ~ 0.2 cm^{-2} s^{-1} MeV^{-1} for protons (Gehrels 1992). However, only the protons can activate the spacecraft material by the production of radioactive nuclei which decay at a delayed time respect to the impinging proton. While during the passage through the SAA the instruments are usually not operative, so that the prompt electron induced background can be neglected, proton induced radioactive decays give rise to delayed events that increase the background level when the spacecraft is out of the SAA region. This is clearly visible in the Suzaku/HXD background light curve of Figure 3.11 (bottom-right panel) published by Kokubun et al. (2007). The PIN Upper Discriminator (UD) in the top panel monitors the charged particle flux (peaks refer to the

SAA), the bottom panel show the cut-off rigidity (COR) and the middle panel the sum of the PIN and GSO light curves (blank parts refer to the SAA passage). After the SAA passage, a sudden background increase is generated by radionuclides with half lives lower than the orbital period, while the longer modulation is generated by nuclides with longer decay time. The aim of the present work is the study of the prompt background, so that we do not evaluate the SAA effect in LEO. However, on the basis of the Suzaku experience and given the lower inclination of the NHXM orbit (less and shorter SAA passages, Gehrels (1992)), we assume that the SAA induced delayed events cause a less than 50% background increase.

3.4 Albedo particles

The term "albedo" generally defines the fraction of incident radiation reflected by a surface. In the context of space radiation environment, the albedo population refers to the class of secondary particles generated by the interaction of Cosmic Rays with the Earth's atmosphere, which produces a moltitude of secondaries of relatively low energy by means of nuclear interaction cascades. Figure 3.12, from Dean et al. (2003), shows a sketch of the main processes and particles involved from the first proton hit (top) to the final secondary population as they cross the atmosphere. A fraction

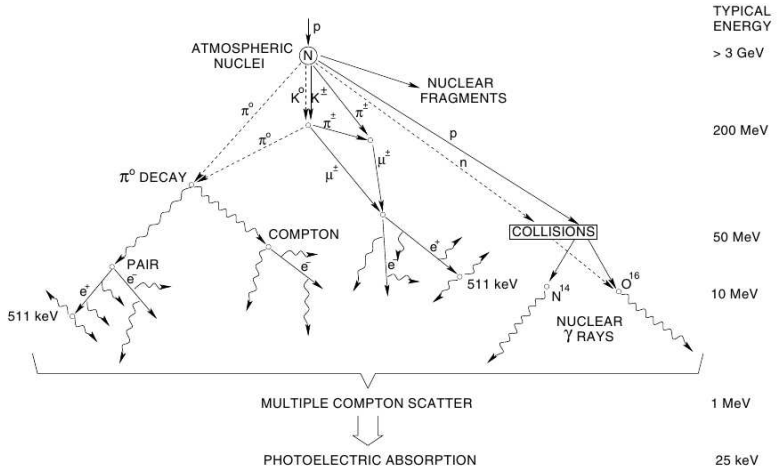

Figure 3.12: The air shower produced by the CR interaction with the Earth's atmosphere as reported in Dean et al. (2003).

of these particles, mainly hadrons, leptons and photons, escapes upward, covering a wide energy range, from a few keV to approximately the primary proton geomagnetic cut-off. Below ~ 50 keV, where the upward photonic component is photoelectrically absorbed, the Compton reflection of the CXB impinging into the atmosphere is the dominant source of radiation. As a result, the LEO path crosses high particle-crowded region, altough with low energy, and a detailed modelling of the albedo population is required to evaluate their contribution to the total LEO background level.

3.4.1 Albedo charged particles

As described in Sec. 3.3, the inner radiation belt is mainly produced by the CR interaction with the Earth's atmosphere. In particular, the high energy protons (E > 100 MeV) are generated by cosmic ray atmospheric neutron decay (CRAND, Selesnick et al. (2007) and references therein). The albedo charged particles (mainly protons, electrons and positrons) populating the low altitude (< 1000 km) region can be seen as a transitioning phase from the free state at the exit of the atmosphere to the magnetospheric trapped population. They are composed by "splash" particles, emerging from the atmosphere, and reentrant albedo particles, travelling backward along the magnetic field line connected to the point of observation (Derome et al. (2000), Bidoli et al. (2002)). There is also a fraction of secondary particles that can remain trapped for several years, bouncing several times in the magnetic field.

The model of the albedo proton spectrum is based on the AMS observation at $\sim$ 400 km given by Alcaraz et al. (2000b) and plotted in Figure 3.9 along with the primary proton flux. According to the AMS results, the secondary upward and downward proton fluxes are nearly identical for magnetic latitudes $< 46°$. At polar latitudes, instead, the downward flux is obscured by the leaking primary GCR.

While the albedo protons are produces by the combination of neutrons decay and collisional processes, the secondary electrons and positrons are mainly due to the decay of charged and neutral pions. The expected energy distribution along the NHXM orbit is based on the AMS (Alcaraz et al. 2000a) and MARYA-2 (Koldashov et al. 1995) experiments as kindly provided by the AGILE team (Tavani et al. 2009), and shown in Figure 3.13. According to Alcaraz et al.

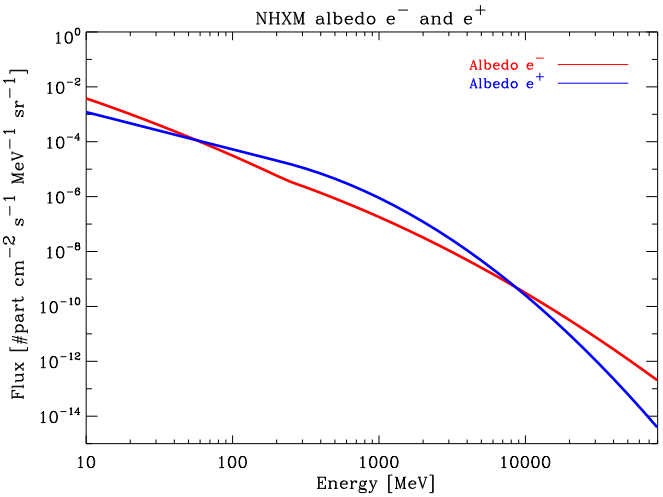

Figure 3.13: Albedo electrons and positrons spectra as expected for the NHXM orbit, based on observations of the AMS and MARYA-2 experiments and provided by the AGILE team.

(2000a), the electron and positron upward and downward fluxes follow the latitude distribution found for the secondary protons. Given the East-West anisotropy of the primary proton flux, the angular distribution of the albedo electrons and positrons shows a similar effect. Since the pion

production cross sections is peaked at forward angles, the secondary leptons follow the direction of the primary protons. At the same time, the interactions with the Earth's magnetic field leads the electrons to be absorbed by the atmosphere, while the positrons turn in the opposite direction reaching higher altitudes (Derome et al. 2001). As a result, in the equatorial region the positron flux should be up to three times higher than the electrons level.
Since the random spacecraft orientation along its orbit 'averages out' the anisotropy (Armstrong et al. 1990), and considering the similarity of downward and upward fluxes, the albedo protons, electrons and positrons can be considered, at low latitudes, isotropic. Regarding the positron excess, the AMS experiment did not detect any difference in the secondary electrons and positrons intensities, so we do not take into account this effect.

3.4.2 Albedo photons

The CXB and cosmic rays interaction causes the Earth's atmosphere to be extremely bright in the X-ray and γ-ray bands, with an intensity comparable or higher than the CXB flux, for the same portion of solid angle. As a consequence, when the spacecraft is close to the Earth, e.g. in LEO, the photonic albedo can be an important source of background.

X-ray albedo

As described in the first chapter of this thesis, the hard X-ray energy band has been studied so far only by indirect imaging or collimated systems. For such missions (e.g. BeppoSAX, INTEGRAL, Swift) the study of the CXB in the hard X-ray domain is complicated by the high particle background that can not be disentangled from the diffuse extragalactic emission due to the low sensitivity. As a consequence, a widely used technique to evaluate the true CXB emission is by indirectly measure the difference between an open sky observation and an Earth occulted exposure, where the collected counts are the sum of the internal background and the Earth X-ray emission. In this context, the accurate modelling of the Earth photonic albedo performed by Churazov et al. (2008) and Sazonov et al. (2007) to study the CXB in the hard X-ray band as seen by INTEGRAL is used to evaluate the X-ray albedo encountered by the NHXM mission.
The total X-ray albedo spectrum (E $<$ 1 MeV) is the sum of the CXB reflection, dominating below $\sim$ 50 keV, and the CR induced X-ray emission. The latter is mainly produced by the bremsstrahlung and positron-electron annihilation emission at higher energies that escapes into free space after multiple Compton down-scatterings, i.e. the emergent photons have lost much of the memory of the parent emission processes (Sazonov et al. 2007). Churazov et al. (2008) computes the CXB reflection by means of Monte Carlo simulations of the CXB photon interaction (photoabsorption, Rayleigh and Compton scattering) with the Earth's atmosphere. The input CXB spectrum is the same on which we base our background analysis (Gruber et al. 1999), altough the shape of the albedo does not depend on the input spectrum below 20-30 keV. The emergent radiation is strongly dependent on the viewing angle: at high energies the higher contribution comes from photons emerging at small angles to the surface (photons scattered only once), while for directions along the normal the photons are backscattered at lower energies. As a result, the

Earth's reflection is limb-brightened at higher energies (> 100 keV) and limb-darkened at lower energies. Since above 50 keV the CR induced emission dominates, the angle averaged flux for the reflected albedo is a good appoximation of this component, in the aim of the background evaluation.
The CXB induced X-ray albedo takes the form:

$$\mathrm{F_{refl}} = \mathrm{A(E)} \times \mathrm{F_{CXB}} \tag{3.16}$$

where $\mathrm{F_{CXB}}$ is given by Gruber et al. (1999) and the angle averaged ratio of the reflected to the incident emission A(E) is

$$\begin{aligned} \mathrm{A(E)} &= \frac{1.22}{(\mathrm{E}/28.5)^{-2.54} + (\mathrm{E}/51.3)^{1.57} - 0.37} && (3.17)\\ &\times \frac{2.93 + (\mathrm{E}/3.08)^4}{1 + (\mathrm{E}/3.08)^4} && (3.18)\\ &\times \frac{0.123 + (\mathrm{E}/91.83)^{3.44}}{1 + (\mathrm{E}/91.83)^{3.44}} \,. && (3.19) \end{aligned}$$

As obviuos given the extragalactic photonic source, this component does not depend on the solar modulation or the geomagnetic cut-off. What changes from the INTEGRAL to the NHXM mission is only the solid angle subtended by the Earth, which increases the total albedo intensity in LEO. On the contrary, above 50 keV the X-ray albedo is strictly connected to the modulation of the primary CR flux. Sazonov et al. (2007) performed a Monte Carlo simulation of the CR interaction with the Earth's atmosphere, obtaining a general model of the Earth's hard X-ray surface brightness in the 25 - 300 keV energy range as a function of the solar modulation parameter (Φ), geomagnetic rigidity cut-off ($\mathrm{R_c}$) and zenith angle θ ($\mu = \cos(\theta)$) of the escaping photons. The differential flux takes the form:

$$\mathrm{F_{CR}} = \frac{\mathrm{C}}{(\mathrm{E}/44\,\mathrm{keV})^{-5} + (\mathrm{E}/44\,\mathrm{keV})^{1.4}}\ \mathrm{phot.\ cm^{-2}\ s^{-1}\ keV^{-1}\ sr^{-1}} \tag{3.20}$$

where the normalization factor C is given by

$$\mathrm{C} = \frac{3\mu(1+\mu)}{5\pi}\ \frac{1.47 \times 0.0178\left[(\Phi/2.8)^{0.4} + (\Phi/2.8)^{1.5}\right]^{-1}}{\left[1 + \left\{\mathrm{R_c}/\left[1.3\Phi^{0.25}\left(1 + 2.5\Phi^{0.4}\right)\right]\right\}^2\right]^{0.5}} \,. \tag{3.21}$$

The sum of the two components describes the INTEGRAL/SPI Earth albedo observation of Churazov et al. (2007), if a normalization factor of 31.7 $\mathrm{keV^2\ cm^{-2}\ s^{-1}\ keV^{-1}\ sr^{-1}}$ is used for the CR induced emission, resulting from angle averaging the surface brightness and adopting a solar modulation parameter $\Phi = 0.45$ GV. The resulting differential flux, in phot. $\mathrm{cm^{-2}\ s^{-1}\ keV^{-1}\ sr^{-1}}$, is plotted in red in Figure 3.14 (left panel), along with the observations of the INTEGRAL/IBIS (Türler et al. 2010) and Swift/BAT (Ajello et al. 2008) instruments, in green and blue respectively, obtained with the same Earth occultation technique (the continuous black line refers to the CXB flux for comparison). The Swift observation is cut at 40 keV because in the spectral fitting the authors do not take into account the CXB reflection, resulting in a sharp cut-off at these energies. The Churazov et al. (2007) model is decomposed in the two components (thinner red lines) and

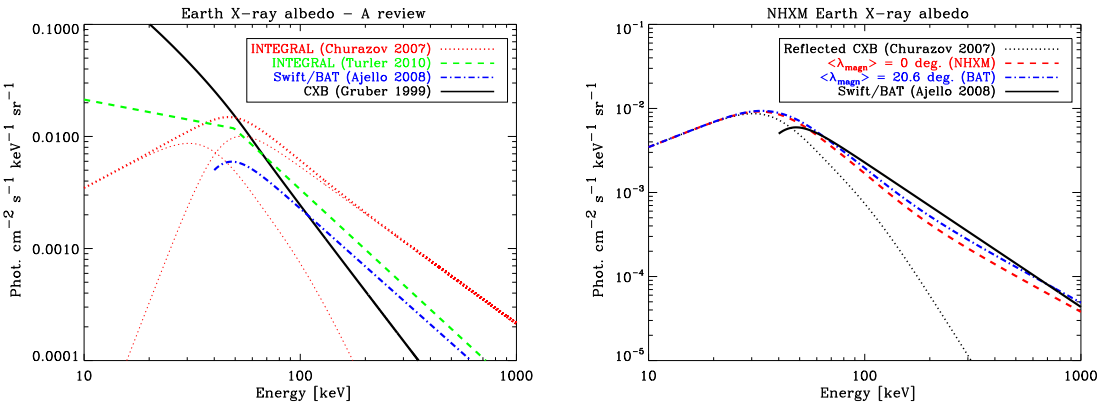

Figure 3.14: *Left panel*: The Earth X-ray albedo as observed by INTEGRAL/SPI (Churazov et al. 2007), INTEGRAL/IBIS (Türler et al. 2010) and Swift/BAT (Ajello et al. 2008). The thin dotted lines show the decomposition of the Churazov et al. (2007) observation in CXB reflection ($<$ 50 keV) and the CR induced emission at higher energies, while the black line refers to the CXB flux for comparison. *Right panel*: The total X-ray albedo modelled for the NHXM (red line) and the Swift/BAT (blue line) orbit. The latter is shown in comparison with the real Swift/BAT observation (continuous black line), while the dotted black line is the modelled CXB induced component, which, in units of solid angle, does not depend on the orbit inclination and it results to be the same fot both orbits.

all the spectra are extended up to 1 MeV for background evaluation reasons. The first fact to be noted is that the Churazov et al. and Turler et al. spectra, altough clearly different, are based on the same INTEGRAL observation. One reason is that in the IBIS fitting the authors achieve a steeper slope in the hard band (1.78), consistent with the results of Ajello et al. (2008), while Churazov et al. (2007) keeps the spectral parameters of Sazonov et al. (2007) fixed and adjusts only the normalization. However the Turler group obtains a higher/lower soft/hard emission even using the same spectral distribution and several hypothesis (the different instruments, the more detailed modelling of intrumental effects, the addition of point sources in the soft domain) are proposed to explain the discrepancy.

Fortunately, the conservative approach of considering the worst case (Churazov flux) coincides also with the more detailed model, and we will neglect the IBIS observation. The lower intensity of the Swift/BAT is explained by the different portion of atmosphere observed. As explained in Sec. 3.2.2, the top of the atmosphere is reached by a flux of GCR characterized by a low energy cut-off that decreases from the equatorial to the polar region. The intensity of the emerging CR induced X-ray photons, as a direct consequence, increases for higher latitudes. INTEGRAL observed the Earth in the polar region (an average latitude of 65° is consistent with the resulting intensity), while the Swift/BAT data are taken at different positions along its orbit, with an inclination of $\sim 21°$. A spacecraft in LEO can only see only a portion of the Earth's surface (Figure 3.15). For an altitude h of 600 km (Swift) at the geomagnetic equator, the maximum latitude region intercepted

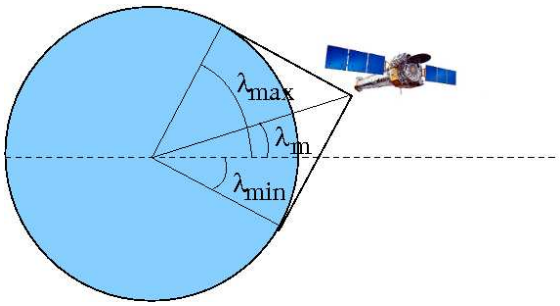

Figure 3.15: The maximum latitude region intercepted by a LEO spacecraft orbiting at a magnetic inclination λ_{m}.

by the line of sight is given by:

$$\lambda_{\mathrm{max}} = \mathrm{acos}\left(\frac{\mathrm{R}_{\oplus}}{\mathrm{R}_{\oplus}+\mathrm{h}}\right) \approx 24^{\circ} \tag{3.22}$$

Along the Swift orbit, albedo photons reacing the spacecraft are generated from a latitude range of $\pm 45^{\circ}$, lower than the INTEGRAL observation. An additional change in the X-ray albedo intensity is due to the modulation by the solar activity, but in this case both observations are taken at solar minimum.
From the Equation 3.20, the intensity of the emerging radiation exhibits a central brightnening as observed for the CXB reflection. In the modelling of the NHXM X-ray albedo, we integrate the CR induced radiation up to the maximum zenith angle ($\pi/2$ sr), computing the normalization factor for a solar minimum Φ =0.45 GV. The rigidity cut-off is calculated by means of Eq. 3.10, for an average latitude at the magnetic equator (NHXM) and of $\sim 21^{\circ}$ (Swift). The resulting flux is summed to the CXB reflection (the same of INTEGRAL) to obtain the total X-ray albedo, plotted in Figure 3.14 (right panel). The modelled Swift/BAT X-ray albedo (blue line) is consistent with the observed data (continuous black line), so that the extracted flux for the NHXM case (red line) represents a good approximation of the real case.

γ-ray albedo

The γ-ray emission ($>$ 1 MeV) of the Earth's atmosphere, as a direct consequence of the CR interaction, is mainly produced by the decay of neutral pions and kaons above 50 keV, while at lower energy the dominant source is the bremsstrahlung radiation from secondary and reentrant electrons and positrons (see e.g. Dean et al. (2003)). The Earth's limb is extremely bright in the γ-ray band, with an intensity ten times higher than the central regions at energies $>$ 100 MeV (Abdo et al. 2009). This is because in the limb the radiation is composed by forward-emitted photons after the tangential interaction of the primary proton, so that the energy loss due to Compton scattering is low. Another visible anisotropy in the γ-ray band is an East-West effect related to the magnetic deflection of the GCR flux. This asimmetry is neglected here since we are interested in the total Earth's disk emissivity.
The γ-ray energy differential flux for the NHXM background evaluation is based on the upward γ-

ray flux of Mizuno et al. (2004), based on observations collected from literature (Thompson (1974), Imhof et al. (1976), Ryan et al. (1979), Gurian et al. (1979)), after applying a rigidity correction factor C_R to normalize for the lower NHXM inclination:

$$C_R = \left(\frac{R_c(\lambda_m = 23°)}{4.5\,GV}\right)^{-1.13} = \left(\frac{11.5\,GV}{4.5\,GV}\right)^{-1.13} . \quad (3.23)$$

The rigidity cut-off is computed not for the average latitude value (0°) but for the maximum intercepted latitude region ($\sim 23°$) because the larger amount of radiation comes from the limb region, where the photonic production is enhanced by the higher CR flux. Here the Mizuno et al. (2004) γ-ray albedo differential flux $F_{\gamma-ray}$, in phot. cm^{-2} s^{-1} MeV^{-1} sr^{-1} takes the form:

$$F_{\gamma-ray}\,(1 - 20\,MeV) = C_R \times 1.01 \times 10^{-2} E^{-1.34} \quad (3.24)$$

$$F_{\gamma-ray}\,(20 - 1000\,MeV) = C_R \times 7.29 \times 10^{-2} E^{-2} \quad (3.25)$$

It is plotted in red in Figure 3.16, along with the X-ray albedo (black line). As a comparison,

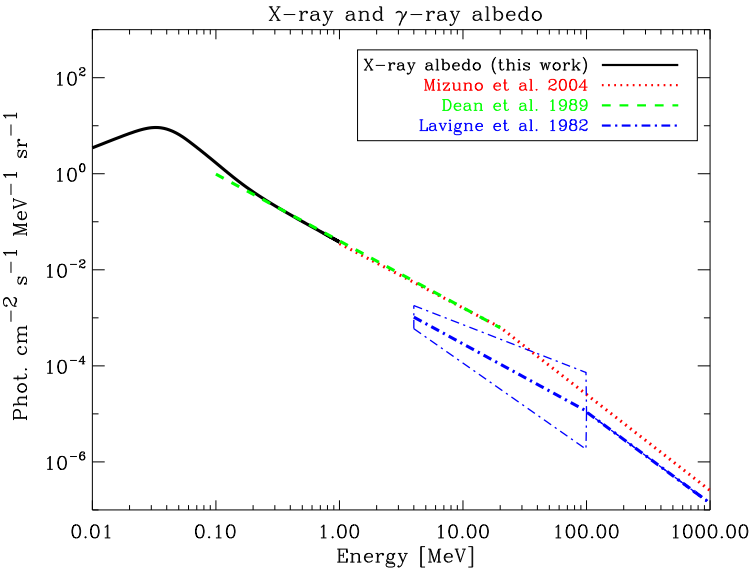

Figure 3.16: The Earth's atmosphere γray albedo as expected along the NHXM orbit (red line, Mizuno et al. (2004)) and as a comparison, the computed spectrum of Dean et al. (1989) at the geomagnetic equator (green line) and the albedo observed by the Agathe experiment (Lavigne et al. 1982) at $\lambda_m = -23.5°$. The black line is the modelled X-ray albedo which connects to the γ-ray emission at 1 MeV.

we also show the γ-ray atmospheric emission computed by Dean et al. (1989) at the geomagnetic equator (green line) and observed by the Agathe balloon (Lavigne et al. 1982) at $\lambda_m = -23.5°$ for an atmospheric pressure of 3 mb (blue line). The latter is consistent with the Mizuno et al. results if the uncertainty is taken into account.

The energy spectra of the X-ray and γ-ray albedo are smoothly connected, altough based on different calculations. This consistency is the proof that the photonic albedo is accurately modelled.

3.4.3 Albedo neutrons

As for γ-ray and charged particles, the source of the atmospheric neutrons is the impinging GCR flux, except for the higher latitude regions ($\lambda_m > 70°$) where also solar protons contribute (Lockwood et al. 1973). The mechanism for neutron production is mainly spallation of nitrogen and oxygen nuclei by GCR collisions, which generate direct knock-out nucleons or charge-exchange reactions, peaking at $\sim$ 100 MeV, and secondary intranuclear cascades followed by the neutron evaporation from highly excited nuclei peaking 1 MeV (Frank et al. (2001), Hajek et al. (2004)). As a result, the energy distribution of the albedo neutrons extends from thermal energies (few keV) to hundreds of MeV.
The most recent measurement has been made by the COMPTEL instrument onboard the CGRO mission (Morris et al. 1998) in 1991-1994, while the majority of the studies regarding the atmospheric neutrons refer to the late 60s and 70s, performed on board rocket (Lockwood & Friling 1968) and balloon (Preszler et al. 1972) flights, the Salyut and MIR space stations (Lobakov et al. 1992) and the OGO-6 satellite (Jenkins et al. (1970), Lockwood et al. (1973)). Among the Monte Carlo simulations of the expected neutron flux, the model by Armstrong et al. (1973) is the most widely used thanks to its extended energy coverage and the accurate validation. In Armstrong & Colborn (1992), the authors predict the upward moving (from 2π sr) neutron flux F_n, in neutr. cm^{-2} s^{-1} MeV, at solar minimum for a magnetic latitude $\lambda_m = 42°$ and an altitude of 45 km. In the energy range of interest (1 keV - 1 GeV) it takes the form:

$$F_n(0.001 - 0.1\,\mathrm{MeV}) = 0.047E^{-0.88} \tag{3.26}$$

$$F_n(0.1 - 1\,\mathrm{MeV}) = 0.40e^{-0.97\,E} \tag{3.27}$$

$$F_n(1 - 10\,\mathrm{MeV}) = 0.15E^{-1.34} \tag{3.28}$$

$$F_n(10 - 200\,\mathrm{MeV}) = 0.0086e^{-0.045\,E} + 0.0021e^{-0.0085\,E} \tag{3.29}$$

$$F_n(200 - 1000\,\mathrm{MeV}) = 1.95E^{-1.61}\,. \tag{3.30}$$

The solar activity influences the neutron flux only for high latitudes ($\lambda_m > 50°$, Lockwood & Friling (1968)): Armstrong et al. (1973) refers a variation of $\sim$ 20% of the 1 - 10 MeV neutron flux during the solar cycle at $\lambda_m = 42°$. A strong dependance on the magnetic latitude, i.e. on the geomagnetic cut-off, is instead found, with a flux at 5 GV about 3.7 times higher (Weidenspointner et al. 1998) than the geomagnetic equator ($\sim$ 15 GV). In Jenkins et al. (1970), from $\sim 40°$ to 0° in latitude the flux is 3 times lower, a value confirmed by Armstrong & Colborn (1992). We assume an isotropic neutron flux, as obtained by Lockwood et al. (1973).
Morris et al. (1995) fits the COMPTEL neutron measurement, at an altitude of 450 km, zenith angle 0° and quiet solar conditions, with the following expressions for the two limiting hardness ratios, in terms of omnidirectional flux (neutr. cm^{-2} s^{-1} MeV^{-1}):

$$F_{\mathrm{Morris}}|_{\mathrm{Up.limit}} = 0.45\,e^{0.152R_c}E^{-1.36} \tag{3.31}$$

$$F_{\mathrm{Morris}}|_{\mathrm{Low.limit}} = 0.82\,e^{0.152R_c}E^{-1.48} \tag{3.32}$$

$$\tag{3.33}$$

We compare the upper limit, computed for a ridigity cut-off $R_c = 4.5$ GV ($\lambda_m \sim 40°$), with the model of Equation 3.26, after normalizing for the different altitude with the factor C_{alt}

$$C_{alt} = \left(\frac{45\,\mathrm{km}}{450\,\mathrm{km}}\right)^2 \tag{3.34}$$

and multipling by 2 to take the ominidirectional flux. The result is plotted in blue in Figure 3.17, where the continuous and dashed lines refer to the Armstrong et al. and Morris et al. equations respectively. The simulated and observed spectra are consistent. We decide to extrapolate the

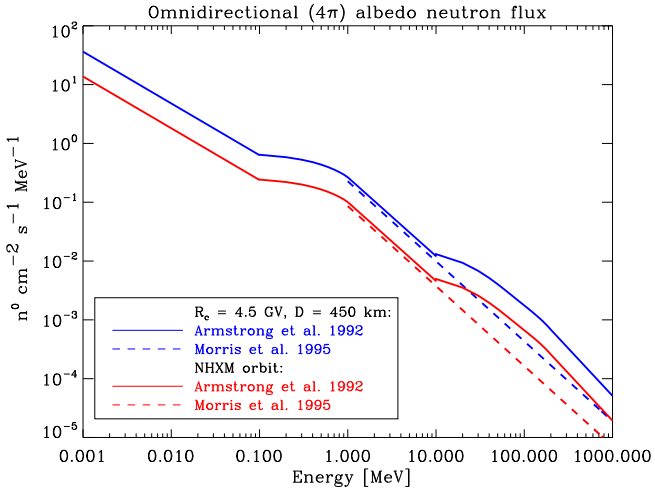

Figure 3.17: The omnidirectional albedo neutron flux, at solar monimum, as modelled by Armstrong & Colborn (1992), continuous line , and Morris et al. (1995), dashed line, for two orbital positions: altitude of 450 km at $\lambda_m = 42°$ (blue lines) and altitude of 550 km at the geomagnetic equator (red line).

expected NHXM albedo neutron flux from the first model, which covers a wider energy range, after correcting for the different altitude (550 km) and latitude (geomagnetic equator). The latter correction is obtained dividing by a factor 3, as discussed before, and the result is plotted by the red continuous line. It must be pointed out that, to achieve the same corrispondence with the COMPTEL data, the Morris et al. (1995) spectrum is computed for a latitude $\sim 20°$ (11.5 GV). This means that the model dependance on the rigidity cut-off does not take into account the smaller decrease in flux observed at lower latitudes, a factor of 2 from 40° to 28° and of 1.4 from 28° to 0°.

3.5 Soft protons

Electrons in the radiation belts and in the outer regions can scatter with the X-ray optics and be collimated to the focal plane. For this reason, X-ray telescopes on board Chandra, XMM-Newton and Swift are equipped with magnetic diverters that avoid electrons to reach the detectors by deflecting their path (see e.g Willingale (2000)). What came unexpected after one month of

operation of the Chandra mission is that low energy protons can be funnelled too by the X-ray optics and cause serious damages to the detectors performances.
A decrease of the Charge Tranfer Efficiency (CTE, see Sec. 4.1.2) of about 2 orders of magnitude was observed in the Chandra/ACIS Front-Illuminated (FI) CCDs after the first eight unprotected perigee passages in September 1999 (O'Dell et al. 2000). On the contrary, no degradation was found for the Back-Illuminated (BI) CCDs. This fact, coupled to the lack of degradation when the ACIS was moved from the field of view during the radiation belt passage, and the type of CTE damage (Prigozhin et al. 2000), led to identify low energy (100 - 200 keV) proton scattering with the mirror shells (Kolodziejczak et al. 2000) as the main source of the damage.
The XMM-Newton mission was launched in December 1999. The $\sim 50\%$ of the damaging proton flux of the ACIS, with same energy range, was expected for the XMM-Newton EPIC/MOS (Nartallo et al. 2002), which is a FI instrument but is partially shadowed by the RGS gratings, while no degradation was foreseen for the BI EPIC/pn (Kendziorra et al. 2000). As a result, the XMM-Newton instruments are protected by special filters for altitudes lower than 70000 km (Nartallo 2002). Unfortunately above this limit, where the instruments are fully operative, the soft

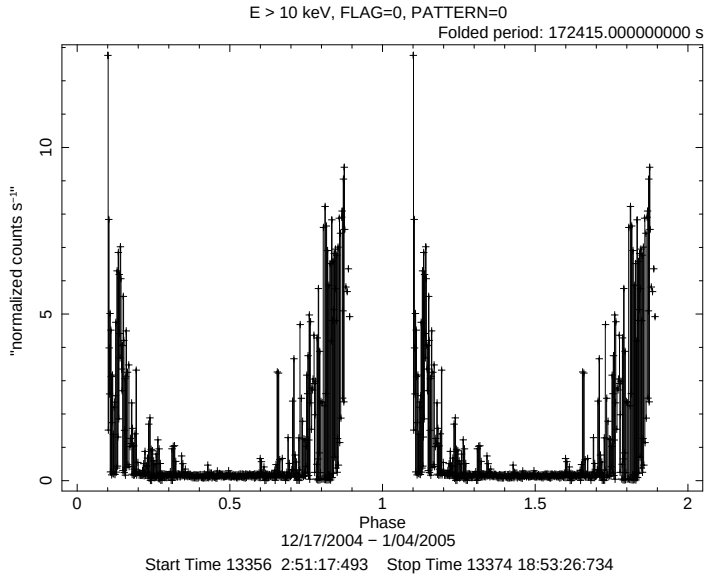

Figure 3.18: Folded light curve of soft proton flares detected by XMM-Newton EPIC/pn along 10 orbits, selecting the events with E> 10 keV, FLAG = 0 and PATTERN = 0 (Fioretti et al. 2006).

proton funnelling is still observed by the XMM-Newton detectors, altough with lower intensity. When entering the FOV, the soft protons cause a sudden increase in the background level, with events that can hardly be disentangled from the source X-ray photons and consequently can not be rejected on board. The so called "soft proton flares" can last from ~ 100 s to hours with an intensity up to three orders of magnitude higher than the quiescent level (De Luca & Molendi 2004), leading to a considerable loss of the observing time. This background component does not affect the Chandra mission due to the lower effective area.
In Figure 3.19 the folded light curve of the EPIC/pn soft proton flares detected along 10 orbits is

shown, selected by taking into account only the single (pattern = 0), best quality (flag = 0) events with an energy deposit higher than 10 keV, where the effective area to true X-ray photons falls off. The blank areas represent the passage through the radiation belts: when the intruments start to be operative, an increase in the flares occurance is visible due to the residual radiation belts proton population, but flares still occur well above an altitude of 70000 km.
Given the low energy range and the orbit region affected by the soft protons induced background, the most probable source is given by solar particle events interacting with the Earth's magnetosphere. However, since the discovery of this particle population is relatively recent, models of the protons low energy distribution are still poor, and are complicated by the fact that soft proton flares are totally uncorrelated with the particle fluxes detected by the radiation monitor on board XMM-Newton, sensitive for protons > 3.5 MeV (Kendziorra et al. 2000). At the same time, the soft proton flares are highly variable, with a seasonal effect as the geotail (the magnetosphere night side) sweeps around the Earth and a short term variability due to the solar and geomagnetic activity (Blackwell et al. 2000). As a proof of the solar origin of such events, missions operating in LEO (e.g. Swift, Suzaku) do not suffer from soft proton flares. Nartallo (2002) extracts the proton spectrum from 30 keV to 1 MeV from the observation of the Equator-S satellite obtained at $\sim$ 70000 km, where XMM-Newton starts to perform observations. The differential flux can be described by a power law with negative slope ~ 2.8, with a measured proton flux of ~ 3 prot. cm^{-2} s^{-1} keV^{-1} sr^{-1} at 100 keV. It is plotted in red in Figure 3.19, while the blue line refers to the solar wind proton spectrum detected by the ACE mission (Spiga et al. 2008), which orbits in L1 at ~ 1.5 million km from the Earth. The proton flux at 70000 km altitude, where the flare peak

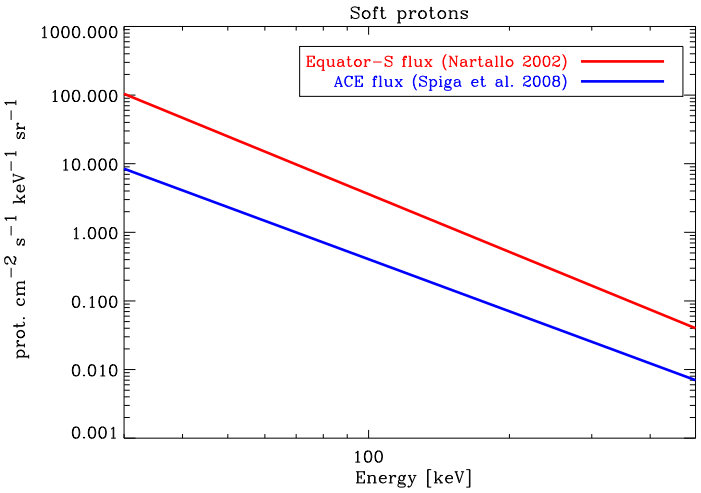

Figure 3.19: Differential flux, in prot. cm^{-2} s^{-1} keV^{-1} sr^{-1}, of the low energy protons as detected by the Equator-S (red line, from Nartallo (2002)) at $\sim$ 70000 km altitude, and by the ACE mission (blue line, from Spiga et al. (2008)) in L1.

is observed, is about an order of magnitude higher than the pure solar wind proton contribution. As expected, at the magnetosphere boundary a considerable fraction of trapped particles is still found, contributing to the total low energy proton flux.

The only solution to avoid soft proton flares for future X-ray telescopes orbiting in HEO is placing a magnetic diverter powerful enough to deflect both electrons and protons exiting the X-ray optics (see e.g. Turner (2006) and Spiga et al. (2008)). The design of the diverter requires a detailed knowledge of the angular and energy distribution of the protons after their interaction with the optics, which is difficult because of the uncertainty of the input models and the occuring physics process when protons are deflected to the focal plane.
The aim of the present thesis is to characterize the quiescent background that is detected when observing the astrophysical target. However, thanks to the flexible architecture of the Monte Carlo simulator (see Chapter 5), in Sec. 6.3 the simulation of an XMM-Newton soft proton flare is performed to study the physics processes causing the reflection and set some preliminary contraints on the diverter design of a hard X-ray focusing telescope.

3.6 Earth's shielding

The Earth's atmosphere acts both as a source of particles and shielding, via occultation. This effect must be taken into account when simulating the total rate of particles impinging into the spacecraft. For an altitude h = 550 km, the solid angle $\Omega_{\oplus}$ subtended by the Earth, after defining the Earth's coverage half angle $\theta_{\oplus}$, is given by:

$$\Omega_{\oplus} = 2\pi \left[1 - rmcos\theta_{\oplus}\right] \simeq 1.2\pi \,\mathrm{sr} \tag{3.35}$$

where

$$\theta_{\oplus} = \mathrm{asin}\left(\frac{\mathrm{R}_{\oplus}}{\mathrm{R}_{\oplus} + \mathrm{h}}\right) . \tag{3.36}$$

Altough we assume an uniform angular distribution for all the simulated particles, the total angle coverage is different according to the Earth's atmosphere effect and/or the particle charge, and it is summarized in Table 3.2.

Angular distribution

Orbit	CXB	GCR	Albedo protons	Albedo electrons	Albedo positrons	Albedo photons	Albedo neutrons
HEO	4π	4π	/	/	/	/	/
LEO	2.8π	2.8π	4π	4π	4π	1.2π	1.2π

Table 3.2: Solid angle, in sr, covered by each class of background source for a HEO and LEO orbit.

In HEO, the Earth's effect is neglected and the CXB and GCR flux comes from the whole sky. On the other hand, in LEO part of CXB and GCR angular distribution is shielded by the Earth, which emits an upward flux of photon and neutrons from a solid angle that is approximately equal to the Earth solid angle. The albedo charged particles, instead, come from 4π sr because of the magnetic field interaction.

3.7 The modelled space radiation environment

The resulting total particle flux expected in HEO and LEO (the NHXM case) is plotted in Figure 3.20, top and bottom panels respectively. These spectra are used as input for the evaluation of the space radiation environment interaction with the spacecraft and detectors material and its consequent effect on the total background level. The energy range of interest, and the integrated particle flux, in #part. cm^{-2} s^{-1}, is listed in the following Table:

PARTICLE FLUX

Source	Energy range	HEO flux[a]	LEO flux
CXB	[1 keV - 100 MeV]	197.2	137.1
Protons[b]	[10 MeV - 100 GeV]	2.31	0.27
Albedo electrons	[10 MeV - 80 GeV]	/	0.59
Albedo positrons	[10 MeV - 80 GeV]	/	0.40
Albedo X-rays	[1 keV - 1 MeV]	/	2.56
Albedo γ-rays	[1 MeV - 1 GeV]	/	0.30
Albedo neutrons	[1 keV - 1 GeV]	/	0.17

[a]The total flux integrated for the subtended solid angle and the energy range in #part. cm^{-2} s^{-1}.
[b]Only GCR flux (HEO) and the sum of the primary and albedo protons (LEO). In the latter case, since the two components are treated together in the background simulation, the GCR flux is evaluated without the Earth shielding, i.e. from 4π sr. This leads to overestimate the primary protons induced background of $\sim 30\%$.

Table 3.3: Energy range and integrated flux of the modelled background sources in HEO and LEO.

We remind the reader that the solar minimum is assumed, i.e. the worst case, in the modelling of the particles intensity. It must be noted that only the sources of quiescent background, i.e. with approximately a prompt[5] costant behaviour along the mission duration, are shown here. The reason is that the flaring background, due to SEP or a SAA passage or to the soft protons funnelling, is so intense, orders of magnitude higher, that it compromises the observation itself. Special solutions, like the switching-off of the instruments or the use of a magnetic diverter (see Sec. 3.5), are applied to increase damages and reduce the observational dead time. The quiescent background, instead, is always present, and it contributes to the total number of counts detected during the observation. As a result, a big amount of the total spacecraft mass is devoted to the shielding system surrounding the focal plane. At the same time, a detailed knowledge of the residual background, i.e. the leaking/secondary particles that reach the detectors despite the shielding, is required to disentangle the astrophysical source photons from the total collected counts.

[5]Protons and neutrons can activate the spacecraft material, producing excited nuclei that decay after short (few seconds) or long (hours/days) time intervals. This delayed background component is not constant, but increases with the mission life.

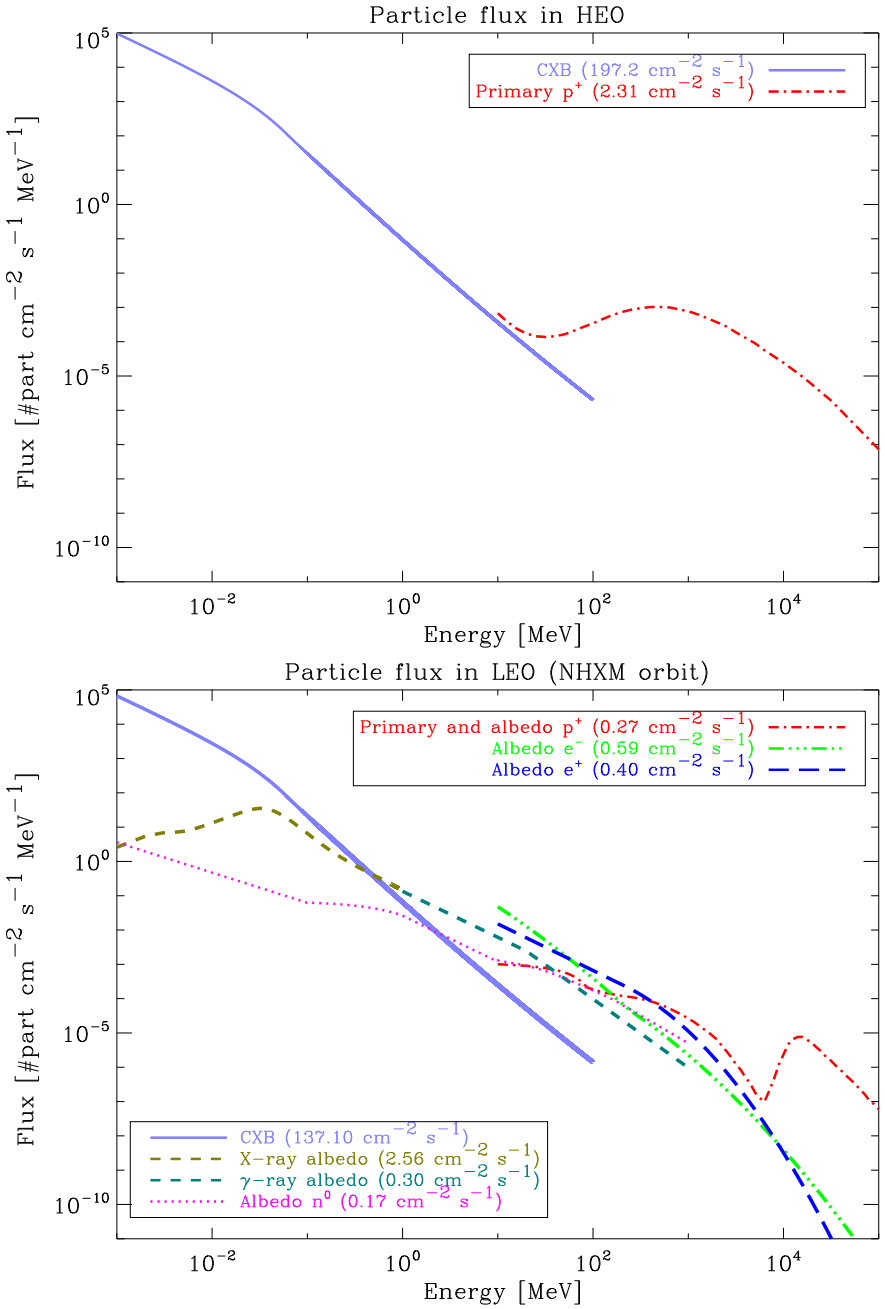

Figure 3.20: The modelled space radiation environment in HEO (top panel) and LEO (bottom panel). The latter refers to the NHXM orbit.

In HEO, when the telescope is above the radiation belts and fully operative, the two major sources of quiescent background are the CXB photons and the GCR protons, impinging into the spacecraft from the entire sky (4π sr). The modelled spectra can be applied to any mission planned with this type of orbit. On the contrary, in LEO the Earth's vicinity adds five more background sources

(albedo particles), resulting in a radiation environment over crowded respect to the open space. The plotted models are evaluated for the NHXM case, with an altitude of 550 km and a low ($< 5°$) inclination, and they can not be generalized to any LEO mission because of the different ridigity cut-off. We would like to note the smooth connection between the albedo neutrons (pink line) and protons (red line) spectra, altough they are derived from different data sets and simulations. This confidency confirms the albedo neutrons as source of the secondary protons by means of decays, and the accuracy of the models.

Chapter 4

Shielding design

Outside the solid angle subtended by the mirror module, where the X-ray photons are focused, high fluxes of charged particles, photons and neutrons are directed to the focal plane, giving rise to the so-called "instrumental" or quiescent background. For this reason, the focal plane must be completely shielded to the space radiation. The design of the shielding, in terms of composition and geometry, depends on many factors:

- the maximum allowed background level, resulting from the top level scientific objectives;
- the way particles of interest interact with matter to efficiently attenuate the incoming radiation;
- the total mass budget available.
- the design of the payload;

As shown in the previus Chapter, the CXB is the most intense source of radiation in the X-ray energy band. The architecture of a hard X-ray telescope, because of the long focal length achieved by means of the formation flight (Simbol-X) or the extendable bench (NHXM), avoids the possibility of using a telescope tube joining the mirror with the focal plane unit to completely shield the detectors. For this reason, new geometrical solutions are needed in the shielding design posing several problems on the mass budget (or mission cost) minimization.
In this Chapter we report a detailed analysis of the passive shielding design (see Sec. 4.2), because it comprises the bigger fraction of the shielding mass budget and so it needs a detailed trade-off study. The computation of the shielding geometry on the basis of the required stopping power represents only the first step in the background minimization, because the shielding acts both as primary particles absorber but also as emitter of secondaries (e.g. fluorescence emission, cascade effects due to charged particles interactions). This means that, once the baseline geometry is settled, a detailed evaluation of the space radiation interaction with the shielding, as well with the focal plane, is necessary to compute the final detected background rate. This analysis represents the bulk of the present thesis, achieved by means of analytical computations (see Sec. 4.6) and Monte Carlo simulations (see Chapter 5).

4.1 Interaction with matter

On the basis of the type of interaction with matter, the space radiation environment is divided in three particles classes:

- photons (X-rays, γ-rays);
- charged particles (protons, electrons and positrons);
- neutrons.

This classification translates into a separation of the total background in several components that require different treatments and shielding solutions.

4.1.1 The photonic component

X-ray and γ-ray photons primarily interact through the photoelectric effect, Compton scattering, and pair production. The probability of undergoing an interaction is an exponential function of the total linear attenuation coefficient μ (in cm^{-2}), given by the sum of the attenuation of the single processes, and the thickness of the material t (in cm). If we define I_0 the intensity of the incident radiation and I the intensity of the transmitted photons, the trasparency of the material is given by:

$$\frac{I}{I_0} = e^{-\mu \times t} . \tag{4.1}$$

The quantity (1 - I/I_0) is the attenuation effiency of the crossed material. The mean free path of the photons λ, i.e. the mean distance crossed by the particle before undergoing an interaction, is defined as:

$$\lambda = \frac{\int_0^\infty x e^{-\mu x} dx}{\int_0^\infty e^{-\mu x} dx} = \frac{1}{\mu} \, cm , \tag{4.2}$$

the inverse of the linear attenuation. The absorption is usually parameterized by the mass attenuation coefficient μ/ρ, which does not depend on the density ρ or physical state of the material. The transparency takes the form:

$$\frac{I}{I_0} = e^{-(\mu/\rho) \times \rho t} , \tag{4.3}$$

where ρt is the absorber column density.
In Figure 4.1 the region of dominance of each process, as a function of the absorber atomic number Z and the energy of the incident photon, is shown.
For high Z materials, the photoelectric effect dominates up to hundreds of keV. The photon is completely absorbed in a single interaction with the atom, with the consequent emission of a photelectron with the energy $E_e = E_X$ - E_b, the latter being the bounding energy of the electron. The photoelectron is typically absorbed within a short distance, so that, for the detector case, the total energy is registered. The probability that an inner K shell electron is emitted is $> 80\%$ for Z$>$ 45 (Krause 1979). After the removal of an inner electron, electrons from outer shells drop down to fill the vacancy, with the consequence emission of X-ray photons (fluorescence) or the emission of an Auger electron (dominant for Z$<$30 keV). Fluorescence emission by an electron passing from

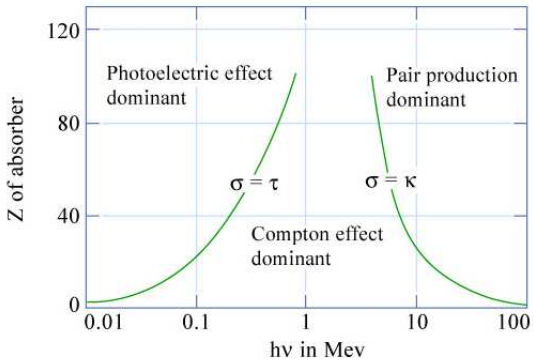

Figure 4.1: The dependence of the dominant process, among the photoelectric effect, Compton scattering and pair production, on the material atomic number and incident photon energy.

the L to the K shell is noted as Kα, where K refers to the vacancy shell and α to the first outer shell. For example, Lα photons are emitted by the shift from the M to the L (Lyman) shell.
In Compton scattering, a part of the photon energy is transferred to the atomic electron, depending on the scattering angle θ. The mimimum energy E_{min} is deposited for $\theta = \pi$, and the angular distribution of the scattered photons is described by the Klein-Nishina formula. If a monochromatic beam of energy E_{inc} is emitted, the escaping photons energy is continuously distributed up to an upper bound $E_c = E_{inc}$ - E_{min} (the so-called Compton edge). The Compton scattering is the dominant process up to few MeV, for high Z materials.
Pair production takes place if the photon energy is twice the mass of the electron ($\sim$ 1.02 MeV), with the production of electron-positron pairs. The excess photon energy translates into kinetic energy shared by the two particles.
The interplay of the photoelectric effect, Compton scattering and pair production generates secondary electrons, positrons and photons that can further interact with the surrounding material.

The photonic background

The X-ray and γ-ray photons induced background in a hard X-ray focusing telescope can be divided in the following components:

- The aperture flux: X-ray photons coming from directions outside the field of view can directly reach the focal plane if a residual opening angle to the sky is left. As discussed later in Sec. 4.3, the primary CXB is so intense that even for small solid angles ($\sim 10^{-4}$ sr) the resulting X-ray flux can overcome of several orders of magnitude the maximum allowed background level.

- Shield leakage: from Eq. 4.1, only an infinite thickness allows to absorbs the 100% of the photons, i.e. a percentage of the incoming primary flux can always cross the shield without interacting ("leaking") and reach the focal plane. In addition, the photons that undergo

Compton scattering can be redirected to the detectors. The shielding surrounding the focal plane is designed, in terms of composition and thickness, to reduce this component.

- Fluorescence emission: the X-ray fluorescence of the spacecraft and shielding material can fall within the operative energy range and cause intense background lines.
- Stray-light: Out-of-FoV X-ray photons that undergo zero or single reflections with the optics can reach the detectors and limit the sensitivity of the telescope. This component is defined "stray-light" and it is of particular concern for hard X-ray focusing optics because of the larger gaps between the shells. Here this component is neglected, but it can be easily minimized by the use of precollimators on the mirror module (see e.g. Cusumano et al. (2007)).

The shielding solution is the use of a high Z, i.e. high photoelectric cross section, absorbing material (passive shielding) that prevents X-ray and γ-ray photons from reaching the detectors through directions outside the telescope field of view. For example, the XMM-Newton (Jansen et al. 2001) mirror assembly is connected to the focal plane by a Lead (Z = 82) covered tube.

4.1.2 Charged particles

In contrast to high energy photons, charged particles deposit energy continuously along their track, interacting by means of Coulomb scattering, with the electric field of the target atom, and nuclear inelastic interactions. The first process leads to excitation and ionization of the atoms along the path, with production of electrons and X-ray fluorescence as consequence of the atomic relaxation. Electrons and positrons can also annihilate giving rise to the characteristic line at 511 keV. Multiple scattering by the high Z coating of the X-ray optics is one of the proposed processes to explain the soft proton deflection to the focal plane (see Sec. 6.3).
An easy way to measure the energetic slowing down due to ionization of a charged particle is the stopping power, in terms of MeV cm^{-2} g, or energy loss per unit length, in MeV cm^{-1}, taking into account the density of the material. In Figure 4.2 the proton (left panel) and electron (right panel) stopping power in Lead is shown. Above 100 keV, protons stopping power slows down, so that energetic protons are more penetrating, reaching the minimum energy loss at $\sim$ 1 GeV. Electrons, on the contrary, reach the same minimum at E$\sim$ 1 MeV, but the stopping power largely increases above this energy due to radiative losses (e.g. bremsstrahlung).
The stopping power also allows to compute the radiation dose in the detector if the charged particles interact with the detectors. In addition, if the proton survives and reaches the focal plane, it can displace the atoms within the lattice structure via nuclear scattering. This effect, defined as non ionizing energy loss (NIEL), degrades the performance of solid state imagers due to the decreased charge transfer efficiency (CTE) and the increased dark current. Single event upsets (SEU) can occurr when a single ionising radiation event deposits enough charge to change the state of a memory cell in the electronic circuit. These interactions are referred to as single event effects (SEE) and are mainly generated by heavy ions and neutrons, all particles that can arise from the impact of energetic protons with the spacecraft material. Nuclear inelastic collisions, in fact, cause the expulsion of the nucleons from the atom and transmutation, through fusion or fission.

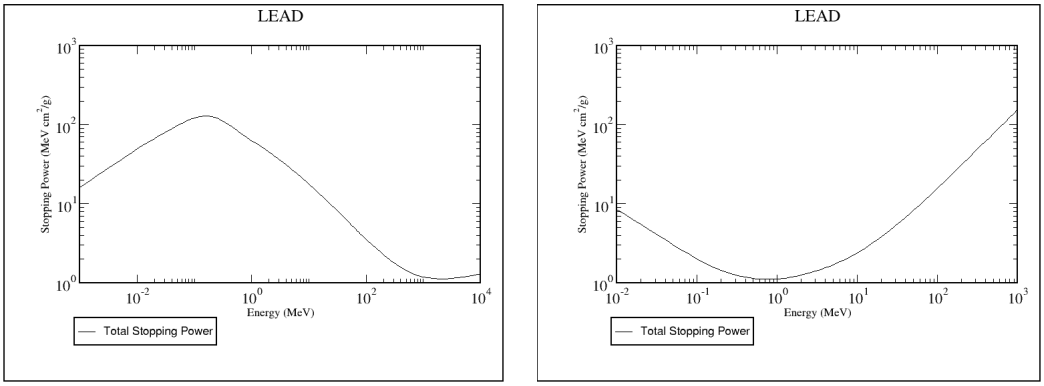

Figure 4.2: Stopping power in Lead (Pb) for protons (left panel) and electrons (right panel), as given by the PSTAR and ESTAR NIST databases respectively.

Cascades of secondary particles, mainly photons, electrons, mesons and neutrons, are produced by further collisions and decays.
The passive shielding, in the interaction with charged particles, has the opposite effect to enhance the production of secondaries, with a final background level directly dependent on the amount of passive material surrounding the detectors. The 80% of the XMM-Newton quiescent background level in the 2 - 8 keV energy range is induced by charged particle interactions (De Luca & Molendi 2004), where only passive shielding is used.
A way to minimize this background component, already adopted in the current hard X-ray (e.g. Suzaku) and γ-ray (e.g. Agile) telescopes, is surrounding the focal plane with a scintillator (the active shielding) acting as an anticoincidence system. The particle interacts with the active shield and generates a signal (when depositing an amount of energy higher then the shield threshold). If the active shield signal is followed by an (almost) coincidence event in the detector, then the detected count can be discarded because it is produced by the same background particle and not by the observed X-ray source. As an example, the Suzaku/HXD background decreases by a factor of 3 if the active anticoincidence is switched on (Kokubun et al. 2007).

The delayed background

The cosmic rays and neutrons collisions leave, in most cases, the atom in a long lived, excited state, decaying after a delayed time interval respect to the first collision, with time scales, depending on the material and the type of nuclide, that can be much longer than the coincidence time ($< \mu$s) of the veto system. As a result, electrons produced by β-decays (see e.g. Gehrels (1985) for a review) generate background events on the detector, the so-called delayed background, that can not be removed by the anticoincidence system. Also β^+ particles (positrons) can be produced, but the annihilation and the consequent emission of 511 keV photons cause these particles to be easily vetoed by the active shielding. Both the shielding material, payload structure and detectors can be subject to activation, which increases with the mission duration. One solution to minimize the

delayed background is reducing the amount of passive material close to the focal plane, as pointed out by Weidenspointner et al. (2005), and, where possible, placing the active shielding in such a way that, if the passive material emits decay products, they can be traced by the anticoincidence system. The effect of radioactive nuclides produced in the detector itself can be minimized only if a prompt γ-ray due to deexcitation of the daughter nuclide of the β-decay can escape and trigger the active shield.
In the present work only the prompt background is analyzed. On the basis of the Suzaku/HXD (Takahashi et al. 2007) and INTEGRAL/SPI (Jean et al. 2003) observed activation, the delayed background affects about the 20 - 50% of the total level below 100 keV. In particular, in the Suzaku/GSO background, it does not exceed a level of $\sim 10^{-4}$ cts cm^{-2} s^{-1} keV^{-1}. In order to take into account the activation effect, the background results presented here should be doubled to extimate the total, prompt and delayed, events.

4.1.3 Neutrons induced background

Neutrons represent a major source of prompt background, especially in LEO where the contribution of the Earth's atmospheric albedo is added to the secondary neutrons produced by the spacecraft material. The MIXE X-ray detector on balloons flights experienced a neutron induced background level 2 - 3 times higher than the atmospheric photonic component $\sim$ 60% due to internal, GCR induced neutrons and $\sim$ 40% due to atmospheric neutrons (Armstrong et al. 1999). The Suzaku/PIN background is also affected by the LEO albedo neutrons (Fukazawa et al. 2009).
Neutrons interact by means of three processes: capture, inelastic and elastic scattering. The neutron capture generates radioactive nuclides and consequent decays, as reviewed in the previous Section. In the inelastic scattering, the neutron excites the nucleus to a higher level energy state, which promptly decays producing a wealth of γ-ray photons in the MeV region that can easily trigger the active shielding (Gehrels 1985). The elastic scattering is, instead, the major process responsible for background production, especially below 100 keV (Dean et al. 2003). In this process, the neutron is scattered isotropically transferring an amount of its kinetic energy to the target nucleus. Unlike charged particles, the neutral charge, i.e. not affected by Coulomb interactions, allows neutrons to cross the active shielding without almost any trigger. As fully described by Gehrels (1985) and Dean et al. (1991), for intermediate and heavy nuclei such as NaI and CsI, which usually compose the inorganic active shields (see Sec.4.2), the maximum recoil energy is less than 20% of the incident neutron energy, so that for an anticoincidence threshold of 200 keV the active shield is only triggered by neutrons with E$>$ 2 MeV. Two are the consequences of the elastic scattering: the neutrons can easily leak through the shielding and, once they interact with the detectors, the recoil energy is so small to fall within the operative energy range. A way to minimize the neutron induced background component is to surround the focal plane with materials that are weak neutrons emitters, to at least reduce the production of secondary neutrons.

4.2 Active and passive shielding

In order to minimize the prompt background, the focal plane shielding system of a hard X-ray telescope is both active and passive.
The selected materials for the passive shielding main absorber are the typical elements used for X-ray absorbers in space, and are described in Table 4.1.

Material	**Z**	**Density [g cm^{-3}]**	**Kα [keV]**
Lead (Pb)	82	11.35	74.97
Tungsten (W)	74	19.30	59.32
Tantalum (Ta)	73	16.65	57.5

Table 4.1: Atomic number, density and Kα fluorescence energy of the main absorber materials under study.

The atomic relaxation of the main absorber, as a consequence of the ionized state due to the photoelectric effect, produces mainly fluorescence Kα and Kβ photons (the Ta K fluorescence yield is about 96% (Krause 1979)) in the hard X-ray range of the spectrum ($>$ 50 keV), where NHXM will be fully operative. As example, the IBIS/ISGRI instrument on board INTEGRAL detects intense W and Pb K lines generated by the shielding structure (Terrier et al. 2003). In order to absorb the main absorber fluorescence emission, a set of Z-graded layers is added. Each layer, with lower Z, absorbs the fluorescence lines of the previous material and re-emits K lines at lower energies. The set of grading materials analyzed in the Simbol-X and NHXM passive shielding trade-off study is Sn + Cu + Al + C, as described in Table 4.2. The last layer, made of Carbon, produces a Kα line at 0.28 keV, below the LED detection sensitivity.

Material	**Z**	**Density [g cm^{-3}]**	**Kα [keV]**
Tin (Sn)	50	7.31	25.37
Copper (Cu)	29	8.96	8.05
Aluminum (Al)	13	2.70	1.49
Carbon (C)	6	2.00	0.28

Table 4.2: Atomic number, density and Kα fluorescence energy of grading materials under study.

The anticoincidence system can be both inorganic (e.g. NaI, BGO) and organic (e.g. Hydrogen-Carbon compounds, generally defined as plastic). Their shielding efficiency and feasibility properties are different, so that the selection of an inorganic, organic, or a combination of the two depends on the major background sources and the payload design.
Tests on balloons flights had shown (see e.g. Bloser et al. (2002)) that inorganic scintillators are more effective in the background minimization, especially the photonic component. In addition, a lower operative threshold, the minimum energy deposit for which the AC is able to detect an event, is possible ($\sim$ 50 keV). At the same time a plastic anticoincidence system requires a lower mass budget and it is more suitable for space application. In terms of residual background, a plastic

scintillator does not produce activation lines on the detector. In the background simulation of Simbol-X and NHXM a plastic scintillator is used. However in Chapter 7, where the background is evaluated for a more general case, the effect of a NaI made active shielding is also shown.
As example, the Astro-H (Takahashi et al. 2010) and Nustar (Harrison et al. 2011) missions actual design envisages the use of inorganic active shieldings, a BGO and CsI scintillator respectively.

4.3 The perfect shielding

Becuse of the impossibility of connecting the focal plane to the mirror module, the passive shielding system is given by the combination of a baffle ("sky screen") placed around the optics, and a cylindrical collimator above the focal plane (Malaguti et al. 2005). In the Simbol-X case, the two shields are on board the Mirror Spacecraft (MSC) and Detector Spacecraft (DSC) respectively.
The sky screen parameters are calculated for a perfect shielding, i.e. the total solid angle covered by the mirror module and focal plane baffles on the focal plane must coincide with the detectors opening angle to the unfocused CXB photons, resulting in a complete ("perfect") shielding of the focal plane to the photonic background. According to Fioretti et al. (2008b), even small solid angles opened to space ($\sim 10^{-4}$ sr) lead to an aperture flux above the background requirement at $\sim$3 keV.
The perfect shielding implies that the sky screen diameter (a circular shape is assumed for the basic geometry computation) depends on the collimator height, and viceversa. Here these two quantities are computed with and without the addition of a lateral tollerance between the focal plane and mirror module central axis, an effect particulary important in a formation flight mission. For a further explanation of all the angles and parameters see Appendix A. The detector is assumed circular, with a diameter equal to the side of the baseline Simbol-X and NHXM instruments (the inscribed circle).

4.3.1 No alignment tolerance case (T = 0)

The perfect shielding assumption translates into the requirement

$$\theta_{\mathrm{coll}} = \theta_{\mathrm{Screen}} \tag{4.4}$$

with no residual opening angle left to the focal plane.
From expression 4.4 and in the absence of misalignment effects, the diameter of the sky screen (adopting the notation defined in Figure 4.3, left panel) can be written as a function of collimator height H:

$$\mathrm{D_{Screen}} = 2\mathrm{FL} \cdot \left(\frac{\mathrm{D_{det}}}{\mathrm{H}}\right) + \mathrm{D_{opt}} - 2\mathrm{D_{det}} \quad . \tag{4.5}$$

The separation s between the collimator and detector edge is necessary to avoid direct shadowing (vignetting) of the focussed photons. From simple trigonometric considerations, we have that:

$$\mathrm{s} = \frac{\mathrm{H} \cdot (\mathrm{D_{opt}} - \mathrm{D_{det}})}{2\mathrm{FL}} \quad , \tag{4.6}$$

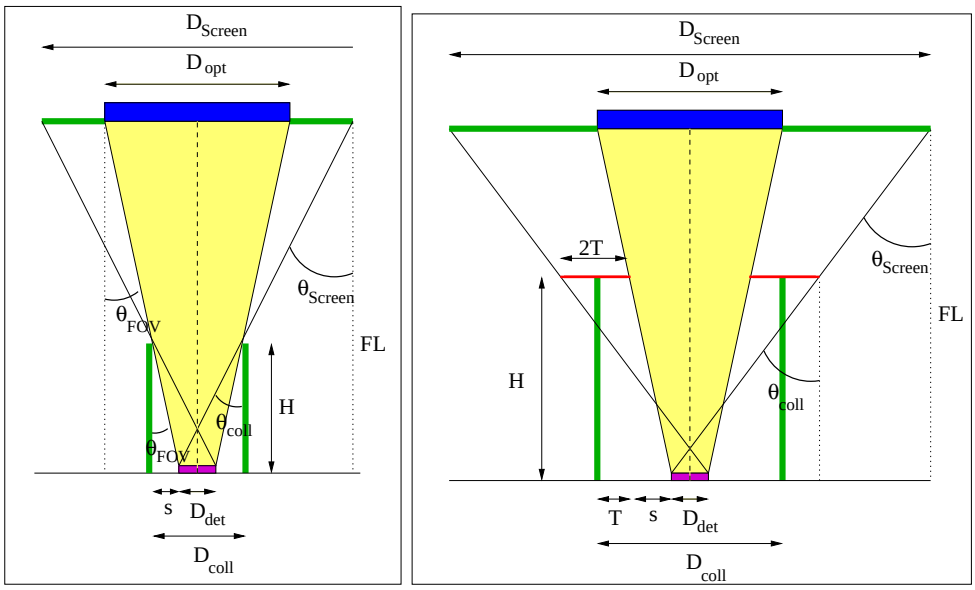

Figure 4.3: The basic simplified geometry of the passive shielding assembly with no misalignment effects (left panel) and with the addition of a lateral tolerance ±T (right panel). The blue horizontal line on the top indicates the external optics diameter, $\mathbf{D_{opt}}$. The green lines represent the sky screen (on the top, with total diameter $\mathbf{D_{Screen}}$) and collimator walls (on the bottom, with height **H**). The purple line on the bottom is the detection plane which has a dimension of $\mathbf{D_{det}}$ and is separated by **s** from the collimator walls. **FL** is the telescope focal length. The horizontal red lines in the right panel account for the spacecrafts alignment tolerance.

and the resulting collimator diameter is given by:

$$D_{coll} = 2s + D_{det} \quad . \tag{4.7}$$

4.3.2 Alignment tolerance (T$\neq$ 0) case

A potential misalignment (commonly tolerance or dithering) between the focal plane and mirror module axis also causes a shift of the shielding with respect to the telescope axis, causing vignetting and, at the same time, opening a residual angle to the unfocused CXB on the other side.
The passive shielding design must account for the formation flight relative motion, as for the mechanical tolerances and thermoelastic deformations. Defined ±T the shift perpendicular to the telescope axis (see Figure 4.3, right panel), the Equation 4.5 is rewritten as follows:

$$D_{Screen} = 2FL \cdot \left(\frac{D_{det} + 2T}{H} \right) + D_{opt} - 2D_{det} \quad , \tag{4.8}$$

with the collimator diameter given by:

$$D_{coll} = 2s + D_{det} + 2T \quad . \tag{4.9}$$

4.4 Simbol-X passive shielding design

On the basis of the current feasibility scenarios, the passive shielding parameters derivation is done via the definition and basic assumptions described in Table 4.3.

SIMBOL-X BASELINE PARAMETERS

Parameter	Description	Value
D_{opt}	External mirror shell diameter	80 cm
D_{det}	Focal plane detector dimension	8 cm
FL	Telescope focal length	20 m

Table 4.3: Basic trade–off analysis definitions.

4.4.1 DSC passive shielding

The current baseline configuration for the DSC collimator is based on Imbert (2008). The choice for the geometry of the collimator is based upon six cylindrical segments with a total length of 194 cm. The first segment is placed at an height of 20 cm above focal plane, This means that, for the MSC sky screen trade-off analysis, the total collimator height H of Equation 4.8 is 2.14 m. The collimator composition is a graded shield made of Tantalum, Tin, Copper, Aluminum, Carbon. A detailed description of the collimator configuration is given in Tables 4.4 and 4.5.

Collimator height (from detector plane)	2.14 m
Tolerance	±5 mm

Table 4.4: DSC collimator baseline configuration.

	Segment 1	Segment 2	Segment 3	Segment 4	Segment 5	Segment 6
Upper end position	319 mm	508 mm	775 mm	1133 mm	1588 mm	2140 mm
Length	119 mm	176 mm	239 mm	304 mm	361 mm	405 mm
Internal radius	46.56 mm	50.05 mm	54.99 mm	61.62 mm	70.04 mm	80.25 mm
Thickness	1.58 mm	1.04 mm	0.69 mm	0.48 mm	0.36 mm	0.27 mm

Table 4.5: DSC collimator segments size.

4.4.2 MSC passive shielding

The MSC baseline configuration and figures described in this section have the only purpose of evaluating the MSC passive shielding geometry, and are courtesy of Ferri (2008).
The shape of the platform is hexagonal: the face–on geometry is shown in Figure 4.4 (a) while a 3D view is represented in Figure 4.4 (b).
The mirror module, with a diameter of 80.2 cm, is placed in the spacecraft center inside the “thrust

cylinder", visible in Figure 4.5 (left) in trasparency. The adapter, the green cone trunk shown in Figure 4.5 (right), is the interface between the mirror module and the thrust cylinder and it is made of Aluminum (4 mm thick). On the lateral and back side of the spacecraft thermal blankets (MLI, Multi Layer Insulation) are placed.

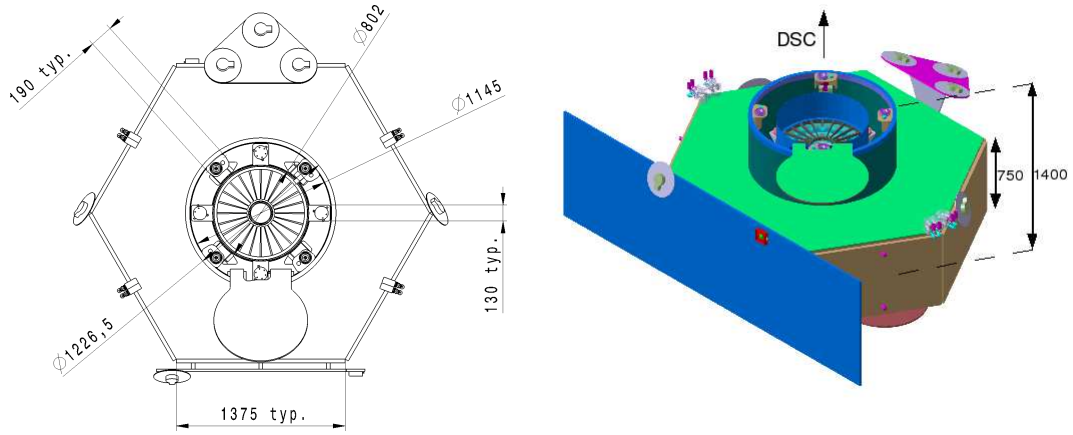

(a) (b)

Figure 4.4: a): Face-on MSC geometry and main dimensions (misures in mm). b): 3D view of the spacraft with height dimension (misures in mm). The arrow shows the DSC direction on flight.

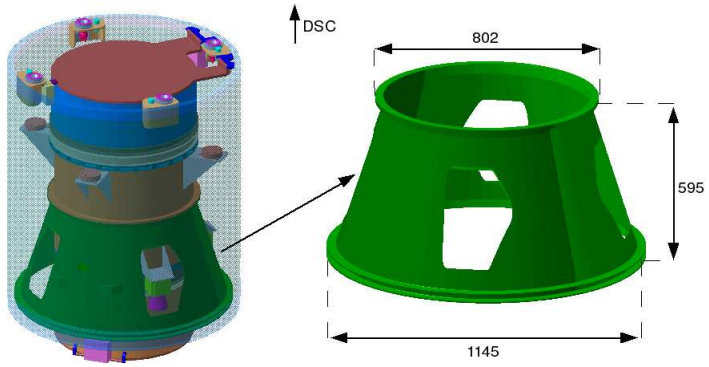

Figure 4.5: 3D view of the mirror module (left) and zoom (right) on the MSC adapter (misures in mm). The arrow shows the DSC direction in flight.

The MSC sky screen should in principle cover the whole area around the mirror module, but the presence of the thrust cylinder around the optics, with a set of instruments placed inside that can not be covered by the passive shield, prevents from using this configuration. A new geometrical solution is required: the thrust cylinder region around the optics is shielded by covering the adapter

with the same passive material of the sky screen.
This cover allows to partially absorb the unfocused CXB photons because of the presence of "holes" in the adapter structure (visibles in Figure 4.5) and the holes contribution to the background level must be evaluated.
The MSC passive shielding configuration is composed by:

1. The sky screen: an hexagonal plane (same shape of the spacecraft) covering the region around the thrust cylinder.

2. The adapter cover: a passive shield with cone trunk shape that covers the adapter on the DSC side (upper surface in Figure 4.5) except for the adapter holes.

The sky screen design

The geometry of the sky screen is a plane of hexagonal shape with same dimension of the mirror spacecraft. Starting from the MSC configuration represented in Figure 4.4, in Table 4.6 a detailed description of the sky screen geometry parameters and dimensions is listed. In Section 4.3, where

Sky screen design

Parameter	Description	Value
D_{cir}	Diameter of the circumscribed circle (corner-to-corner)	275 cm
D_{ins}	Diameter of the inscribed circle (flat-to-flat)	238.2 cm
L	Hexagon side	137.5 cm
D_{cyl}	Diameter of the thrust cylinder	122.65 cm
A_{screen}	Sky screen surface area	37314 cm^2

Table 4.6: MSC sky screen dimensions.

the basic parameters for a perfect shielding have been defined, we call D_{Screen} the external sky screen diameter in the case of a circular shield. This parameter coincides, for the hexagonal sky screen, with the flat-to-flat diameter:

$$D_{Screen} = D_{ins} \quad , \tag{4.10}$$

and for a perfect shielding, D_{ins} must totally cover the detector opening angle.
The surface area of the sky screen is given by:

$$A_{screen} = \left[\left(\frac{L \cdot (D_{ins}/2)}{2} \right) \cdot 6 \right] - \pi \left(\frac{D_{cyl}}{2} \right)^2 \quad . \tag{4.11}$$

The adapter cover design

The passive shielding of the thrust cylinder area around the optics is obtained by covering the adapter of a passive high absorbing layer. The basic parameters and dimensions of the cone trunk shaped adapter (see Figure 4.5 for a 3D visualization of the geometry) are listed in Table 4.7.

ADAPTER DESIGN

Parameter	Description	Value
D_{max}	Major diameter	114.5 cm
D_{min}	Minor diameter	80.2 cm
H_{ada}	Adapter height	59.5 cm
L_{ap}	Cone trunk apothem	61.9 cm
d	Distance Sky screen - adapter	15.5 cm
A_{holes}	Adapter holes area	3000 cm^2
$A_{adapter}$	Adapter area (without holes area)	15938 cm^2
F_{holes}	Adapter holes area fraction	15.84%
$\theta_{L_{ap}}$	Lateral surface angle	16.1 deg

Table 4.7: MSC adapter dimensions.

The lateral surface of the adapter is given by:

$$A_{adapter} = \left[\pi \left(\frac{D_{max} + D_{min}}{2}\right) \cdot L_{ap}\right] - A_{holes} \quad . \tag{4.12}$$

The CXB flux is isotropic and it depends directly on the aperture solid angle of Simbol–X detectors. An analytical evaluation of the background level caused by the adapter holes is therefore possible by calculating the solid angle subtended by the holes to the focal plane.
If we define θ_{opt} the angle subtended by the mirror module on the focal plane (FWHM) and θ_{cyl} the angle subtended by the thrust cylinder (FWHM), the solid angle Ω_{holes} covered by the holes is given by the following expressions:

$$\theta_{opt} = \tan^{-1}\left(\frac{D_{opt} + D_{det}}{2FL}\right) = 0.022 \quad \text{rad} \tag{4.13}$$

$$\theta_{cyl} = \tan^{-1}\left(\frac{D_{max} + D_{det}}{2FL}\right) = 0.031 \quad \text{rad} \tag{4.14}$$

$$\Omega_{holes} = F_{holes} \cdot [2\pi\,(\cos(\theta_{opt}) - \cos(\theta_{cyl}))] = 2 \times 10^{-4} \quad \text{sr} \tag{4.15}$$

Multypling the CXB flux for Ω_{holes} is possible to evaluate the background level caused by the unfocused CXB photons that arrive on the focal plane.
In Figure 4.6 (left panel) the CXB flux (in photons cm^{-2} s^{-1} keV^{-1}), calculated at 5 keV (blue line), 30 keV (red line), and 80 keV (green line), is reported versus the opening solid angle. The dotted vertical line is Ω_{holes}, the solid angle covered by the adapter holes.
The background level caused by the holes at 5 keV is higher (about 2×10^{-4} ph cm^{-2} s^{-1} keV^{-1}) than the maximum total background level and, considering that the residual background caused by the MSC passive shielding should be small (e.g. at least 10 times less than the total background), even at 30 keV the estimated background is too high. This problem could be resolved taking into account the absorption power of the spacecraft behind the adapter or by the thermal blankets covering the lateral and back side: an evaluation of this shielding effect is reported in Chapter 6.
In addition, in Figure 4.6 the CXB flux passing through the solid angle covered by the combination

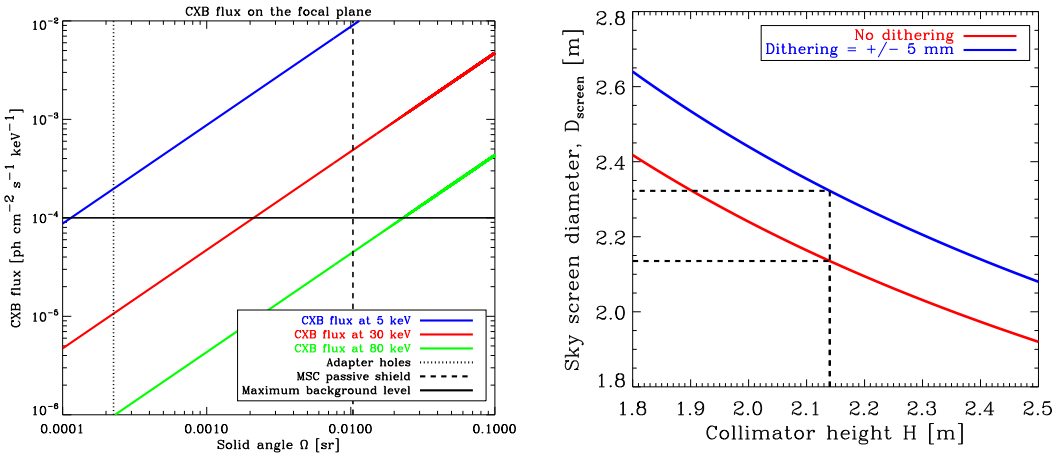

Figure 4.6: *Left panel*: The CXB flux, in photons cm^{-2} s^{-1} keV^{-1}, calculated at three different energies as a function of the emission solid angle (in sr). *Blue line*: the CXB flux at 5 keV; *red line*: the CXB flux at 30 keV; green line: the CXB flux at 80 keV. The continuous horizontal black line refers to the total maximum background level. The dotted and dashed vetical lines are respectively the solid angle covered by the adapter holes and by the MSC passive shielding on the focal plane. *Right panel*: The sky screen diameter as a function of the collimator height with (blue line) and without (red line) the lateral dithering.

of sky screen and adapter is shown (dashed vertical line): the purpose is underlining the necessity of a passive shielding system on the MSC absorbing a CXB flux that, otherwise, can cause a background level much higher then the total level required by the feasibility study.

Perfect shielding results

Starting from the derivation of Appendix A and from the DSC collimator design described in Section 4.4.1, the MSC passive shielding diameter required to ensure a perfect shielding, is calculated for the case without misalignment effect and for an alignment tolerance of ±5 mm, as plotted in Figure 4.6 (right panel).

1. **No tolerance case (T = 0):**
   In absence of misalignment effects, a collimator height H of 2.14 m (see Table 4.4) from the focal plane requires, through the Equation 4.5, a sky screen diameter $D_{Screen} = 2.135$ m.
   For an exagonal sky screen, the parameter D_{Screen} translates into a flat-to-flat diameter D_{ins}. Since the sky screen inscribed circle has a diameter (see Table 4.6) of 238.2 cm, the Simbol–X detection plane is **perfectly shielded**.

2. **Alignment tolerance case (T=±5 mm):**
   Setting the misalignment effects, given by the spacecrafts relative motion, to a value of ±5 mm, the DSC collimator assessed design requires, from Equation 4.8, an external MSC sky screen diameter $D_{Screen} = 2.32$ cm.
   Even in this case, the sky screen flat-to-flat diameter D_{ins} is higher than the required screen

diameter D_{Screen} and **the passive shielding is perfect**.

4.4.3 MSC passive shielding mass

From Equation 4.1, the sky screen and adapter cover thickness is calculated for an absorption efficiency of 99% at 40 keV (main absorber) and of 99% at fluorescence emission (grading).
Since the adapter cover is placed at an angle of about 16° with respect to the telescope axis, the unfocused CXB photons cross a higher thickness to reach the focal plane. This trigonometric consideration allows a decrease of the adapter cover thickness as follows:

$$t_{adapter} = t_{screen} \times \sin\left(\theta_{L_{ap}}\right) \quad , \tag{4.16}$$

that is the adapter cover thickness is only the 30% of the sky screen thickness. The resulting thickness values and mass are listed in Table 4.8. The MSC passive shielding total mass is clearly

MSC SHIELDING MASS BUDGET

	Sky screen		**Adapter cover**		
Element	**Thickness [cm]**	**Mass [kg]**	**Thickness [cm]**	**Mass [kg]**	**Total mass [kg]**
Pb	0.028	11.86	0.0076	1.40	13.26
Sn	0.18	49.10	0.050	5.81	54.91
Cu	0.026	8.69	0.0072	1.03	9.72
Al	0.034	3.42	0.0094	0.41	3.83
C	0.004	0.30	0.0011	0.04	0.34
Total	0.272	73.37	0.0753	8.68	**82.05**
W	0.022	15.84	0.0061	1.87	17.71
Sn	0.096	26.19	0.027	3.10	29.29
Cu	0.026	8.69	0.0072	1.03	9.72
Al	0.034	3.42	0.0094	0.41	3.83
C	0.004	0.30	0.0011	0.04	0.34
Total	0.182	54.44	0.0508	6.44	**60.89**
Ta	0.027	16.78	0.0075	2.00	18.78
Sn	0.079	21.55	0.022	2.55	24.1
Cu	0.026	8.69	0.0072	1.03	9.72
Al	0.034	3.42	0.0094	0.41	3.83
C	0.004	0.30	0.0011	0.04	0.34
Total	0.17	50.74	0.05	6.00	**56.75**

Table 4.8: Thickness and mass of MSC passive shielding required to absorb the 99% of photons at 40 keV (main absorber) and the 99% of fluorescence photons for the graded layers.

unfeasible and an optimization study is required.
Analyzing these preliminary results, we find that a combination of Pb plus grading requires the higher mass budget. At the same time, Pb alone implies about 4 kg less than W, and about 5 kg less than Ta. The reason is that the Pb is the lower density main absorber (see Table 4.1), so that the Pb alone implies a smaller mass budget. If we instead add the grading, the higher fluorescence line energy of Pb causes an increase of the required Sn thickness, thus increasing the mass.

This means that for a main absorber only configuration, Pb satisfies the requirements, but it acts as a monochromator at its fluorescence lines. If a grading is necessary (this is evaluated in Chapter 6) to absorb the fluorescence emission, then a main absorber made of W or Ta is the best choice.

4.5 NHXM passive shielding

In Sec. 4.3, we generally compute the shielding design for a single detector placed at a distance from the sky screen equal to the focal length. In reality, for both Simbol-X and NHXM missions, the focal plane is hybrid, composed by a Low Energy Detector (LED) and a High Energy Detector (HED), sharing the same axis, and the focal length defines the distance from the mirror module to the position centered between LED and HED. As a result, the minimum distance of the collimator walls from the detector edge to avoid vignetting (see Eq. 4.7), and the consequent collimator mass budget, is different if we base the analysis on the LED or the HED positions and dimensions.
In the NHXM passive shielding study, we compute the shielding design for both the cases. The baseline parameters on which is based the analysis are shown in Table 4.9. In Figure 4.7 the

NHXM Baseline Design

Parameter	Description	LED	HED
D_{opt}	External mirror shell diameter	40 cm	
D_{mod}	Mirror module diameter	50 cm	
D_{det}	Detector side	5.12 cm	4.02 cm
$LED–HED_{dist}$	LED–HED distance	1.2 cm	
FL_{Eff}	Effective focal length	9.994 m	10.006 m
$Coll_{dist}$	Collimator base - detector distance	4.3 cm	5.6 cm
H_{coll}	Collimator height	90 cm	
T	Tolerance	±5 mm	

Table 4.9: NHXM baseline dimensions for the passive shielding trade-off analysis.

sky screen diameter is computed as a function of the collimator height for both LED (left panel) and HED (right panel), with and without the lateral dithering. Respect to the Simbol-X case, the shorter focal length (10 m) allows to reduce the collimator height (more than a half, from 194 to 90 cm) while keeping the total sky screen diameter well below 2 m. A lower sky screen dimension, i.e. mass budget, is achieved if the geometry is computed from the HED point view, so that a small vignetting is caused on the LED plane. All the results are listed in Table 4.10

NHXM Sky Screen Diameter ($H_{coll} = 90$ cm)

Tolerance	LED point of view	HED point of view
0	1.38 m	1.16 m
±5 mm	1.59 m	1.37 m

Table 4.10: NHXM sky screen diameter for a perfect shielding.

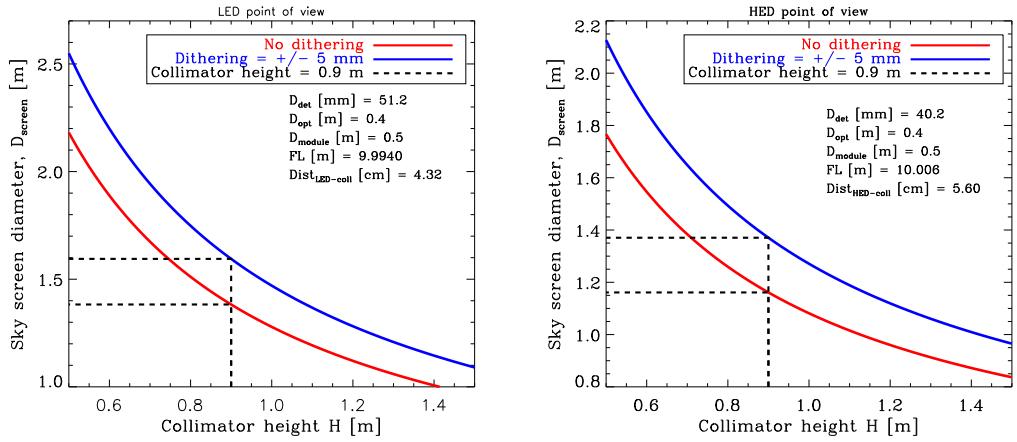

Figure 4.7: The sky screen diameter as a function of the collimator height with (blue line) and without (red line) the lateral dithering .

4.6 Shielding analytical optimization: the IXO case

The passive shielding X-ray photonic transparency, depending on the material thickness and total attenuation cross section according to Equation 4.1, defines the number of CXB photons that can leak through the shields and reach the focal plane. In addition to the primary photons, a secondary radiation arises due to various processes (e.g. fluorescence emission, Compton scattering). A secondary component that can be increased by the shielding thickness, contrary to the leaking photons. The total number of X-ray photons interacting with the detectors constitutes the CXB induced residual background.

As resulting from the previous Sections, if the passive shielding thickness is chosen to avoid any leaking photons, the total mass budget is unfeasible. In this context, the shielding optimization is a revers process that defines the absorbers material and thickness starting from the background requirement and total mass budget, following the main scheme of Figure 4.8.

On the basis of the attenuation cross sections and the fluorescence production yields tabulated from literature, it is possible to analytically compute the expected CXB induced residual background as a function of the shielding design. This method represents the first necessary step in the shielding design evaluation. Here we present the analytical evaluation performed for the passive shielding optimization study of IXO mission (Barcons et al. 2011), focusing on the important results that such a simple approach can achieve and, at the same time, on the necessary assumptions and missing ingredients that can be fullfilled by Monte Carlo simulations. The IXO mission hosts a hard X-ray focusing telescope which requires a long focal length (20 m) achieved by means of an extendable bench. As for Simbol-X and NHXM, the passive shielding is placed both around the detectors and the mirror module, so that the same shielding problems are encountered. The following results regard the focal plane assembly shielding optimization only, where the collimator length and mass budget is reduced by means of a set of concentric disks at the detectors top. This

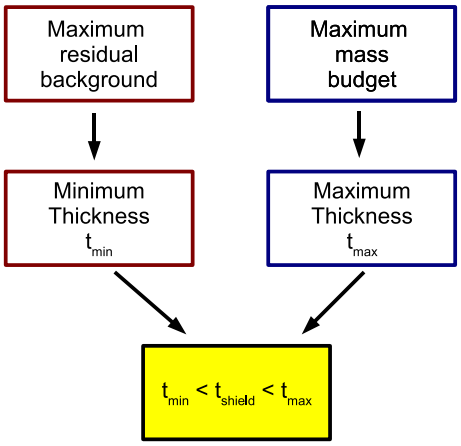

Figure 4.8: Schematic view of the passive shielding system optimization process.

work has been reported in Fioretti & Malaguti (2010) as part of the Thales Alenia Space IXO technical assessment study.

4.6.1 IXO X-ray attenuation requirements

On the basis of the focal plane assembly design as described in the 2009 ESA technical report "IXO payload definition document", all IXO instruments, except for the XGS, share the same X-ray shielding system. This means that the attenuation achieved by the passive absorber must satisfy the requirements of all the intruments, listed in Table 4.11, with a dash reported when the value is not available.

IXO REQUIREMENTS

Instrument	Energy range	X-ray leakage	Maximum background level [phot. cm^{-2} s^{-1} keV^{-1}]
WFI	0.2 - 20 keV	1/e at 28 keV (37%)	5×10^{-5}
HXI	10 - 40 keV	1/e at 70 keV (37%) $(1/e)^5$ at 40 keV (0.7%)	5×10^{-4}
XMS	0.3 - 10 keV	$< 10\%$ at E$<$ 10 keV	0.005 - 0.01
HTRS	0.3 - 15 keV	/	7×10^{-5}
XPOL	2 - 10 keV	$< 1\%$ at 10 keV	/

Table 4.11: IXO instruments X-ray background and attenuation requirements.

It is important to underline that the two requirements (X-ray leakage and the maximum background level) need a different computational and analysis approach. The X-ray leakage is calculated according to the transparency Eq. 4.1.
The evaluation of the residual background level on IXO focal plane instead requires, in addition to

the fraction of leaking photons, the geometry of the shielding system, the evaluation of the related fluorescence emission and the CXB intensity and spectral distribution.

4.6.2 Single layer configuration results

The passive shielding thickness and residual background is first evaluated for a single layer configuration, i.e. only a high Z absorber (the main layer) is used to stop the CXB photons.

Single layer composition and thickness

The materials selected as main absorber for this preliminary trade-off study are Gold (Au) and Tantalum (Ta). The Tantalum properties are again listed (Table 4.12), with the addition of the Lyman fluorescence emission, to highlight the differences with an Au composition The X-ray

Single layer configuration

Material	Z	Density [g cm^{-3}]	Main fluorescence lines [keV]			
			Lα	Lβ	Kα	Kβ
Au	79	19.32	9.7	11.4	68.8	78
Ta	73	16.65	8.2	9.3	57.5	65.2

Table 4.12: Single layer materials under study and their main properties.

absorbing power is calculated using the cross sections and X-ray attenuation coefficients given by the National Institute of Standards and Technology[1](NIST). In order to evaluate the minimum thickness with an X-ray attenuation meeting the requirements, the X-ray transparency, i.e. the fraction of photons leaking through the shield, is calculated for three Line of Sight (LoS) thickness values (based on the current baseline of 200 μm): 150, 200 and 259 μm (Figure 4.9).
A 150 μm thickness of Au (blue line of Figure 4.9, left panel) is the minimum value in order to meet the requirements, while a Ta absorber, with lower photoelectric cross sections, requires a 200 μm thickness (green line of Figure 4.9, right panel). A comparison of the X-ray transparency for the two resulting thicknesses is shown in Figure 4.10.
Even if the Ta is characterized by a lower density than Au, the increase in thickness results in a slightly greater surface density and a consequent higher mass budget, from 0.28 g cm^{-2} for Au to 0.33 g cm^{-2} for Ta. These values translate, for a 1 m^2 shield, to a 2.8 and 3.3 kg mass budget respectively. At the same time the lower Ta K absorption edge allows a X-ray transparency below 1/e ($< 37\%$) even for energies higher than 70 keV, while the Au leakage reaches a value of $\sim 55\%$ in the same energy range.

CXB induced residual background

The evaluated thicknesses meet the requirements in terms of X-ray attenuation, but the resulting background level on the IXO focal plane depends on the solid angle shielded by the absorbing

[1]www.nist.com

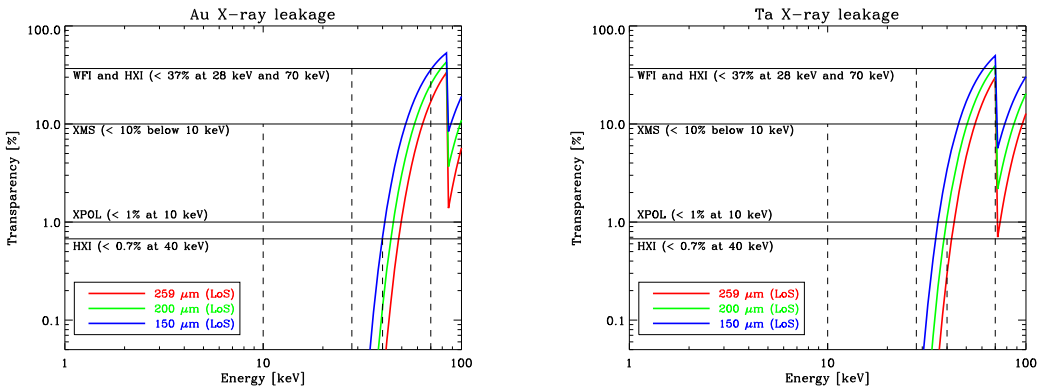

Figure 4.9: Au (left panel) and Ta (right panel) X-ray transparency (%) as a function of the incident photon energy for a thickness of 259 μm (red line), 200 μm (green line) and 150 μm (blue line). The black horizontal and dashed lines show the instruments maximum allowed transparency and the energy for which is required respectively.

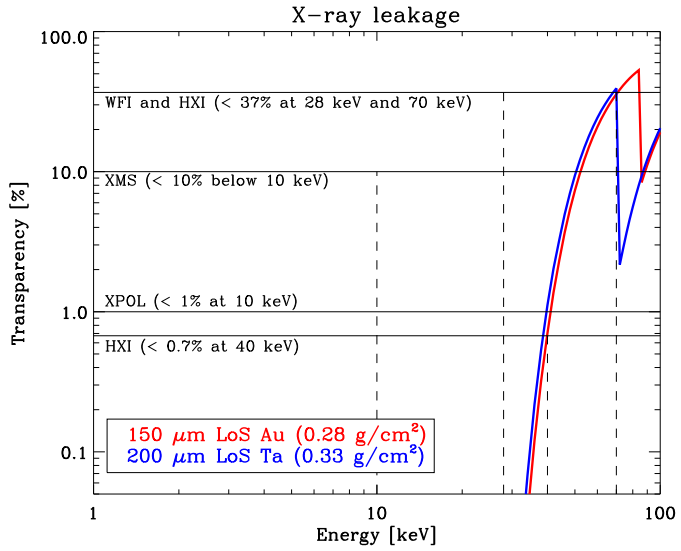

Figure 4.10: X-ray transparency (%) for a 150 μm thich Au (red line) and a 200 μm thick (blue line) Ta layer.

material. The analysis presented here refers to the shielding on the focal plane assembly, composed by a cylindrical collimator around the instruments and two annular disks above the focal plane, sharing the same axis of the mirror module. Figure 4.11 shows a simplified representation of the passive shielding design (in purple). The baseline geometry parameters on which is based the analysis are:

- Collimator height = 30 cm
- Collimator diameter = 17.6 cm

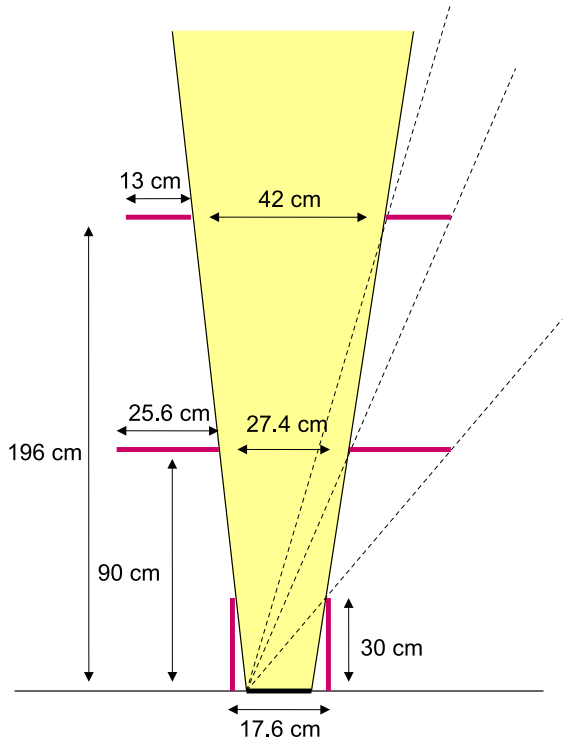

Figure 4.11: Simplified not-in-scale design of the passive shielding system (in purple) on the IXO focal plane assembly.

- Lower disk internal diameter = 27.4 cm
- Lower disk radius = 25.6 cm
- Lower disk height = 90 cm
- Upper disk internal diameter = 42 cm
- Upper disk radius = 13 cm
- Upper disk height = 196 cm

The incident CXB flux, based on Gruber et al. (1999), crosses the Au (or Ta) layer through the solid angle covered by the shield (collimator plus disks) and a fraction, given by the evaluated X-ray transparency, reaches the detectors generating a continuous background flux. At the same time a fraction of the absorbed photons generates X-ray fluorescence lines, at characteristic energies, with an intensity depending, among other parameters, on the area covered by the shield and the solid angle subtended by the focal plane. The resulting background level is analytically calculated on the basis of the following assumptions:

- the input CXB flux extends up to 1 MeV;

- the leaking photons have the same energy of the incident ones, while a small fraction of the incident flux at high energies (> 100 keV) is subjected to Compton scattering with a consequent decrease of the photon energy;
- the fluorescence intensity is based on approximated fluorescence production cross sections and yields based on Hubbell et al. (1994), Krause (1979) and Kücükönder et al. (2004).
- the background spectrum does not take into account the detection efficiency and spectral resolution of the instruments, so that it reflects the energy of the photons crossing the focal plane (in units of number of photons, not counts).

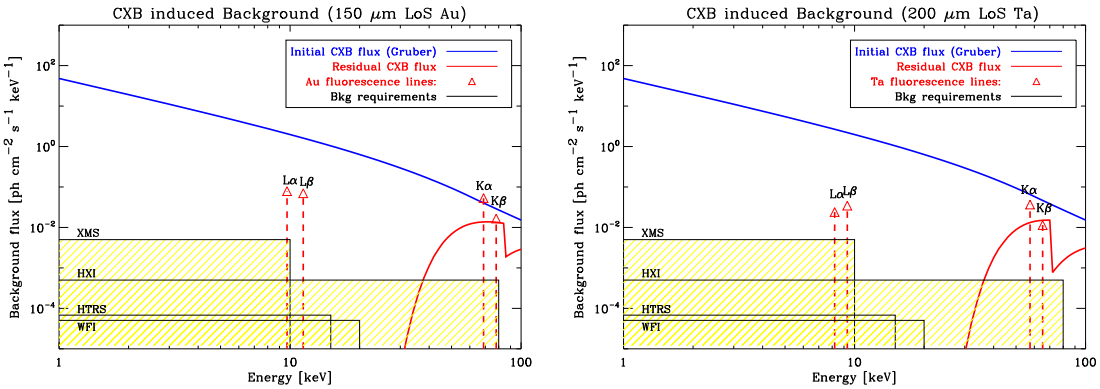

Figure 4.12: CXB induced residual X-ray background on the IXO focal plane for a Au (left panel) and Ta (right panel) composition. *Blue line*: incident CXB flux; *red continuous line*: residual background flux; *red dashed line*: fluorescence lines; *yellow boxes*: maximum allowed background level required by each instrument.

Figure 4.12 shows the resulting residual background, in phot. cm^{-2} s^{-1} keV^{-1}, for a single layer passive shielding made of Au (150 μm thick) and Ta (200 μm thick), in the left and right panels respectively:

- Blue line = incident CXB flux
- Red continuous line = background flux on the IXO focal plane
- Red vertical line and triangles = fluorescence lines
- Yellow box = maximum allowed background level

If the red line falls above the yellow boxes, then the resulting background is too high and the shielding thickness must be increased.

Background evaluation results

If we consider the X-ray leaking photons reaching the detector (continuous red line), the chosen thickness, for both Au and Ta, efficiently shields the energy range covered by the XMS, HTRS

and WFI instruments. The HXI requires a different analysis, because at present it is not clear if the required background level must be extended up to 40 keV (the instrument maximum operative energy) or to higher energies (70 - 80 keV). The residual flux crosses the HXI required background level (5×10^{-4} phot. cm^{-2} s^{-1} keV^{-1}) at 40 keV, but it is about 20 times higher at 70 keV.
The use of a single high Z absorber as passive shielding causes secondary fluorescence emission reaching the detector. Altough the spectrum is the result of a conservative computation, i.e. the plotted fluorescence emission must be intended as an upper limit, the Lα and Lβ intensity is from 2 (XMS) to 4 (WFI) orders of magnitude higher than the required background level. In the case of the HXI instrument, the Kα and Kβ emission, in the 50 - 70 keV energy range, could also represent a source of background.
It is important to point out that the Lα and Lβ residual emission is only generated by the CXB photons interacting with the disks on the detector side, while in the collimator case the Lyman fluorescence is self-absorbed.
In order to decrease the residual background level below the HXI requirement at 80 keV, the Au (or Ta) thickness should be increased, with a consequent higher mass budget. In Figure 4.13 the background is computed for an Au thickness of 800 μm (left panel) and a Ta thickness of 900 μm (right panel).

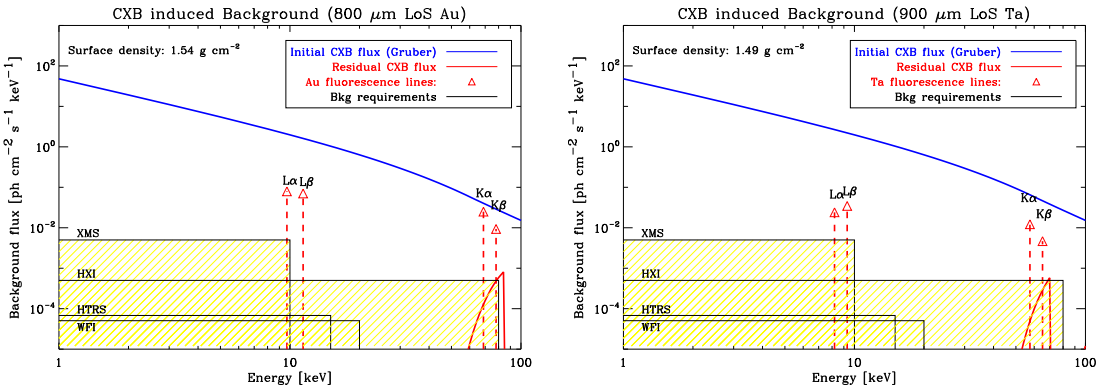

Figure 4.13: CXB induced residual X-ray background for an Au thickness of 800 μm (left panel) and a Ta thickness of 900 μm (right panel).

If we want the single layer configuration to meet the HXI requirement up to 80 keV, the mass budget, for a surface of 1 m^2, increases from $\sim$ 3 kg to $\sim$ 15 kg. The greater thickness has also the effect of decreasing the K lines because of intrinsic absorption, while the L lines are not affected by the thickness change since, as already explained, they are generated by the disks detector side.

4.6.3 Graded shielding configuration

Two sets of graded layers are selected in order to absorb the Au (or Ta) fluorescence emission (see Section 4.2 for the materials properties):

- Set 1: Sn + Cu + Al + C

- Set 2: Al + C

Tin (Sn) and Aluminum (Al), sets 1 and 2 respectively, are the materials chosen to attenuate the main absorber emission. Since two different upper energy limits for background minimization are analyzed (40 and 80 keV), the second layer thickness is computed in order to absorb the 99% of the Lα emission (Case A) on the Kα (Case B) emission. The other graded layers (Cu + Al + C, or only C) thickness is instead evaluated to absorb the 99% of the Kα emission of the previous layers (e.g. the Cu thickness stops the 99% of the Sn Kα photons). In addition to the two sets of graded materials, it is also computed the required thickness of a C layer (Set 3) to absorb the Au (or Ta) Lα emission, since this material is often used as carrying structure of the passive shielding. The grading thickness and surface density for a main absorber of Au and Ta are listed in Tables 4.13 and 4.14 respectively.

Au grading design

Au		Case A (< 40 keV)			Case B (< 80 keV)		
	Material	Thickness [mm]	Surface density [g cm^{-2}]		Thickness [mm]	Surface density [g cm^{-2}]	
Set 1	Sn	0.065	0.05	0.41	1.388	1.01	1.37
	Cu	0.290	0.26		0.290	0.26	
	Al	0.345	0.09		0.345	0.09	
	C	0.040	0.01		0.040	0.01	
Set 2	Al	0.964	0.26	0.27	72.58	19.60	19.61
	C	0.040	0.01		0.040	0.01	
Set 3	C	17.55	2.84	2.84	/	/	/

Table 4.13: Grading thickness and surface density for a main absorber of Au

Ta grading design

Ta		Case A (< 40 keV)			Case B (< 80 keV)		
	Material	Thickness [mm]	Surface density [g cm^{-2}]		Thickness [mm]	Surface density [g cm^{-2}]	
Set 1	Sn	0.038	0.03	0.39	0.857	0.63	0.99
	Cu	0.290	0.26		0.290	0.26	
	Al	0.345	0.09		0.345	0.09	
	C	0.040	0.01		0.040	0.01	
Set 2	Al	0.533	0.14	0.15	57.82	15.61	15.62
	C	0.040	0.01		0.040	0.01	
Set 3	C	9.84	1.59	1.59	/	/	/

Table 4.14: Grading thickness and surface density for a main absorber of Ta

For the Case A requirement, a combination of Al + C gives the lowest mass budget for both Au and Ta, while higher Z graded layers (Sn + Cu + Al + C) are needed if the Au (or Ta) K lines must be attenuated. An other important result is that the Carbon structure alone, with thicknesses well below 1 cm, is not sufficient to reduce the main absorber fluorescence.

Residual background for a graded passive shielding

The CXB induced residual background for the grading sets 1 and 2 is computed using the thicknesses of the previous Tables.

- Main absorber: 150 μm LoS Au

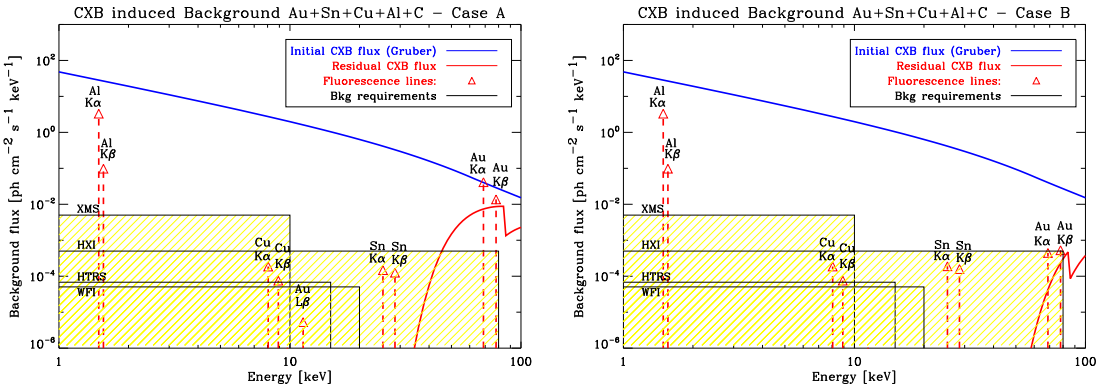

Figure 4.14: Residual background for a main absorber of Au (150 μm LoS) and a grading of Sn + Cu + Al + C in order to shield the CXB up to 40 keV (Case A, left panel) and 80 keV (Case B, right panel).

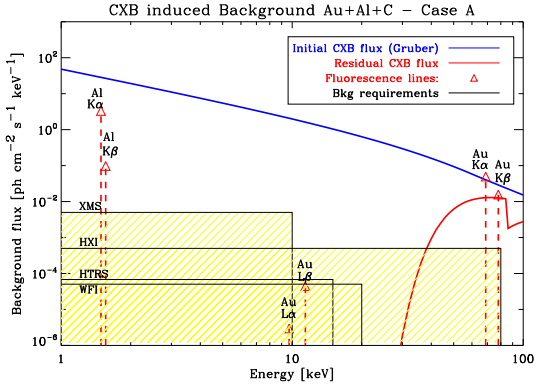

Figure 4.15: Residual background for a main absorber of Au (150 μm LoS) and a grading of Al + C in order to shield the CXB up to 40 keV (Case A).

The residual background for the Set 2 is only shown for the Case A requirement (Figure 4.15), because the Aluminum attenuation is too low to shield the Au K fluorescence lines.
The intensity of the Al fluorescence lines is extremely high. This effect is due to the sum of the CXB photons that arrive from the detector side, i.e. crossing only the C layer, and the triggering by the Cu fluorescence. However the Carbon thickness, analytically computed to absorb the 99% of the Al K photons, is low (40 μm). If we use a more feasible C thickness of 0.5 mm (with a surface density of 0.08 g cm^{-2}), the Al fluorescence lines are efficiently absorbed, as shown in Figure 4.16

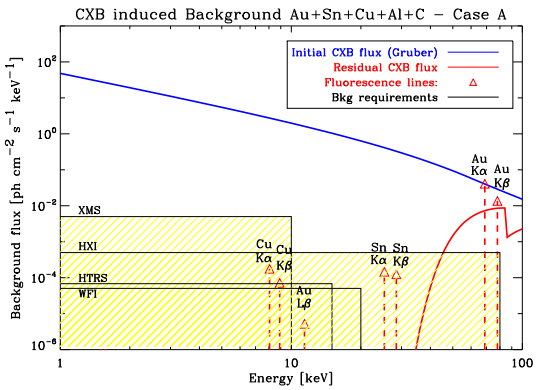

Figure 4.16: Residual background for a main absorber of Au and the grading Set 1 (Case A) using a C thickness of 0.5 mm.

for the Case A study of the Set 1. The fluorescence lines of the Au and graded layers (Set 1 and Set 2) meet the IXO background requirements, and for the Case B study the CXB continuous leakage is reduced to a level of $\sim 10^{-4}$ phot. cm^{-2} s^{-1} keV^{-1} and it satisfies the HXI requirement.

- Main absorber: 200 μm LoS Ta

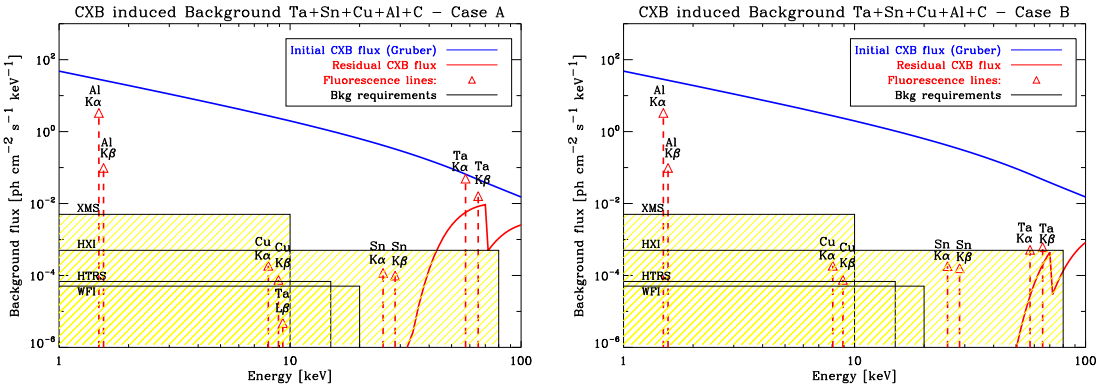

Figure 4.17: Residual background for a main absorber of Ta (200 μm LoS) and a grading of Sn + Cu + Al + C in order to shield the CXB up to 40 keV (Case A, left panel) and 80 keV (Case B, right panel).

Similar results are obtained in the minimization of the Ta fluorescence lines for both Set 1 and 2 graded layers (Figures 4.17 and 4.18), but it must be pointed out that, given the lower fluorescence energies respect to Au, the graded layers for a Ta main absorber require a lower mass budget.

4.6.4 General results and missing ingredients

The analytical evaluation of the CXB interaction with the passive shielding allows to achieve the following important results:

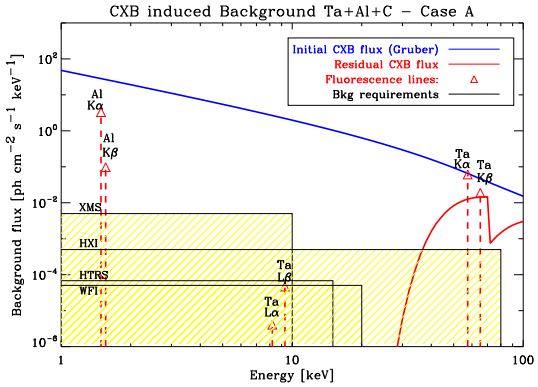

Figure 4.18: Residual background for a main absorber of Ta (200 μm LoS) and a grading of Al + C in order to shield the CXB up to 40 keV (Case A).

- For a single layer composition, the higher Z material (Au) results in a lower ($\sim$ 15%) mass budget, as already found in the Simbol-X passive shielding analysis (Sec. 4.4.3). On the contrary, the lower Z material must be preferred if the grading is present.
- The residual background for a single layer configuration is characterized by intense fluorescence lines, 2 - 4 orders of magnitude higher than the requirement. For an operative energy range $<$ 40 keV, well below the main absorber K lines, prominent Lyman features arise if disks are used above the focal plane. The grading is required.
- The passive shielding side that is irradiated by the CXB is an important source of fluorescence lines if this side is seen by the detectors, as the case of the concentric disks above the focal plane, because the fluorescence emission is not self-absorbed and attenuated by the shielding itself.
- The use of the disks to reduce the collimator mass budget potentially increases the background level.
- If the operative energy range is below 40 keV, a low Z grading (Al + C) efficiently shields the CXB, while optically thicker materials, like Sn + Cu + Al + C, are needed to attenuate the CXB up to 80 keV.

With a simple analytical computation, we setted the basic parameters of the passive shielding. However the spectra shown here are not the total CXB induced background because the Compton scattering is not taken into account. The interaction with matter gets more complex if we consider the charged particles that give rise to thousands of secondaries. The only solution is the development of Monte Carlo simulations that are able to explore the probability function of each process and allow to evaluate the background level as if the spacecraft is actually operating in space. The following Chapters are dedicated to this topic, but always keeping in mind that even the most complex simulation must be compared to analytical computations to validate the result.

Chapter 5

BoGEMMS: the Bologna Geant4 Multi-Mission Simulator

Before the advent of particle transport codes, and the increase of the computing performances, the background of a space mission was predicted by means of semiempirical methods and scaling laws on the basis of the background experienced by the operative missions and ground experiments (see e.g. Gehrels (1985)). This limitations of such approach, due to the different design of the instruments and the complexity of particle interactions, led to big uncertanties in the final background evaluation, well far from the accuracy needed in the reconstruction of the true source signal. The development of Monte Carlo[1] based simulations of the particles interaction with matter, coupled with computer 3D models of the spacecraft and instruments design, allows to track the particles and their secondaries from the first hit to the final energy deposit on the detection plane, producing the spatial and energy distribution of the detected background counts with the resolution of a real observation in space (Dean et al. (2003), Weidenspointner et al. (2005)). The possibility of creating a virtual model of the telescope and exposing it to the space radiation environment has fundamental benefits along the entire project development: the shielding optimization, the production and characterization of the background flux, the calibration validation, the treatment and filtering of the observation data sets.

The accuracy of the background Monte Carlo simulations depends on many factors:

- the modelling of the space radiation environment (fully reported in Chapter 3);
- the reliability of the interaction cross sections and parameterization of the physics processes;
- the building of the spacecraft and instruments geometry and composition model.

Among many nuclear and particles physics codes, we chose the open source C++ based Geant4 Monte Carlo toolkit (Agostinelli et al. (2003), Allison et al. (2006)). Developed by CERN and maintened by a large, international collaboration[2], the Geant4 toolkit was first conceived for the

[1] The Monte Carlo method generally refers to a stochastic computational algorithm based on the use of randomly generated numbers to solve a problem with a well known probability distribution that can not be analytically computed (Metropolis & Ulam 1949). An example is the angular direction of a photons after it is Compton scattered by the interaction with an electron.

[2] To learn more on the Geant4 collaboration and the Geant4 software, see the website www.geant4.org.

high energy experiments involved at particles accelerators and then extended to "lower"energy ranges, i.e. the X-ray and γ-ray domain, and it is now a widely used particle transport code for Astrophysics missions. The code not only provides a set of classes and libraries to describe the interactions of particles with matter down to low energies (250 eV), but it also allows to easily build the 3D model of the spacecraft and to generate the energy and spatial distribution of the particles in space. Validation testing results can be found in Amako et al. (????), Guatelli et al. (2007) and Wright (2010).
On the basis of the Geant4 set of libraries, the BoGEMMS, Bologna Geant4 Multi-Mission Simulator, project for prompt background evaluation has been developed at the INAF/IASF Bologna (Bulgarelli et al. in prep.), which allows to interactively set the geometrical and physical parameters (e.g. physics list, materials and thicknesses), recording the interactions (e.g. energy deposit, position, interacting particle) in FITS format output files and filtering the output as a real observation in space, to finally produce the background detected count rate and spectra.
The BoGEMMS is a multi-mission tool, generally designed to be applied to any high energy mission for which the shielding and instruments performances analysis is required. As a matter of fact, in the present thesis Geant4 simulations are performed for the detection efficiency and background evaluation of the Simbol-X and NHXM missions, as well as for the XMM-Newton soft protons funnelling and the general analysis of the shielding efficiency in LEO. The results presented here refer to the Geant4 9.1 release, but the system is currently being upgraded to the last 9.4 release (December 2010).

5.1 The algorithm in three steps

The Geant4 software provides all the libraries needed to perform the simulation, but the user has the responsibility to choose the physics needed for its virtual experiment and to select which kind of information must be provided (e.g. the energy deposit, the particle energy or direction, the type of interaction), all features that can be modified only in the hard-coded Geant4 working files. As a direct consequence, for each new experiment a new simulator has to be developed.
The BoGEMMS solves this problem by allowing the user to set the simulator by means of a configuration file read in input by the simulator. The general features of the configuration file are:

- the setting of the physics list (e.g. electromagnetic, hadronic, both), see Sec. 5.1.1;
- the selection of the output file among three types, providing information on the particle energy and track, or the volumes energy deposit, or the physics process in play for each step, and the possibility to write only a set of volumes to speed up the analysis (see Sec. 5.1.2);
- in case of simple geometries, the possibility to build directly the instruments and shielding design, as well as the creation of empty non interacting volumes ("stepping volumes") to track or remove the particles (e.g the presence of the mirror module at the center of the Simbol-X sky screen, or the protons angular and spatial distribution at the exit of the optics).

In addition to the configuration file, the simulator takes in input the energy, angular and spatial distribution of the impinging particles, efficiently coded in a single file provided by the Geant4 General Particles Source (GPS) tool (Ferguson 2000).

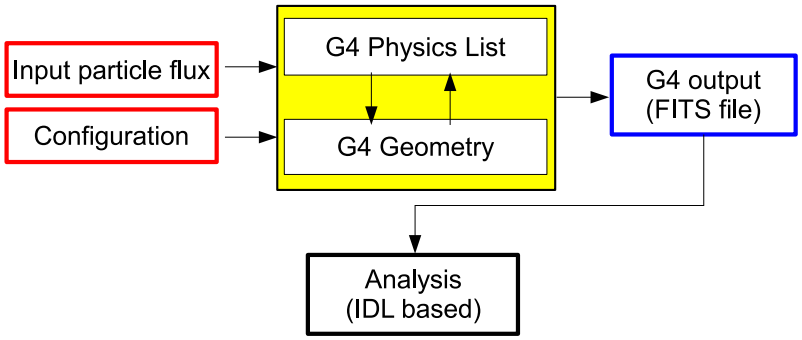

Figure 5.1: The BoGEMMS architecture: the simulator, composed by the physics and geometry libraries, receives in input the particle flux and the configuration file setting the geometry, the physics processes and the output file, that is finally produced in FITS format and read by the IDL based analysis software, which returns in the end the background and AC spectral files.

The BoGEMMS working algorithm, schematized in Figure 5.1, can be divided in three main steps:

1. the input files where the user sets the emitted particles and the simulator physics, geometry and output files;

2. the BoGEMMS core, where the Geant4 libraries are called according to the input files and the outputis produced in FITS format;

3. the IDL based software analysis (see Sec. 5.2), that filters the output (e.g. the removal of the active shield coincidence counts) and produces, for example, the background and AC spectral files, in FITS format.)

A detailed report of the BoGEMMS core architecture will be found in Bulgarelli et al (in prep.). Here we only describe the general features needed to understand the results presented in the next Chapters.

5.1.1 Physics processes

The detailed list of all the particles and physics processes activated in BoGEMMS is reported in Appendix B. We remind that the radioactive decay is not taken into account, since we are only evaluating the prompt background level, but we have to note that the 9.1 radioactive decay module does not model correctly the background decay lines (Zoglauer et al. 2008), and validation tests are still ongoing (Hauf et al. 2010). The Geant4 releases up to the 9.3 require the user to choose between the standard electromagnetic processes, faster but unable to well reproduce the low energy (E$<$ 100 keV) domain, and the low energy extension, which introduces the atomic relaxation (X-ray fluorescence and Auger electrons emission). The latter is used for the present simulations, since our goal is to evaluate the X-ray background. In Figure 5.2 a comparison between the two

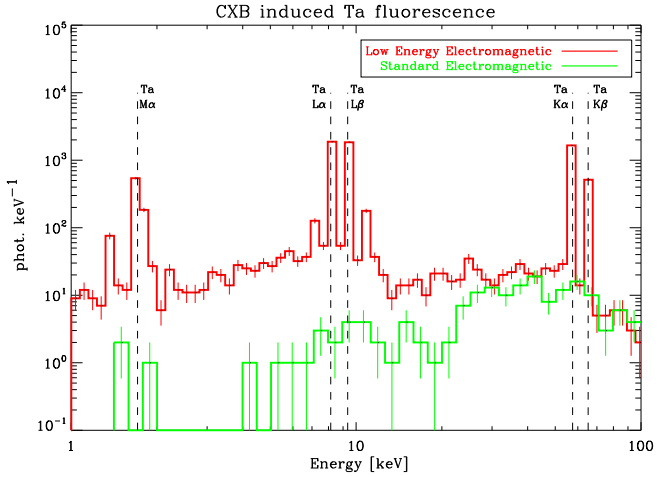

Figure 5.2: The energy distribution of X-ray photons exiting a slab of 1.5 mm thick Ta after the CXB interaction, for the activation of the low energy (red line) and standard (green line) electromagnetic processes. The dashed lines refer to the Ta fluorescence emission.

electromagnetic packages is shown by simulating the CXB interaction with a plane ("slab") of 1.5 mm thick Ta: the energy distribution of the exiting photons is plotted, with clearly visible Ta fluorescence lines when using the low energy module.

5.1.2 Geant4 output

The Geant4 output is produced in FITS (Flexible Image Transport System, Wells et al. (1981)) files, a widely used format in the Astrophysical data analysis field. Three different types of output can be produced by the BoGEMMS:

- IN-OUT type: the particles properties (type, energy, direction, position and interacting volume) are written at the entrance and exit of each touched volume for the entire path. If secondaries are produced, they are also written starting from the production volume. This type of file is useful to study, for example, the particles interact with the detection plane and generate the background counts or to trace the properties of the protons after they interact with the X-ray optics.

- ENERGY type: the sum of the energy deposits, due to the sum of primaries and secondaries, for each volume and each emitted particle is written. This allows to produce smaller files, easier to be handled by the analysis software, used to evaluate the instruments and active shield detected counts;

- STEP type: the Geant4 simulator follows the particles for each interaction step, allowing to write the physics process in play, as well as the particle properties during the interaction. This output type can be used only for a small number of input particles, given the big amount of data, and it is used to test and validate the simulation.

The production threshold (range cut or cut off) is a cut in range for the production of secondaries that can be associated to particles (required for gammas, electrons and positrons) and/or to a region. It is defined as a distance, which is converted to an energy cut off for individual materials and particles. If the secondary particle energy is below the cut, it is not produced and the equivalent amount of energy is locally deposited. A range cut of 1 μm is used for the present simulations.

5.2 Analysis

The Geant4 output is treated as a real observation in space, from the screening phase (e.g. reconstruction of the detected count, anticoincidence triggering) to the differential spectra production in counts cm^{-2} s^{-1} keV^{-1}.
In the analysis of the Simbol-X and NHXM background levels, the energy ranges of the LED and the HED are respectively set to 0.5 - 20 keV and 5 - 100 keV, while in the XMM-Newton simulation the soft protons induced counts are selected in the 1 - 100 keV energy range. A LED (HED) count is defined as the sum of the energy deposits, generated by the same primary particle, within the defined energy range. It is possible to flag coincidence counts between the LED and the HED and group them as a separate class of events. The analysis software is also designed to select the events according to the number of pixels detecting the event (pattern selection), in order to apply the pattern recognition in the reduction of the proton induced background.
An event is anticoincided if the same primary particle generates an event in the active shield (energy deposit above the AC threshold) and a LED (HED) count within the detection energy range. All the AC events generated by the same primary particle are considered as one single count, despite the different volume involved. The triggered LED (HED) counts are then removed in "AC on" mode, while the total AC count rate is calculated with the total number of detected events by the active shield.
Two additional features are also possible in the analysis process: the evaluation of the first volume hit by the primary particle, to look for a leakage in the shielding and to select the volumes responsible for the highest background fraction (see Sec. 6.2.2), and recording the energy distribution of the particles finally interacting with the detection plane (see Sec. 7.1.1).

5.2.1 Normalization of an isotropic flux in space

The simulation normalization is intended as the process that leads from the number N of emitted particles to a count rate in counts s^{-1}. In the interaction of a detector with an isotropic particle flux, as the present case, the detected count rate is related to the incident particle rate by a factor of proportionality (Sullivan 1971) defined by the particles source configuration. The particle are emitted from a spherical surface of radius R_{ext} within a cone of half angle (q), following a cosine law angular distribution, that subtends an inner sphere of radius R_{in} enclosing the spacecraft (Figure 5.3). Limiting the emission angle from 2π to a cone increases the simulation statistics, because a higher fraction of the emitted particles reaches the target. If we define the energy integrated

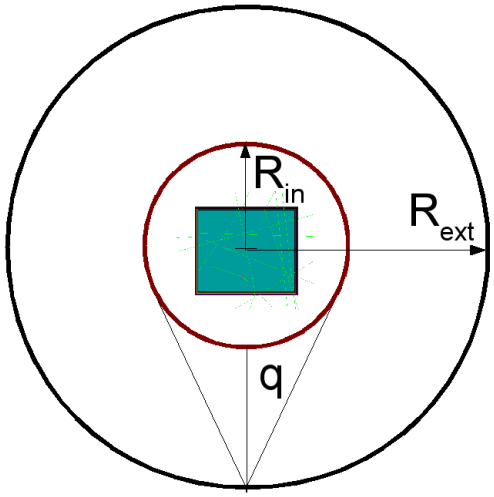

Figure 5.3: Angular and spatial distribution of the simulated particles.

particle flux Φ as particles cm^{-2} s^{-1} sr^{-1}, the rate P, in particle s^{-1}, is given by

$$P = \Phi \times A_{ext} \times \Omega \, , \tag{5.1}$$

where A_{ext} and Ω are respectively the surface of the external source sphere and the emitting cone solid angle.
In the calculation of the solid angle of the emission cone, we must account for the cosine of the polar angle θ, since the flux for each direction is proportional to the cosine of the angle between the source direction θ and the local normal to the sphere surface:

$$\Omega = \int_{\phi}\int_{\theta} \cos\theta \sin\theta d\theta d\phi = \int_{0}^{2\pi}\int_{0}^{q} \cos\theta \sin\theta d\theta d\phi = \pi \sin^2(q) \ \ sr \, . \tag{5.2}$$

The simulated particles rate P is then given by:

$$P = \Phi \times (4\pi R_{ext}^2) \times (\pi \sin^2(q)) = \Phi \times 4\pi^2 R_{ext}^2 \sin^2(q) = \Phi \times 4\pi^2 R_{in}^2 \, , \tag{5.3}$$

where R_{in} is the radius of the inner sphere.
The equivalent exposure time T, in seconds, to the isotropic flux depends on the number of simulated particles N as follows:

$$T = \frac{N}{P} = \frac{N}{\Phi \times 4\pi^2 R_{in}^2} \, . \tag{5.4}$$

The detected background count rate B, in counts s^{-1}, is obtained by dividing the number of detected counts C for the exposure time T:

$$B = C/T = C \times N^{-1} \times \Phi \times 4\pi^2 \times R_{in}^2 \, . \tag{5.5}$$

For example, the simulated GCR flux for the Simbol-X background evaluation is 2.31 protons cm^{-2} s^{-1}. For 10^7 protons emitted from a 50 m source sphere within a cone of half angle 0.01 rad, the simulated exposure time is $\sim$ 551 s.
The energy averaged background flux in terms of counts cm^{-1} s^{-1} keV^{-1} is obtained by dividing the background rate, in cts s^{-1}, for the detectos area and the operating energy range (e.g ΔE = 100 - 5 keV = 95 keV for the HED).

5.3 Preliminary tests

In Sec. 4.6 the analytical computation of the CXB induced background spectrum is presented, using the tabulated cross sections and fluorescence yields from literature. The same analysis can be easily performed by BoGEMMS without the need to modify the C++ code. Here we present two examples: the result of the CXB interaction with a 1.5 mm thick slab of Ta and a box of Ta, with the same thickness, surrounding the focal plane.

5.3.1 Interaction with a slab

The Geant4 model of a 1.5 mm thick Tantalum slab, shown in green in Figure 5.4 in front of a simplified model of the NHXM hybrid focal plane, is irradiated by a planar beam of photons using the energy distribution of the CXB flux.

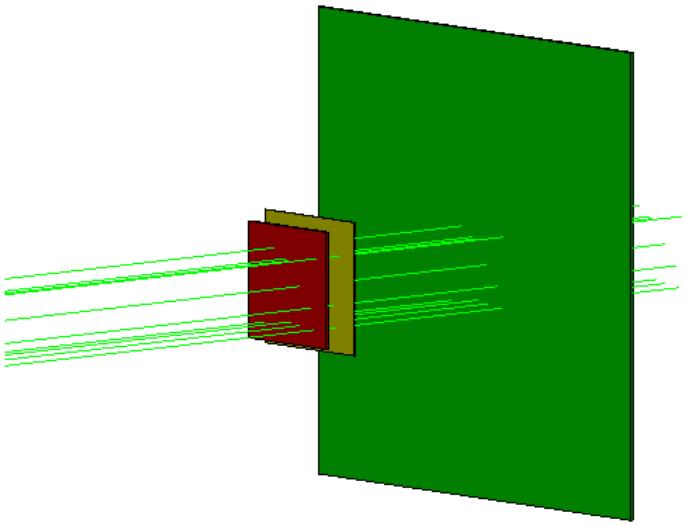

Figure 5.4: The Geant4 3D model of a slab of Tantalum (at right) placed in front of the simplified NHXM hybrid focal plane, composed by the LED (in yellow) and the HED (in red). The green lines show the trajectory of the CXB photons emitted by a parallel beam from the right.

A fraction of the CXB leaks through the shield, while secondaries are produced both backwards (the sky side, at right) and to the focal plane (at left). The total energy distribution of the exiting

photons, in phot. keV^{-1}, for the two sides, is plotted in Figure 5.5. In the plot of the photons

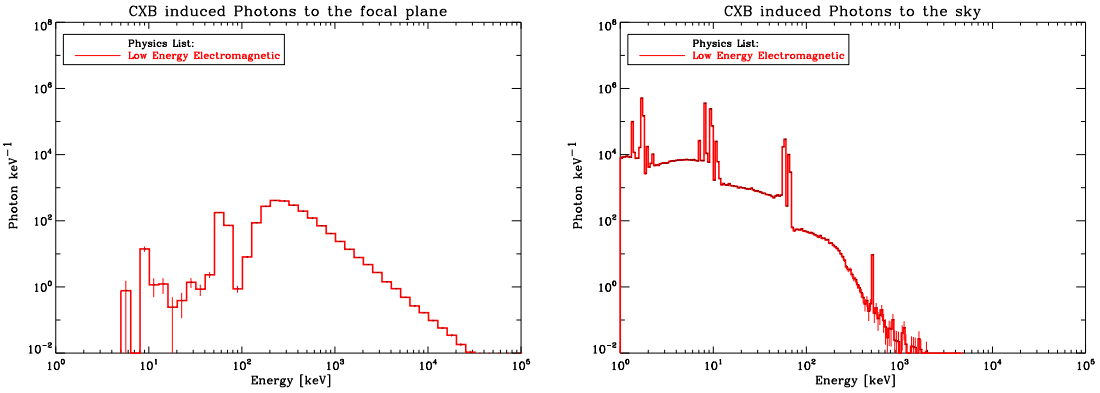

Figure 5.5: Photons exiting from the 1.5 mm thick Ta slab after the CXB interaction and directed to the focal plane (left panel) and to the sky (right panel).

directed to the focal plane the power law distribution of the CXB is visible at E> 100 keV, referring to the leaking primary photons that are not stopped by photoelectrical interactions. Below 100 keV, the Ta absorbing efficiency starts to arise, and only the Ta fluorescence lines are visible. A different scenario appears if we consider the photons that are directed backwards, where the CXB flux reached the slab (the sky for a real shielding in space). We do not obviously see the primary CXB flux, but a wealth of lines is produced, from the Ta X-ray fluorescence to the 511 keV annihilation line, because these secondaries dot not cross the entire Ta thickness and are not self-absorbed, as happens for the particles directed to the focal plane.
With a simple, fast simulation we achieve the same important result obtained by the IXO shielding optimization: if parts of the shielding where the CXB is impinging, as the IXO concentric disks, are facing the focal plane, intense low energy (E> 40 keV) fluorescence lines are emitted, representing a dangerous source of background.

5.3.2 Interaction with a box

We now consider a box of Ta, 1.5 mm thick, completely shielding the focal plane. Using the analytical computation of Sec. 4.6, the residual background reaching the detectors, is evaluated in phot. cm^{-2} s^{-1} keV^{-1} (the left panel of Figure 5.6, red line). The dashed lines represent the Ta K fluorescence lines. We remind that the latter are an upper limit, since we are not taking inot account the detection efficiency. The residual flux is well below a background requirement of $\sim 10^{-4}$ cts cm^{-2} s^{-1} keV^{-1}, because a 1.5 mm thick Ta layer ensures an X-ray attenuation >99% below 150 keV. The K emission is instead intense, because no grading is applied.
The same Ta geometry is simulated with Geant4, with the addition of the NHXM focal plane, and the residual background evaluated (Figure 5.6, right panel), following the analysis described in Sec. 5.2. The intensity of the Ta K lines is consistent, within a factor 2-4, but the background continuum is detected along the entire X-ray energy range because of the Compton scattering that allows the high energy photons to leave an energy deposit within the detector energy range.

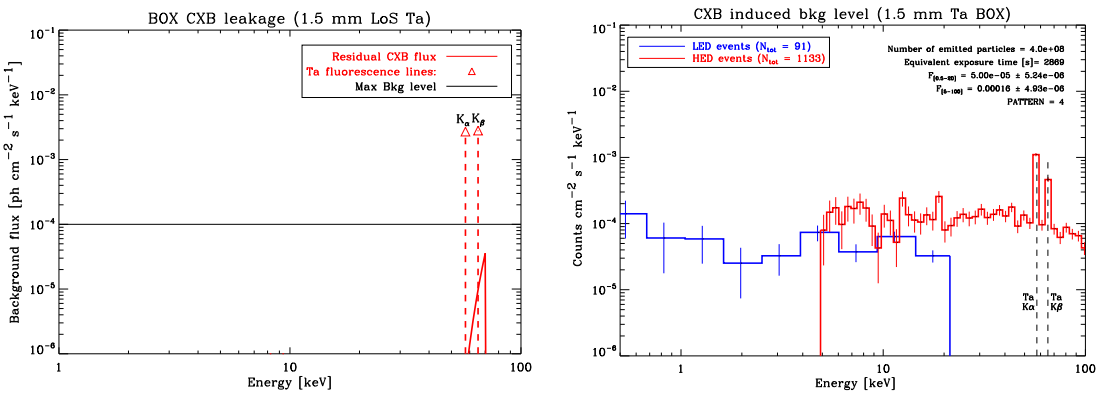

Figure 5.6: *Left panel*: CXB induced residual background (red line) reaching the focal plane for a 1.5 mm thick Ta shielding. The dashed lines refer to the Ta K fluorescence lines. *Right panel*: CXB induced background on LED (blue line) and HED (red line) for a 1.5 mm thick Ta layer completely surrounding the focal plane.

As already pointed out at the end of the previous Chapter, altough analytical computations are fundamental for a general shielding analysis, only Monte Carlo simulations can take into account the complexity of the physics processes in play.

Chapter 6

Background evaluation

The models of the space radiation environment for the chosen orbit, the shielding optimization and the simulation of the particles trasport through matter allow to achieve, at the end, the background count rate, to be compared with the maximum allowed background defined by the mission top scientific requirements.
In this Chapter, the main results regarding the Simbol-X and NHXM background evaluation are presented. In the case of the NHXM mission, the background spectra refer to a simplified geometry, and have the only aim to underline the effect of the geomagnetic cut-off on the GCR induced background in LEO. For a comprehensive analysis of all the background components in LEO, see Chapter 7.
In HEO, a major source of the flaring background is represented by the soft protons funnelling by the X-ray optics. In the last Section, BoGEMMS is exploited to study the angular and energy distribution of the protons at the exit of the X-ray optics, in order to set the magnetic diverter design.

6.1 Simbol-X background

The DSC shielding is both active and passive. The plastic anticoincidence surrounds the focal plane, while passive material is placed both within the active shield and at the top of the detectors as a cylindrical tube. The remaining focal plane aperture solid angle is covered by the combination of the passive sky screen and adapter cover. The CXB and GCR induced background and active shield count rate is evaluated for the DSC mass model, while for the MSC case only the CXB contribution is analyzed. The reason is that the solid angle covered by the MSC passive shielding is so small that the proton rate passing through the collimator aperture can be neglected. On the contrary, as shown in Figure 4.6, the perfect shielding is required for the CXB induced background minimization. In addition, the whole sky screen structure is so extended that the passive materials thickness must be reduced, decreasing the X-ray attenuation power. In Figure 6.1 the total Simbol-X Geant4 mass model is shown. The DSC collimator (at left) is visible in purple (the green line is the telescope axis), while the grey structure refers to the spacecraft mass below the focal plane. The DSC mass model has been developed by the Simbol-X background group, which we gratefully

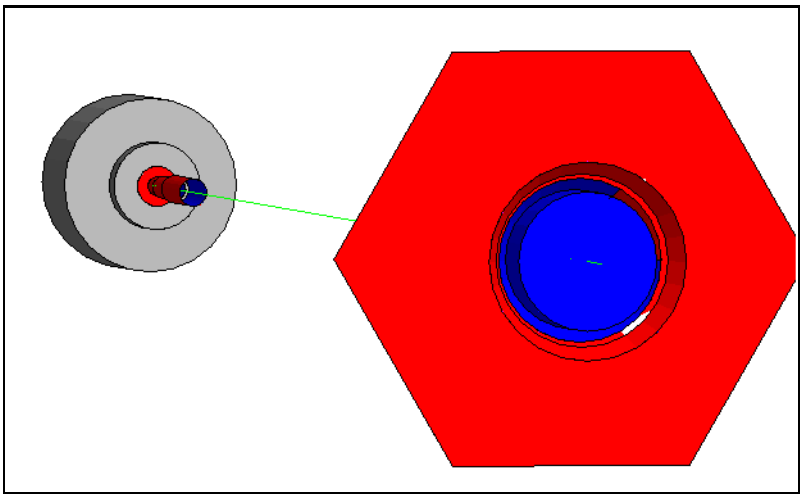

Figure 6.1: The Simbol-X Geant4 mass model on which is based the background simulation. The DSC is shown in grey at the left, while the MSC passive shielding is shown in red. The green line is the telescope axis, passing through the collimator aperture (in purple).

thank to allow us the use of this detailed 3D model to perform a complete background study of the Simbol-X mission. In the right part, the hexagonal red structure is the MSC sky screen (the blue central region represents the mirror module). The MSC passive shielding mass model development is instead an original work, as part of the Simbol-X auxiliary items assessment study.

6.1.1 MSC passive shielding optimization

The solid angle covered by DSC collimator on the focal plane is given by:

$$\theta_{\rm coll} = \tan^{-1}\left(\frac{\rm D_{det}+s}{\rm H}\right) \tag{6.1}$$

$$\Omega_{\rm coll} = 2\pi\left[\cos\left(\theta_{\rm coll}\right)\right] = 6.27 \quad {\rm sr} \quad , \tag{6.2}$$

while the solid angle covered by the MSC passive shielding (the dashed line of Figure 4.6) is 0.01 sr, about 3 orders of magnitude less then $\Omega_{\rm coll}$. This implies that even the unfocused CXB photons passing through the sky screen cause a background level about 1000 times lower than that transmitted by the collimator, allowing a decrease of the sky screen and adapter cover thickness. This shielding optimization requires a great care in the background evaluation because a lower thickness increases the sky screen residual background caused by shield leakage and fluorescence emission. This last point appears as the most crytical from Table 4.8, since a great amount of mass results from the grading and in particular from the Sn layer that absorbs the main absorber Kα line: reducing the mass budget decreases the attenuation of the fluorescence emission.
The Geant4 background simulator allows, in this context, to easily analyze the residual photonic emission at the focal plane as a function of the mass budget. We assume a maximum residual background level of $\sim 10^{-5}$ phot. cm^{-2} s^{-1} keV^{-1}, about an order of magnitude less than the total level. The residual background upper limit results in the minimum required shielding thickness,

i.e. the minimum mass budget. As a result of the Simbol-X Phase A study, the maximum mass budget that can be allocated to the MSC passive shielding is 15 kg, divided in $\sim$ 13.5 kg for the sky screen and $\sim$ 1.5 kg for the adapter cover. We test the feasibility of this requirement by performing the background simulation for a main absorber of Pb or Ta, with and without the addition of the graded layers. We remind the reader that, for a 99% attenuation efficiency, the total mass budget is more than 60 kg (see Sec. 4.4.3). A simplified Geant4 mass model of the sky screen and adapter cover has been created (Figure 6.2).

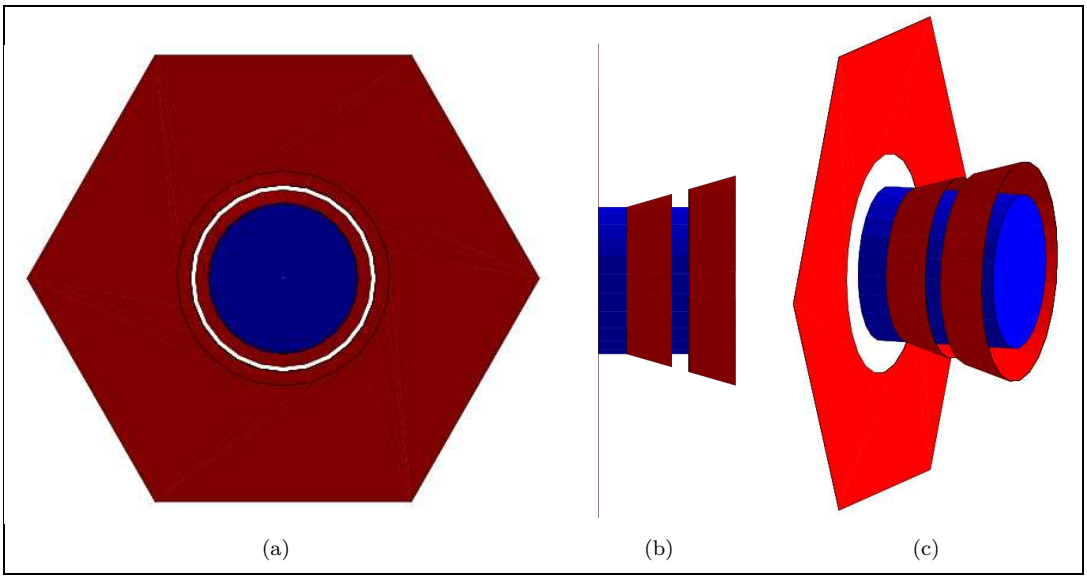

Figure 6.2: Face-on (a), lateral (b) and backside (c) visualization of the MSC passive shielding mass model: the hexagonal sky screen and adapter cover are shown in red while the blue cylinder approximates the mirror module. In (b) and (c) panels the DSC direction is on the left.

The adapter holes are approximated by a cone trunk hole with the same area covered by the adapter holes, visible in red in Fig. 6.2(b). The central blue cylinder is an empty volume representing the mirror module: if a photon enters the X-ray optics volume, it is removed because either absorber of focused to the focal plane, so that it does not contribute to the background. The absorption effect of the MSC is simulated with a 3.5 mm thick layer of Al on the back side of the shielding, with the addition of a 1 mm thick layer of Carbon to represent the thermal blankets. Fig. This structure is not plotted for clarity reasons, but it is placed in the right side of Fig. 6.2(b).
The CXB flux is emitted from a 5 m radius sphere enclosing the MSC passive shielding, within a 0.3 sr half aperture cone (the semi-angle subtended by the whole structure at a 5 m distance) to increase the simulation statistics. The CXB interacts with the shielding and a fraction of unabsorbed or secondary photons arrive at the Simbol-X detectors. Here we do not take into account the detection efficiency of the focal plane, so that the residual photonic flux, in phot. cm^{-2} s^{-1} keV^{-1}, in the 1 - 200 keV energy range is evaluated. The spectrum of the residual background is plotted in Figure 6.3:

- blue line: the CXB flux, in phot. cm^{-2} s^{-1} keV^{-1}, as generated by the Geant4 simulator;
- red line: total residual background flux on the focal plane;
- green line: the residual background flux leaking through the adapter holes;
- black line: the residual background flux without the contribution of the adapter holes;
- black dot-dashed line: the maximum accepted background level (10^{-5} phot. cm^{-2} s^{-1} keV^{-1});
- black dashed line: fluorescence lines.

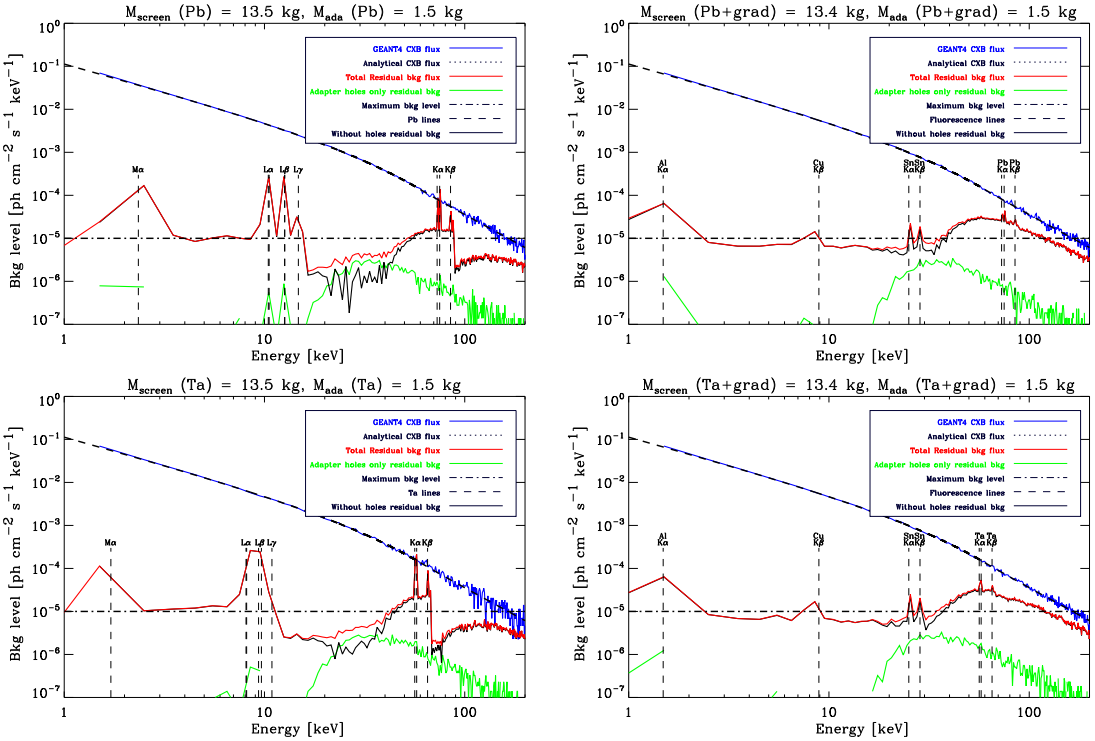

Figure 6.3: MSC passive shielding residual backgrund induced by the CXB interaction for a total mass budget of 15 kg. The simulation is performed for a main absorber of Pb (top panels) and Ta (bottom panels), with (right panels) and without (left panels) the addition of the graded layers.

The simulation results can be summarized as follows:

Geometry: The background spectra indicate that the thrust cylinder holes leakage (green lines) remains below the maximum allowed background level thanks to the MSC and thermal covering absorption.

Composition: If only the main absorber is applied, the fluorescence emission is almost 100 times intense as respects the requirements. The addition of the grading allows a significant

fluorescence attenuation ($> 90\%$), but the CXB continuum leakage, due to the decrease of the main absorber thickness, arises above ~ 40 keV, reaching a value $\sim 2 - 3 \times 10^{-5}$ phot. cm^{-2} s^{-1} keV^{-1}.

Mass budget: The feasibility study shows that a decrease of the MSC passive shielding mass budget to 15 kg, while keeping a low residual background, is possible. However the loss of the shielding performance, in terms of background reduction, causes the CXB leakage flux to be 2-3 times higher than the requirement.

The sky screen optimization study can be also applied to the NHXM mission. In this case, the shorter focal length allows to decrease the sky screen diameter (Sec. 4.5), so that for the same 15 kg mass budget the residual background would be lower than what expected for the Simbol-X mission.

6.1.2 Detection efficiency

In Figure 6.4 the Geant4 mass model wired view of the DSC, including the focal plane, the shielding system and the external carrying structure, is shown. The MSC is at the top side (where a part of the collimator is visible). The green line represents a 1 MeV photon beam emitted from the MSC, which crosses the detectors, at the image center, without interacting and then it is partially reflected by the bottom surface. A way to validate the Geant4 model of the Simbol-X hybrid

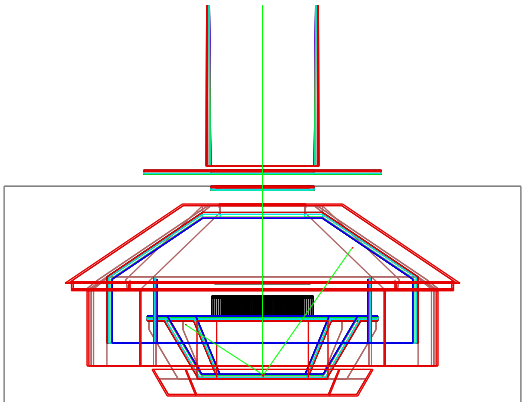

Figure 6.4: The Simbol-X DSC Geant4 mass model wired view. Part of the collimator is visible at the top, the rectangular shape is the external Al box, while the two detectors are placed in the center. The green line is the trajectory followed by 1 MeV photon beam, crossing the focal plane without interacting and then partially reflected by bottom surface.

focal plane and, at the same time, to debug the BoGEMMS code is the evalution of the detection efficiency, and the comparison of the simulated result with the analitically computed absorption efficiency from the mass attenuation parameters distributed by the NIST[1] database. The analysis presented here is part of the Simbol-X background group simulation results (Tenzer et al. 2009), and it has been reported in Fioretti et al. (2008a).

[1]Hubbell, J. H. and Seltzer, S. M., NIST X-ray attenuation coefficients, National Institute of Standards and Technology

Simbol-X focal plane

The Simbol-X focal plane (Laurent et al. 2008) is hybrid and composed of two imaging detectors: the Low Energy Detector (LED) optimized for energies below 20 keV, and the High Energy Detector (HED), placed beneath the LED, with high detection efficiency up to 100 keV (Figure 6.5).

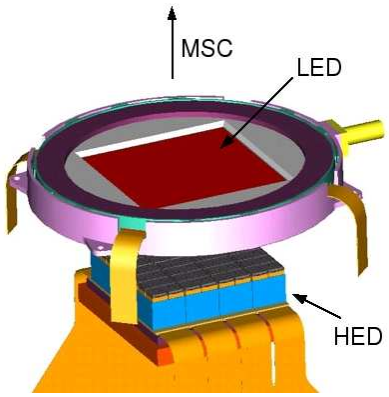

Figure 6.5: Schematized configuration of the Simbol-X focal plane as given by Dirks et al. (2006). The Mirror Spacecraft (MSC) is at the top. The LED is represented in red while the HED is shown in light blue.

The LED is a monolithic crystal detector. The imaging plane is electronically divided into 128×128 pixels and the readout scheme of the pixel detector is that of an active pixel sensor, that is a Silicon drift detector with an integrated DEPFET (Depleted P-Channel Field Effect Transistor). The pixels, with a thickness of 0.45 mm, have a lateral side of 0.625 mm. The LED detector is logically and functionally divided into four quadrants of 64×64 pixels each, which can be read in parallel. The HED is made of arrays of 1 cm^2 area modules to constitute 8 sectors of 2×4 modules. Segmented electrodes are defined on each monolithic crystal, by a photolithography process, to define an array of 16×16 pixels, with a lateral side of 0.625 mm. The material of each module is a 2 mm thick CdZnTe.
The pixellization is reproduced in the Geant4 model, with the following configuration:

GEANT4 FOCAL PLANE DESIGN

Detector	Side	Height	N pixels	Pixel side	Pitch-to-pitch[a] distance	Dead area
LED	8 cm	0.45 mm	128×128	0.625 mm	0.625 mm	0
HED	8.4375 cm	2 mm	128×128	0.625 mm	10.625 mm	10.1%

[a]The distance between two pixels center for the LED and distance between two modules center for the HED.

Table 6.1: LED and HED Geant4 configuration.

The electronic readout scheme of the LED is represented by 128×128 pixels, without dead area. The HED is divided into 64 (8×8, 1 cm side) modules with a pitch-to-pitch distance of 10.625

mm, i.e are separated by a distance of 0.625 mm. Each module is divided into 16×16 contiguous pixels. The HED dead area is $\sim 10\%$.

Simulation set–up

The detection efficiency analysed in this report is intended as the fraction of the events detected by the Simbol-X focal plane, N_{det}, as respects to the initial amount of emitted photons, N_{emi}. If we call Eff the detection efficiency, it can be described as:

$$\mathrm{Eff} = \frac{N_{det}}{N_{emi}} \,. \tag{6.3}$$

This definition of the detection efficiency includes the presence of dead area on the focal plane: a fraction of the emitted photons does not cross the HED, that can detect at most the 89.9% of the emitted photons.
A monochromatic planar beam of photons, parallel to the telescope axis, is emitted to the detectors. The source area is a circle of radius 3.5 cm. The reason is that both the calibration wheel and the base ring (an annular structure at the collimator base) partially cover the LED and HED starting from a radiu of 4.5 cm and 5 cm respectively. The resulting vignetting is visible in Figure 6.6, where the LED (in grey) and a radiation beam of squared source (in green) are visualized. The

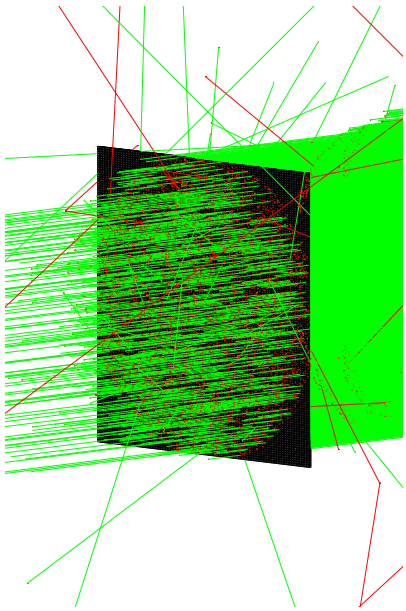

Figure 6.6: Interaction of a monochromatic planar beam of 100 keV photons (green lines) with LED (in grey). The source surface is a square (8 cm side) placed above the focal plane (on the right). The base ring of annular shape shadows the LED and the detection active area is reduced to a circle. The red lines are electrons.

beam is monochromatic at 100 keV and emitted from the right. At these energies the absorption of the LED is low (1.91%) and a great fraction of the photons cross the LED without being absorbed. The leaking photons show a circular shape and it is clear that the open calibration wheel and the

base ring, made of Tantalum plus grading, shadow the LED at the edges. Emitting the photons from a 8×8 cm square, the efficiency would be under-extimated. To ensure a correct efficiency evaluation, a source circular area has been chosen. The photons are isotropically emitted from the surface, placed at a 3 m distance from the LED, as monochromatic beams at 15 different energies (0.5, 2.5, 5, 10, 12.5, 15, 17.5, 20, 22.5, 25, 30, 40, 50, 75 and 100 keV).
It is necessary, from Equation 6.3, to define what kind of energy deposit can be considered as a detected event in order to calculate the quantity N_{det} and evaluate the detection efficiency. The first point to be clarified is that all the secondaries, if present, are tracked and can generate an event. The main assumptions and event definitions on which is based the analysis are:

- Energy range:
  - LED energy range = 0.2 - 60 keV
  - HED energy range = 2 - 160 keV
- LED/HED event: all the energy deposits, that fall within the LED/HED energy range and have been caused by the same primary photon, are summed. If the total energy deposited by the primary photon is within the LED/HED energy range, then it is considered as a LED/HED count. If the primary photon generating the LED/HED count does not cause a coincidence count on the HED/LED, then the LED(HED count is classified as LED event. The total number of LED/HED events is N_{det} of Equation 6.3.
- Total efficiency: the total efficiency is the fraction of events that deposit an energy amount within the energy range as respects the total number of emitted photons, i.e. it includes also the photons that only deposit a fraction of their energy.

Results

In Table 6.2 the LED and HED absorption for the energies of interest is calculated with the X-ray mass attenuation coefficients provided by the NIST database. The analytical evaluation of the absorption efficiency is given by the Equation 4.1. The HED absorption efficiency must be weighted for the Si absorption, which reduces the incoming flux, and the HED dead area. The resulting HED relative absorption is shown in the fourth column of Table 6.2.
The simulated detection efficiency, with erros bars as given by the Poisson statistics, is shown in Figure 6.7:

- blue line: the LED total efficiency;
- red line: the HED total efficiency:
- green line: the fraction of LED-HED coincidence events as respects the emitted photons;
- black line: total aggregate detection efficiency with the addition of the coincidence events;
- dotted blue/red/black lines: NIST LED/HED/total efficiency, with the HED values as given by the relative absorption of Table 6.2

LED AND HED ATTENUATION EFFICIENCY

Energy keV	LED efficiency [%]	HED efficiency [%]	HED relative efficiency [%]
1	100.0	100.0	0.0
2.5	100.0	100.0	0.0
5	100.0	100.0	0.0
10	97.1	100.0	2.6
12.5	84.2	100.0	14.2
15	66.0	100.0	30.5
17.5	49.8	100.0	45.1
20	37.4	100.0	56.3
22.5	28.4	100.0	64.4
25	21.9	100.0	70.2
30	14.0	100.0	77.3
40	7.1	100.0	83.5
50	4.5	100.0	85.9
75	2.5	98.2	86.1
100.	1.9	84.6	74.6

Table 6.2: Analytical evaluation of LED and HED absorption efficiency.

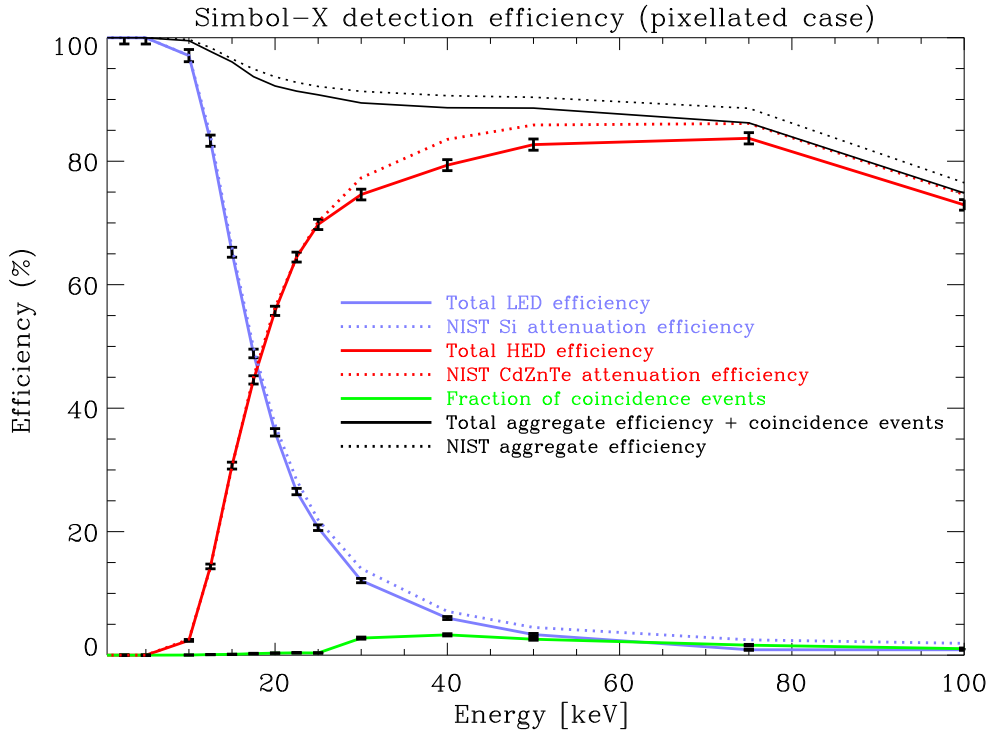

Figure 6.7: Simbol-X total detection efficiency (continuous line) resulting from the Geant4 simulation of the pixellated configuration compared to the analytical absorption efficiency (dotted line) calculated with the NIST attenuation coefficients.

The efficiency curves for the G4 simulation and NIST values show the same trend. The HED efficiency curve is lower than the analytical one above 25 keV because at these energies the HED K shell absorption edges cause the production of electrons and/or fluorescence photons that are absorbed by the LED. These secondary particles lead to classify the HED real detection as a coincidence count, and the direct proof of this effect is the coincidence events green line of Figure 6.7, that increases above 25 keV.
The detection efficiency reaches the same value for LED and HED at about 20 keV. The simulated and analytical LED efficiency are consistent within the statistical error bars. The same result comes from the HED efficiency if we take into account the fraction of coincidence events. This is clear considering the total aggregate efficiency that is consistent with the analytical one within the statistical fluctuations.
The main result of the present simulation is that the performances of the Si Low Energy Detector and CdZnTe High Energy Detector are well reproduced by the Geant4 Simbol-X simulation.

6.1.3 DSC background results

The second step of the Simbol-X DSC background evaluation, after the detection efficiency validation, is to simulate the hadronic and photonic flux impinging into the spacecraft and the related shielding efficiency of both the active and passive shields on minimizing the resulting background level on LED and HED. A schematic view of the shielding design on board the DSC is shown in Figure 6.8: the plastic AC is placed externally as respects the passive layers, made of Ta plus grading. We remind that the collimator thicknesses are computed for the photons line of

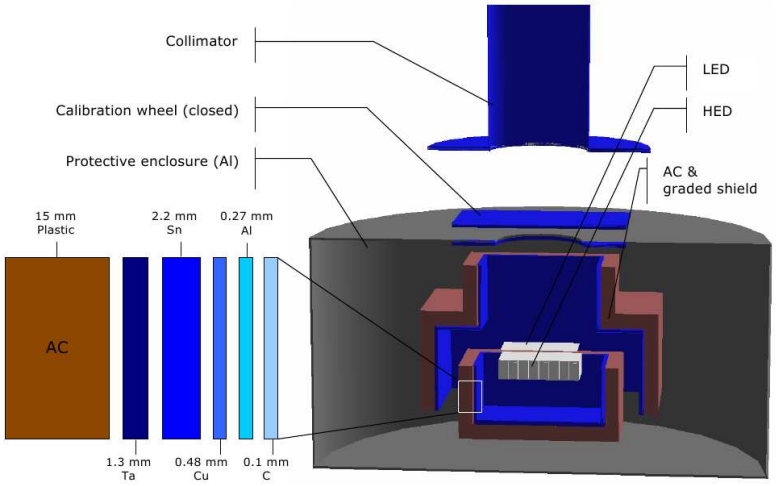

Figure 6.8: Schematized view of the active and passive shielding on board the Simbol-X DSC. Figure from Chipaux et al. (2008).

sight to the focal plane, which is higher than the projected normal, allowing a reduction of the collimator thicknesses as respects the passive structure surrounding the detectors (see Sec. 4.4.1). The background evaluation is performed for an AC threshold of 1 MeV and a maximum pattern,

i.e. the number of pixels detecting the count, of 4, following the Geant4 output analysis explained in Sec. 5.2. The LED-HED coincidence events are removed. The sources of quiescent prompt background are the CXB and GCR flux impinging from 4π (see Sec. 3.7).
The presence of the MSC, at a 20 m distance, is accounted for by the addition of a circular empty volume (stepping volume, see Sec. 5.1) with the diameter required to perfectly shield the focal plane (see Sec. 4.4.2): if a simulated particle crosses the empty volume, it is removed, since the impact of the CXB interaction with the MSC sky screen is evaluated separately in the previous section. The same approach is assumed for the NHXM background simulation.
The CXB induced background spectrum is only plotted in "AC on" mode (Figure 6.9) due to the low interaction with the active shield.

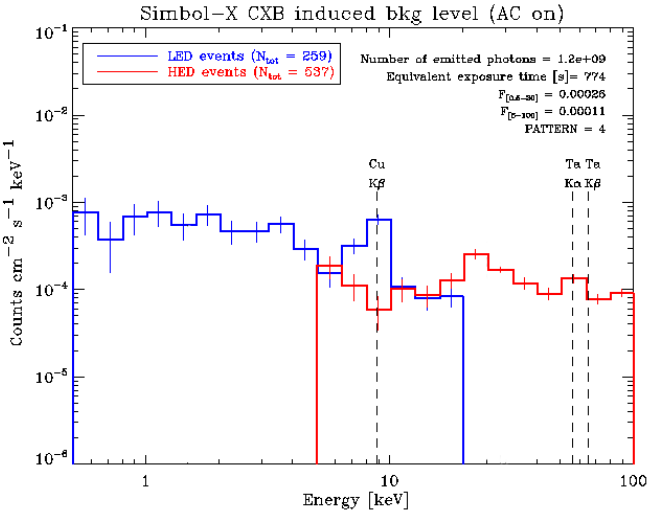

Figure 6.9: LED, blue line, and HED, red line, CXB induced background spectra in the 0.5 - 20 keV and 5 - 100 keV energy ranges respectively. The AC is switched on, i.e. the coincidence events with the active shield are removed, and the plotted counts refer to a maximum pattern of 4. The vertical dashed lines show the K fluorescence of the passive layers.

The first clear result is that the LED spectrum shows a decreasing slope: this is the effect of a space left between the collimator base and the top of the FPA which lets a small fraction of the CXB photons to leak and reach directly the LED. The HED is instead not affected because it is placed below the LED, which is able to stop the leaking photons. The fluorescence emission of the passive shielding is still visible in the background spectrum, especially the Cu Kβ line, despite the presence of the grading. A further optimization of the graded layers is required.
In Figure 6.10 the GCR induced background spectra, in "AC off" (left panel) and "AC on" (right panel), are shown. The overall behaviour is constant, the prominent Cu Kβ line disappears but the fluorescence K emission of the Cd and Te composing the HED are now visible. The statistics significance after the removal of the AC events is too low for the LED background to see any emission line feature.
The energy averaged background levels are listed in Table 6.3. The Simbol-X top level scientific

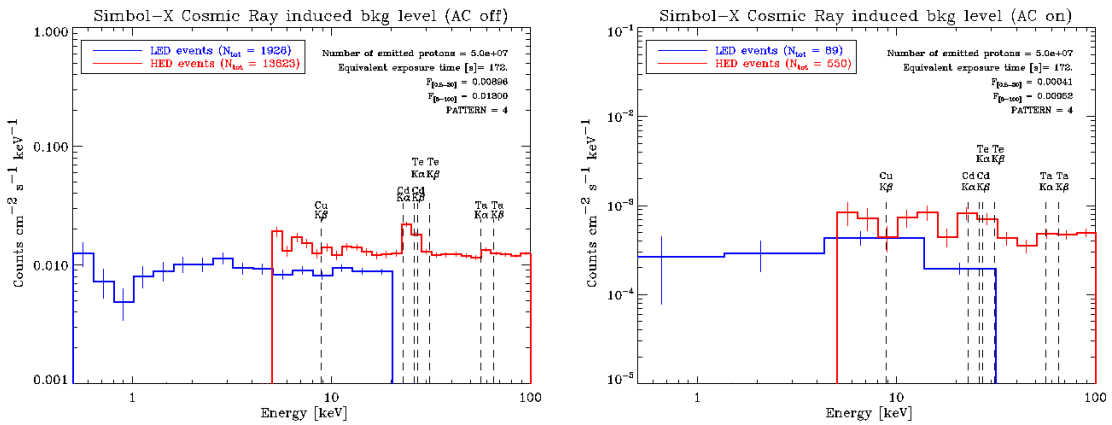

Figure 6.10: LED, blue line, and HED, red line, GCR induced background spectra in the 0.5 - 20 keV and 5 - 100 keV energy ranges respectively, in "AC off" (left panel) and "AC on" (right panel) for a pattern ≤ 4. The vertical dashed lines show the K fluorescence of the passive layers and of the HED Cd and Te materials.

SIMBOL-X BACKGROUND LEVEL

Particle	Detector	Energy range	AC off	AC on	AC rate [cts s^{-1}]
CXB	LED	0.5 - 20 keV	2.6×10^{-4}	2.6×10^{-4}	2.9
	HED	5 - 100 keV	1.1×10^{-4}	1.1×10^{-4}	
GCR	LED	0.5 - 20 keV	9.0×10^{-3}	4.1×10^{-4}	1947.9
	HED	5 - 100 keV	1.3×10^{-2}	5.2×10^{-4}	
Total	LED	0.5 - 20 keV	9.3×10^{-3}	6.7×10^{-4}	1950.8
	HED	5 - 100 keV	1.3×10^{-2}	6.3×10^{-4}	

Table 6.3: The Simbol-X LED and HED energy averaged background level in cts cm^{-2} s^{-1} keV^{-1}.

requirements set an allowed maximum background level of $\sim 2 \times 10^{-4}$ cts cm^{-2} s^{-1} keV^{-1}, in "AC on" mode, a level reached by the CXB induced background alone. Altough the AC shields more than 95% of the GCR induced counts, the residual background level is too high, and the total simulated background flux is 3 times higher than the requirement.

The analysis of the pattern on ground could reduce a fraction of the protonic background. Charged particles showers in fact usually produce counts detected by several pixels, creating a pattern configuration that differs from the focused X-rays. This kind of analysis, called "pattern recognition" is not applied here, but we can show that the Geant4 simulator confirms this pattern behaviour. In Table 6.4 the distribution of the proton induced counts in pattern is shown with and without the removal of the AC triggering. After the removal of the AC coincidence events, only counts with pattern < 2 are found, because the AC efficiency is higher for the most energetic protons, which usually cause energy deposits in more than one pixel due to the elevated number of secondary particles.

SIMBOL-X PATTERN ANALYSIS

N. pattern	LED		HED	
	AC off	AC on	AC off	AC on
1	3104	112	14365	552
2	201	7	1506	33
3	7	0	85	0
4	1	0	3	0

Table 6.4: The proton induced background counts pattern distribution for LED and HED.

Simbol-X dead time

The LED signals are readed frame by frame as consequent snapshots of the observed source, with a finite read-out time for each frame. If a coincidence event between the AC and the LED happens, the full frame, collecting both source and background events, is removed and it translates into dead time. The AC count rate does not instead affect the HED dead time, with an indipendent read-out mode for each CdTe cristal. The dead time computation as a function of the AC count rate is performed for a full frame total read-out time of 256 μs on the basis of the baseline Simbol-X LED design (4 μs per row for 64 rows, Bombelli et al. (2008)).

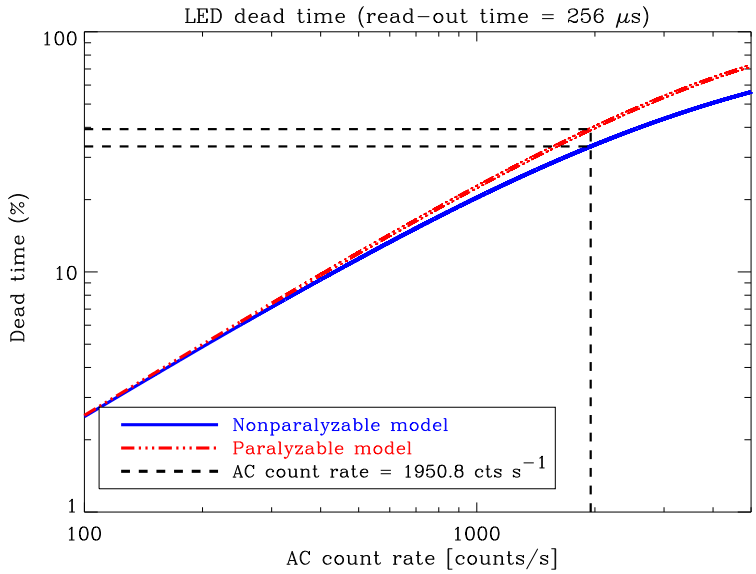

Figure 6.11: Percentage of dead time affecting the LED for a read-out time of 256 μs as a function on the AC count rate. The dead time is calculated following a simple, nonparalyzable (continuous line) and a paralyzable response model (continuous–dotted line).

The dead time losses fraction is derivated for both a nonparalyzable, simple response model (DT_{NP}) and a paralyzable model (DT_P), respectively the blue and red lines of Figure 6.11, as given by:

$$DT_{NP} = 1 - \frac{1}{1 + n \cdot \tau} \quad (6.4)$$

$$DT_P = 1 - e^{-n \cdot \tau}, \quad (6.5)$$

where n is the AC count rate and τ the read out time (see e.g. Knoll (2000) for a review).
The dashed line refers to the resulting total AC count rate of 1950.8 cts s^{-1}, translating into an observation time loss of 35 - 40% for an AC threshold of 1 MeV.
In order to reduce the GCR induced background level, the AC threshold could be decreased, increasing the AC rate. However a dead time higher than 40% in unacceptable. It is clear that the shielding design must be optimized to decrease the AC rate. A solution could be represented by placing the AC inside the passive shielding. The effect of this configuration is explored in Chapter 7.

6.2 NHXM background

For the preliminary evaluation of the NHXM background level, a simplified Geant4 mass model of one of the three cameras hosting the X-ray imaging spectrometers has been developed (Figure 6.12), composed by the hybrid focalplane, not pixellated, the active and passive shielding surrounding the detectors and the passive collimator. The aim is evaluating the background level for a set of configurations with increased complexity in the shielding and detectors design, in order to easily characterize the major sources of background and drive the optimization study. The results presented here refer to the first NHXM geometry release (NHXM001).

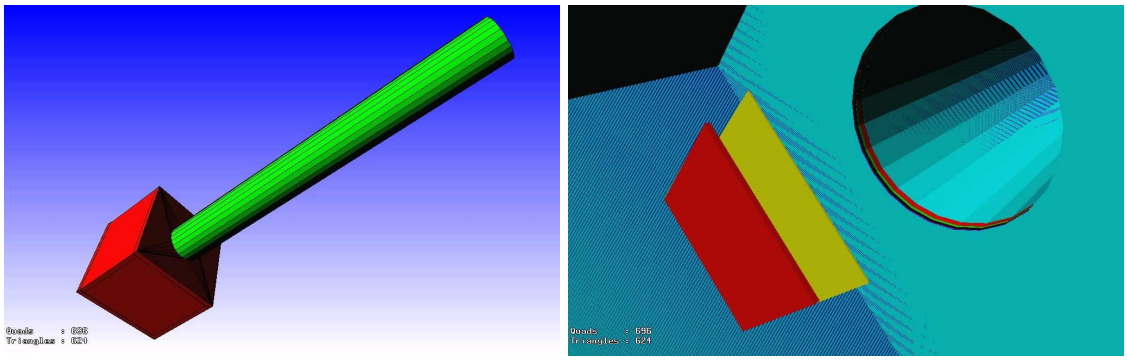

Figure 6.12: *Left panel*: The Geant4 mass model of the camera hosting the X-ray detectors. The red box surrounds the LED and HED and it is contituted by the plastic AC, placed externally, and the passive graded layers. The green structure is the passive collimator, and the whole camera is less than 1.5 m long. *Right panel*: A zoom to the LED (in yellow) and HED (in red) detectors hosted within the camera. The collimator aperture is visible in the right part of the image.

The LED and HED are simulated by single, not-pixellated volumes: a $57 \times 57 \times 0.45$ mm thick Silicon (Si) layer, the LED, and a $5 \times 5 \times 1.5$ mm thick Cadmium Telluride (CdTe) layer, the HED, separated by a 1.2 cm distance. The distance between the detectors and the shielding walls on top and bottom sides is 10 cm, so that the surrounding box height is 21.2 cm, with a side of 25 cm. The collimator height, starting from the box surface, is 90 cm, as already reported in Sec. 4.5. Since the detectors are not divided in pixels, the pattern analysis is not evaluated here (all events with pattern = 1).
The selected materials and thicknesses for the graded passive shielding are based on the design

of the Simbol-X mission, with the only difference that the collimator is not optimized for the projected stopping power. The main absorber is a 1.5 mm thick Tantalum layer, ensuring an X-ray attenuation >99% below 150 keV (see Figure 6.13), while the selected graded layers, from higher Z to lower Z, are Tin, Copper, Aluminum and Carbon. Each grading layer thickness is calculated for an attenuation efficiency > 99.99% at the fluorescence energy of the previous layer. The plastic active shielding is made of Polystyrene, with a thickness of 3.8 mm. A summary of the

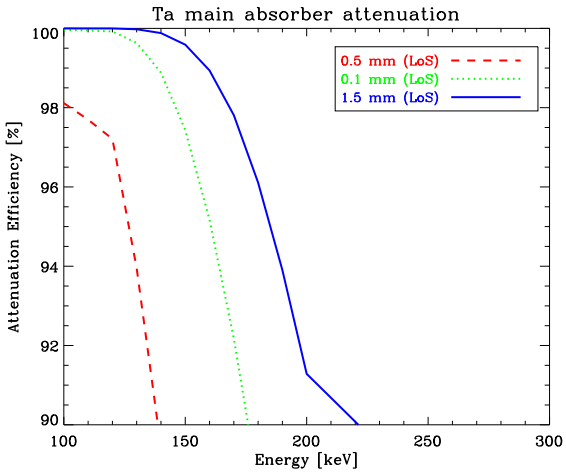

Figure 6.13: Attenuation efficiency of a Tantalum main absorber, based on the X-ray attenuation coefficients provided by the NIST database, for a Line of Sight (LoS) thickness of 1.5 mm (continuous line), 1 mm (dotted line) and 0.5 mm (dashed line).

shielding configuration and resulting mass budget is listed in Table 6.5.

NHXM001 SHIELDING DESIGN

	AC	Ta	Sn	Cu	Al	C	Total
Thickness [mm]	3.8	1.5	2.2	0.48	0.27	0.1	8.35
Collimator mass [kg]	/	8.24	5.31	1.42	0.24	0.06	15.26
Box mass [kg]	1.22	7.55	4.86	1.30	0.22	0.05	15.20

Table 6.5: Composition and mass budget of the NHXM preliminary shielding design.

The passive shielding is surrounded by the anticoincidence system: if an ideal, non interacting particle is emitted to the box, it would respectively cross the active shield, the passive walls and finally it would arrive to the focal plane.

6.2.1 Background results

A comprehensive analysis of the total background in LEO will be presented in the next Chapter. Here we show, as a comparison with the Simbol-X simulation results, the background induced by

the CXB and the proton flux. Contrary to the Simbol-X case, the latter is given by the sum of the GCR flux, with a low energy cut off below $\sim$ 10 GeV, and the albedo secondary protons. It is interesting, in this context, to analyze the effect of the low energy protons on the background level. The AC threshold is 1 MeV, as for the Simbol-X background analysis.
The CXB induced background (Figure 6.14) on the LED does not show any decrescent slope, and the background level is lower than the HED, because there is no CXB leaking in the NHXM shielding. The background decrease is more than 50% as respects the Simbol-X case, a reduction

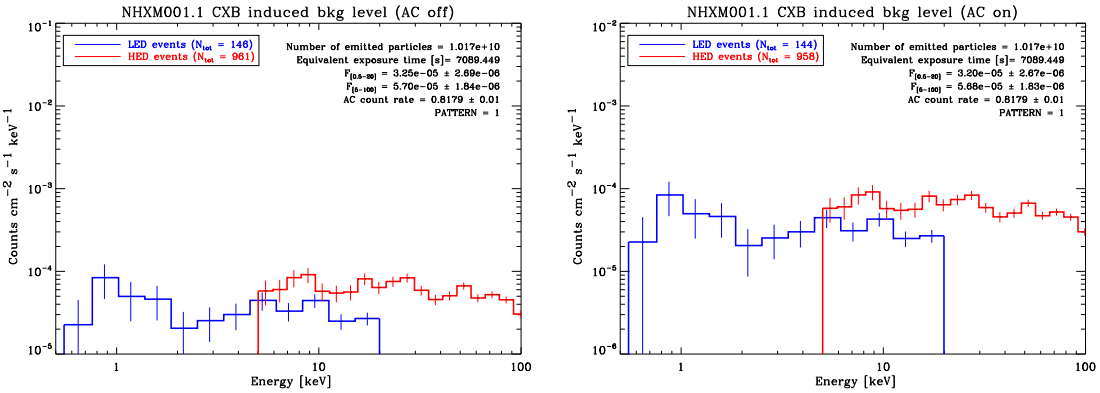

Figure 6.14: The NHXM LED (blue line) and HED (red line) simulated background spectra induced by the CXB flux, in "AC off" (left panel) and "AC on" (right panel) mode.

that can not be accounted for only by the Earth's atmosphere shielding ($\sim$ 30%). One reason is probably the simplified NHXM geometry, which does not include the additional spacecraft material, while in the Simbol-X DSC geometry a 1 m height Al cylinder has been added to simulate the platform additional mass. However we would like to point out that in the NHXM case the detectors are hosted by the extendable structure, so that below the HED there is no satellite, contrary to the Simbol-X DSC, and the platform mass budget is lower.
The most important result is **the proton induced bakground and AC count rate, decreasing of about an order of magnitude as respects Simbol-X** (Figure 6.15)
The simulation actually confirms the proton stopping power energy distribution (see Figure. 4.2), which predicts a higher energy loss for proton at lower energies, so that the most energetic protons can be more penetrating through the shields, sometimes without even triggering the AC. As a result, the higher flux of low energy albedo protons is less damaging as respects the GCRs unshielded by the geomagnetic interaction.
It is also interesting the HED background descendent behaviour, that could be visible in the NHXM spectrum thanks to the higher statistics significancy of the simulation. Finally, we do not see any fluorescence line: the grading, for this preliminary simulation, is well configured. The lack of Cd and Te K lines is instead due to LED and HED designed as single, not-pixellated volumes.
The summary of the background results, for the incoming CXB and protons flux, is listed in Table 6.6.

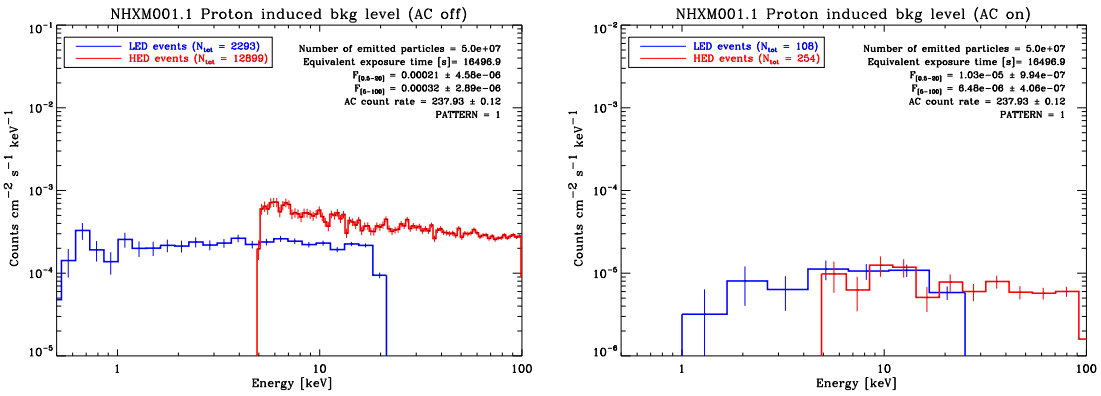

Figure 6.15: The NHXM LED (blue line) and HED (red line) simulated background spectra induced by the proton flux, in "AC off" (left panel) and "AC on" (right panel) mode.

NHXM BACKGROUND LEVEL

Particle	Detector	Energy range	AC off	AC on	AC rate [cts s^{-1}]
CXB	LED	0.5 - 20 keV	3.3×10^{-5}	3.2×10^{-5}	0.8
	HED	5 - 100 keV	5.7×10^{-5}	5.7×10^{-5}	
Proton	LED	0.5 - 20 keV	2.2×10^{-4}	1.0×10^{-5}	239.7
	HED	5 - 100 keV	3.3×10^{-4}	0.7×10^{-5}	
Total	LED	0.5 - 20 keV	2.5×10^{-4}	4.2×10^{-5}	240.5
	HED	5 - 100 keV	3.9×10^{-4}	6.4×10^{-5}	

Table 6.6: The NHXM LED and HED energy averaged background level in cts cm^{-2} s^{-1} keV^{-1}.

6.2.2 Characterization of the shielding efficiency

In order to evaluate the impact of different DSC volumes on the simulated count rate, it is possible, as first, simple analysis, to evaluate which external volume has been crossed by the primary emissed particle before the production of the detected counts. It does not mean that the secondaries are produced by that particular volume, but it allows to easily extract some important considerations on the shielding efficiency. Table 6.7 lists the external volumes of the camera assembly and the related fraction of background counts generated by a first interaction with the external volume.
After the removal of the AC coincidence counts, more than 85% of the background counts is generated by protons directed to the collimator, which is composed only by passive material. Secondary showers redirect a high flux of particles to the focal plane without crossing the active shield. Altough a more accurate analysis of this effect is needed, we can affirm that **the use of an active collimator could reduce the charged particles induced background**.

6.3 Soft protons induced background

A magnetic diverter for charged particles is a device composed by a set of magnets, usually placed along the optics spider arms (detector side) to avoid vignetting, that are able to deflect, by means

NHXM SHIELDING EFFICIENCY

Volume	LED		HED	
	AC off	AC on	AC off	AC on
Collimator external layer	13.1%	**92.6%**	10.9%	**88.2%**
Collimator internal layer	0.2%	1.9%	0.1%	1.2%
AC bottom panel	13.9%	0%	20.1%	2.0%
AC top panel	13.2%	0%	11.7%	0.8%
AC lateral panels	**59.6%**	5.5%	**57.2%**	7.8%

Table 6.7: The fraction of proton induced background counts generated by a first interaction with the listed external volumes.

of the resulting tangential magnetic field, both protons and electrons, with opposite directions (see e.g. Spiga et al. (2008)). The main issue for the development of such a device is that the proton is ~ 2000 times heavier than the electron, so that if we take into account the curvature radius ρ of a charged particle in a magnetic field:

$$\rho = \frac{1}{\mathrm{B}}\sqrt{\frac{2\,\mathrm{E\,m}}{\mathrm{e}}}\,, \tag{6.6}$$

where E, m and e refer to the particle energy, mass and charge respectively, protons require a magnetic field strength B$\sim$ 40 times higher respect to electrons to achieve the same curvature radius. In Turner (2006) a deviation angle of 3.5° is analytically computed to deflect protons out of a 14' FOV, similar to the Simbol-X case, requiring a magnetic strength B per magnetic depth l of ~ 1700 Gauss cm.
In the feasibility study of a proton diverter, the accurate knowledge of the angular, energy and spatial distribution of the protons exiting the optics is required, in order to estimate the strength of the diverter, the residual proton flux to the focal plane and the possible production of secondary background events due to the deflected proton interaction with other parts of the spacecraft. This kind of analysis needs:

1. the model of the proton flux entering the field of view;
2. the physics processes producing the proton reflection;
3. a Monte Carlo simulator able to reproduce the particle transport, the mirror module and detectors design.

The first two points are still matter of debate. A detailed Geant4 simulation of the XMM-Newton proton scattering has been developed by Nartallo (2001), based on the multiple scattering process, followed by an update (Lei et al. 2004) where also the Firsov scattering is taken into account, increasing the proton efficiency. Both simulations use as input both monochromatic beams and

the Equator-S proton spectrum (see Sec. 3.5). Despite the important result of proving the ability of the protons to be funnelled to the focal plane, a comparison between the observed and the simulated soft proton spectrum is still missing to validate the physics process in play and the reliability of the input proton flux, altough their results are consistent, within the uncertainty, with laboratory tests (Rasmussen et al. 1999).
Here we use the BoGEMMS architecture to develop a preliminary simulation of an XMM-Newton soft proton spectrum, comparing it with real data, using the work of Nartallo (2001) as reference. In the last section, some results on the expected Simbol-X proton scattering efficiency are presented.

6.3.1 Soft protons funnelling

Three physics processes have been proposed so far to describe the proton scattering (see e.g. Spiga et al. (2008)):

- In the multiple Rutherford scattering, the first process proposed to explain the reflection, protons interact with the electric field of the nuclei and lose part of their energy. Consecutive (multiple) scatterings allow the protons to be deflected to the focal plane, with a final energy and angular spread depending on the number of scatterings, the incident proton energy and incident angle. The simulations performed with the TRIM code (Kolodziejczak et al. 2000) and the preliminary Geant4 implementation (Nartallo 2002) for Chandra and XMM-Newton respectively are based on the multiple scattering process.

- As firstly noted by Dichter & Woolf (2003), the multiple scattering does not correctly reproduce the proton scattering for low incident angles ($< 1°$), where the proton does not collide with the layer's nuclei but instead interact with the electron plasma cloud outside the surface. From 30 to 710 keV the most probable energy loss is $\sim$3 keV, contrary to the broad distribution of energy losses expected from the multiple scattering. The angular distribution is more peaked, and it is described by the Firsov scattering law:

$$\mathrm{N}(\psi,\theta) = \frac{3}{2\pi\psi}\frac{(\psi\theta)^{3/2}}{\psi^3+\theta^3}\,, \tag{6.7}$$

  where ψ and θ are the incident and scattering angles respectively. It is clear that both the energy and scattering angle of the protons are weakly dependent on the initial proton energy and scattering material. The Firsov scattering, for gracing incident angles, increases the proton funnelling efficiency, because it results in a much more collimated proton beam, while the lower energy loss decreases the minimum proton energy required to cause a background event. With the addition of the Firsov scattering in the Geant4 simulation (Lei et al. 2004), the number of protons reaching the focal plane is 5 times higher.

- In Aschenbach (2007) a totally different model is proposed, where the proton funnelling is described as the reflection of a de Broglie wave on the internal potential of the layer, resulting in an efficient reflection without energy losses and angular spread, as for X-rays. The angular dispersion is accounted for by Spiga et al. (2008) as the effect of the mirror surface roughness.

The Geant4 Firsov scattering code implemented by Lei et al. (2004) has been adapted to the Geant4 9.1 release, and used in combination to the multiple scattering for the XMM-Newton simulation. In Santin et al. (2009) the code has also been used for the evaluation of the protons and electrons scattering through the IXO X-ray optics.
As first preliminary test, a beam of 500 keV proton is emitted towards a slab composed by a 1 mm thick Nickel (Ni) coated by a 50 nm Gold (Au) layer, as the XMM X-ray optics, for two incident angles (as respects the slab surface or the telescope axis): 0.2° and 3°. In Figure 6.16 the energy loss (top panel) and scattering angle (bottom panel) probability distribution is plotted with and without the addition of the Firsov scattering. The latter being activated only for incident angles lower than 1°. For an incident angle of 3°, both cases give the same result, since the Firsov

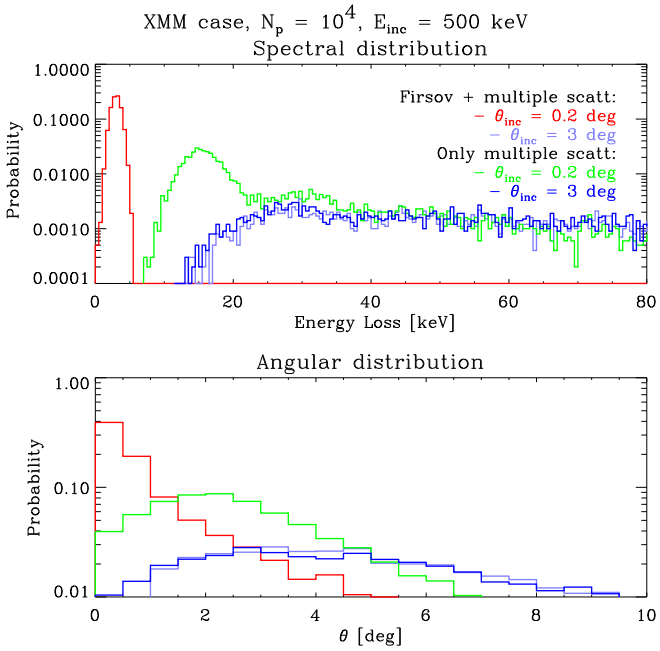

Figure 6.16: Probability distribution of the energy loss (top panel) and angular distribution (bottom panel), as respects the telescope axis, of 500 keV protons after the interaction with an XMM mirror shell. The red and light blue lines refer to the activation of the multiple and Firsov scattering for an incident angle, as respects the telescope axis, of 0.2° and 3°, while the green and blue lines refer to the only multiple scattering, for the same incident angles as the Firsov case.

scattering is not effective: the proton energy loss is equally distributed above 20 keV, and a broad scattering angular distribution is obtained up to 10°. For an incident angle of 0.2°, the multiple scattering induced losses are peaked at $\sim$ 15 keV but still with a broad tail, while the exiting proton distribution is more collimated. However this results is still far from what obtained through the Firsov scattering, inducing a lower energy loss ($\sim$ 3 keV) and a gracing proton deflection. The same results have been published by Lei et al. (2004): the ability to reproduce their work allows

us to validate the present XMM-Newton simulation.

6.3.2 Interaction with the XMM-Newton optics

A simplified model of the XMM-Newton mirror module has been developed (Figure 6.17), based on the XrayTel example provided by the Geant4 user support team. It is composed of 58 shells, made

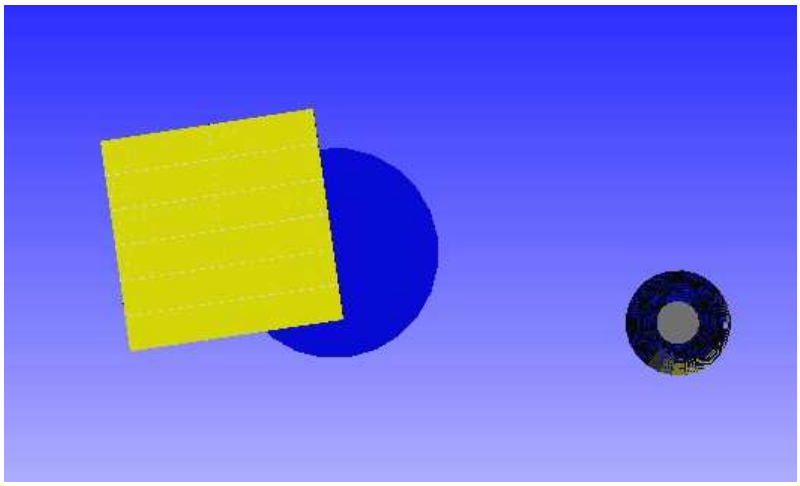

Figure 6.17: The XMM-Newton simplified Geant4 model: the mirror module is at right, the EPIC/pn is visualized in yellow and the circular blue structure in front of the detector is the thick filter.

of a 1 mm thick Ni layer covered by a 50 nm Au coating, divided in four sections to approximate the Wolter–1 design. The total length is 60 cm, covering an annular region from $\sim$ 15 to $\sim$ 35 cm. The focal plane is based on the EPIC/pn design (Strueder et al. 2000): 6×2 modules, of dimension 30×9.6 mm, divided into 200×64 squared pixels, with a side of 150 μm and a thickness of 0.3 mm. The modules are centrally divided by a gap of 41 μm, and spaced from each other by 198 μm.
The thick optical blocking filter[2] is placed on top of the detector, with composition and thickness listed in Table 6.8 and taken from Tiengo (2007). The presence of the filter reduces the proton

The XMM-Newton Thick Filter

Layer	Composition	Thickness [μm]
1	Polypropylene (PP)	0.33
2	Aluminum (Al)	0.11
3	Tin (Sn)	0.045

Table 6.8: The composition and thickness of the thick optical blocking filter. The layer number starts from the closest position to the detector.

[2]A thin, medium and thick filter is provided for the EPIC CCDs to block the IR, visible and UV light of the target and avoid contamination to the X-ray observation.

energy, and it must be taken into account when comparing the results to a real observation.
The Equator-S input proton spectrum, in the 30 - 500 keV energy range, as described in Sec. 3.5 is emitted from an annular planar source placed on the top of the X-ray optics, with the same shape of the mirror, within an angle of $\pm 2^\circ$ to increase the simulation statistics.
The first result is that we are able to reproduce the proton vignetting, a property of the soft proton flares (see e.g. Kuntz & Snowden (2008)): the radial distribution of the detected protons is plotted in Figure 6.18, for all the deposited energies (left panel) and with the selection of the counts below 10 keV (right panel). The vignetting is similar to what obtained by Strueder et al. (2000) in an EPIC/pn soft proton flare, with a $\sim 50\%$ decrease from the inner to the outer region.
In Figure 6.19 the count rate image of the simulated soft proton flare is shown, with the lighter

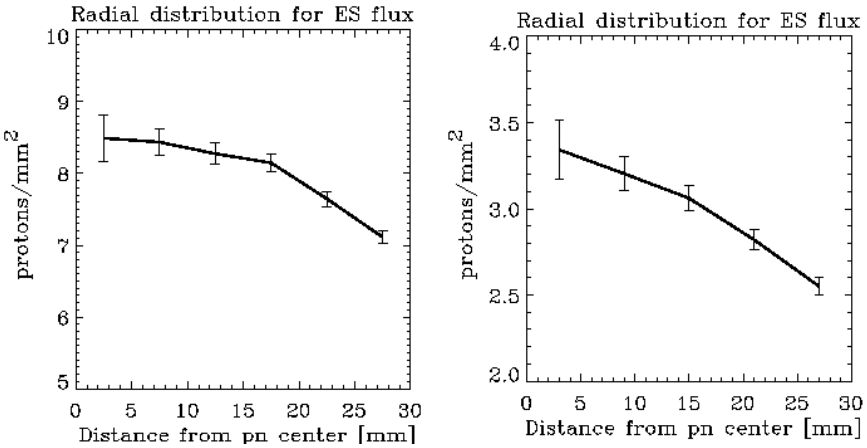

Figure 6.18: The radial distribution of the detected protons, in prot. mm^{-2}, for radial bins of 5 mm. The left panel refers to total proton flux, while the right panels shows the protons generating a count below 10 keV.

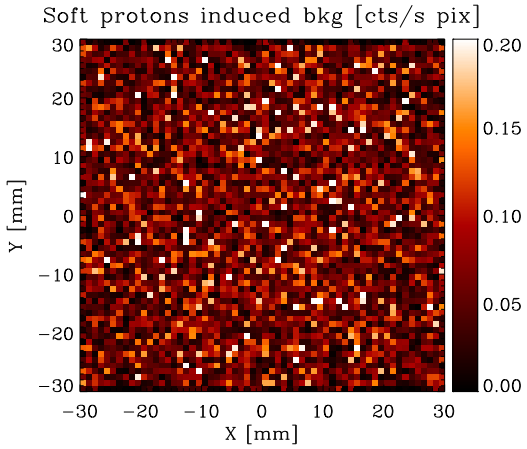

Figure 6.19: The image of the simulated soft proton flare. The counts rate is plotted in unit of cts s^{-1} per pixel.

pixels referring to the higher count rate level. The maximum rate (white pixels) is ~ 0.2 cts s^{-1} per pixel, but in Kendziorra et al. (2000) a proton flux < 0.2 prot. cm^{-2} s^{-1} in the 100 - 200 keV energy range is reported from an EPIC/pn observation, which is clearly higher than the simulated rate.

A long exposure observation of a soft proton flare detected by the EPIC/pn and EPIC/MOS instruments with the use of the thick filter has been kindly provided by A. Tiengo (INAF/IASF Milano Institute). Their spectra is compared to the simulation in Figure 6.20, in the left and right panel respectively. Altough the focal plane is based on the EPIC/pn design, since a simplified Geant4 model is used it is also interesting to compare the MOS spectrum.

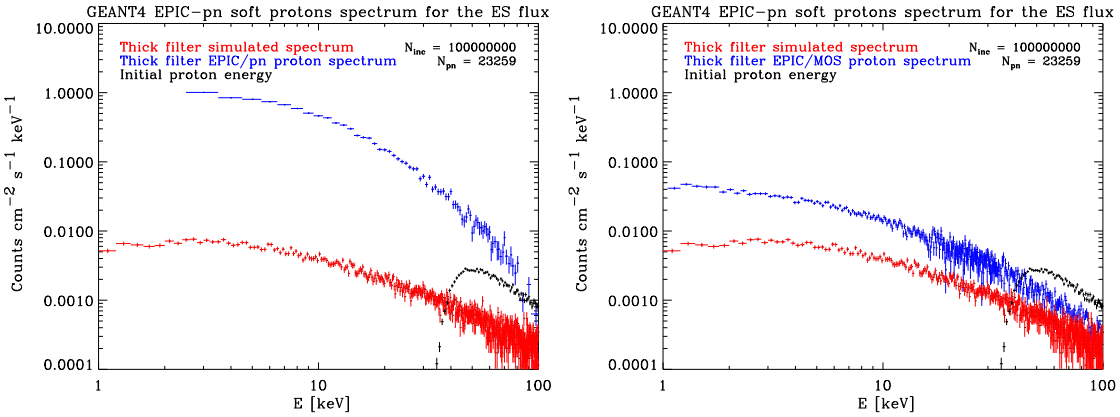

Figure 6.20: The simulated proton induced background spectrum (in red) compared to the observation (in blue) of the EPIC/pn (left panel) and EPIC/MOS (right panel). The intial energy distribution of the protons generating the counts is shown in black.

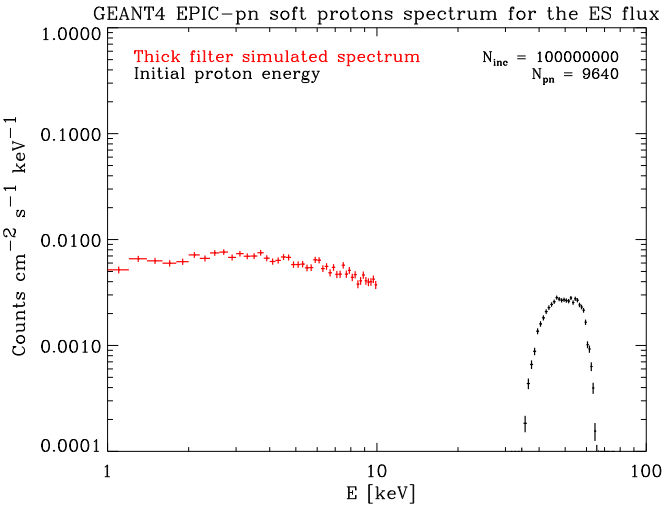

Figure 6.21: The simulated proton induced background spectrum below 10 keV, and the related energy distribution

The red counts refer to the simulated proton induced background spectrum, reaching a maximum level of 0.01 cts cm^{-1} s^{-1} keV^{-1}, which results to be ~ 5 times lower than the MOS detection and 100 times lower than the pn one (in blue). The soft proton flare simulation underestimates the real case. However it must be noted that the soft proton flares are extremely variable, so that one single observation is not representive of the general behaviour. The solution would be the use of a time averaged input proton flux, and an average proton spectrum obtained by folding together the soft proton flares detected along several orbits. The present results must be intended as a preliminary step in the comprehension of the soft proton scattering by the X-ray optics.
It is interesting to note the energy distribution of the primary protons that cause the background counts, falling off below 30 keV due to the absorption of the thick filter. It is also possible to select the protons that deposit an amount of energy below 10 keV, the real source of background during an astrophysical observation. The result is plotted in Figure 6.21: the major contribution to the background comes from protons peaked at 50 keV, contrary to the source of the CTE damage identified by the Chandra team in the 100 - 200 keV energy protons.

6.3.3 Interaction with the Simbol-X optics

Only a preliminary test, using a monochromatic 500 keV proton beam, has been runned for the Simbol-X case, without the addition of the Firson scattering. Respect to XMM-Newton, the Simbol-X mirror module is composed by 100 shells, coated by a graded Pt/C multilayer. As for the previous simulation, the protons are generated from an annular planar source above the optics, this time within an angle of $\pm 5°$. The energy and angular distribution of the exiting protons is shown

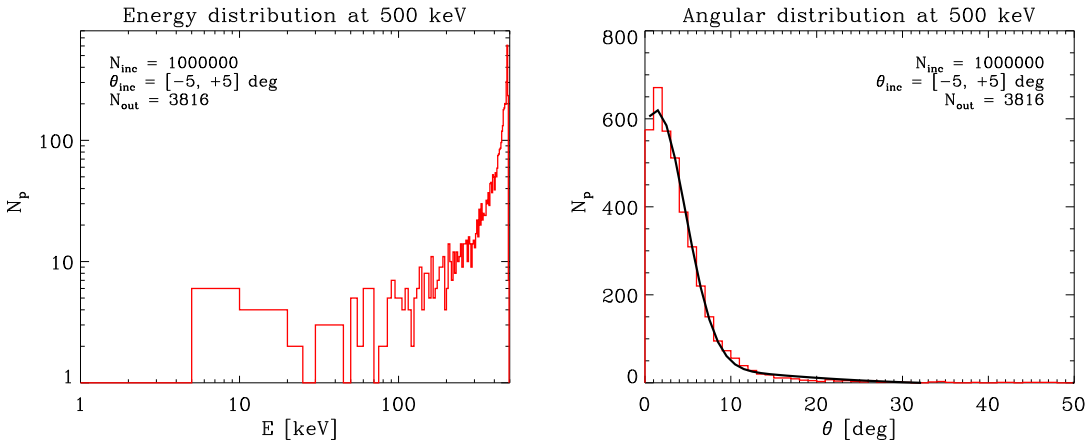

Figure 6.22: The energy (left panel) and angular (right panel) distribution of the protons exiting the Simbol-X optics. Only the multiple scattering is applied.

in Figure 6.22, left and right panels respectively. The angular distribution can be approximatively described by a gaussian profile with $\sigma = 2.8$. We remind the reader that Turner (2006) reports a 5σ angular spread of 3.5°, i.e. a much more collimated beam. The broad distribution of the proton energy loss, which characterizes the multiple scattering, is also obtained.

Chapter 7

The background in LEO: general results

In order to fully characterize the LEO radiation effects on the shielding and the detection plane, we developed an extremely simplified, box shaped shielding system surrounding a monolithic LED and HED assembly based on the NHXM focal plane design. Given the simplified geometry, the results presented here are not the expected NHXM background count rate but they represent a first fundamental step to select the major sources of background and, consequently, to optimize the shielding design.
Respect to the Simbol-X and NHXM shielding geometry, there is no collimator and no aperture to the sky: the focal plane is completely shielded. The AC count rate strongly affects the observation dead time for a frame-by-frame detection read out. The use of a simplified Geant4 model of the NHXM camera allows to easily explore the dependence of the background and active shield count rate as a function of the shielding design. The baseline shielding concept, already employed in the NHXM001 Geant4 geometry release, is composed by a plastic scintillator surrounding a graded passive shielding. In the present Chapter, the background simulation is performed for three shielding configurations:

- Active shielding (plastic) surrounding the passive shielding (the baseline), defined as Case A;
- Active shielding (plastic) enclosed by the passive shielding, defined as Case B;
- Active shielding (inorganic) enclosed by the passive shielding, defined as Case C.

The materials composing the plastic and inorganic active shielding are Polystyrene and NaI respectively. The simulation results are compared with the aim of selecting the active shield design that ensures the best response in terms of background and active shield count rate, given the space radiation environment of a Low Earth Orbit (LEO), low inclination ($< 5°$) mission.
The Geant4 simulator architecture allows to easily analyze not only the resulting background spectrum but also the energy distribution and class of the particles interacting with the detectors.

7.0.4 The simulation set–up

The LEO space radiation environment acting as source of prompt background is fully explained in Chapter 3. We show here again the summary plot (Figure 7.1), to better refer our results.

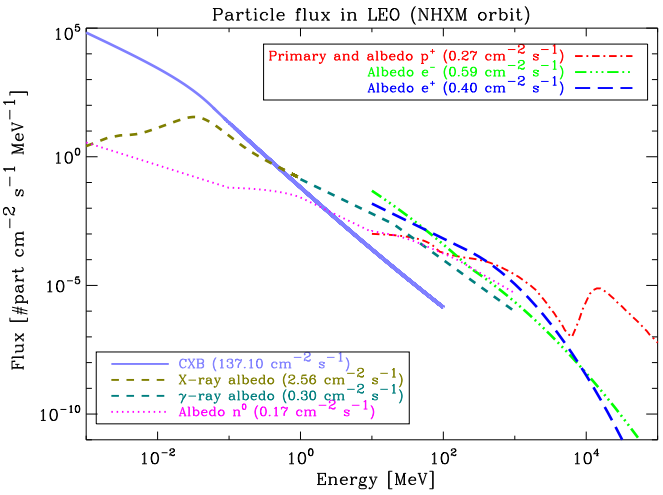

Figure 7.1: The modelled space radiation environment in LEO for the NHXM orbit.

A cut view of the camera Geant4 mass model is shown in Figure 7.2, with the green, blue and red lines being the trajectories of the interacting photons, protons and electrons respectively. A full

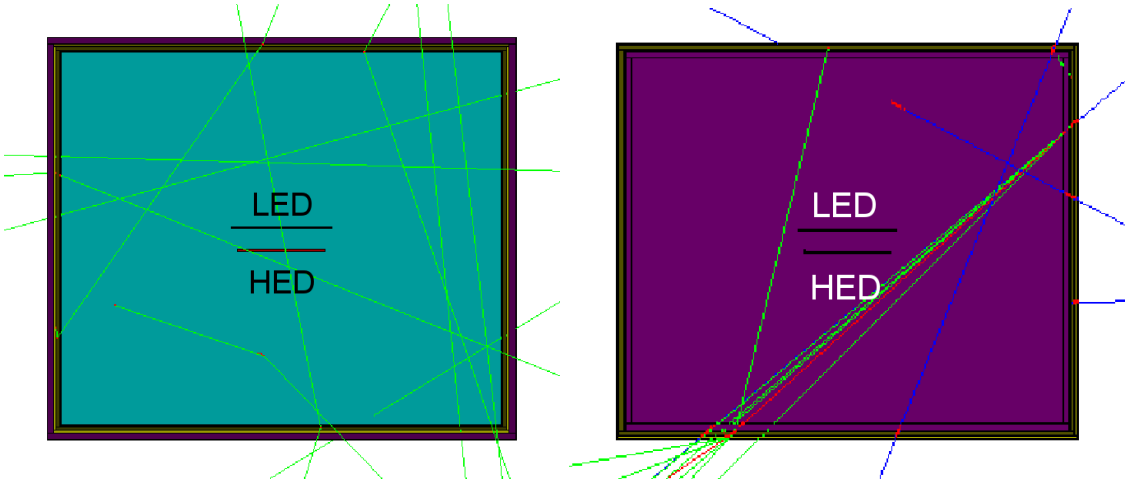

Figure 7.2: The box Geant4 mass model as seef from the side (the mirror module is at the top). The left and right figures refer to an external and internal AC configuration respectively.

description of the composition and thicknesses can be found in Sec. 6.2. The LED and HED are seen from the side (the mirror module would be placed at the top of the figure). The shielding system is a box completely surrounding the focal plane, leaving no aperture flux to the detection plane, with a height of 21.2 cm and a side of 25 cm.

7.1 Case A background evaluation

In order to achieve the outstanding NHXM sensitivity, the required maximum total background level, given by the sum of instrumental (due to prompt and delayed particle interactions with the spacecraft material) and field of view induced signals, i.e. due to particles entering the mirror modules (e.g. stray-light), is $\sim 1 \times 10^{-3}$ cts cm^{-2} s^{-1} keV^{-1} in the LED 0.5 - 20 keV energy range, including the eventes triggered by the AC, and $\sim 2 \times 10^{-4}$ cts cm^{-2} s^{-1} keV^{-1} in the HED 5 - 100 keV energy range, achieved by means of the removal of the AC counts. A detailed analysis is presented for the background level resulting from an AC threshold of 200 keV, altough the dependance of the background and AC rate on the AC threshold, in the range 200 keV - 1 MeV is also evaluated.
The simulated count rate in cts cm^{-2} s^{-1} keV^{-1} is normalized for the LED and HED area and divided for the detection energy range (defined in Sec. 5.2). The results presented here refer to the

AC (plastic) + Passive Case A		Background count rate [cts cm^{-2} s^{-1} keV^{-1}]			
Input	Det.	AC off	AC on	Trig. counts	AC [cts s^{-1}]
CXB	LED	$(1.48 \pm 0.11) \times 10^{-5}$	$(1.43 \pm 0.11) \times 10^{-5}$	3.1%	6.4
	HED	$(5.09 \pm 0.10) \times 10^{-5}$	$(5.00 \pm 0.10) \times 10^{-5}$	1.8%	
Protons	LED	$(1.53 \pm 0.02) \times 10^{-4}$	$(0.30 \pm 0.10) \times 10^{-6}$	99.8%	185.4
	HED	$(2.36 \pm 0.01) \times 10^{-4}$	$(0.33 \pm 0.05) \times 10^{-6}$	99.9%	
Albedo electrons	LED	$(1.81 \pm 0.04) \times 10^{-4}$	0	100%	411.1
	HED	$(4.21 \pm 0.03) \times 10^{-4}$	0	100%	
Albedo positrons	LED	$(2.10 \pm 0.03) \times 10^{-4}$	$(0.18 \pm 0.09) \times 10^{-6}$	99.9%	273.2
	HED	$(4.70 \pm 0.02) \times 10^{-4}$	$(0.45 \pm 0.07) \times 10^{-6}$	99.9%	
X-ray albedo	LED	$(1.14 \pm 0.03) \times 10^{-5}$	$(1.06 \pm 0.03) \times 10^{-5}$	6.9%	5.4
	HED	$(3.78 \pm 0.02) \times 10^{-5}$	$(3.53 \pm 0.02) \times 10^{-5}$	6.6%	
γ-ray albedo	LED	$(2.65 \pm 0.04) \times 10^{-5}$	$(1.47 \pm 0.03) \times 10^{-5}$	44.5%	24.3
	HED	$(6.20 \pm 0.03) \times 10^{-5}$	$(3.55 \pm 0.03) \times 10^{-5}$	42.8%	
Albedo neutrons	LED	$(1.89 \pm 0.06) \times 10^{-5}$	$(1.52 \pm 0.06) \times 10^{-5}$	19.9%	17.7
	HED	$(1.78 \pm 0.03) \times 10^{-5}$	$(1.33 \pm 0.03) \times 10^{-5}$	25.5%	
Total	LED	$(6.14 \pm 0.11) \times 10^{-4}$	$(5.53 \pm 0.24) \times 10^{-5}$	/	923.4
	HED	$(1.30 \pm 0.01) \times 10^{-3}$	$(1.35 \pm 0.02) \times 10^{-4}$		

Table 7.1: Background count rate, in cts cm^{-2} s^{-1} keV^{-1}, for the Case A configuration. The last two columns show the fraction of LED and HED counts triggered by the AC and the total AC count rate (in cts s^{-1}). The AC threshold is 200 keV.

background level obtained after the removal of the LED–HED coincidence counts, since they would be treated as a separate class of events in a real observation in space. In the present simulations, they affect the 5%-9% and the 1%-2% of the total number of counts for respectively the LED and the HED. A summary of the LED and HED background level induced by each class of particles is presented in Table 7.1 in "AC off" and "AC on" mode, i.e. with and without the triggered events by the AC. The AC efficiency in decreasing the background count rate is presented as the percentage of events anticoincided. The total AC count rate, shown in the last column, defines,

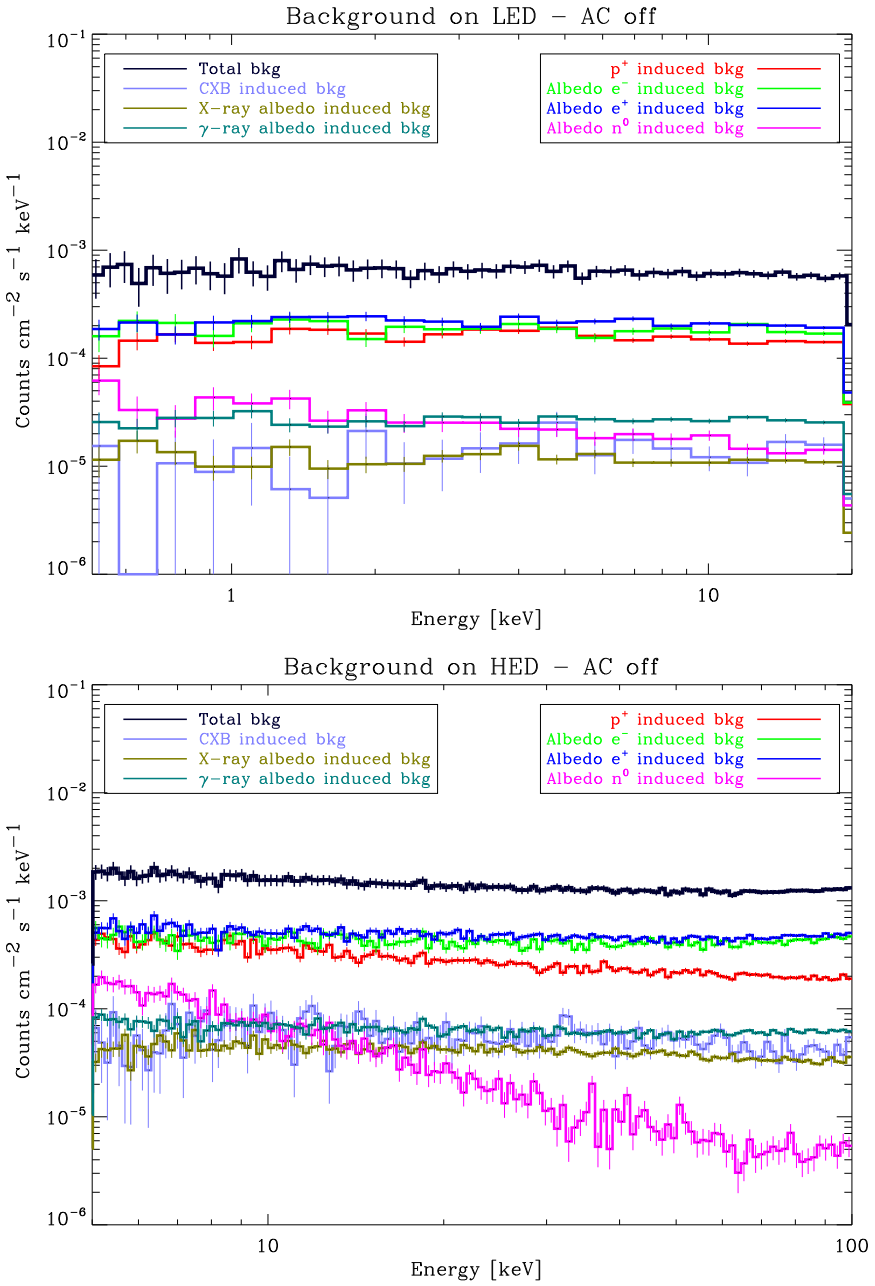

Figure 7.3: LED (top panel) and HED (bottom panel) background spectra for the Case A configuration in "AC off" mode for each class of emitted particles. The black line refers to the total background flux. The AC threshold is 200 keV.

for a given read-out mode and time of the detectors, the dead time affecting the observation. The errors are computed on the basis of the simulation Poisson fluctuations, i.e. if N is the number of detected counts, the error is given by $\sqrt{N}$.

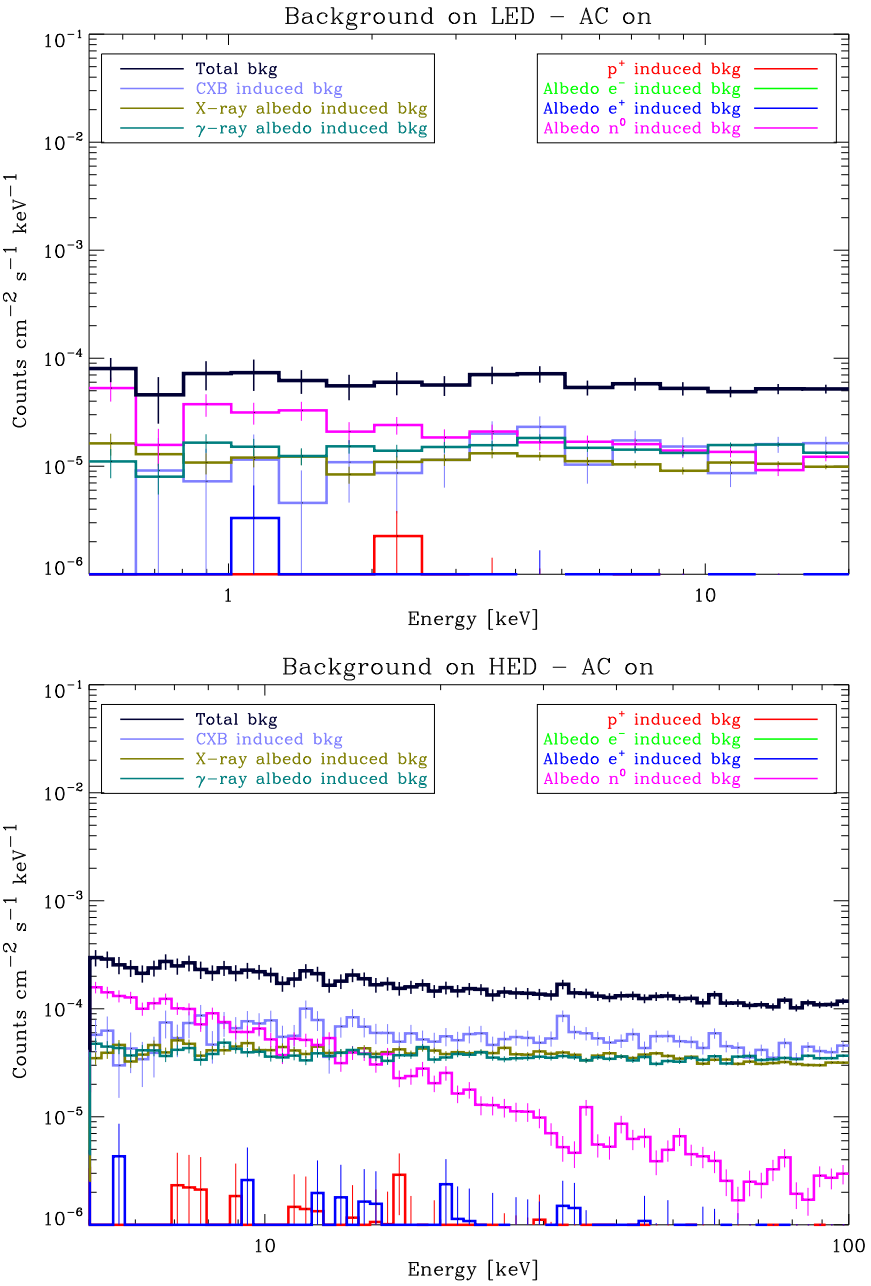

Figure 7.4: LED (top panel) and HED (bottom panel) background spectra in "AC on" mode for each class of emitted particles. The black line refers to the total background flux. The AC threshold is 200 keV.

The HED count rate is a factor 2-3 higher than the LED detected background. This is justified by the HED thickness, about 3 times higher than the LED detection layer. The only exception is the proton induced background: the HED count rate is about 50% higher in "AC off" mode, while the background levels become comparable, within the errors, in "AC on" mode. The total background

count rate, obtained by summing the contribution of each class of particles is $\sim 6 \times 10^{-4}$ and $\sim 1 \times 10^{-4}$ cts cm^{-2} s^{-1} keV^{-1} for LED (AC off) and HED (AC on) respectively. These levels are in agreement with the NHXM background requirements: altough we are using a simplified geometry, which does not account for the satellite mass budget, this result shows that **the NHXM sensitivity can be actually achieved and the top level scientific requirements satisfied**. In Figures 7.3 and 7.4 the LED and HED simulated background spectra are plotted, in "AC off" and "AC on" modes respectively. The total background level is shown by the black line. The overall background shape is approximately constant, altough the albedo neutrons induced HED background shows a power law form, keeping memory of the incident neutron flux. Without the removal of the AC events, the major source of background is represented by the charged particles (protons, electrons and positrons), accounting for $> 85\%$ of the total level for both the instruments. We remind that for the XMM-Newton EPIC background, where no active shield is applied, the quiescient Non X-ray Background is responsible for $\sim 80\%$ of the total level in the 2 - 8 keV energy range. After switching on the AC, the efficiency in removing the charged particles induced events in more than 99%, and the background is dominated by the space photonic environment, CXB and albedo X-ray/γ-ray emission, plus $\sim 80\%$ of the albedo neutrons induced events, showing the same steep behaviour. We would like to note that the zero level for the electronic background means that, for the simulated exposure time to the electron flux, all the electrons induced events are triggered by the AC. The energy resolution of the plotted spectra depends on the simulated exposure time: we are not taking into account the spectral resolution of the detectors, only the quantum efficiency. For the present simulation statistics, no significant fluorescence lines are visible, as obtained in the NHXM background spectra. We can affirm that **the applied shielding configuration efficiently attenuates the secondary emission of each layer**.

7.1.1 Background sources

After a particle is emitted, it interacts with the box material and generates a cascade of secondary particles. Evaluating which particles are, in the final interaction with the focal plane, responsible for the background counts is fundamental to foresee radiation damages due to NIEL and, consequently, design dedicated shielding solutions. Tables 7.2 and 7.3 show the percentage of detected counts generated by a particular class of particles, in "AC off" and "AC on" mode. Only particles that cause at least the 0.1% of the energy deposits are listed: photons, protons, electrons, positrons and neutrons. With "others" we classified all the counts generated by particles not listed here.
The total fraction of the detected counts induced by a given particle interaction with the detectors is normalized for the incoming flux of each class, so that the listed values must be intended for each second of spacecraft exposure to the radiation environment.
More than 60% of the final background counts are induced by photonic interactions, especially if the emitted source is given by X–rays (CXB and X-ray albedo). Electrons follow as second source of background, with a fraction in the 20% - 30% range. We do not find a significant fraction of events induced by leaking primary protons (included in the "others" class), that can be responsible for the instruments loss of performances. As already cited, the shape of the neutron

Case A: AC (plastic) + Passive shield - AC off

Particle	Det.	Photons	Electrons	Positrons	Neutrons	Others
CXB	LED	90.7%	9.3%	/	/	/
	HED	94.8%	5.0%	0.2%	/	/
Protons	LED	24.5%	66.9%	1.3%	4.2%	3.1%
	HED	43.4%	50.5%	1.3%	2.2%	2.6%
Albedo electrons	LED	58.0%	40.3%	1.7%	/	/
	HED	73.5%	25.0%	1.5%	/	/
Albedo positrons	LED	54.7%	36.9%	9.4%	/	/
	HED	71.4%	22.8%	5.9%	/	/
X-ray albedo	LED	90.2%	9.8%	/	/	/
	HED	95.8%	4.2%	/	/	/
γ-ray albedo	LED	58.1%	37.3%	4.6%	/	/
	HED	70.9%	24.7%	4.4%	/	/
Albedo neutrons	LED	5.0%	3.8%	/	91.2%	/
	HED	16.2%	3.8%	/	79.7%	0.3%
Total	LED	59.3%	29.5%	2.4%	8.4%	0.5%
	HED	71.4%	19.2%	1.77%	7.24%	0.4%

Table 7.2: Percentage of detected counts generated by photons, electrons, positrons and neutrons in "AC off" mode ("others" collects the sum of counts induced by others particles). The total values are normalized for the number of detected counts induced by each class of particles and the simulated exposure time.

Case A: AC (plastic) + Passive shield - AC on

Particle	Det.	Photons	Electrons	Positrons	Neutrons	Others
CXB	LED	91.4%	8.6%	/	/	/
	HED	95.1%	4.5%	0.2%	/	/
Protons	LED	9.1%	72.7%	/	9.1%	7.2%
	HED	21.4%	61.9%	/	11.9%	4.8%
Albedo electrons	LED	/	/	/	/	/
	HED	/	/	/	/	/
Albedo positrons	LED	75.0%	25.0%	/	/	/
	HED	76.9%	15.4%	7.7%	/	/
X-ray albedo	LED	90.5%	9.5%	/	/	/
	HED	95.8%	4.2%	/	/	/
γ-ray albedo	LED	59.3%	36.7%	4.1%	/	/
	HED	70.9%	24.8%	4.4%	/	/
Albedo neutrons	LED	2.9%	1.9%	/	95.2%	/
	HED	9.1%	1.8%	/	88.8%	0.2%
Total	LED	62.5%	23.1%	0.2%	12.8%	1.5%
	HED	67.7%	16.9%	2.1%	12.5%	0.8%

Table 7.3: Percentage of detected counts generated by photons, electrons, positrons and neutrons in "AC on" mode ("others" collects the sum of counts induced by others particles). The total values are normalized for the number of detected counts induced by each class of particles and the simulated exposure time.

induced background spectra is steep, as the emitted neutron flux. The reason is that the neutrons, thanks to the neutral charge, weakly interact with the shielding, and are able to directly reach the

focal plane: we find that more than 80% of the detected counts are induced by neutrons. If the AC removes the coincidence events, about 20% of the proton induced background is given by the sum of neutrons and other secondary particles. Protons are in fact an important source of secondary neutrons within the shielding (see e.g. Gehrels (1992)), which in turn can trigger the production of radioactive nuclides.

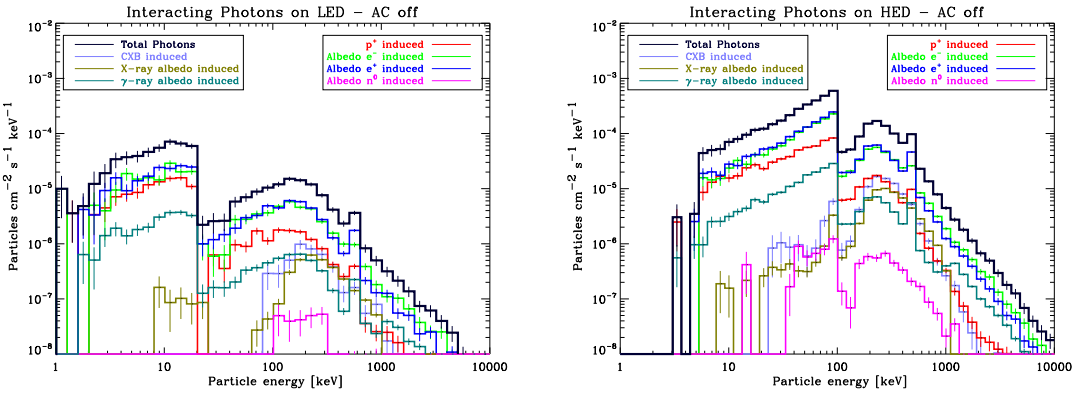

Figure 7.5: LED (left panel) and HED (right panel) energy distribution of the photons that finally interact with the detection plane, for the Case A configuration in "AC off" mode.

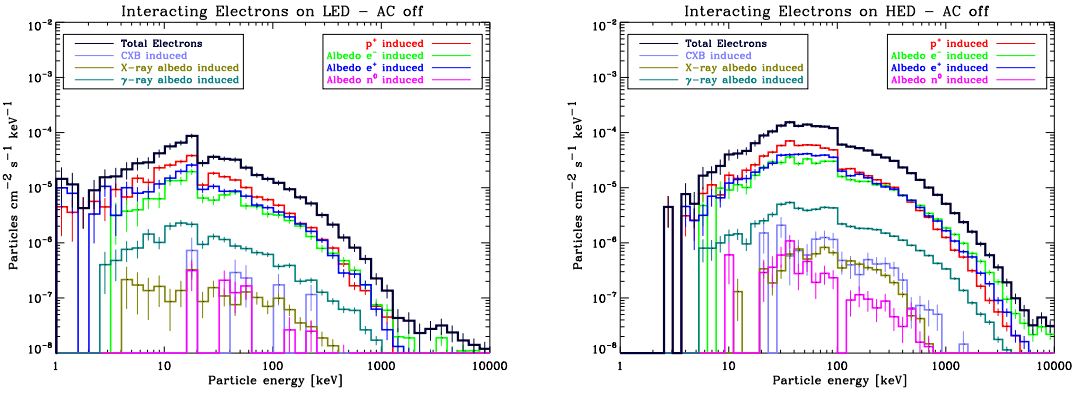

Figure 7.6: LED (left panel) and HED (right panel) energy distribution of the electrons that finally interact with the detection plane, for the Case A configuration in "AC off" mode.

In Figures 7.5 and 7.6 the energy distribution of the photons and electrons depositing an energy amount within the operative energy range of LED and HED, contributing to the detected counts,are plotted. Only the "AC off" case is shown due to the better statistics, but the energy shape is similar with the removal of the AC counts.

In the next sections each background component is fully reviewed, but some general considerations can be anticipated. The energy distribution shows a cut in corrispondence of the upper energy bound of the detectors bandwidth, because we are only plotting the particles that contribute to the background level in the 0.5 - 20 keV (LED) and 5 - 100 keV (HED). Below the cut, the particles

have a kinetic energy within the operative energy rang, and most of them are completely absorbed by the detectors. On the contrary, fast particles above the energy limit are still able to generate background counts by means of scattering or radiative processes. To be noted the 511 keV line, caused by electron-positron annihilations, contributing to the background continuum in Figure 7.5. In addition, the electron and photons energy distribution is similar for all the emitted particles, with different intensity, because the production mechanisms are the same.
The spectrum of the final particle population interacting with the focal plane is also compared to the amount of the energy deposited in the detectors. As defined in Sec. 5.2, the energy deposits produced by the same emitted particle are summed in the analysis process to obtain a count, i.e. the spectral distribution of the energy deposits is not the background spectrum.

7.1.2 CXB component

As expected, the CXB photons, with an energy density peaking in the 10-40 keV band, are almost invisible to a 200 keV threshold active shield, with only the 3.1% of LED and the 1.8% of HED triggered events. In the CXB induced background spectrum, the count rate is roughly constant along the energy range and there is no evidence of significant X-ray fluorescence lines from the passive shielding or the detectors themselves, for the present spectral resolution.
The graded passive shield is designed on the basis of the X-ray attenuation requirements, ensuring an energy averaged CXB induced background level below the limit. In reality, the shielding design must undergo a detailed feasibility study driven by the available mass budget, which could decrease the shielding efficiency as analyzed for the Simbol-X MSC. However the Geant4 simulator allows to easily modify the shielding and spacecraft configuration, and the multi-mission analysis software to correct the AC threshold, so that all the simulations presented here can be rapidly runned with the specifics given by the feasibility study.
Regarding the particles generating the signals, more than 90% of the counts is photon induced, with the electrons more affecting the LED background (9% respect to 5% for the HED). The focal

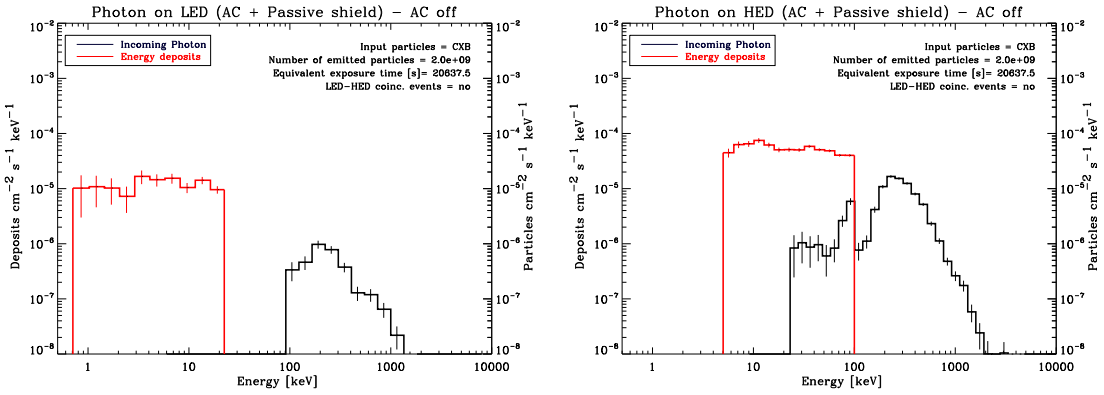

Figure 7.7: CXB induced photons generating the counts on the LED (left panel) and HED (right panel). *black line*: Photons energy distribution; *red line*: photons induced energy deposits on the focal plane.

plane is completely surrounded by an highly attenuating passive shielding below 150 keV leaving no escape to leakage photons in the detection energy range, but background counts are still detected because of Compton scattering. High energy photons (E > 100 keV) can in fact leak through the shield, and reach the focal plane. Where the photoelectric effect loses its efficiency, above 20 keV and 100 keV for respectively the Si and CdTe, the Compton scattering is the dominant process, so that photons with energies above the detectors bandwidth can still deposit an amount of energy within the operative energy range by Compton scatteringd. The proof is the spectral distribution peaking above 100 keV of the photons depositing energy on the focal plane, shown in black in Figure 7.7 for the LED (left panel) and the HED (right panel) while the red curve represents the deposits in the LED and HED energy range. All LED events are generated by photons above 100 keV, while only a small fraction of the HED counts is given by photons in the detection energy range. In the figure it is also clear that no X-ray fluorescence photons from the passive shield hit the focal plane.

7.1.3 Proton component

The active shields, for a 200 keV threshold, removes more than 99% of the proton induced counts, decreasing the HED background level from $\sim 2 \times 10^{-4}$ to $\sim 3 \times 10^{-7}$ cts cm^{-2} s^{-1} keV^{-1}, well below the requirement. The LED overall shape is constant, within the statistical fluctuations, while the HED spectrum shows a steep slope towards higher energies. The analysis of the particle energy distribution generating the counts is presented only for the "AC off" case, due to the low statistics achieved after the AC events removal. The LED background level is mainly affected by electrons induced energy deposits (66.9%, 3 times higher than the photonic component) while an higher impact of the photons is found in the HED count rate. A low fraction of not triggered events is produced by protons (< 3%) and neutrons ($\sim$ 4%). The major source of prompt background around 100 keV for a Ge detector is elastic neutron scattering (Gehrels 1992), without considering the aperture flux (i.e. particles directly reaching the focal plane). Having in mind the low statistical relevance of a 40 counts detection for the HED, a $\sim$ 12% of neutrons induced events is found after the AC triggering.

If a greater passive layers thickness reduces the X-ray leakage, it also increases the proton stopping power with a more intense emission of cascade particles, including photons within the detection energy range. This effect is shown in Figure 7.8 for both the LED (left panel) and the HED (right panel). Respect to the CXB induced background, more X-ray photons with E < 100 keV interact with the focal plane. The HED plot clearly shows the contribution of the absorbed X-ray photons, falling off below 20 keV, and the Compton effect induced energy deposits of the high energy photons, with a constant resulting background level. The 511 keV line, from electron-positron annihilation, is also visible. The descendent slope of the HED background is generated by the electron interactions on the focal plane, plotted in Figure 7.9 (right panel). The electron stopping power decreases of about 1 order of magnitude from 10 keV to 1 MeV, so that a 1 MeV electron releases the 10% of a 10 keV electron energy deposit for the same path length. While low energy electrons are completely absorbed by the HED, hard electrons can still generate signals in

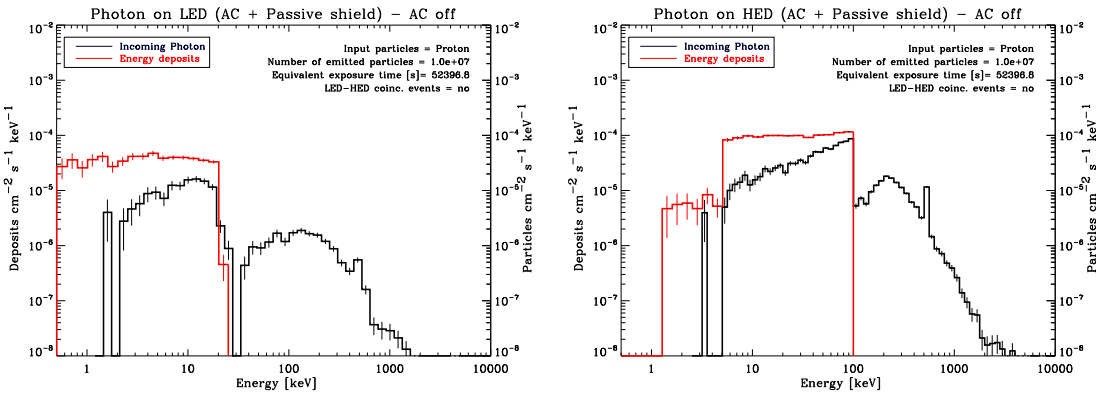

Figure 7.8: Proton induced photons generating the counts on the LED (left panel) and HED (right panel). *black line*: Photons energy distribution; *red line*: Photons induced energy deposits on the focal plane.

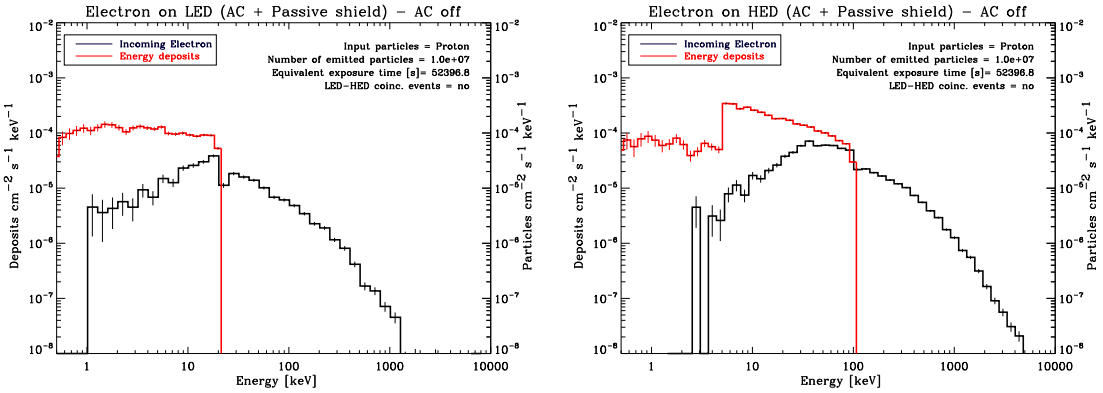

Figure 7.9: Proton induced electrons generating the counts on the LED (left panel) and HED (right panel). *black line*: Electrons energy distribution; *red line*: Electrons induced energy deposits on the focal plane.

the detection energy range, producing in this case a steep slope. The LED background spectrum is also affected by high energy (E > 100 keV) electrons but still keeping a constant shape (Figure 7.9, left panel). The effect of the electrons on the HED background shape is also visible in the NHXM proton induced background spectra (Figure 6.15.)

The triggered proton induced background level is well below the limit, but here the focal plane is completely surrounded by the active shield. If a part of the detector aperture is covered by an only passive material, as in the case of a passive collimator above the LED, a fraction of secondary photons and electrons would hit the detection plane without being triggered, as proved in the NHXM background evaluation. At the same time the spacecraft structure itself, not modelled here, would be an important source of secondary particles.

7.1.4 Electron and positron component

The electron and positron induced spectra overall shape, in "AC off" mode, is approximately constant. Within the statistical fluctuations, no evidence for emission lines is found. As already pointed out, the electron induced background is completely removed by the active shield. The electrons and positrons interaction contribute the $\sim$ 70% of the total AC count rate, for an AC threshold of 200 keV: $\sim$ 690 cts s^{-1} respect to $\sim$ 190 cts s^{-1} for the incoming protons. In the case of the LED background, if the AC events are not removed, the sum of the background level caused by the albedo electrons and positrons account for $\sim$ 50% of the total background level. The high impact of X-ray photons on the HED background hides the descendent slope caused by

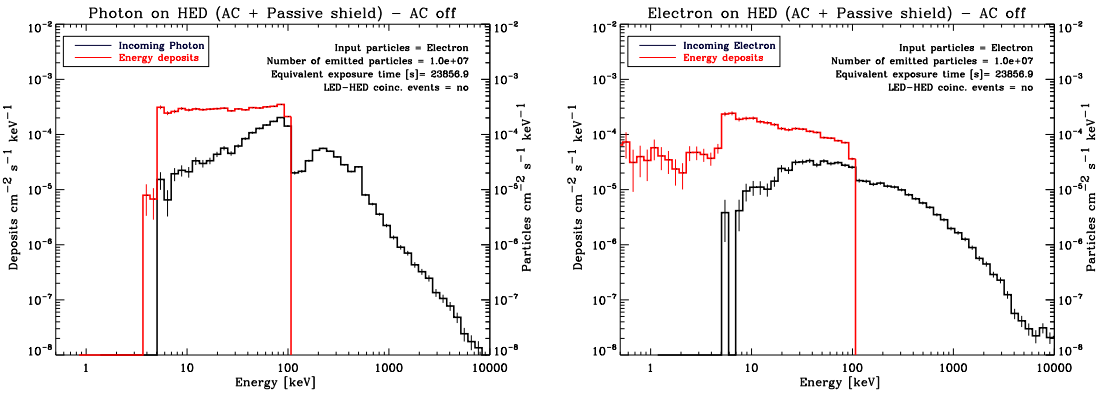

Figure 7.10: Electron induced photons (left panel) and electrons (right panel) generating the counts on the HED. *black line*: Energy distribution; *red line*: Energy deposits on the focal plane.

electron interaction. This is shown in Figure 7.10, with the energy distribution of the photons (left panel) and electrons (right panel) hitting the HED (plotted in black). The positron induced particle spectra are not shown here for simplicity since the same result is found. We can generally affirm that the HED background generated by electronic interactions decreases from lower to higher energies for all the primary charged particles (protons, electrons and positrons).

7.1.5 Albedo photons component

If we do not apply the AC triggering, the γ-rays induced background is two times higher respect to the flux caused by the X-ray albedo. However, the higher energy allows the AC to be more efficient ($\sim$ 40% for γ-rays), so that the residual flux after the removal of the AC events is comparable. The albedo γ-rays are also responsible for a high flux of electrons (25% - 35%) on the detection plane. It is interesting to compare the photonic flux causing the background counts for the two atmospheric photons populations, plotted in Figures 7.11 and 7.12 for X-rays and γ-rays respectively. As for the CXB, most of the interacting photons have energies above 100 keV, but if γ-ray photons ($>$ 1 MeV) are emitted, the cascades of secondaries result in a higher flux of low energy photons, totally absorbed by the detectors. The γ-ray albedo also triggers the production of 511 keV annihilation photons, depositing energies also in the LED bandwidth.

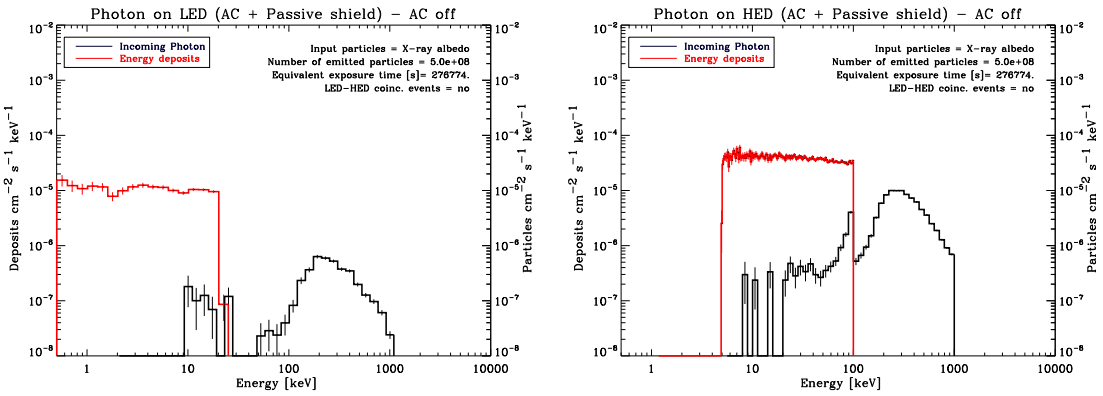

Figure 7.11: The X-ray albedo induced photons generating the counts on the LED (left panel) and HED (right panel). *black line*: Energy distribution; *red line*: Energy deposits on the focal plane.

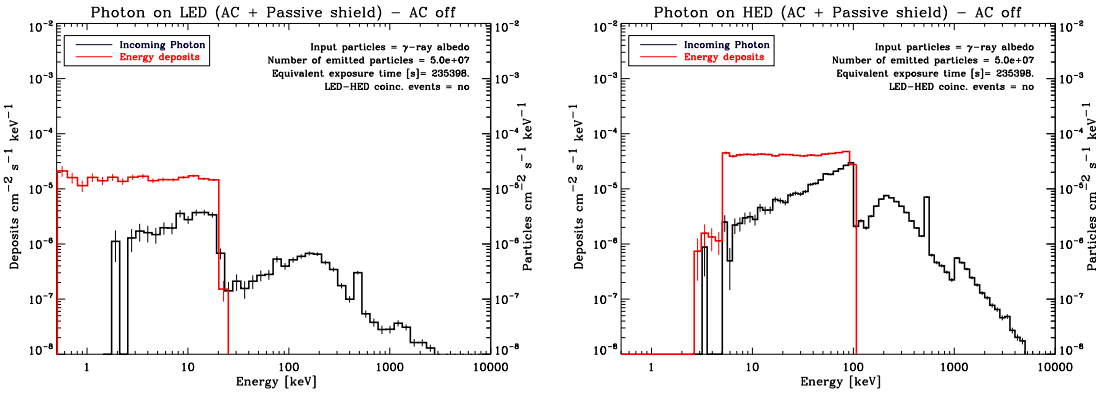

Figure 7.12: The γ-ray albedo induced photons generating the counts on the LED (left panel) and HED (right panel). *black line*: Energy distribution; *red line*: Energy deposits on the focal plane.

7.1.6 Albedo neutrons component

The neutrons induced background spectra are extremely steep for the HED case, contrary to the LED background. The energy averaged background levels are low, $\sim 2 \times 10^{-5}$ cts cm^{-2} s^{-1} keV^{-1}, with and without the AC events. However, the HED background reaches a value of $\sim 10^{-4}$ cts cm^{-2} s^{-1} keV^{-1} in the 5 - 10 keV energy range, so the albedo neutrons can heavy affect the soft part of the spectrum. Contrary to the charged particles, where Coulomb interactions dominate, the neutrons can easily cross the AC without depositing an amount of energy above the threshold (see Sec. 4.1.3), and leak to the focal plane. As result, the AC rate is low (~ 6 cts s^{-1}) and $> 80\%$ of the particles interacting with the detectors are neutrons. In Figure 7.13 the energy distribution of the interacting neutron flux is plotted for LED (left panel) and HED (right panel).
In Sec. 4.1.3 we anticipated that neutrons prompt background can be caused by elastics scatterings. This effect is nicely visualized in the HED neutron energy distribution. The interacting neutrons are distributed in the 100 keV - 10 MeV energy range, while the energy deposits fall below 100 keV,

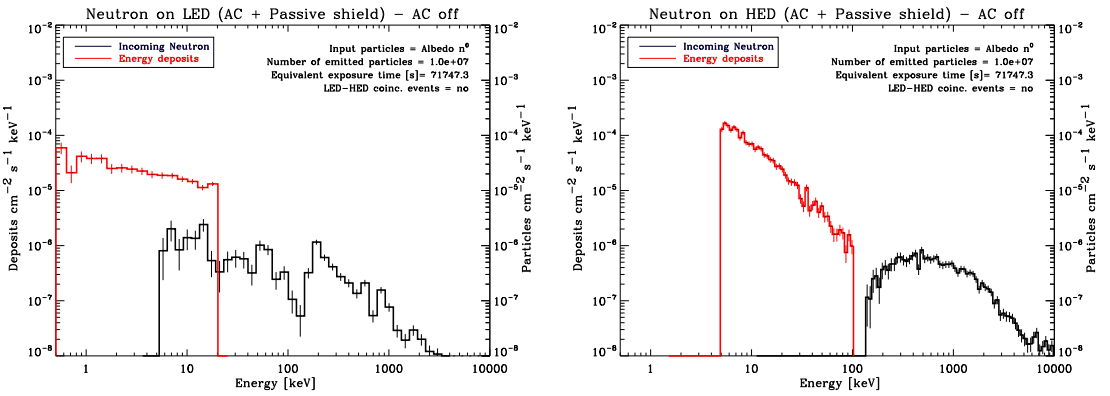

Figure 7.13: The albedo leaking neutrons generating the counts on the LED (left panel) and HED (right panel). *black line*: Energy distribution; *red line*: Energy deposits on the focal plane.

with a decreasing beheaviour that reflects the power law distribution of the space albedo neutrons. In the interaction with the LED Si layer, the neutrons elastic scattering is intead less effective in the background production, probably due to both the Si lower atomic number and operative energy range.

7.2 Case B background evaluation

The active shield count rate could be reduced by passively absorbing the incoming radiation before the interaction with the AC. The second configuration (Case B) analyzed keeps a plastic scintillator as AC (with a threshold of 200 keV), but placed inside the passive shielding system. The resulting background spectra are shown in Figures 7.14 and 7.15. As for the Case A study, the summary

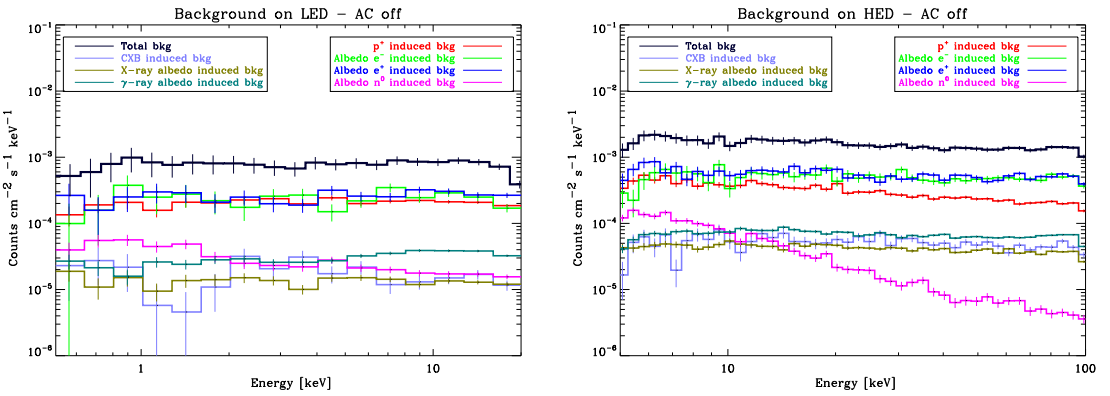

Figure 7.14: LED (left panel) and HED (right panel) background spectra for the CaseB configuration in "AC off" mode for each class of emitted particles. The black line refers to the total background flux. The AC threshold is 200 keV.

of the background results is listed in Table 7.4. The total background count rate, obtained by summing the contribution of each class of particles is $\sim 8 \times 10^{-4}$ and $\sim 3 \times 10^{-4}$ cts cm^{-2} s^{-1}

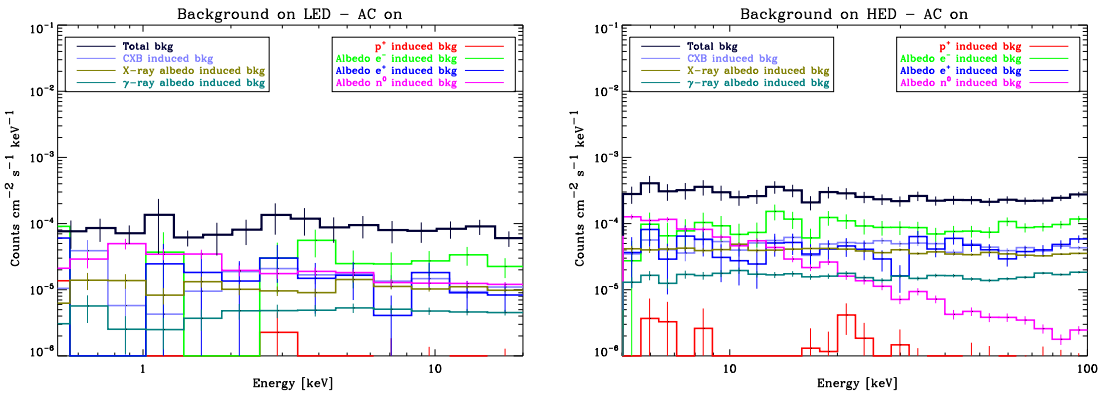

Figure 7.15: LED (left panel) and HED (right panel) background spectra for the Case B configuration in "AC on" mode for each class of emitted particles. The black line refers to the total background flux. The AC threshold is 200 keV.

Passive + AC (plastic) Case B		Background count rate [cts cm^{-2} s^{-1} keV^{-1}]			
Input	Det.	AC off	AC on	Trig. counts	AC [cts s^{-1}]
CXB	LED	$(1.58 \pm 0.11) \times 10^{-5}$	$(1.30 \pm 0.10) \times 10^{-5}$	17.9%	5.5
	HED	$(4.94 \pm 0.10) \times 10^{-5}$	$(4.51 \pm 0.10) \times 10^{-5}$	8.6%	
Protons	LED	$(2.01 \pm 0.05) \times 10^{-4}$	$(0.50 \pm 0.22) \times 10^{-6}$	99.8%	148.0
	HED	$(2.57 \pm 0.03) \times 10^{-4}$	$(0.75 \pm 0.01) \times 10^{-6}$	99.7%	
Albedo electrons	LED	$(2.37 \pm 0.13) \times 10^{-4}$	$(2.65 \pm 0.42) \times 10^{-5}$	88.8%	177.3
	HED	$(4.00 \pm 0.10) \times 10^{-4}$	$(9.23 \pm 0.40) \times 10^{-5}$	81.5%	
Albedo positrons	LED	$(2.71 \pm 0.11) \times 10^{-4}$	$(1.20 \pm 0.23) \times 10^{-5}$	95.6%	178.8
	HED	$(5.30 \pm 0.08) \times 10^{-4}$	$(5.49 \pm 0.23) \times 10^{-5}$	91.7%	
X-ray albedo	LED	$(1.31 \pm 0.04) \times 10^{-5}$	$(1.08 \pm 0.04) \times 10^{-5}$	17.8%	4.4
	HED	$(3.99 \pm 0.03) \times 10^{-5}$	$(3.62 \pm 0.03) \times 10^{-5}$	9.1%	
γ-ray albedo	LED	$(3.36 \pm 0.06) \times 10^{-5}$	$(4.67 \pm 0.23) \times 10^{-6}$	86.1%	25.2
	HED	$(6.64 \pm 0.45) \times 10^{-5}$	$(1.62 \pm 0.02) \times 10^{-5}$	75.6%	
Albedo neutrons	LED	$(2.06 \pm 0.07) \times 10^{-5}$	$(1.54 \pm 0.06) \times 10^{-5}$	25.5%	17.4
	HED	$(1.73 \pm 0.03) \times 10^{-5}$	$(1.27 \pm 0.03) \times 10^{-5}$	26.8%	
Total	LED	$(7.98 \pm 0.31) \times 10^{-4}$	$(8.26 \pm 0.89) \times 10^{-5}$	/	556.8
	HED	$(1.46 \pm 0.02) \times 10^{-3}$	$(2.47 \pm 0.08) \times 10^{-4}$		

Table 7.4: Background count rate, in cts cm^{-2} s^{-1} keV^{-1}, for the Case B configuration, resulting from an AC threshold of 200 keV.

keV^{-1} for LED (AC off) and HED (AC on) respectively.

Placing the plastic AC within the passive shielding casues an extreme increase of the electron and positrons induced background levels, despite the removal of the AC coincidence events, with a value of $\sim 9 \times 10^{-5}$ cts cm^{-2} s^{-1} keV^{-1} for the electronic HED background, accounting for $\sim 30\%$ of the total level. The reason must be found in the presence of the passive layers as first volume encountered by the charged particles: the primary particle is completely absorbed, but in turn it produces a wealth of secondary particles at lower energies, some of them falling below the AC

threshold. In the Case A, instead, the AC is directly exposed to the space radiation environment, and it is able to trigger the charged particles interactions. In operative telescopes in space, an amount of passive material, as carrying structure, is always present outside the scintillator, so that the resulting background level in the Case B is closer to what expected in a real observation. We have to point out, however, that the main absorber and grading materials are optically thicker than a single layer of 1 - 2 mm thich Al expected for the external AC structure. The simulation of the Case A with the addition of an external layer of Al would clarify this effect.
The slowing down of the particles as approaching the AC is also evident from the γ-ray albedo induced background. In this case, photons above 1 MeV lose their energy by scattering and produce secondaries that are intercepted by the AC, which is able to trigger more than 70% of the emitted γ-rays.
As expected, placing the AC inside the passive shielding decreases the AC count rate: from Case A to Case B, the AC rate is reduced of $\sim 50\%$.

7.3 Case C background evaluation

The use of organic scintillators as active shield allows to reduce the mass budget, thanks to the lighter components, with no secondary activation lines and an higher feasibility respect to inorganic (BGO, NaI) anticoincidence systems, which in turn ensure an higher absorption efficiency. The choice between an organic and inorganic active shield should follow a detailed analysis of the background and AC count rate as a function of the AC threshold, with a parallel comparison of the background spectra. As a first step, we show the background flux for an inorganic AC shield made of NaI, placed within the passive shielding. The evaluation is only performed for an AC threshold of 200 keV, to compare the results, altough lower operative energies (tens of keV) can be achieved by means of inorganic scintillators. Also the same thickness (3.8 mm) is used for the NaI scintillator, even if it requires higher volumes. The background spectra are shown in Figures 7.16 and 7.17, for the "AC off" and "AC on" modes. The simulated total background levels are

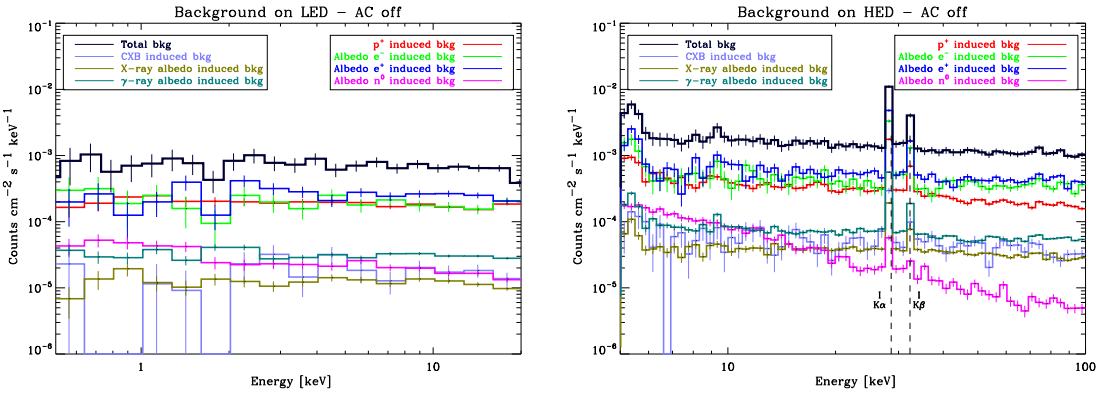

Figure 7.16: LED (top panel) and HED (bottom panel) background spectra for the Case C configuration in "AC off" mode for each class of emitted particles. The black line refers to the total background flux. The AC threshold is 200 keV.

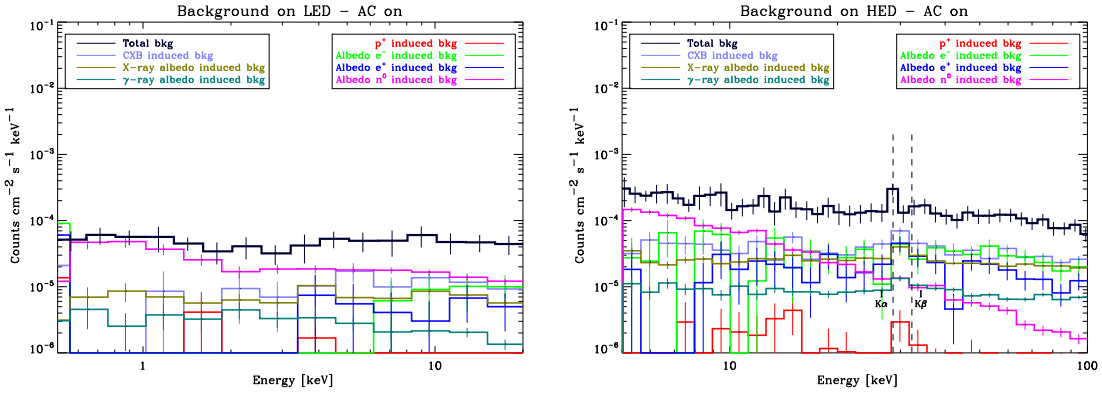

Figure 7.17: LED (top panel) and HED (bottom panel) background spectra for the Case C configuration in "AC on" mode for each class of emitted particles. The black line refers to the total background flux. The AC threshold is 200 keV.

Passive + AC (NaI) Case C		Background count rate [cts cm^{-2} s^{-1} keV^{-1}]			
Input	Det.	AC off	AC on	Trig. counts	AC [cts s^{-1}]
CXB	LED	$(1.71 \pm 0.16) \times 10^{-5}$	$(1.06 \pm 0.13) \times 10^{-5}$	38.4%	35.0
	HED	$(4.75 \pm 0.14) \times 10^{-5}$	$(3.38 \pm 0.12) \times 10^{-5}$	28.8%	
Protons	LED	$(1.80 \pm 0.42) \times 10^{-4}$	$(0.20 \pm 0.14) \times 10^{-6}$	99.9%	148.1
	HED	$(2.69 \pm 0.03) \times 10^{-4}$	$(0.63 \pm 0.13) \times 10^{-6}$	99.8%	
Albedo electrons	LED	$(1.88 \pm 0.11) \times 10^{-4}$	$(6.62 \pm 2.09) \times 10^{-6}$	96.5%	247.4
	HED	$(4.41 \pm 0.09) \times 10^{-4}$	$(2.84 \pm 0.22) \times 10^{-5}$	93.6%	
Albedo positrons	LED	$(2.49 \pm 0.11) \times 10^{-4}$	$(4.41 \pm 1.39) \times 10^{-6}$	98.2%	216.0
	HED	$(5.56 \pm 0.08) \times 10^{-4}$	$(1.70 \pm 0.14) \times 10^{-5}$	96.9%	
X-ray albedo	LED	$(1.19 \pm 0.04) \times 10^{-5}$	$(7.03 \pm 0.28) \times 10^{-6}$	40.8%	25.6
	HED	$(3.65 \pm 0.03) \times 10^{-5}$	$(2.35 \pm 0.03) \times 10^{-5}$	35.7%	
γ-ray albedo	LED	$(3.07 \pm 0.06) \times 10^{-5}$	$(2.25 \pm 0.16) \times 10^{-6}$	92.7%	51.3
	HED	$(7.11 \pm 0.05) \times 10^{-5}$	$(8.0 \pm 0.15) \times 10^{-6}$	88.8%	
Albedo neutrons	LED	$(1.98 \pm 0.07) \times 10^{-5}$	$(1.66 \pm 0.06) \times 10^{-5}$	15.8%	7.2
	HED	$(2.09 \pm 0.04) \times 10^{-5}$	$(1.50 \pm 0.03) \times 10^{-5}$	28.3%	
Total	LED	$(6.96 \pm 0.03) \times 10^{-4}$	$(4.77 \pm 0.59) \times 10^{-5}$	/	730.6
	HED	$(1.44 \pm 0.02) \times 10^{-3}$	$(1.26 \pm 0.06) \times 10^{-4}$		

Table 7.5: Background count rate, in cts cm^{-2} s^{-1} keV^{-1}, for the Case C configuration, resulting from an AC threshold of 200 keV.

$\sim 7 \times 10^{-4}$ cts cm^{-2} s^{-1} keV^{-1} for the LED (AC off) and $\sim 10^{-4}$ cts cm^{-2} s^{-1} keV^{-1} for the HED (AC on), below the top level requirements for the NHXM mission.

If we only consider the energy averaged background level, the background, in "AC on" mode is lower respect to the Case B, altough the inorganic AC is placed within the passive shielding. The shielding efficiency for the NaI is in fact higher respect to plastic scintillators, and it also results is a lower AC count rate respect to the Case A ($\sim$ 730 cts s^{-1}). The use of an inorganic scintillator seems to guarantee the best performance, if only the energy averaged background level is

analyzed. Here comes the necessity, in the background analysis, of producing not only the energy averaged count rate but most of all the spectral distribution of the background counts. In the HED background spectra intense Iodium K fluorescence lines appear, an emission still present in the spectra produced with the removal of the AC events. The latter is also characterized by a lower statistical significancy, so that the larger energy bin reduces the line intensity. The production of secondary emission by inorganic scintillators is a well known effect, and it validates the consistency of the simulation.
The bump below 6 keV visible in the HED spectrum in "AC off" mode is the sum of unresolved escape peaks emission lines. The I K lines are so intense to trigger the CdTe fluorescence emission: the Iodium Kα and Kβ photons are photoelectrically absorbed, while the resulting CdTe X-ray fluorescence escapes from the detection plane, leaving an energy deposit, due to the electron cloud locally absorbed, equal to the difference between the Iodium and the CdTe fluorescence energies. Since the HED energy range start from 5 keV, we only see the effect of the Cd escape peaks, with a difference between the main I Kα (28.6 keV) and Cd Kα (23.2 keV) of $\sim$ 5.4 keV. Without the events detected by the AC, a considerable fraction of the I fluorescence emission is removed, so that in the HED spectrum in "AC on" mode the escape peaks are no more visible.
It is worth noticing the higher NaI efficiency in triggering the background events induced by X-ray and γ-ray photons, resulting in a lower photonic induced baclground level.

7.4 AC threshold analysis

All the previous results in "AC on" mode are based on a 200 keV threshold of the active shielding. The Geant4 simulator analysis software allows to change the minimum operative energy of the AC without running a new simulation. Here we take into account the Case B configuration, i.e. composed by an external passive shielding surrounding the plastic AC, to evaluate the dependancy of the background and AC rate as a function of the AC threshold, for the following values: 200 keV (fully analyzed in the previous Sections), 400 keV, 600 keV, 800 keV and 1 MeV. The reason for chosing the Case B geometry is that the presence of external passive layers is probably closer to the actual results for the attenuation of the albedo electrons and positrons induced background. The inorganic AC, instead, is usually operated at lower thresholds.
In Figure 7.18 (left panel) the AC count rate, in cts s^{-1}, is plotted as a function of the AC operative energy: lowering the AC threshold from 1 MeV to 200 keV produces a slight increase of the AC rate, from $\sim$ 430 cts s^{-1} to $\sim$ 550 cts s^{-1}. It also uniformly increases from 1 MeV to 600 keV and from 400 keV to 200 keV, but in the 400 - 600 keV range the AC rate is weakly influenced by the threshold change. If we analyze the effect on the total background level (Figure 7.18, right panel), the LED (blue line) and HED (red line) background flux is reduced of a factor $\sim$ 2 in the range of the evaluated AC thresholds. It is also visible the 2 - 3 factor higher HED background respect to the LED, due to the higher thickness and atomic number. Similarly to the AC count rate, the background level decreases of $\sim$ 40% from 1 MeV to 600 keV, but of only $\sim 15 - 20\%$ from 600 keV to 200 keV.
Evaluating the impact of each class of particles on the background flux helps to better understand

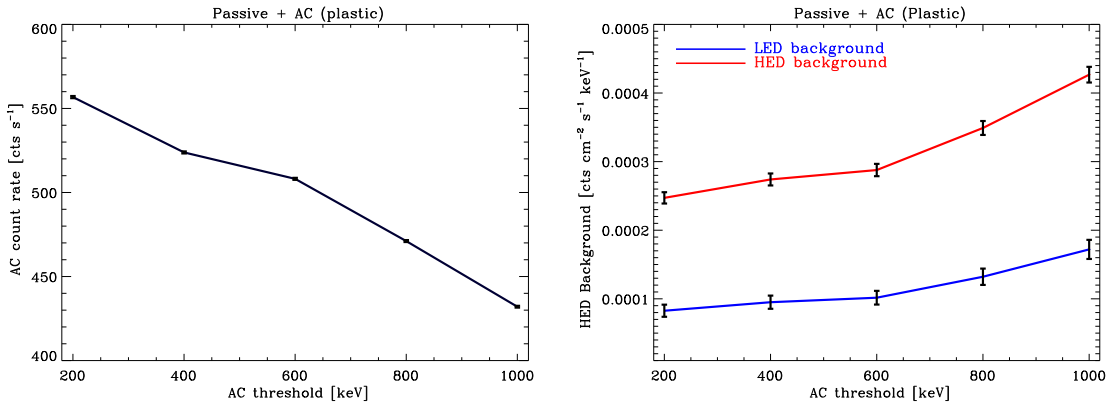

Figure 7.18: AC count rate (left panel) and a comparison (right panel) of the LED (blue line) and HED (red line) background levels as a function of the AC thresholds.

this behaviour, as plotted in Figure 7.19 for the LED (left panel) and HED (right panel), with the black line referring to the total values. Among all the interacting particles, the albedo electrons and

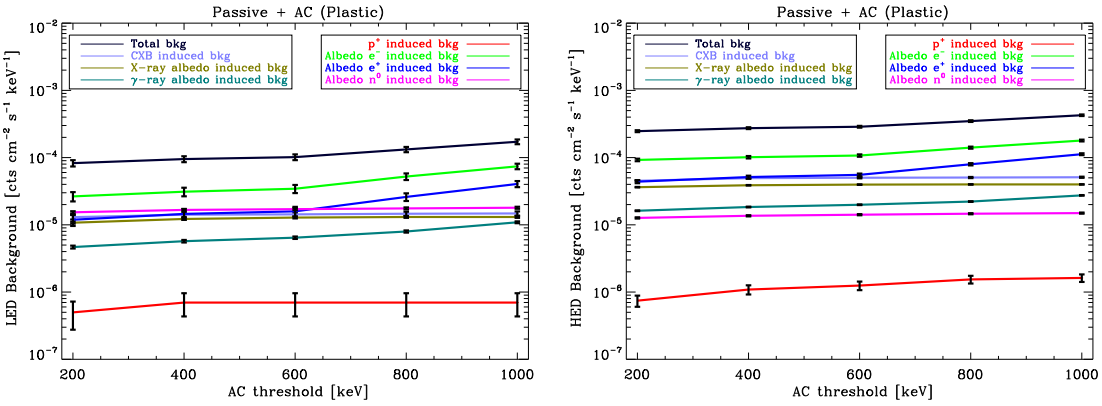

Figure 7.19: LED (left panel) and HED (right panel) energy averaged background levels, in "AC on" mode, for different AC thresholds. To be noted that the y-axis is plotted in a logarithmic scale.

positrons and γ-rays induced background slope, becoming steeper for a threshold above 600 keV, affects the overall behaviour. The most probable reason is that these particles generate a wealth of secondary electrons and photons with E> 600 keV that strongly contribute to the background, also by means of the 511 annihilation line, and that can be traced by the AC. A lower AC threshold, as a consequence, does not produce the same increment in the active shield triggering efficiency.

7.5 Summary of the results

The interaction of the LEO space radiation environment with a simplified active and passive shielding geometry is performed to analyze the impact of each class of particle on the background

level and AC count rate for three different configurations of the active shield:

- Case A: plastic AC placed outside the passive layers;
- Case B: plastic AC placed inside the passive layers;
- Case C: inorganic AC placed inside the passive layers;

The background is evaluated for an AC threshold of 200 keV, but the dependency of the background flux and AC rate on the active shield operating energy is also analyzed for the Case B.
The energy averaged background levels, in "AC off" mode for the LED and in "AC on" mode for the HED, for the three cases are summarized in Figure 7.20, left and right panels respectively, while the Figure 7.21 shows a comparison of the resulting AC count rates. The labels X-ray and γ-ray refer to the albedo emission.

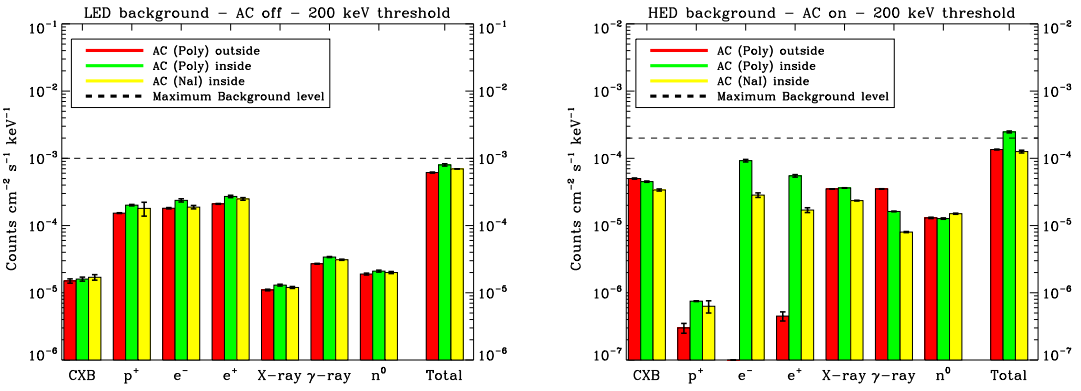

Figure 7.20: The LED, left panel, and HED, right panel, energy averaged background levels, in "AC off" and "AC on" mode respectively, for the Case A (external plastic AC, red columns), Case B (internal plastic AC, green columns) and Case C (internal NaI AC, yellow columns).

The general results regarding the prompt background evaluation of a hard X-ray focusing telescope in LEO are:

- If a plastic AC shield is applied, the total background level is roughly constant, within the statistical fluctuations, both with and without the removal of the AC events, while the NaI as active scintillator produces intense Iodium fluorescence lines.
- Among all the background sources, the neutron induced background level shows a steep slope, especially in the HED spectrum, reaching a value of $\sim 10^{-4}$ cts cm^{-2} s^{-1} keV^{-1} in the 5 - 10 keV energy range, because of elastic scattering of the leaking primary neutrons. Considering the low interaction with the AC, this background source could be reduced by an extremely low AC threshold.
- No evidence for statistically significant passive shield X-ray fluorescence lines is found, i.e. the graded shield is well designed.

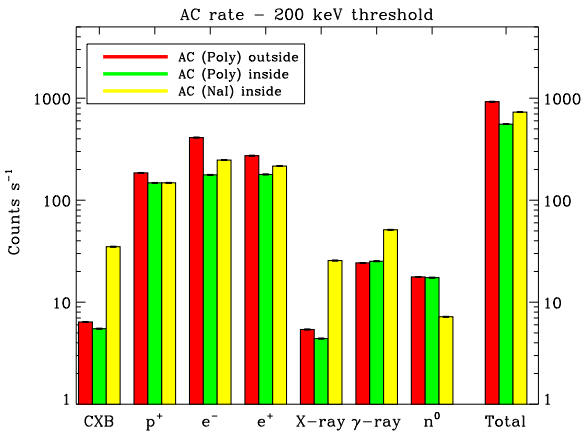

Figure 7.21: The AC count rate for the Case A (external plastic AC, red columns), Case B (internal plastic AC, green columns) and Case C (internal NaI AC, yellow columns).

- If the active shield triggering is not applied, more than 85% of the background counts is generated by the interaction of the charged particles population in LEO, which are confirmed to be the major source of background for an only passive shielding system.

- Applying the removal of the AC events, the background results are different depending on the AC design. If the AC is placed outside without any surrounding structure (Case A), the major source of background is photonic. If the passive layers are placed outside (Case B), electrons and positrons generate secondaries below the AC threshold, affecting the 30% of the total level if the plastic AC is used, while reaching values comparable to the photonic component for an inorganic active shield. The shielding efficiency to protons is instead slightly affected by the external passive material.

- The averaged background level obtained is in general agreement with the NHXM maximum allowed background level, if we also add an increase of 50% due to the delayed background component.

- Altough the simulated Geant4 mass model does not take into account the spacecraft mass budget or the presence of the collimator above the focal plane, this result shows that, with an accurate shielding optmization, the NHXM top level scientific requirements can be achieved.

- From the analysis of the particles interacting with the detectors plane, the photons contribute to more than 60% of the background counts, followed by electrons. A significant fraction ($\sim$ 10%) of neutrons induced counts is also found, as induced by the primary leaking or proton induced neutrons.

- Altough the passive shielding avoids the X-ray photons to reach the focal plane, a constant photonic induced background is found as produced by Compton scattering of the leaking high energy ($>$ 100 keV) photons.

- The total AC count rate ranges from $\sim$ 900 cts s^{-1} for the Case A to $\sim$ 500 cts s^{-1} for the Case B, that in turn would produce a dead time fraction $< 20\%$ for the Simbol-X LED design. A small increase in the AC rate ($\sim$ 100 cts s^{-1}) is produced by reducing the AC threhsold, for the Case B, from 1 MeV to 200 keV, while achieving a factor 2 gain in the background reduction.

- The NaI scintillator, placed within the passive layers, still gives a lower AC rate respect to the Case A, but without increasing the energy averaged background level.

Selecting the best configuration is not easy. If we consider the best performances in terms of background and AC rate, an inorganic scintillator seems to be the best choice, if the fluorescence emission can be removed by the calibration or on ground filtering criteria. We have also to underline that the AC placed inside the passive shielding could reduce the latter delayed emission, but the detectors would also be reached by the AC decays, and the inorganic scintillator are proved to be high sources of delayed emission (Armstrong & Colborn 1992). The best choice could be represented by a combination of the two types, a plastic and inorganic AC, to fully exploit their performances. As example, a shielding configuration with an external passive shielding, an internal inorganic AC and the addition of a plastic active shield close to the focal plane could ensure a low prompt background and AC count rates, but also reduce the delayed background component.
The Simbol-X DSC background, referring to a shielding configuration similar to the Case A, is strongly affected by the GCR flux in HEO (Sec. 6.1.3), which also causes $\sim$ 40% observation time losses on the LED due to the high AC rate. Placing the plastic AC inside the passive layers largely increase the albedo electrons and positrons induced background, that are not present in HEO, while slightly affects the protonic background, resulting below 10^{-6} cts cm^{-2} s^{-1} keV^{-1}. As result, **placing the AC system within the passive shielding helps to reduce the AC count rate of an X-ray telescope operating in HEO, while keeping the same background flux**.

Chapter 8

Summary and future remarks

Hard X-ray focusing telescopes will increase the sensitivity achieved by collimated or indirect imaging systems by more than two orders of magnitude, increasing the effective area in the hard X-ray domain by means of high reflectivity optics, a large field of view and long focal lengths (> 10 m). Since the minimum detectable flux is strictly connected to the background level, the evaluation and characterization of the background flux and spectrum is a key requirement for its minimization and the selection of efficient shielding solutions. Altough the Simbol-X, NHXM and IXO missions have been proposed as case studies for the present thesis, the achieved results can be generalized to any future hard X-ray focusing telescope, given the common technological concept and the related background issues.
The whole background minimization process that leads from the modelling of the space radiation environment to the background spectra production is reported. The original contribution can be summarized as follows:

AGN hard X-ray view: The study of the accretion-reflection processes and the search for highly absorbed AGN, a research field that will be deeply improved by the future hard X-ray telescopes, is presented for four Swift/BAT high luminosity AGN. The full energy range spectral analysis is achieved by adding together the Suzaku soft (XIS, at the focus of the X-ray telescope) and hard (the collimated, non imaging HXD) instruments, plus the 9-month averaged BAT spectrum. A significant Compton reflection is found in 3C 452, the only Compton thick candidate of the sample. Despite the similarity in terms of column density and radio emission respect to 3C 105, the latter shows an obiquitous flux variability in the soft band, probably associated to the scattering component, while only an upper limit to the Compton reflection is found. For a full understanding of this observational dichotomy, high sensitivity and resolution observations in the hard X-ray domain are required, as proved by the NHXM simulated view of 3C 105.

Space radiation environment: The background flux strongly depends on the mission orbit, because it defines the space radiation environment encountered by the spacecraft. The flux and energy distribution of the particles classes selected as the major sources of prompt background are analyzed in detail for a High Elliptical Orbit (e.g. XMM-Newton and

Chandra) and a Low Earth Orbit (e.g. Suzaku, Swift), the latter modelled for the low inclination planned for the NHXM mission. The CXB flux is common for both the orbits, altough it is partially shielded by the Earth in LEO, but high energetic protons (the GCR flux) are expected in HEO. On the contrary, the Earth's magnetic field shielding translates into a low energy cut off ($\sim$ 10 GeV) for primary protons in LEO, but the spacecraft proximity to the Earth's atmosphere adds high fluxes of low energy albedo particles. The resulting spectral models are used as input for the background Monte Carlo simulations.

Shielding design: The focal plane aperture solid angle outside the field of view must be completely covered by the shielding system, to stop the particles, especially CXB photons, directed to the instruments. The long focal length, achieved by means of an extendable bench or the formation flight technique, avoids the possibility of using a telescope tube joining the mirror unit to the focal plane. The instruments residual aperture is instead blocked through the summed contribution of a collimator on top the intruments and a planar sky screen around the mirror module. The design of the system is evaluated in terms of the geometry and mass budget for the Simbol-X and NHXM missions, accounting for a possible lateral dithering ($\pm$5 mm) between the focal plane and the mirror module. The evaluated sky screen diameter ranges from 1.2 m (NHXM) to more than 2 m (Simbol-X), and the resulting mass budget, for the thicknesses required to efficiently stop photons below 150 keV, is unfeasible. These results led to a significant reduction of the sky screen passive shielding thickness. In the analysis of the shielding composition, a main absorber of Pb, thanks to the lower density and the higher attenuation power, is preferable if the grading is not applied, while a Ta or W main absorber must be chosen to decrease the grading mass budget.

Shielding optimization: The shielding optimization, in this case a lower thickness driven by the maximum mass budget available, requires a careful analysis of the residual background level, by means of both analytical calculations and Monte Carlo particles transport codes simulations. The IXO collimator length is reduced by adding a set of concentric disks on the top of the focal plane, sharing the same telescope axis. An analytical computation of the residual CXB induced background, due to the sum of the leaking and secondary photons, has been developed for the preliminary shielding trade-off study. Altough the baseline HXI upper operative energy is 40 keV, so that the Kα and Kβ fluorescence falls above the limit, the presence of the concentric disks, facing the CXB flux at the detector side, causes intense Lyman lines around 10 keV, and the grading is required.

The BoGEMMS project: On the basis of the Geant4 Monte Carlo toolkit, the BoGEMMS, Bologna Geant4 Multi-Mission Simulator, has been developed at INAF/IASF Bologna. The code is a multi-mission flexible tool, designed to be applied to any high energy mission for which the shielding and instruments performances are required. It allows to interactively build a 3D model of the payload and to produce background spectra as a real observation in space. Its capabilities are exploited to characterize the background flux for the Simbol-X and NHXM missions, as well for the analysis of the XMM-Newton soft proton scattering and

to test the active and passive shielding efficiency in LEO.

Background evaluation: The Simbol-X MSC and DSC background flux is simulated, after validating the BoGEMMS code by simulating the LED and HED detection efficiency and comparing it to the tabulated values from literature. Starting from an available mass budget of 15 kg, the MSC passive shielding model is created and exposed to the CXB flux. Despite the fact that X-ray fluorescence lines are still visible in the spectrum, the overall shape is consistent with an allowed maximum level of 10^{-5} cts cm^{-2} s^{-1} keV^{-1}. The DSC payload design instead requires a further optimization, since an intense CXB leakage below 10 keV is found and the GCR induced background alone is more than two times the requirement. The total AC count rate of ~ 2000 cts s^{-1} would also translate into an observation time loss of $\sim 40\%$, for a LED read out time of 256 μs. An important results comes from the NHXM proton induced background level, where the geomagnetic cut off produces a decrease of more than 50% respect to the Simbol-X case, with an AC count rate 5 times lower. The analysis of the proton path allows to discover that more than 85% of the background counts is generated by protons directed to the passive collimator, after the removal of the AC events, and the use of an active collimator could efficiently reduce the charged particle induced background.

Soft protons funnelling: A simplified model of the XMM-Newton optics and focal plane is created to simulate the soft proton induced background spectrum and compare it to a real observation, for the input proton flux detected by the Equator-S satellite at a 70000 km altitude and the activation of both the multiple and Firsov scattering. We are able to reproduce the proton vignetting on the focal plane, but the simulated count rate still underestimates the observed intensity. The proton angular distribution at the exit of the Simbol-X optics is simulated for a preliminary design of the proton diverter.

The background in LEO: The total background flux for different shielding configurations in LEO, using a simplified geometry model, is simulated to select the major sources of background and consequently optimize the payload design. The overall background shape is constant. In "AC off" mode the charged particles induced background dominates, but the protons are efficiently removed by the AC. If the passive shielding is placed externally, the electrons and positrons induced background level is considerable high in "AC on" mode, for an AC threshold of 200 keV. Albedo neutrons are weakly interacting and are able to directly reach the focal plane, depositing energy by means of elastic scatterings. As a result, the neutron induced HED background spectrum shows a power law shape. Altough the passive shielding is designed to stop X-ray photons up to 150 keV, a constant residual background is found due to the Compton scattering of leaking high energy (100 keV - 1 MeV) photons. The best shielding configuration in terms of background and AC rate is given by an inorganic shield placed inside the passive layers, with the addition of an internal plastic scintillator or a passive layer to trigger/absorb the intense fluorescence lines of the active shield.

The Simbol-X and NHXM background evaluation has been included in the missions feasibility studies within the respective background group activities. The analysis of the four BAT AGN with

Suzaku will be published in a dedicated paper, as well as the general results on the background flux in LEO.
Finally, some considerations on the future perspectives. The achievement of the scientific objectives of the future hard X-ray telescopes is background driven. With the present thesis we show that the background evaluation is a complex process that requires more than the evaluation of the shielding stopping power. A flexible particle transport code is instead required, coupled with a dedicated analysis software, able to quickly reply to the evolution of the payload design and to reproduce the expected background spectrum in space. However, we also show that the background requirement settled by the scientific goals can be satisfied, and that the proposed breakthrough in the hard X-ray domain observation can be actually achieved. Waiting for that moment, the BoGEMMS project will represent a fundamental tool for the payload design of the future hard X-ray telescopes.

Appendix A

Derivation of a perfect shielding geometry parameters

In this appendix the Simbol–X passive shielding main formulas are derived, starting from the definitions and basic assumption of Section 4.3.
From the perfect shielding requirement, the combination of MSC sky screen and DSC colimator totally shields the focal plane from unwanted photons. As shown in Figure 4.3, this translates into the equivalence:

$$\tan(\theta_{\mathrm{coll}}) = \tan(\theta_{\mathrm{Screen}}) \quad . \tag{A.1}$$

1. **No tolerance case (Section 4.3.1)**
   Following a simple trigonometric approach, we have that:

$$\tan(\theta_{\mathrm{coll}}) = \frac{\mathrm{D_{det}} + \mathrm{s}}{\mathrm{H}} \tag{A.2}$$

$$\tan(\theta_{\mathrm{Screen}}) = \frac{\mathrm{D_{Screen}} + \mathrm{D_{det}}}{2\mathrm{FL}} \quad . \tag{A.3}$$

   From Equation A.1, this risults into:

$$\frac{\mathrm{D_{det}} + \mathrm{s}}{\mathrm{H}} = \frac{\mathrm{D_{Screen}} + \mathrm{D_{det}}}{2\mathrm{FL}} \tag{A.4}$$

   From this expression, we can obtain the diameter of MSC sky screen once the collimator height H is defined. Obviously, even the collimator height can be derived from the sky screen diameter definition. We have:

$$\mathrm{D_{Screen}} = 2\mathrm{FL} \cdot \left(\frac{\mathrm{D_{det}} + \mathrm{s}}{\mathrm{H}} \right) - \mathrm{D_{det}} \tag{A.5}$$

   The distance s between the collimator walls and detection plane is given by the following considerations:

$$\tan(\theta_{\mathrm{FOV}}) = \frac{\mathrm{D_{opt}} - \mathrm{D_{det}}}{2\mathrm{FL}} \tag{A.6}$$

$$= \frac{\mathrm{s}}{\mathrm{H}} \tag{A.7}$$

$$\mathrm{s} = \frac{\mathrm{H}(\mathrm{D_{opt}} - \mathrm{D_{det}})}{2\mathrm{FL}} \tag{A.8}$$

$$\mathrm{D_{coll}} = \mathrm{D_{det}} + 2\mathrm{s} \tag{A.9}$$

Replacing the expression A.8 in the A.5, the MSC sky screen diameter formula shown in Section 4.3.1 is given:

$$D_{Screen} = 2FL \cdot \left(\frac{D_{det}}{H} \right) + D_{opt} - 2D_{det} \quad . \tag{A.10}$$

2. **Alignment tolerance case (Section 4.3.2)**
With an alignment tolerance $\pm T$ perpendicular to the telescope axis, the collimator diameter becomes:

$$D_{coll} = D_{det} + 2s + 2T \tag{A.11}$$

and the equivalence A.4 translates into:

$$\frac{D_{det} + s + 2T}{H} = \frac{D_{Screen} + D_{det}}{2FL} \quad . \tag{A.12}$$

The final MSC sky screen diameter, from Equations A.8 and A.12, is then given by:

$$D_{Screen} = 2FL \cdot \left(\frac{D_{det} + 2T}{H} \right) + D_{opt} - 2D_{det} \quad . \tag{A.13}$$

Appendix B

The BoGEMMS physics list

B.1 Particles

- Bosons: charged geantino, gamma, geantino, optical photon
- Leptons: electron, positron, mu$^-$, mu$^+$, tau$^-$, tau$^+$, electron neutrino, muon neutrino, tau neutrino, anti-electron neutrino, anti-muon neutrino, anti-tau neutrino
- Mesons: pi$^+$, pi$^-$, pi^0, K$^+$, K$^-$, K0L, K0S
- Baryons: proton, neutron, lambda, sigma$^+$, sigma$^-$, sigma^0, xi$^-$, xi^0, omega$^-$, anti-proton, anti-neutron, anti-lambda, anti-sigma$^+$, anti-sigma$^-$, anti-sigma^0, anti-xi$^-$, anti-xi^0, anti-omega$^-$
- Ions: deuteron, triton, helium-3, alpha, generic ion[1]

B.2 Electromagnetic processes

- Gamma:
  - Low Energy Rayleigh Scattering
  - Low Energy Photoelectric Effect
  - Low Energy Compton Scattering
  - Low Energy Gamma Conversion
- Electron:
  - Multiple Scattering
  - Low Energy Ionization
  - Low Energy Bremsstrahlung

[1] All nuclei except ^{1}H, ^{2}H, ^{3}H, ^{3}He, and ^{4}He.

- Positron:
  - Multiple scattering
  - Ionization
  - Bremsstrahlung
  - Annihilation
- Mu^-:
  - Multiple scattering
  - Ionization
  - Bremsstrahlung
  - Pair production
  - Capture
- Mu^+:
  - Multiple scattering
  - Ionization
  - Bremsstrahlung
  - Pair production
- Tau^-, Tau^+:
  - Multiple scattering
  - Ionization
- Generic ion, charged short lived particles:
  - Multiple scattering
  - Low Energy Ionization
- Proton, anti-proton, pi^+, pi^-, K^+, K^-, $sigma^-$, anti-$sigma^-$, $sigma^+$, anti-$sigma^+$, Xi^-, anti-Xi^-, $omega^-$,anti-$omega^-$:
  - Multiple scattering
  - Ionization

B.3 Hadronic processes

- Proton:
  - Elastic Scattering
  - Inelastic Scattering
- Neutron:
  - Elastic Scattering
  - Inelastic Scattering
  - Fission
  - Capture
- Deuteron, triton, alpha, generic ion, :
  - Elastic Scattering
  - Inelastic Scattering
- Anti-proton:
  - Elastic Scattering
  - Inelastic Scattering
  - Annihilation
- Anti-neutron:
  - Elastic Scattering
  - Inelastic Scattering
  - Annihilation
- Pi^+, K^+, K0L, K0S, lambda, anti-lambda, $sigma^-$, anti-$sigma^-$, $sigma^+$, anti-$sigma^+$, Xi^-, anti-Xi^-, Xi^0, anti-Xi^0, $omega^-$, anti-$omega^-$:
  - Elastic Scattering
  - Inelastic Scattering
- Pi^-, K^-:
  - Elastic Scattering
  - Inelastic Scattering
  - Absorption

Bibliography

Abdo, A. A., Ackermann, M., Ajello, M., et al. 2010, ApJ

Abdo, A. A., Ackermann, M., Ajello, M., et al. 2010a, Phys. Rev. Lett., 104, 101101

Abdo, A. A., Ackermann, M., Ajello, M., et al. 2009, Phys. Rev. D, 80, 122004

Adriani, O., Bazilevskaya, G. A., Barbarino, G. C., et al. 2009, Bulletin of the Russian Academy of Science, Phys., 73, 568

Agostinelli, S., Allison, J., Amako, K., et al. 2003, Nuclear Instruments and Methods in Physics Research Section A: Accelerators, Spectrometers, Detectors and Associated Equipment, 506, 250

Ajello, M., Greiner, J., Sato, G., et al. 2008, ApJ, 689, 666

Alcaraz, J., Alpat, B., Ambrosi, G., et al. 2000a, Physics Letters B

Alcaraz, J., Alvisi, D., Alpat, B., et al. 2000b, Physics Letters B, 472, 215

Allison, J., Amako, K., Apostolakis, J., et al. 2006, IEEE Trans. Nucl. Sci., 53, 270

Alonso-Herrero, A., Pérez-González, P. G., Alexander, D. M., et al. 2006, ApJ, 640, 167

Amako, K., Guatelli, S., Ivanchencko, V., et al. ????

Anders, E. & Grevesse, N. 1989, Geochim. Cosmochim. Acta, 53, 197

Antonucci, R. 1993, ARA&A, 31, 473

Armstrong, T. & Colborn, B. 1992, International Journal of Radiation Applications and Instrumentation. Part D. Nuclear Tracks and Radiation Measurements, 20, 101 , special Issue Space Radiation

Armstrong, T. W., Chandler, K. C., & Barish, J. 1973, J. Geophys. Res, 78, 2715

Armstrong, T. W., Colborn, B. L., Dietz, K. L., & Ramsey, B. D. 1999, in High Energy Radiation Background in Space, ed. P. H. Solomon, 82–+

Armstrong, T. W., Colborn, B. L., & Watts, J. W. 1990, NASA STI/Recon Technical Report N, 91, 15953

Arnaud, K. A. 1996, in Astronomical Society of the Pacific Conference Series, Vol. 101, Astronomical Data Analysis Software and Systems V, ed. G. H. Jacoby & J. Barnes, 17–+

Aschenbach, B. 2007, in Proc. of SPIE, Vol. 6688

Ballantyne, D. R., Everett, J. E., & Murray, N. 2006, ApJ, 639, 740

Ballantyne, D. R., Fabian, A. C., & Ross, R. R. 2002, MNRAS, 329, L67

Balucinska-Church, M. & McCammon, D. 1992, ApJ, 400, 699

Barcons, X., Barret, D., Bautz, M., et al. 2011, ArXiv e-prints

Barth, J. 1997, Applying Computer Simulation Tools to Radiation Effects Problems, IEEE Nuclear and Space Radiation Effects Conference

Bassani, L., Dadina, M., Maiolino, R., et al. 1999, ApJS, 121, 473

Baum, S. A., Heckman, T. M., Bridle, A., van Breugel, W. J. M., & Miley, G. K. 1988, ApJS, 68, 643

Beckmann, V., Soldi, S., Ricci, C., et al. 2009, A&A, 505, 417

Bianchi, S., Guainazzi, M., & Chiaberge, M. 2006, A&A, 448, 499

Bidoli, V., Casolino, M., de Pascale, M., et al. 2002, Annales Geophysicae, 20, 1693

Biermann, P. L., Gaisser, T. K., & Stanev, T. 1995, Phys. Rev. D, 51, 3450

Black, A. R. S., Baum, S. A., Leahy, J. P., et al. 1992, MNRAS, 256, 186

Blackwell, W. C., Minow, J. I., O'Dell, S. L., et al. 2000, in Proc. of SPIE, Vol. 4140, 111–122

Bloser, P. F., Narita, T., Jenkins, J. A., et al. 2002, in Proc. of SPIE, ed. K. A. Flanagan & O. H. W. Siegmund, Vol. 4497, 88–99

Boezio, M., Carlson, P., Francke, T., et al. 1999, ApJ, 518, 457

Boldt, E. 1987, in IAU Symposium, Vol. 124, Observational Cosmology, ed. A. Hewitt, G. Burbidge, & L. Z. Fang, 611–615

Bombelli, L., Fiorini, C., Ricca, A. A., et al. 2008, IEEE Nuclear Science Symposium Conference, 1772

Braito, V., Reeves, J. N., Sambruna, R. M., & Gofford, J. 2011, ArXiv e-prints

Brandt, W. N. & Hasinger, G. 2005, ARA&A, 43, 827

Brautigam, D. H. & Bell, J. T. 1995, Environmental Research Papers, PL-TR-95-2128

Cappi, M., Panessa, F., Bassani, L., et al. 2006, A&A, 446, 459

Chiaberge, M., Macchetto, F. D., Sparks, W. B., et al. 2002, ApJ, 571, 247

Chipaux, R., Briel, U., Bulgarelli, A., et al. 2008, Mem. S.A.It., 79, 234

Churazov, E., Sazonov, S., Sunyaev, R., & Revnivtsev, M. 2008, MNRAS, 385, 719

Churazov, E., Sunyaev, R., Revnivtsev, M., et al. 2007, A&A, 467, 529

Claret, A. 2006, CEA/Dapnia/SAp Internal report

Comastri, A., Setti, G., Zamorani, G., & Hasinger, G. 1995, A&A, 296, 1

Cusumano, G., Artale, M. A., Mineo, T., et al. 2007, in Society of Photo-Optical Instrumentation Engineers (SPIE) Conference Series, Vol. 6688, Society of Photo-Optical Instrumentation Engineers (SPIE) Conference Series

Daly, E. J., Lemaire, J., Heynderickx, D., & Rodgers, D. J. 1996, IEEE Trans. Nucl. Sci., 43, 403

De Luca, A. & Molendi, S. 2004, A&A, 419, 837

Dean, A. J., Bird, A. J., Diallo, N., et al. 2003, Spa. Sci. Rev., 105, 285

Dean, A. J., Fan, L., Byard, K., Goldwurm, A., & Hall, C. J. 1989, A&A, 219, 358

Dean, A. J., Lei, F., & Knight, P. J. 1991, Space Science Reviews, 57, 109

Derome, L., Buénerd, M., Barrau, A., et al. 2000, Physics Letters B, 489, 1

Derome, L., Buenerd, M., & Liu, Y. 2001, Physics Letters B, 515, 1

Diamond-Stanic, A. M., Rieke, G. H., & Rigby, J. R. 2009, ApJ, 698, 623

Dichter, B. K. & Woolf, S. 2003, IEEE Trans. Nucl. Sci., 50, 2292

Dickey, J. M. & Lockman, F. J. 1990, ARA&A, 28, 215

Dirks, B. P. F., Ferrando, P., Briel, U., et al. 2006, in Proc. of SPIE, Vol. 6276

Donzelli, C. J., Chiaberge, M., Macchetto, F. D., et al. 2007, ApJ, 667, 780

Eguchi, S., Ueda, Y., Terashima, Y., Mushotzky, R., & Tueller, J. 2009, ApJ, 696, 1657

Evans, D. A., Worrall, D. M., Hardcastle, M. J., Kraft, R. P., & Birkinshaw, M. 2006, ApJ, 642, 96

Ferguson, C. 2000, UoS-GSPM-Tech Technical note

Ferrando, P., Arnaud, M., Cordier, B., et al. 2004, in Proc. of SPIE, Vol. 5168, 65–76

Ferrarese, L. & Merritt, D. 2000, ApJL, 539, L9

Ferri, A. 2008, Thales Alenia Space

Fiore, F., Arnaud, M., Briel, U., et al. 2008, Mem. S.A.It., 79, 38

Fiore, F., Perola, G. C., Pareschi, G., et al. 2004, in Proc. of SPIE, Vol. 5488, 933–943

Fiore, F., Puccetti, S., Brusa, M., et al. 2009, ApJ, 693, 447

Fioretti, V. & Malaguti, G. 2010, INAF/IASF Bologna Technical Report

Fioretti, V., Malaguti, G., Foschini, L., & Bulgarelli, A. 2008a

Fioretti, V., Malaguti, G., Mereghetti, S., & Pareschi, G. 2008b, Mem. S.A.It.

Fioretti, V., Malaguti, G., & Palumbo, G. G. C. 2006, Master thesis

Frank, M. I., Prussin, S. G., Peterson, P. F., & Tobin, M. T. 2001, Journ. Radioan. Nucl. Chem., 249, 145

Fukazawa, Y., Mizuno, T., Watanabe, S., et al. 2009, Publ. Astron. Soc. Japan, 61, 17

Gehrels, N. 1985, Nuclear Instruments and Methods in Physics Research, Section A, 239, 324

Gehrels, N. 1992, Nuclear Instruments and Methods in Physics Research, Section A, 313, 513

Ghisellini, G., Haardt, F., & Matt, G. 1994, MNRAS, 267, 743

Giacconi, R., Gursky, H., Paolini, F. R., & Rossi, B. B. 1962, Physical Review Letters, 9, 439

Giacconi, R., Reidy, W. P., Vaiana, G. S., van Speybroeck, L. P., & Zehnpfennig, T. F. 1969, Space Science Reviews, 9, 3

Gilli, R., Comastri, A., & Hasinger, G. 2007, A&A, 463, 79

Gilli, R., Salvati, M., & Hasinger, G. 2001, A&A, 366, 407

Gleeson, L. J. & Axford, W. I. 1968, ApJ, 154, 1011

Gold, R. E., Krimigis, S. M., Hawkins, III, S. E., et al. 1998, Space Science Reviews, 86, 541

Gruber, D. E., Matteson, J. L., Peterson, L. E., & Jung, G. V. 1999, ApJ, 520, 124

Guainazzi, M., Matt, G., & Perola, G. C. 2005, A&A, 444, 119

Guatelli, S., Mantero, A., Mascialino, B., Pia, M., & Zampichelli, V. 2007, IEEE Trans. Nucl. Sci., 54, 594

Gurian, I. A., Mazets, E. P., Proskura, M. P., & Sokolov, I. A. 1979, Geomagn. Aeron., 19, 11

Haardt, F. & Maraschi, L. 1991, ApJL, 380, L51

Hajek, M., Berger, T., & Vana, N. 2004, Radiation Protection Dosimetry, 110, 343

Hardcastle, M. J., Alexander, P., Pooley, G. G., & Riley, J. M. 1998, MNRAS, 296, 445

Harrison, F., Boggs, S., Christensen, F., et al. 2011, in Bulletin of the American Astronomical Society, Vol. 43, American Astronomical Society Meeting Abstracts #217, 254.25–+

Hasinger, G. 2008, A&A, 490, 905

Hathaway, D. H., Wilson, R. M., & Reichmann, E. J. 1993, in Bulletin of the American Astronomical Society, Vol. 25, Bulletin of the American Astronomical Society, 1216–+

Hauf, S., Kuster, M., Hoffmann, D. D. H., et al. 2010, Proceedings of the SNA-MC2010 Monte Carlo Conference

Heber, B., Kopp, A., Gieseler, J., et al. 2009, ApJ, 699, 1956

Heynderickx, D., Kruglanski, M., Pierrard, V., et al. 1999, IEEE Trans. Nucl. Sci., 46, 1475

Hodges-Kluck, E. J., Reynolds, C. S., Cheung, C. C., & Miller, M. C. 2010, ApJ, 710, 1205

Holt, S. S., Mushotzky, R. F., Boldt, E. A., et al. 1980, ApJL, 241, L13

Hopkins, P. F., Hernquist, L., Cox, T. J., Robertson, B., & Springel, V. 2006, ApJS, 163, 50

Hubbell, J. H., Trehan, P. N., Singh, N., et al. 1994, Journal of Physical and Chemical Reference Data, 23, 339

Ikeda, S., Awaki, H., & Terashima, Y. 2009, ApJ, 692, 608

Imbert, C. 2008, Detector payload meeting, DCT/TV/MT

Imhof, W. L., Nakano, G. H., & Reagan, J. B. 1976, J. Geophys. Res, 81, 2835

Inoue, Y., Totani, T., & Ueda, Y. 2008, ApJL, 672, L5

Isobe, N., Tashiro, M., Makishima, K., et al. 2002, ApJL, 580, L111

Itoh, T., Done, C., Makishima, K., et al. 2008, Publ. Astron. Soc. Japan, 60, 251

Jackson, N. & Rawlings, S. 1997, MNRAS, 286, 241

Jansen, F., Lumb, D., Altieri, B., et al. 2001, A&A, 365, L1

Jean, P., Vedrenne, G., Roques, J. P., et al. 2003, A&A, 411, L107

Jenkins, R. W., Lockwood, J. A., Ifedili, S. O., & Chupp, E. L. 1970, J. Geophys. Res, 75, 4197

Kappadath, S. C., Ryan, J., Bennett, K., et al. 1996, A&AS, 120, C619+

Kendziorra, E., Clauss, T., Meidinger, N., et al. 2000, in Proc. of SPIE, Vol. 4140, 32–41

Knoll, G. F. 2000, Radiation detection and measurements, 3rd Ed., ed. John Wiley and Sons, Inc., New York

Kokubun, M., Makishima, K., Takahashi, T., et al. 2007, Publ. Astron. Soc. Japan, 59, 53

Koldashov, S. V., Mikhailov, V. V., & Voronov, S. A. 1995, in International Cosmic Ray Conference, Vol. 4, International Cosmic Ray Conference, 993–+

Kolodziejczak, J. J., Elsner, R. F., Austin, R. A., & O'Dell, S. L. 2000, in Proc. of SPIE, Vol. 4140, 135–143

Krause, M. O. 1979, J. Phys. Chem. Ref. Data.

Kücükönder, A., Durdu, B., Söğüt, O., & Büyükkasap, E. 2004, Journal of Radioanalytical and Nuclear Chemistry, 260, 89

Kuntz, K. D. & Snowden, S. L. 2008, A&A, 478, 575

La Franca, F., Fiore, F., Comastri, A., et al. 2005, ApJ, 635, 864

Laing, R. A., Jenkins, C. R., Wall, J. V., & Unger, S. W. 1994, in Astronomical Society of the Pacific Conference Series, Vol. 54, The Physics of Active Galaxies, ed. G. V. Bicknell, M. A. Dopita, & P. J. Quinn, 201–+

Laurent, P., Lechner, P., Authier, M., et al. 2008, Mem. S.A.It., 79, 32

Lavigne, J. M., Niel, M., Vedrenne, G., et al. 1982, ApJ, 261, 720

Leahy, J. P., Black, A. R. S., Dennett-Thorpe, J., et al. 1997, MNRAS, 291, 20

Lei, F., Nartallo, R., Nieminen, P., et al. 2004, IEEE Trans. Nucl. Sci., 51, 3408

Li, G., Webb, G. M., Le Roux, J. A., Zank, G. P., & Wiedenbeck, M. E. 2008, in Astronomical Society of the Pacific Conference Series, Vol. 385, Numerical Modeling of Space Plasma Flows, ed. N. V. Pogorelov, E. Audit, & G. P. Zank, 31–+

Lobakov, A., Lyagushin, V., Panasyuk, M., Petrov, V., & Shavrin, P. 1992, International Journal of Radiation Applications and Instrumentation. Part D. Nuclear Tracks and Radiation Measurements, 20, 55 , special Issue Space Radiation

Lockwood, J. A. & Friling, L. A. 1968, J. Geophys. Res, 73, 6649

Lockwood, J. A., Ifedili, S. O., & Jenkins, R. W. 1973, J. Geophys. Res, 78, 7978

Lumb, D. H., Warwick, R. S., Page, M., & De Luca, A. 2002, A&A, 389, 93

Madrid, J. P., Chiaberge, M., Floyd, D., et al. 2006, ApJS, 164, 307

Magdziarz, P. & Zdziarski, A. A. 1995, MNRAS, 273, 837

Maiolino, R., Salvati, M., Bassani, L., et al. 1998, A&A, 338, 781

Malaguti, G., Bassani, L., Cappi, M., et al. 1999, A&A, 342, L41

Malaguti, G., Pareschi, G., Ferrando, P., et al. 2005, in Proc. of SPIE, ed. O. Citterio & S. L. O'Dell, Vol. 5900, 159–171

Marshall, F. E., Boldt, E. A., Holt, S. S., et al. 1980, ApJ, 235, 4

Massaro, F., Harris, D. E., Tremblay, G. R., et al. 2010, ApJ, 714, 589

Matt, G., Brandt, W. N., & Fabian, A. C. 1996, MNRAS, 280, 823

McHardy, I. M., Koerding, E., Knigge, C., Uttley, P., & Fender, R. P. 2006, Nature, 444, 730

Meffert, J. D. & Gussenhoven, M. S. 1994, Environmental Research Papers, PL-TR-94-2218

Menn, W., Hof, M., Reimer, O., et al. 2000, ApJ, 533, 281

Metropolis, N. & Ulam, S. 1949, J. Amer. Stat. Ass., 44, 335

Metzger, A. E., Anderson, E. C., Van Dilla, M. A., & Arnold, J. R. 1964, Nature, 204, 766

Miller, L., Turner, T. J., & Reeves, J. N. 2008, A&A, 483, 437

Miniutti, G., Fabian, A. C., Anabuki, N., et al. 2007, Publ. Astron. Soc. Japan, 59, 315

Mitsuda, K., Bautz, M., Inoue, H., et al. 2007, Publ. Astron. Soc. Japan, 59, 1

Mizuno, T., Fukazawa, J., Takahashi, H., et al. 2008, JX-ISAS-SUZAKU-MEMO-2008-03

Mizuno, T., Kamae, T., Godfrey, G., et al. 2004, ApJ, 614, 1113

Morris, D. J., Aarts, H., Bennett, K., et al. 1995, J. Geophys. Res, 100, 12243

Morris, D. J., Aarts, H., Bennett, K., et al. 1998, Advances in Space Research, 21, 1789

Murphy, K. D. & Yaqoob, T. 2009, MNRAS, 397, 1549

Mushotzky, R. F., Done, C., & Pounds, K. A. 1993, ARA&A, 31, 717

Nandra, K. & Pounds, K. A. 1994, MNRAS, 268, 405

Nartallo, R. Daly, E. E. H. N. P. F. L. T. P. 2001, IEEE Trans. Nucl. Sci., 48, 1815

Nartallo, R. 2002, Esa/estec/tos-ema/02-067/RN Tech. Report

Nartallo, R., Evans, H., Daly, E., et al. 2002, Esa/estec/tos-em/00-015/RN Tech. Report

Oberlack, U. 2010, Physics, vol. 3, Issue , id. 21, 3, 21

O'Dell, S. L., Bautz, M. W., Blackwell, W. C., et al. 2000, in Society of Photo-Optical Instrumentation Engineers (SPIE) Conference Series, Vol. 4140, Society of Photo-Optical Instrumentation Engineers (SPIE) Conference Series, ed. K. A. Flanagan & O. H. Siegmund, 99–110

Ogle, P., Whysong, D., & Antonucci, R. 2006, ApJ, 647, 161

Pareschi, G., Basso, S., Citterio, O., et al. 2005, in Proc. of SPIE, Vol. 5900, 47–58

Pareschi, G., Tagliaferri, G., Attinà, P., et al. 2009, in Proc.of SPIE, Vol. 7437

Pareschi, G. & the HEXIT-SAT and SIMBOL-X collaborations. 2004, Memorie della Societa Astronomica Italiana Supplementi, 5, 362

Preszler, A. M., Simnett, G. M., & White, R. S. 1972, Physical Review Letters, 28, 982

Prigozhin, G. Y., Kissel, S. E., Bautz, M. W., et al. 2000, in Proc. of SPIE, Vol. 4140, 123–134

Rasmussen, A., Chervinsky, J., & Golovchenko, J. 1999, RGS-COL-CAL-99009 XMM Project Document

Raymond, J. C. & Smith, B. W. 1977, ApJS, 35, 419

Reames, D. V., Meyer, J. P., & von Rosenvinge, T. T. 1994, ApJS, 90, 649

Reeves, J. N., Gofford, J., Braito, V., & Sambruna, R. 2010, ApJ, 725, 803

Renaud, M., Gros, A., Lebrun, F., et al. 2006, A&A, 456, 389

Risaliti, G. 2002, A&A

Risaliti, G., Elvis, M., & Nicastro, F. 2002, ApJ

Risaliti, G., Maiolino, R., & Salvati, M. 1999, ApJ, 522, 157

Ryan, J., Lockwood, J., & Debrunner, H. 2000, Space Science Reviews, 93, 35, 10.1023/A:1026580008909

Ryan, J. M., Jennings, M. C., Radwin, M. D., Zych, A. D., & White, R. S. 1979, J. Geophys. Res, 84, 5279

Santin, G., Rodgers, D. J., & Fioretti, V. 2009, IEEE Nuclear Science Symposium Conference, 459

Sanuki, T., Motoki, M., Matsumoto, H., et al. 2000, ApJ, 545, 1135

Sazonov, S., Churazov, E., Sunyaev, R., & Revnivtsev, M. 2007, MNRAS, 377, 1726

Schoenmakers, A. P., Mack, K., Lara, L., et al. 1998, A&A, 336, 455

Selesnick, R. S., Looper, M. D., & Mewaldt, R. A. 2007, Space Weather, 5, 4003

Seo, E. S., Ormes, J. F., Streitmatter, R. E., et al. 1991, ApJ, 378, 763

Setti, G. & Woltjer, L. 1989, A&A, 224, L21

Shikaze, Y., Abe, K., Anraku, K., et al. 2003, in International Cosmic Ray Conference, Vol. 7, International Cosmic Ray Conference, 4027–+

Simpson, C. 2005, MNRAS, 360, 565

Simpson, J. G. 1983, Ann. Rev. Nucl. Part. Sci., 33, 323

Smart, D. F. & Shea, M. A. 2005, Advances in Space Research, 36, 2012

Snowden, S. L., Plucinsky, P. P., Briel, U., Hasinger, G., & Pfeffermann, E. 1992, ApJ, 393, 819

Sobolewska, M. A. & Papadakis, I. E. 2009, MNRAS, 399, 1597

Spiga, D., Fioretti, V., Bulgarelli, A., et al. 2008, in Proc. of SPIE, Vol. 7011

Sreekumar, P., Bertsch, D. L., Dingus, B. L., et al. 1998, ApJ, 494, 523

Stassinopoulos, E. G., Brucker, G. J., Nakamura, D. W., et al. 1996, IEEE Trans. Nucl. Sci., 43, 369

Störmer, C. 1930, Z. Astrophys., 1, 237

Strong, A. W., Moskalenko, I. V., & Reimer, O. 2004, ApJ, 613, 962

Strueder, L., Meidinger, N., Pfeffermann, E., et al. 2000, in Proc. of SPIE, Vol. 4012, 342–352

Sullivan, J. D. 1971, 95, 5

Tagliaferri, G., Argan, A., Bellazzini, R., et al. 2010, in Proc. of SPIE, Vol. 7732

Takahashi, T., Abe, K., Endo, M., et al. 2007, Publ. Astron. Soc. Japan, 59, 35

Takahashi, T., Mitsuda, K., Kelley, R., et al. 2010, in Proc. of SPIE, Vol. 7732

Tavani, M., Barbiellini, G., Argan, A., et al. 2009, A&A, 502, 995

Tenzer, C., Briel, U., Bulgarelli, A., et al. 2009, in American Institute of Physics Conference Series, Vol. 1126, American Institute of Physics Conference Series, ed. J. Rodriguez & P. Ferrando, 75–78

Terrier, R., Lebrun, F., Bazzano, A., et al. 2003, A&A, 411, L167

Thompson, D. J. 1974, J. Geophys. Res, 79, 1309

Tiengo, A. 2007, SX-INAF-IASFMI-TN-0001 Tech. Report

Tozzi, P., Gilli, R., Mainieri, V., et al. 2006, A&A, 451, 457

Treister, E., Natarajan, P., Sanders, D. B., et al. 2010, Science, 328, 600

Tueller, J., Baumgartner, W. H., Markwardt, C. B., et al. 2010, ApJS, 186, 378

Tueller, J., Mushotzky, R. F., Barthelmy, S., et al. 2008, ApJ, 681, 113

Tumer, T. O., Finger, M. H., Gordon, E. E., et al. 2004, in Proc. of SPIE, Vol. 5165, 548–553

Türler, M., Chernyakova, M., Courvoisier, T., et al. 2010, A&A, 512, A49+

Turner, M. 2006, SCI-SA/AP/06/0412/cv Tech. Report

Turner, T. J., George, I. M., Nandra, K., & Mushotzky, R. F. 1997, ApJS, 113, 23

Turner, T. J. & Pounds, K. A. 1989, MNRAS, 240, 833

Ueda, Y., Akiyama, M., Ohta, K., & Miyaji, T. 2003, ApJ, 598, 886

Ueda, Y., Eguchi, S., Terashima, Y., et al. 2007, ApJL, 664, L79

Van Allen, J. A. 1959, Sci. Am, 200, 39

Vette, J. I. 1991, NSSDC/WDC-A-R&S

Weidenspointner, G., Bennett, K., van Dijk, R., et al. 1998, Advances in Space Research, 21, 1781

Weidenspointner, G., Harris, M. J., Sturner, S., Teegarden, B. J., & Ferguson, C. 2005, ApJS, 156, 69

Wells, D. C., Greisen, E. W., & Harten, R. H. 1981, A&AS, 44, 363

Wiedenbeck, M. E., Davis, A. J., Leske, R. A., et al. 2005, in International Cosmic Ray Conference, Vol. 2, International Cosmic Ray Conference, 277–+

Willingale, R. 2000, XRT-LUX-RE-011/1 Technical Report

Wills, K. A., Tadhunter, C. N., Robinson, T. G., & Morganti, R. 2002, MNRAS, 333, 211

Wilms, J., Allen, A., & McCray, R. 2000, ApJ, 542, 914

Winter, L. M., Lewis, K. T., Koss, M., et al. 2010, ApJ, 710, 503

Winter, L. M., Mushotzky, R. F., Reynolds, C. S., & Tueller, J. 2009a, ApJ

Winter, L. M., Mushotzky, R. F., Terashima, Y., & Ueda, Y. 2009b, ApJ

Winter, L. M., Mushotzky, R. F., Tueller, J., & Markwardt, C. 2008, ApJ, 674, 686

Wright, D. 2010, Proceedings of the MC2010 Monte Carlo Conference

Zdziarski, A. A., Poutanen, J., & Johnson, W. N. 2000, ApJ, 542, 703

Zoglauer, A., Weidenspointner, G., Wunderer, C. B., & Boggs, S. E. 2008, IEEE Nuclear Science Symposium Conference

Acknowledgements

"...I seem to have been only like a boy playing on the sea-shore, and diverting myself in now and then finding a smoother pebble or a prettier shell than ordinary, whilst the great ocean of truth lay all undiscovered before me..."

Memoirs of the Life, Writings, and Discoveries of Sir Isaac Newton (1855) by Sir David Brewster

If I am now writing the acknowledgements of my PhD thesis is only thanks to the efforts of many people that I met along the road.
First of all I would like to thank Prof. Giorgio Palumbo, who has been an endless source of wise advices on science and life from the first day when, still an undergrad student, I asked him where to do some "technological stuff". He introduced me to the INAF/IASF Bologna institute, where I met Pino Malaguti, who gave me a pc and a problem to solve. I thank him not only for teaching me anything he could but especially for giving me the freedom of expressing and following my ideas, even when they were wrong, and for always pushing me to the boundaries. Without him and his "Geant4 obsession", the Bologna background group wouldn't exist. He also tried to teach me the dark side of the scientific research (the politics). I hope he failed.
I deeply thank the C++ master Andrea Bulgarelli. Working with him was not only a pleasure but fundamental for my research, giving my ideas a hard-coded form. Without him, the simulator would still be printing "Hello World". I also thank Fulvio Gianotti and Massimo Trifoglio for developing and maintening the hardware/software systems.
I thank Lorella Angelini for giving me the chance to work at the NASA GSFC, where the Suzaku spectral analysis has been conducted, and Richard Mushotzky, for giving me the access to its data and to its deep astrophysical knowledge. They introduced me to the data analysis field, finally teaching me how to use an X-ray telescope, besides "building" it.
I thank all the INAF/IASF Bologna researchers for giving me a relaxed and friendly place to work, and all the PhD team (Margherita, Giulia, Daniela, Pietro, Eleonora, ...) who shared the stress, and will share the party, with me.
I apologize to Fra a Cartu and all the friends in Tolentino for disappearing in the last months: I'll come alive soon.
I thank my family, of course.